UNIVERSIDAD POLITÉCNICA DE MADRID
ESCUELA TÉCNICA SUPERIOR DE INGENIERÍA DE MONTES,
FORESTAL Y DEL MEDIO NATURAL

Seguimiento de las tendencias a largo plazo de la calidad de las aguas continentales a partir del análisis de datos de teledetección: un caso de estudio en la Península Ibérica.

TESIS DOCTORAL

Presentada para optar al título de Doctor por:

Lady Carolina Echavarría Caballero
Ingeniera Topográfica, MSc. Geoinformatics engineering

Madrid, 2024

UNIVERSIDAD POLITÉCNICA DE MADRID
Escuela Técnica Superior de Ingeniería de Montes,
Forestal y del Medio Natural

Doctorado en Ingeniería y Gestión del Medio Natural

Seguimiento de las tendencias a largo plazo de la calidad de las aguas continentales a partir del análisis de datos de teledetección: un caso de estudio en la Península Ibérica.

TESIS DOCTORAL

Presentada para optar al título de Doctor por:

Lady Carolina Echavarría Caballero
Ingeniera Topográfica, MSc. Geoinformatics engineering

Bajo la dirección de:
Dr. María Jesús García García
Dr. José Antonio Domínguez Gómez

Madrid, 2024

Título: Seguimiento de las tendencias a largo plazo de la calidad de las aguas continentales a partir del análisis de datos de teledetección: un caso de estudio en la Península Ibérica.

Autor: Lady Carolina Echavarría Caballero

Programa de Doctorado:Doctorado en Ingeniería y Gestión del Medio Natural

Dirección de tesis:

Dr. María Jesús García García (directora)

Dr. José Antonio Domínguez Gómez (codirector).

Revisores externos:

Tribunal de tesis:

Fecha de defensa:

Con agradecimiento eterno a las mujeres que me precedieron y que pelearon por los derechos que disfruto hoy.

Agradecimientos

Me gustaría expresar mi más profundo agradecimiento a todos aquellos que me han apoyado y guiado a lo largo de esta investigación. En primer lugar, estoy profundamente agradecido a mi directora María Jesús, por su invaluable orientación, paciencia y aliento. Sus valiosos comentarios y su apoyo inquebrantable han sido fundamentales para la finalización de esta tesis.

Estoy en deuda con mis colegas y amigos, los profesores del área de expresión gráfica de mi departamento, quienes me brindaron apoyo moral, asistencia técnica y valiosas discusiones a lo largo de este viaje. Su aliento han sido una fuente de fortaleza.

También me gustaría agradecer el apoyo de mi familia. A mis padres, Argenis y Libardo, gracias por su infinito amor, sacrificios y aliento. A mi pareja, Álvaro, gracias por su confianza inquebrantable en mí y por ser mi apoyo durante los tiempos difíciles. Y a mi Federico, que ha hecho que crezca en mi una fuerza interior que desconocía.

Gracias a todos por vuestro inquebrantable apoyo y aliento. Este logro no hubiera sido posible sin ustedes.

Abstract

Surface continental water bodies play essential roles in ecosystem functioning and human well-being. They serve as habitats for a wide variety of plant and animal species, provide crucial ecosystem services, and are primary sources of freshwater, supporting agricultural production, industry, and urban populations worldwide. Effective management and conservation measures are essential to safeguard biodiversity, ensure water security, and promote sustainable development in the face of environmental challenges.

In the Iberian Peninsula, reservoirs and lakes are vital for water supply, energy production, flood control, ecological health, and socioeconomic development. These water bodies offer numerous benefits that extend beyond their immediate environment, impacting regional and national scales. However, their water quality is highly vulnerable due to a combination of climatic, land use, pollution, biological, and hydraulic factors. The Mediterranean climate, characterized by hot, dry summers and mild, wet winters, exacerbates these vulnerabilities. Climate change is expected to worsen these conditions, leading to more frequent and severe droughts.

Efforts aimed at monitoring these water bodies in the Iberian Peninsula are essential to protect and manage these ecosystems. Long-term monitoring provides crucial data to enable early actions in response to pollution, habitat degradation, or other stressors such as climate change. It also evaluates the effectiveness of management strategies aimed at preserving water quality and ecosystem integrity.

The use of remote sensors is an effective and increasingly popular tool for obtaining essential information to monitor the quality of continental water bodies. Remote sensing offers large-scale coverage, high spatial resolution, and frequent temporal sampling.

Consequently, this thesis aims to study the water quality of continental water bodies based on remote sensing data in the Iberian Peninsula, considering their size and seasonal and long-term variability. The specific objectives are: (1) identify and evaluate remote sensors and derived products that allow the study of water quality in this context; (2) analyse the spatio-temporal variation of water quality based on certain parameters; and (3) study the influence of geographical factors on specific water quality parameters.

To meet these objectives, the atmospherically corrected Landsat TM5 surface reflectance product was initially evaluated and used with the Landsat Ecosystem Disturbance Adaptive Processing System (LEDAPS). This system was used to inventory and study the evolution of water quality in gravel pit lagoons within the Southeast Regional Park (PRSE) in Madrid from 1984 to 2011, based on the transparency parameter measured through the Secchi disk. Surface reflectance values were compared with field-measured reflectance in water bodies, revealing an overestimation of surface reflectance derived from Landsat data. Consequently, a new regression equation was proposed to link in situ Secchi depth (DS) measurements to surface reflectance measured by Landsat 5. This regression was validated and subsequently applied to each image, providing a DS value for each pixel in the time series. The recovered DS values were used to calculate the trophic state of the water masses according to the Organization for Economic Cooperation and Development (OECD) classification. The results show an increase in the surface area of water bodies in the PRSE from 1984 to 2006, as well as an improvement in water quality.

The time series of Secchi disk values obtained from Landsat 5 images were used to analyse temporal and spatial patterns of water quality in the PRSE gravel ponds. The study revealed a seasonal behaviour in water quality, with higher transparency values in autumn and winter (December-February) and lower values in summer (July-August). This pattern can be explained by the relationship between Secchi disk values, temperature, and solar radiation. Furthermore, the 1994 regional park administrative declaration has had a positive impact on water quality, leading to a gradual improvement in the trophic state of the studied water bodies, although they have not yet reached the oligotrophic state.

Using the Landsat 5 surface temperature product, warming trends in lakes and reservoirs across peninsular Spain from 1994 to 2011 were assessed, examining seasonal and geographical variations. The analysis revealed that 87% of the water masses exhibit a warming trend, with an average annual increase in water surface temperature of +0.037 ºC. The greatest temperature increases were observed in the Ebro and Guadalquivir depressions. Temperature changes vary across the peninsula, generally linked to surface air temperature, altitude in mountainous areas, and Atlantic winds in western depressions. The trends indicate a seasonal pattern: in summer, the number of water masses with high temperatures increases, while in autumn, there are more lakes and reservoirs with intermediate temperatures. In winter and spring, the number of water masses with low temperatures decreases and they are located further north.

In conclusion, satellite images, specifically those from the Landsat satellite, have proven to be powerful tools for studying the water quality of continental water bodies in the Iberian Peninsula. The moderate spatial resolution and wide temporal coverage of Landsat make it particularly suitable for studying the numerous bodies of water of different sizes and conditions in this region. The Landsat Collection 2 level 2 product, which includes global surface temperature and surface reflectance products, provides valuable information for water quality monitoring. These products allow the derivation of accurate time series of water quality parameters, such as Secchi disk transparency and water surface temperature, thanks to their atmospheric correction and rigorous methodologies.

Resumen

Los cuerpos de agua continentales superficiales desempeñan funciones indispensables en el funcionamiento de los ecosistemas y el bienestar humano: sirven como hábitat para una gran variedad de especies de plantas y animales, brindan servicios ecosistémicos cruciales, son fuentes primarias de agua dulce, que sustentan la producción agrícola, la industria y las poblaciones urbanas en todo el mundo, por lo que implementar medidas efectivas de gestión y conservación es esencial para salvaguardar la biodiversidad, garantizar la seguridad hídrica y promover el desarrollo sostenible frente a los desafíos ambientales.

En la península Ibérica, los embalses y lagos son indispensables para el suministro de agua, la producción de energía, el control de inundaciones, la salud ecológica y el desarrollo socioeconómico del país, proporcionando numerosos beneficios que se extienden más allá de su entorno inmediato, impactando las escalas regional y nacional, pero la calidad de estas masas de agua es muy vulnerable debido a una combinación de factores climáticos, usos del suelo, contaminación, biológicos, hidráulicos, que se agudizan debido a que esta región se caracteriza por un clima mediterráneo, que incluye veranos calurosos y secos e inviernos suaves y húmedos. Se espera que el cambio climático exacerbe estas condiciones, lo que provocará sequías más frecuentes y graves.

Por lo tanto, los esfuerzos encaminados al monitoreo de estas masas de agua en la península Ibérica son esenciales para proteger y gestionar estos ecosistemas, dado que el seguimiento a largo plazo no solamente proporciona datos esenciales para llevar acciones tempranas en respuesta a la contaminación, la degradación del hábitat u otros factores estresantes como el cambio climático, sino también evaluar la efectividad de las estrategias de gestión destinadas a preservar la calidad del agua y la integridad de los ecosistemas.

El uso de sensores remotos representa una herramienta eficaz y cada vez más utilizada para obtener esta información esencial para llevar a cabo dicho monitoreo de la calidad de las masas de agua continentales, dado que proporcionan una cobertura a gran escala, alta resolución espacial y muestreo temporal frecuente.

En consecuencia, esta tesis tiene como objetivo estudiar la calidad de agua en masas de agua continentales a partir de datos de teledetección en la península Ibérica teniendo en cuenta su tamaño y su variabilidad estacional y a largo plazo, a partir de los siguientes objetivos específicos: (1) identificar y evaluar sensores

remotos y productos derivados que permitan estudiar la calidad de las masas de agua en este contexto; (2) analizar la variación a nivel espacio – temporal de la calidad de agua a partir de determinados parámetros; y (3) estudiar la influencia de factores geográficos sobre determinados parámetros de calidad de agua.

Para cumplir con estos objetivos, inicialmente se ha evaluado y utilizado el producto de reflectancia superficial de Landsat TM5 corregido atmosféricamente con el Sistema de procesamiento adaptativo de perturbaciones del ecosistema Landsat (LEDAPS por sus siglas en inglés), para llevar a cabo el inventario y estudio de la evolución de la calidad del agua en las lagunas de gravera dentro del Parque Regional del Sureste (PRSE) en Madrid, desde 1984 hasta 2011 a partir del parámetro de transparencia medida a través del disco de Secchi. Para esto, se compararon los valores de la reflectancia superficial con la reflectancia medida en el campo en las masas de agua, y el resultado muestra una sobreestimación de la reflectancia de la superficie derivada de los datos Landsat. Por lo tanto, se propuso una nueva ecuación de regresión que vincula las mediciones de profundidad de Secchi (DS) in situ con la reflectancia de la superficie medida por Landsat 5. Esta regresión se validó y posteriormente se aplicó a cada imagen, proporcionando un valor de DS para cada píxel en la serie temporal. Finalmente, los valores de DS recuperados se utilizaron para calcular el estado trófico de las masas de agua según la clasificación de la Organización para la Cooperación y el Desarrollo Económico (OCDE). Los resultados muestran un aumento en la superficie de los cuerpos de agua en el PRSE de 1984 a 2006, así como una mejora en la calidad del agua.

Estas series de tiempo de valores de discos de Secchi obtenidos de las imágenes Landsat 5 se utilizaron para estudiar patrones temporales y espaciales de la calidad del agua en las lagunas de gravera del PRSE. Se obtiene que existe un comportamiento estacional en la calidad del agua, con valores más altos de transparencia en otoño e invierno (diciembre-febrero) y valores más bajos en verano (julio-agosto), lo que puede explicarse por la relación entre los valores del disco de Secchi y la temperatura y la radiación solar. Encontramos que la declaración administrativa del parque regional de 1994 ha tenido un impacto positivo en la calidad del agua. El estado trófico de las masas de agua estudiadas ha mejorado lentamente, aunque estas no han alcanzado el estado oligotrófico.

A partir del producto de temperatura superficial de Landsat 5 se determinó si existen tendencias de calentamiento en los lagos y embalses de la España peninsular entre 1994 y 2011. y si estas tendencias varían según la estación o la ubicación geográfica mediante el procesamiento de datos de series. Este análisis reveló que el 87% de las masas de agua exhiben una tendencia al calentamiento, con un aumento promedio en la temperatura de la superficie del agua de +0,037 ºC por año. Las depresiones del Ebro y Guadalquivir presentaron los mayores incrementos de temperatura. Sin embargo, los cambios de temperatura varían a lo largo de la península, generalmente asociados con la temperatura de la superficie del aire, y están influenciados por la altitud en las zonas montañosas y los vientos atlánticos en las depresiones del oeste. Las tendencias indican un patrón estacional: en verano aumenta el número de masas de agua con temperaturas altas, mientras que en otoño hay más lagos y embalses con temperaturas intermedias. En invierno y primavera el número de masas de agua con bajas temperaturas disminuye y se sitúan más al norte.

Como conclusión, se determina que las imágenes satelitales, específicamente del satélite Landsat, demostraron ser una poderosa herramienta para estudiar la calidad del agua de las masas de agua continentales de la Península Ibérica, ya que su resolución espacial moderada y su amplia cobertura temporal lo hacen particularmente adecuado para estudiar los numerosos cuerpos de agua de diferentes tamaños y diferentes condiciones existentes en esta región. Especialmente, el producto de Landsat Colección 2 nivel 2 que incluye productos de temperatura superficial y reflectancia de superficie a nivel global proporciona información relevante en el monitoreo de la calidad del agua, ya que permite derivar series de tiempo precisas de parámetros de calidad del agua como la transparencia del disco de Secchi y la temperatura superficial del agua, dado que son productos atmosféricamente corregidos con métodos rigurosos y listos para ser utilizados

Tabla de Contenido

Lista de Figuras

Lista de Tablas

Abreviaturas y Acrónimos

UPM	Universidad Politécnica de Madrid
DS	Disco de Secchi
PRSE	Parque Regional del Sur Este
SDD	Transparencia medida con el disco de Secchi
TSS	Sólidos suspendidos totales
TUR	Turbidez
Chla-a	Concentración de lorofila-a
CDOM	Materia orgánica disuelta coloreada
T	Temperatura
RS	Reflectancia superficial
PIO	Propiedades ópticas inherentes
MODIS	Moderate Resolution Imaging Spectroradiometer
MERIS	Medium Resolution Imaging Spectrometer
OLCI	Ocean and Land Cover Instrument
MSS	Multispectral Scanner
TM	Thematic Mapper
ETM+	Enhanced Thematic Mapper
OLI	Operational Land Imager
MSI	MultiSpectral Instrument
Kd	Coeficiente de atenuación difusa
TOA	Reflectancia en la parte superior de la atmósfera ó Top Of Atmosfere)
DSF	Dark spectrum fitting
DOS	Dark Object Substraction
FLAASH	Fast Line-of-sight Atmospheric Analysis of Spectral Hypercubes
6S	Second Simulation of the Satellite Signal in the Solar Spectrum
QUAC	Quick Atmospheric Correction

RTM	Radiative Transfer Model
QAA	Quasi-analytical algorithm
NDVI	Índice de vegetación de diferencia normalizado
NDWI	Índice de diferencia de agua normalizada
RNA	Redes neuronales artificiales
RF	Random forests
MLP	Multilayer perceptron regressor
SVM	Support vector machines
ODS	Objetivos de Desarrollo Sostenible
UAV	Vehículos aéreos no tripulados
MITECO	Ministerio para la Transición Ecológica y el Reto Demográfico
LEDAPS	Landsat Ecosystem Disturbance Adaptive Processing System
RMSE	Error cuadrático medio
MAE	Error absoluto medio
MAPE	Error porcentual absoluto medio
MICE	imputación multivariada por ecuaciones encadenadas
SEADEC	Imputación de valores perdidos estacionalmente descompuestos
EOF	Análisis empírico de función orthogonal
OCDE	Organización para la Cooperación y el Desarrollo Económico
NIR	Infrarrojo cercano
SWIR	Infrarrojo de onda corta
USGS	U.S. Geological Survey

1. Introducción

Este capítulo explora el marco teórico para el uso de satélites de observación de la Tierra para estudiar la calidad de masas de agua continentales, enfatizando la importancia de las técnicas de corrección atmosférica para garantizar valores precisos de reflectancia de la superficie; analiza parámetros cuantificables de calidad del agua con sensores remotos, examina métodos para modelar estos parámetros y resume los principales factores que influyen en la calidad de las masas de agua continentales. Por otro lado, se revisa el estado actual del campo, destacando avances significativos y desafíos. Finalmente, el capítulo justifica la investigación enfatizando la importancia de la teledetección para proporcionar datos frecuentes y a gran escala sobre la calidad del agua, que complementan los métodos tradicionales y abordan sus limitaciones, apoyando en última instancia una mejor gestión ambiental.

1.1. Marco teórico

En este capítulo se sintetizan los conceptos teóricos de la investigación: la descripción de los diferentes satélites de observación de la tierra utilizados en estudios de calidad de agua, así como sus ventajas y desventajas; los diferentes métodos de corrección atmosférica empleados para eliminar las distorsiones de la atmósfera en estudios de calidad de agua; los parámetros de calidad de agua de masas de agua superficiales que más se estudian a partir de datos de teledetección; los diferentes métodos para estudiar la calidad de agua con teledetección y los principales factores que influyen en la calidad de las masas de agua continentales.

1.1.1. Satélites de observación de la Tierra utilizados en estudio de calidad de masas de agua continentales

Los sensores ópticos pasivos de satélites capaces de realizar estudios de calidad de agua a partir de datos de teledetección a gran escala son: Moderate Resolution Imaging Spectroradiometer (MODIS); Medium Resolution Imaging Spectrometer (MERIS); Sentinel-3 A/B Ocean and Land Cover Instrument (OLCI); La constelación Landsat conformada por Multispectral Scanner (MSS), Thematic Mapper (TM), Enhanced Thematic Mapper (ETM+), y Operational Land Imager (OLI); y Sentinel 2 A/B MultiSpectral Instrument (MSI).

Los sensores mencionados varían significativamente en su aplicabilidad, basándose en gran medida en sus resoluciones espaciales, temporales, espectrales y radiométricas Tabla 1.1 (Dekker & Hestir, 2012; Dörnhöfer & Oppelt, 2016; Mouw et al., 2015; Topp et al., 2020). Las resoluciones temporales y espaciales determinan la escala de procesos que puede capturar un sensor determinado. En general, los sensores de superficie terrestre tienen una resolución espacial más fina (~10–30 m) pero una resolución temporal más gruesa (~1–2 semanas), lo que les permite detectar patrones espaciales en la calidad del agua en cuerpos de agua más pequeños (por ejemplo, pequeños lagos y ríos), pero con solo 1 o 2 observaciones por mes dependiendo del sensor y las condiciones de la nubosidad.

Por otro lado, los sensores de color del océano se caracterizan por resoluciones espaciales gruesas (~300–1000 m) pero resoluciones temporales más finas (~diarias), lo que limita las observaciones a grandes masas de agua, pero facilita el examen de procesos que ocurren en períodos de tiempo cortos.

Tabla 1.1: Satelitales utilizados para el estudio de la calidad de masas de agua continentales. Resolución espacial = área del terreno cubierta por un píxel; resolución temporal = período de tiempo entre que un sensor puede obtener imágenes de la misma área en la superficie terrestre.

Sensor	# Bandas espectrales (Nº)	Resolución espacial (m)	Resolución temporal (días)	Tiempo operativo
MODIS	36	250 -1000	1	Desde 1999
Envisat	15	300	2-3	2002- 2012
Sentinel-3	21	300	27	Desde 2016
Landsat 5 TM	7	30 (banda 6: 120)	16	1984-2011
Landsat 7 ETM+	4	15, 30, 60	16	Desde 1999
Landsat 8 OLI & TIRS	11	15, 30, 100	16	Desde 2013
Landsat 9 OLI & TIRS	12	15, 30, 100	17	Desde 2023
Sentinel-2	9	10	5	Desde 2016

A continuación, se describen las bandas espectrales de los satélites que se utilizan en estudios de calidad de agua y que están actualmente activos:

Tabla 1.2: Descripción de las bandas espectrales de los satélites activos utilizados para el estudio de la calidad de masas de agua continentales.

Banda	Usos Principales	Longitud de onda (µm)	Resolución (m)
MODIS			
1	Límites de Tierra/Nubes/Aerosoles	0.620 - 0.670	250
2		0.841 - 0.876	
3	Propiedades de Tierra/Nubes/ Aerosoles	0.459 - 0.479	500
4		0.545 - 0.565	
5		0.1230 - 0.1250	
6		0.1628 - 0.1652	
7		0.2105 - 0.2155	
8	Biogeoquímica/Color del Océano/ Fitoplancton	0.405 - 0.420	1000
9		0.438 - 0.448	
10		0.483 - 0.493	
11		0.526 - 0.536	
12		0.546 - 0.556	
13		0.662 - 0.672	
14		0.673 - 0.683	
15		0.743 - 0.753	
16		0.862 -0.877	
17	Vapor de Agua Atmosférico	0.890 - 0.920	
18		0.931 - 0.941	
19		0.915 - 0.965	
20		3.660 - 3.840	
21	Temperatura de Superficie/Nubes	0.3929 - 0.3989	
22		3.929 - 3.989	
23		4.020 - 4.080	
24	Temperatura Atmosférica	4.433 - 4.498	

Banda	Usos Principales	Longitud de onda (µm)	Resolución (m)
MODIS			
25	Temperatura Atmosférica	4.482 - 4.549	
26	Vapor de Agua Nubes Cirrus	1.360 - 1.390	
27		6.535 -6.895	
28		7.175 - 7.475	
29	Propiedades de Nubes	8.400 - 8.700	
30	Ozono	9.580 - 9.880	
31	Temperatura de Superficie/Nubes	10.780 - 11.280	
32		11.770 -12.270	
33	Altitud Máxima de Nubes	13.185 - 13.485	
34		13.485 -13.785	
35		13.785 - 14.085	
36		14.085 - 14.385	

Banda	Nombre	Longitud de onda (µm)	Resolución (m)
LANDSAT 5			
1	Azul	0.45-0.52	30
2	Verde	0.52-0.60	30
3	Rojo	0.63-0.69	30
4	Infrarrojo cercano (NIR)	0.76-0.90	30
5	Infrarrojo de onda corta 1 (SWIR 1)	1.55-1.75	30
6	Térmica	10.40-12.50	120 (30)
7	Infrarrojo de onda corta 2 (SWIR 2)	2.08-2.35	30
LANDSAT 7			
1	Azul	0.450 - 0.515	30
2	Verde	0.525 - 0.605	30
3	Rojo	0.630 - 0.690	30
4	Infrarrojo cercano (NIR)	0.775 - 0.900	30
5	Infrarrojo de onda corta 1 (SWIR 1)	1.550 - 1.750	30
6	Térmica	10.40 - 12.50	60

Banda	Nombre	Longitud de onda (µm)	Resolución (m)
LANDSAT 7			
7	Infrarrojo de onda corta 2 (SWIR 2)	2.090 - 2.35	30
8	Pancromático	0.520 - 0.900	15
LANDSAT 8 Y 9			
1	Costera - Aerosoles	0.435 - 0.451	30
2	Azul	0.452 - 0.512	30
3	Verde	0.533 - 0.590	30
4	Rojo	0.636 - 0.673	30
5	Infrarrojo cercano (NIR)	0.851 - 0.879	30
6	Infrarrojo de onda corta 1 (SWIR 1)	1.566 - 1.651	30
10	(TIR 1)	10.60 - 11.19	100
11	(TIR 2)	11.50 - 12.51	100
7	Infrarrojo de onda corta 2 (SWIR 2)	2.107 - 2.294	30
8	Pancromática	0.503 - 0.676	15
9	Cirrus	1.363 - 1.384	30
SENTINEL 2			
1	Aerosoles	0.43 - 0.45	60
2	Azul	0.45 - 0.52	10
3	Verde	0.54 - 0.57	10
4	Rojo	0.65 - 0.68	10
5	Borde rojo 1	0.69 - 0.71	20
6	Borde rojo 2	0.73 - 0.74	20
7	Borde rojo 3	0.77 - 0.79	20
8	Infrarrojo cercano (NIR) 1	0.78 - 0.90	10
8a	Infrarrojo cercano (NIR) 2	0.85 - 0.87	20
9	Vapor de agua	0.93 - 0.95	60
10	Infrarrojo de onda corta – Cirrus	1.36 - 1.39	60
11	Infrarrojo de onda corta (SWIR) 1	1.56 - 1.65	20
12	Infrarrojo de onda corta (SWIR) 2	2.10 - 2.28	20

Landsat ofrece varias ventajas respecto a otros satélites de observación de la tierra para el estudio de las masas de agua en la Península Ibérica, especialmente dadas las características y requisitos específicos de esta región: (1) Registro de datos a largo plazo, dado que ha estado operativo desde la década de 1984 (Tabla 1.1) y proporciona un registro histórico continuo y extenso de observaciones de la Tierra; (2) la resolución espacial de 30 metros del Landsat (Tabla 1.1) logra un buen equilibrio entre detalle y cobertura, lo que es muy adecuado para monitorear masas de agua de tamaño mediano que se encuentran comúnmente en España. Esta resolución es suficiente para capturar características y variaciones significativas en la calidad del agua y al mismo tiempo cubrir grandes áreas; (3) Landsat tiene un tiempo de revisita relativamente frecuente de 16 días, que es adecuado para monitorear cambios temporales en los parámetros de calidad del agua. Esta regularidad ayuda a detectar variaciones estacionales y de corto plazo, que son importantes para las masas de agua que experimentan cambios rápidos; (4) Acceso gratuito y abierto: los datos de Landsat están disponibles gratuitamente para el público, lo que los convierte en una opción viable para la investigación y el monitoreo ambiental a largo plazo; (5) las imágenes multiespectrales: los sensores de Landsat capturan datos en múltiples bandas espectrales, incluidas las visibles, el infrarrojo cercano y el infrarrojo de onda corta (Tabla 1.2), que son esenciales para evaluar diversos parámetros de calidad del agua. Aprovechando estas ventajas, se han seleccionado las imágenes de este satélite para monitorear y analizar la calidad de las masas de agua en la Península Ibérica.

1.1.2. Corrección atmosférica

La teledetección analiza la radiación medida por un sensor distante para derivar información de un determinado objeto o, en este caso de la masa de agua (Dörnhöfer & Oppelt, 2016). Para obtener información sobre las propiedades de los cuerpos de agua, como la transparencia, la biota y la hidrología, se utiliza la radiancia proveniente del agua en las longitudes de onda visible e infrarroja cercana, es decir, la región de longitud de onda donde el agua refleja y dispersa la mayor parte de la radiación solar entrante (400–900 nm) de gran interés (Dekker & Hestir, 2012). Antes de que la radiación solar incidente interactúe con la masa de agua, tiene que pasar la atmósfera donde se modifica mediante absorción y dispersión. En la superficie del agua, la radiación se refleja o pasa a través de la superficie del agua según la ley de Snell y se propaga a través de la masa de agua. En la columna de agua, los constituyentes ópticamente activos, por ejemplo, los sólidos en suspensión (TSS), la Materia orgánica disuelta coloreada (CDOM) y la clorofila -a (Chl-a), alteran la radiación mediante las características de absorción y dispersión de cada constituyente. La suma de estos constituyentes representa las propiedades ópticas inherentes de un cuerpo de agua (Odermatt et al., 2012). Las propiedades ópticas aparentes, como la atenuación (representada por el coeficiente de atenuación difusa Kd) o la reflectancia (es decir, la relación entre la radiación que sale del agua y la irradiancia que desciende) dependen del agua misma y, además, de la geometría de la radiación (por ejemplo, parámetros como los ángulos solares o el ángulo de la radiación entrante sobre la superficie del agua, es decir, el ángulo de incidencia) (Dekker & Hestir, 2012). En aguas ópticamente profundas, la superficie del agua, la masa de agua y los constituyentes del agua son las principales fuentes de radiación dentro de la masa de agua. En aguas ópticamente poco profundas, la radiancia proveniente del agua incluye en parte radiación que se ha reflejado en el fondo. Al pasar por la superficie del agua, la radiación que sale del agua se refracta nuevamente y, en su camino hacia el sensor aéreo o satelital, se ve nuevamente afectada por la absorción y dispersión atmosférica. En total, alrededor del 90% de la señal en las bandas azul y verde, y una fracción mayor en rojo obtenida por un sensor remoto se origina en contribuciones de la superficie del agua y la atmósfera (IOCCG, 2010; Mouw et al., 2015). El 2-6% restante incluye la señal interesante para la teledetección del agua, es decir, la radiación proveniente del agua. Por esa razón, es esencial una eliminación precisa de los efectos debidos a la atmósfera y la superficie del agua (Dekker & Hestir, 2012; Mouw et al., 2015).

La corrección atmosférica en aguas continentales y costeras es uno de los principales desafíos pendientes en la teledetección acuática, ya que a menudo dificulta la obtención de variables biogeoquímicas y el análisis de su variabilidad espacial y temporal dentro de los ambientes acuáticos (Pahlevan et al., 2021).

El objetivo de la corrección atmosférica es estimar la reflectancia acuática adimensional, también denominada reflectancia saliente del agua (*water-leaving reflectance*) en la literatura. En ausencia de reflejo solar (es decir, reflexión especular directa del haz solar) y efectos atmosféricos, la señal total expresada como reflectancia en la parte superior de la atmósfera (TOA por sus siglas en inglés *Top Of Atmosfere*) $\rho_t(\lambda)$, se puede simplificar como (Pahlevan et al., 2021):

$$\rho_t(\lambda) = t\hat{\rho}_\omega(\lambda) + [\rho_r(\lambda) + \rho_a(\lambda) + \rho_{ar}(\lambda)] \qquad 1$$

Donde, t es la transmisión difusa, $\hat{\rho}_\omega$ es la reflectancia acuática derivada de satélite, ρ_r es la reflectancia de Rayleigh en ausencia de aerosol, ρ_a es la reflectancia del aerosol y ρ_{ar} es la radiancia que surge de la dispersión múltiple de aerosoles de Rayleigh. Dependiendo de la metodología adoptada para la corrección atmosférica, las tres componentes se calculan como un parámetro desconocido, es decir, ρ_{path}, o separando las contribuciones de Rayleigh y de aerosol. La transmisión difusa también se calcula conociendo las transmisiones debidas a moléculas de aire y gas, así como a aerosoles (Mouw et al., 2015; Pahlevan et al., 2021). Entre todos los componentes desconocidos, estimar la contribución de los aerosoles es la tarea más difícil, y pequeños errores pueden generar grandes incertidumbres en la evaluación.

Se han propuesto varios enfoques para la eliminación de los efectos atmosféricos sobre océanos abiertos, que difieren principalmente en la metodología utilizada para la eliminación de la contribución del aerosol, pero los autores coinciden en que el rendimiento de los métodos de corrección atmosférica es en general aceptable en aguas oceánicas claras, donde la radiación que sale del agua en el infrarrojo cercano (NIR) es insignificante y los aerosoles marítimos (no absorbentes) son los tipos de aerosoles dominantes (IOCCG, 2010; Mouw et al., 2015; Pahlevan et al., 2021). Pero, tanto en aguas interiores como costeras, la radiancia que sale del agua en el NIR a menudo no es despreciable debido a la presencia de abundantes materiales dispersos (por ejemplo, sedimentos suspendidos o intensa proliferación de algas), y los efectos atmosféricos debidos a la dispersión múltiple del suelo circundante pueden contribuir a la trayectoria ρ_{path} (Mouw et al., 2015; Pahlevan et al., 2021) por lo que la corrección atmosférica en aguas interiores y costeras sigue siendo un área importante de investigación y desarrollo.

A continuación, se describen los métodos más comunes de corrección atmosférica aplicados a estudios de calidad de agua continentales. Estos métodos varían en complejidad, requisitos computacionales e idoneidad para diferentes tipos de imágenes y aplicaciones. La elección del método depende de factores como las características del sensor, el rango espectral, las condiciones atmosféricas y el nivel de precisión deseado:

- **Calibración empírica:** Se basa en la relación lineal entre la reflectancia de la superficie y la radiancia del sensor para objetivos de calibración con valores de reflectancia conocidos. Al medir la radiancia de los objetivos de calibración en las masas de agua de la imagen y compararlos con sus valores de reflectancia conocidos, estima los coeficientes de corrección atmosférica para cada banda espectral (Domínguez Gómez et al., 2009; Gilabert et al., 1994).
- **Dark spectrum fitting (DSF):** Es un algoritmo de corrección atmosférica desarrollado en 2018 (Vanhellemont & Ruddick, 2018). Este método se basa en el concepto de utilizar el "espectro oscuro", que representa el espectro de un objetivo perfectamente oscuro, como aguas profundas o vegetación densa, en ausencia de efectos atmosféricos de dispersión y absorción. El método DSF implica varios pasos: (1) Selección de píxeles oscuros: los píxeles oscuros se identifican dentro de las imágenes y normalmente corresponden a regiones de masas de agua profundas. Se supone que estos píxeles oscuros tienen una reflectancia mínima en las bandas visible e infrarroja cercana; (2) Derivación del espectro oscuro: la firma espectral de los píxeles oscuros

se extrae y se utiliza como "espectro oscuro" de referencia. Este espectro representa la reflectancia inherente del objetivo en ausencia de efectos atmosféricos; (3) Estimación de parámetros atmosféricos: Los parámetros atmosféricos, como el espesor óptico del aerosol y el contenido de vapor de agua, se estiman basándose en el espectro oscuro y los modelos de transferencia radiativa atmosférica. Estos parámetros caracterizan las condiciones atmosféricas y su impacto en las señales espectrales observadas; y (4) Corrección atmosférica: los parámetros atmosféricos estimados se utilizan para modelar y eliminar los efectos atmosféricos de todo el conjunto de datos de imágenes. Este proceso de corrección tiene en cuenta la dispersión y la absorción atmosféricas, lo que da como resultado imágenes corregidas atmosféricamente que representan con mayor precisión la reflectancia de la superficie. El método DSF ofrece ventajas como simplicidad, eficiencia computacional y efectividad para corregir efectos atmosféricos en áreas con objetivos oscuros homogéneos. Sin embargo, puede encontrar desafíos en entornos de cobertura terrestre heterogéneos o mixtos y en regiones con condiciones atmosféricas variables. (Abdelal et al., 2022; M. Chen et al., 2022; Ghirardi et al., 2023; Guo et al., 2023; Hafeez et al., 2022; Song et al., 2020; D. Wang et al., 2019; Z. Yang et al., 2023; Yépez et al., 2024).

- **Dark object subtraction (DOS):** parte del supuesto básico de que dentro de la imagen algunos píxeles están en completa sombra (radiancia mínima) y sus radiancias recibidas en el satélite se deben a la dispersión atmosférica; y el valor de esta celda, por lo tanto, se resta de los otros píxeles de la imagen (Abdelal et al., 2022). La radiancia del satélite debe convertirse en reflectancia de la superficie mediante corrección de los efectos solares y atmosféricos. El modelo/ecuación general utilizado para hacer esto es (Bonansea et al., 2015; Markogianni et al., 2018, 2020; Mohsen et al., 2021; Moran et al., 1992; Mushtaq et al., 2022; Nascimento Silva et al., 2017; Rani et al., 2019; Shahzad et al., 2018)

$$REF = \frac{(\pi * (Lsat \ - Lp))}{(TAUv * (E0 \ * Cos\ (Tz) * TAUz \ + Edown))} \qquad 2$$

Donde, REF es la reflectancia espectral de la superficie; $Lsat$ es la radiancia espectral en el satélite de la banda espectral correspondiente; Lp es la radiancia de la trayectoria atmosférica; $TAUv$ es la Transmitancia atmosférica a lo largo del camino desde la superficie del suelo hasta el sensor; $E0$ es la irradiancia espectral solar; Tz es el ángulo de incidencia; $TAUz$ es la transmitancia atmosférica a lo largo del camino desde el sol hasta la superficie del suelo; y $Edown$ es la irradiancia espectral descendente.

En el método DOS Lp es obtenido de la imagen digital utilizando el criterio de objeto oscuro; $TAUv$ y $TAUz$ son iguales a 1.0 (ignora la transmitancia atmosférica); y $Edown$ es igual a 0.0 (ignora la irradiancia espectral descendente). El resto de los parámetros se pueden leer desde los metadatos de las imágenes o en el sitio web de USGS.

Las principales ventajas del modelo DOS son: (1) es estrictamente un procedimiento basado en imágenes y (2) no requiere mediciones de campo *in situ*. Las principales desventajas son: (1) para valores de reflectancia superiores a aproximadamente el 15% la precisión a menudo no es aceptable y (2) la selección de los valores de turbiedad debe hacerse con cuidado.

- **FLAASH (Fast Line-of-sight Atmospheric Analysis of Spectral Hypercubes):** fue desarrollado sobre la base del código MODTRAN (TRANsmisión atmosférica de resolución moderada) y es particularmente eficaz para datos de alta resolución espectral. Tiene una solución única para cada imagen, porque los parámetros atmosféricos se estiman a partir de las características de la atmósfera en píxeles de la imagen, y la información atmosférica se evalúa mediante el método del objetivo oscuro basado en la propia imagen. Tanto el modelo atmosférico estándar como el modelo de aerosol de MODTRAN se utilizan para reemplazar los parámetros atmosféricos en tiempo real, lo que amplía la aplicación del FLAASH y mejora su estabilidad. FLAASH es conocido por su precisión y solidez a la hora de corregir los efectos atmosféricos, sin embargo, requiere una parametrización y validación cuidadosas para garantizar resultados precisos, especialmente en terrenos complejos y condiciones atmosféricas variables. Además, requiere un uso intensivo de computación, particularmente para grandes conjuntos de datos, lo que requiere algoritmos de procesamiento y recursos computacionales eficientes (Adler-Golden et al., 1999; Ha et al., 2017; He et al., 2021; Hicks et al., 2013a; Kutser, 2012; Watanabe et al., 2015; H. Yang et al., 2022; X. Yang et al., 2020; H. Zhang et al., 2022).
- **Second Simulation of the Satellite Signal in the Solar Spectrum (6S): La s**egunda simulación de la señal de satélite en el espectro solar, desarrollado por el Centre d'Etudes Spatiales de la Biosphère (CESBIO) en Francia,

simula la transferencia de radiación solar a través de la atmósfera terrestre para predecir la radiancia espectral observada a nivel del sensor (Vermote et al., 1997). El método 6S funciona con los siguientes pasos: (1) obteniendo los parámetros de entrada: requiere varios parámetros de entrada para simular las condiciones atmosféricas con precisión. Estos parámetros incluyen la ubicación geográfica de la escena, fecha y hora de adquisición, perfiles atmosféricos (por ejemplo, aerosoles, vapor de agua), geometrías solares y de sensores, y propiedades de la superficie (por ejemplo, albedo, elevación); (2) Simulación de transferencia radiativa: utilizando los parámetros de entrada, simula la transferencia de radiación solar a través de la atmósfera. Explica varios fenómenos atmosféricos, incluida la dispersión de Rayleigh por moléculas de aire, la dispersión de Mie por aerosoles, la absorción por gases (por ejemplo, ozono, vapor de agua) y la reflexión de la superficie; (3) Cálculo de parámetros atmosféricos: basándose en los parámetros de entrada y las simulaciones de transferencia radiativa, calcula varios parámetros atmosféricos, como la transmitancia atmosférica, la radiancia del cielo y la radiancia de la trayectoria. Estos parámetros cuantifican los efectos atmosféricos sobre la radiación solar entrante y la señal observada en el sensor; y (4) Corrección atmosférica: utiliza los parámetros atmosféricos calculados para corregir la radiancia observada del sensor en función de los efectos atmosféricos. Elimina las contribuciones de la dispersión y absorción atmosférica, aislando la información de reflectancia de la superficie de la señal observada. El método de corrección atmosférica 6S se utiliza ampliamente, está bien documentado y ofrece un enfoque sólido para corregir los efectos atmosféricos en imágenes de teledetección. Es aplicable a diversos sensores y plataformas, incluidos instrumentos satelitales, aéreos y terrestres, y puede adaptarse a diferentes condiciones atmosféricas y de superficie. Sin embargo, como cualquier método de corrección atmosférica, los resultados precisos dependen de la calidad de los parámetros de entrada y de las suposiciones hechas en el proceso de simulación. Por lo tanto, una parametrización y validación cuidadosas son esenciales para obtener resultados de corrección confiables (Lamaro et al., 2013; Lobo et al., 2015; V. S. Martins et al., 2018; Ren et al., 2018; Setiawan et al., 2019; Y. Zhang et al., 2016; Zhu et al., 2020).

- **QUAC (Quick Atmospheric Correction):** es un algoritmo basado en objetivos oscuros. Se consideran tres supuestos: (1) la imagen debe presentar más de

10 píxeles espectralmente diferentes; (2) la desviación estándar de la reflectancia de los píxeles del conjunto final es espectralmente independiente y puede usarse para calcular la transmitancia; y (3) hay un número relevante de píxeles oscuros para calcular una línea base invariante, asumida como una medida de atenuación (dispersión y absorción) y el efecto de adyacencia. La velocidad computacional del método de corrección atmosférica es significativamente más rápida que la de los métodos basados en modelos de transferencia radiativa porque QUAC no involucra cálculos de transferencia radiativa de primeros principios y solo requiere una especificación aproximada de las ubicaciones de las bandas (es decir, longitudes de onda centrales) y su calibración radiométrica (Malahlela, 2019; Moses et al., 2012; Oliphant et al., 2018).

Para el caso específico de la banda térmica, los métodos de corrección atmosférica utilizados son:

- **Método Single-channel para obtener la temperatura de la superficie terrestre:** suponiendo que se conoce la emisividad, solo se utiliza el contenido total de vapor de agua atmosférico, la longitud de onda efectiva del sensor y los datos del sensor (temperatura de brillo o radiancia en el sensor) (Jimenez-Munoz et al., 2009; Simon et al., 2014a).
- **Radiative Transfer Method (RTM):** La radiancia espectral debe corregirse teniendo en cuenta tres partes; es decir, la radiación de la superficie, la reflejada hacia la superficie desde la atmósfera, y hacia el sensor desde la atmósfera. Este método, requiere como entrada datos de radiosondeo *in situ* obtenidos cerca del área de estudio y cerca del momento de adquisición de la imagen (Lamaro et al., 2013; Simon et al., 2014a).

1.1.3. Parámetros de calidad de aguas continentales cuantificables mediante teledetección

Los parámetros de calidad del agua que pueden cuantificarse mediante teledetección más estudiados son (Dekker & Hestir, 2012; Dörnhöfer & Oppelt, 2016; Liu et al., 2003; Mouw et al., 2015; Topp et al., 2020; Zandaryaa, 2018):

- **Sedimentos en suspensión**. Los sólidos suspendidos totales (TSS por sus siglas en inglés) se refieren a partículas tanto inorgánicas como orgánicas mantenidas en suspensión a lo largo de una columna de agua. En la literatura se hace referencia a ella como materia suspendida total, concentración de sedimento suspendido y materia particulada (Topp et al., 2020). Los sedimentos en suspensión ingresan a una masa de agua través de sus afluentes y se originan a partir de la erosión del suelo y del lecho rocoso en su interior o de la resuspensión interna (Dörnhöfer & Oppelt, 2016). Por tanto, son un importante portador de nutrientes y contaminantes. Los sedimentos en suspensión atenúan la luz, lo que conduce a una menor transparencia al aumentar sus concentraciones, pero también dispersan la luz, lo que resulta en un aumento de la radiancia saliente del agua (Giardino et al., 2014). TSS ha sido ampliamente estudiado con teledetección (Tabla 1.3), ya que es fácil detectar de forma remota los sedimentos suspendidos en una masa de agua debido a su fuerte retrodispersión de la radiación incidente, aunque se restringen a aguas cercanas a la superficie (Liu et al., 2003).

Tabla 1.3: Artículos analizados que estudian los sedimentos en suspensión con teledetección.

Autores	**Área de estudio**	**País**	**Período de estudio**	**Satélite**	**Método**
(Hicks et al., 2013a)	34 lakes	New Zealand	2000-2009	Landsat 5	Semi-empírico
(Lobo et al., 2015)	Tapajós River Basin	Brazil	1973-2013	Landsat 5	Semi-empírico
(Imen et al., 2015)	Lake Mead	United States	2005-2009	Landsat 5	Machine Learning
(Lymburner et al., 2016)	19 lakes	Australia	1988-2013	Landsat 5	Semi-analítico
(Concha & Schott, 2016)	Long Pond and Cranberry Pond	United States	3 fechas (2013, 2014, 2015)	Landsat 8	Semi-empírico
(Y. Zhang et al., 2016)	Xin'anjiang Reservoir	China	Diciembre 2013 - abril 2015	Landsat 8	Semi-analítico
(Alcântara, Curtarelli, et al., 2016)	Itumbiara hydroelectric reservoir	Brazil	2014	Landsat 8	Semi-analítico
(Robert et al., 2017)	Agoufou Lake	Mali	2000-2017	Landsat 7 y 8	Semi-empírico
(Nascimento Silva et al., 2017)	Reservoir of Tocantins river	Brazil	2007 - 2014	Landsat 7	Machine Learning
(Shahzad et al., 2018)	Indus Delta Region	Pakistan	Noviembre 6, 2001; marzo 22, 2005; y marzo 20, 2016	Landsat 7	empírico
(C. Wang et al., 2018)	Pearl River Estuary	China	1987–2015	Landsat 5, 7 y 8	Semi-empírico

Autores	Área de estudio	País	Período de estudio	Satélite	Método
(Malahlela, 2019)	5 Dams	South Africa	2014 - 2018	Landsat 8	Semi-empírico
(Bernardo et al., 2019)	six reservoirs	Brazil	2014 y 2016	Landsat 8	Semi-analítico
(Du et al., 2020)	Songnen Plain	China	1984 to 2018	Landsat 5, 7 y 8	Semi-empírico
(Zhu et al., 2020)	West Lake	China	2013 - 2017	Landsat 8	Semi-empírico
(Bernardo et al., 2020)	Tietê River Cascade System	Brazil	2014 y 2016	Landsat 8	Semi-empírico
(Mohsen et al., 2021)	Lake Burullus	Egypt	2010-2013	Landsat 7	Semi-empírico
(Arias-Rodriguez et al., 2021)	Five lakes	Mexico	2012-2018	Landsat 8	Machine Learning
(Q. Wang et al., 2021)	Hulun Lake	China	1986 - 2017	Landsat 7 y 8	Semi-empírico
(Adusei et al., 2021)	Owabi reservoir	Ghana	dic-19	Landsat 8	Machine Learning
(Yin et al., 2022)	Lake Taihu	China	1984 - 2020	Landsat 5 y 8	Semi-empírico
(Hafeez et al., 2022)	Eight lakes	China	2013-2019	Landsat8	Semi-empírico
(W. ; Li et al., 2022)	Lake Qinghai	China	1986 - 2020	Landsat 5, 7 y 8	empírico
(Pahlevan et al., 2022)	Global	Global	Sin información	Landsat 8	Machine Learning
(Arias-Rodriguez et al., 2023)	Global	Global	2021-2022	Landsat 8	Machine Learning
(Villota-González et al., 2023)	Cajititlán and Zapotlán lakes	Mexico	2013-2023	Landsat 8	Machine Learning
(Jakovljevic et al., 2023)	main water bodies	Serbia	1984-2021	Landsat 5, 7 y 8	Machine Learning
(Ghirardi et al., 2023)	Gravel and sand Pit lakes in Po River basin	Italy	1990 - 2021	Landsat 5, 7 y 8	empírico
(Bangira et al., 2024)	Olushandja Dam	Namibia	2014- 2015	Landsat 8	Semi-empírico
(Tian et al., 2024)	Qianwu, Longjing and Nanshan reservoir	China	2021-2022	Landsat 7	Semi-empírico
(Sun et al., 2024)	Pearl River Estuary	China	1987-2022	Landsat 5, 7 y 8	Semi-analítico
(Doña et al., 2014)	Albufera y Parque regional del Sureste	Spain	1985-2006	Landsat 5 y 7	empírico

- **Turbidez** (TUR) La turbidez es un parámetro clave de la calidad del agua y se utiliza como medida relativa de claridad. Está relacionada linealmente con la dispersión de la luz dentro de una columna de agua causada por partículas suspendidas y disueltas (Topp et al., 2020). También está relacionado linealmente con la Materia Total en Suspensión (TSM) para valores de turbidez bajos a moderados. La unidad de medida es la Unidad de Turbidez de Formazina [FTU], que es similar a la Unidad de Turbidez Nefelométrica [NTU]. 1FTU corresponde a 0,0118/m de retrodispersión a 550 nm. La turbidez a partir de mediciones satelitales se determina midiendo la retrodispersión de la luz entre 450 y 800 nm (Tabla 1.4) (Zandaryaa, 2018).

Tabla 1.4: Artículos analizados que estudian la turbidez con teledetección.

Autores	**Área de estudio**	**País**	**Período de estudio**	**Satélite**	**Método**
(Hicks et al., 2013a)	34 lakes	New Zealand	2000-2009	Landsat 5	Semi-empírico
(Papoutsa et al., 2014)	Asprokremmos Reservoir	Cyprus	Mayo 2010–oct 2010	Landsat 7	empírico
(Masocha et al., 2018)	two reservoirs	Zimbabwe	jun-13	Landsat 8	Semi-empírico
(S. Martins et al., 2018)	Sobradinho reservoir	Brazil	2013–2017	Landsat 8	empírico
(Surisetty et al., 2018)	Chilika Lagoon	India	2014	Landsat 8	empírico
(Dave et al., 2019)	Narmada River and Reserviors Bargi, Ukai, and Ujjani	India	2017-2018	Landsat 8	Semi-empírico
(Erena et al., 2019)	Mar Menor lagoon	Spain	2015-2017	Landsat 8	Semi-empírico
(Amado-Alvarez et al., 2019)	Vírgenes dam, the Colina lake, and La Boquilla dam	Mexico	22-mar-11	Landsat 5	Semi-empírico
(Peterson et al., 2020)	Several waterbodies in Midwestern	United States	2013–2018	Landsat8	Machine Learning
(Arias-Rodriguez et al., 2021)	Five lakes	Mexico	2012-2018	Landsat 8	Machine Learning
(Adusei et al., 2021)	Owabi reservoir	Ghana	dic-19	Landsat 8	Machine Learning
(Caballero et al., 2022)	Mar Menor lagoon	Spain	2021	Landsat 8	Semi-analítico
(Abdelal et al., 2022)	King Talal Dam	Jordan	2018 - 2019	Landsat 8	Semi-empírico

Autores	Área de estudio	País	Período de estudio	Satélite	Método
(El-Alem & Chokmani, 2022)	Lakes in Quebec	Canada	2014-2017	Landsat 7 y 8	Machine Learning
(Meng et al., 2022)	Shanmei Reservoir	China	2020 - 2022	Landsat 8-9	Semi-empírico
(Arias-Rodriguez et al., 2023)	Global	Global	2021-2022	Landsat 8	Machine Learning
(Villota-González et al., 2023)	Cajititlán and Zapotlán lakes	Mexico	2013-2023	Landsat 8	Machine Learning
(Z. Yang et al., 2023)	Taihu Lake	China	2018 - 2022	Landsat 8 y 9	Machine Learning
(Bangira et al., 2024)	Olushandja Dam	Namibia	2014- 2015	Landsat 8	Semi-empírico
(Tian et al., 2024)	Qianwu, Longjing and Nanshan reservoir	China	2021-2022	Landsat 7	Semi-empírico
(Yépez et al., 2024)	Laguna Grande de San Pedro de la Paz	Chile	2014–2022	Landsat 8	Semi-empírico

- **Concentración de clorofila a** (Chl-a por sus siglas en inglés) Las clorofilas son los compuestos fotosintéticamente activos que convierten la luz en energía para la fotosíntesis (Topp et al., 2020). Es un indicador de la biomasa del fitoplancton, estado trófico y de nutrientes y es el índice más utilizado a nivel mundial sobre la calidad del agua y el estado de los nutrientes (Tabla 1.5) (Dekker & Hestir, 2012). Los pigmentos del fitoplancton se componen principalmente de clorofila a, b y c, de la cual la clorofila a se puede derivar mediante teledetección (Liu et al., 2003).

Tabla 1.5: Artículos analizados que estudian la concentración de clorofila -a con teledetección.

Autores	Área de estudio	País	Período de estudio	Satélite	Método
(Mancino et al., 2009)	Monticchio lakes	Italy	2001	Landsat 5	empírico
(Chao Rodríguez et al., 2013)	Lake Arreo	Spain	2000 - 2012	Landsat 5	empírico
(Tebbs et al., 2013)	Lake Bogoria	Kenya	2003 - 2005	Landsat 7	empírico
(Markogianni et al., 2014)	Koumoundourou Lake	Greece	2003 - 2011	Landsat 5	Semi-empírico
(Bonansea et al., 2015)	Río Tercero reservoir	Argentina	2003 - 2010	Landsat 5	empírico

Autores	Área de estudio	País	Período de estudio	Satélite	Método
(Watanabe et al., 2015)	Barra Bonita reservoir	Brazil	2013 - 2014	Landsat8	Semi-empírico
(Concha & Schott, 2016)	Long Pond and Cranberry Pond	United States	3 fechas (2013, 2014, 2015	Landsat 8	Semi-empírico
(Kutser et al., 2016)	Nohipalu Mustjärv, Meelva, and Mustjärv lakes	Estonia	Julio 2013	Landsat8	Semi-empírico
(Coelho et al., 2017)	Marengo, Paus Branco and São Nicolau reservoirs	Brazil	2014 - 2015	Landsat 8	Semi-empírico
(Nascimento Silva et al., 2017)	Reservoir of Tocantins river	Brazil	2007 - 2014	Landsat 7	Machine Learning
(Ha et al., 2017)	10 hypertrophic lakes in Hanoi	Vietnam	2015 - 2016	Landsat 8	empírico
(Masocha et al., 2018)	two reservoirs	Zimbabwe	Junio 2013	Landsat 8	Semi-empírico
(Markogianni et al., 2018)	Trichonis Lake	Greece	Octubre 2013 y ago 2014	Landsat 8	Semi-empírico
(Oliphant et al., 2018)	the Vaal Dam	South Africa	2014 – 2016	Landsat 8	Semi-empírico
(Dave et al., 2019)	Narmada River and Reserviors Bargi, Ukai, and Ujjani	India	2017 - 2018	Landsat 8	Semi-empírico
(Erena et al., 2019)	Mar Menor lagoon	Spain	2015 - 2017	Landsat 8	Semi-empírico
(Ledesma et al., 2019)	Cassaffousth reservoir	Argentina	2016 - 2017	Landsat8	Semi-empírico
(Vinh et al., 2019)	Thac Ba Reservoir	Vietnam	2018	Landsat 5, 7 y 8	empírico
(Markogianni et al., 2020)	50 lakes	Greece	2013 - 2016 y 2018	Landsat 7 y 8	Semi-empírico
(L. Wang et al., 2020)	12 lakes	United States	2013 - 2017	Landsat 7 y 8	Machine Learning
(Peterson et al., 2020)	Several waterbodies in Midwestern	United States	2013 - 2018	Landsat8	Machine Learning
(X. Yang et al., 2020)	Donghu Lake	China	1987 - 2018	Landsat 5, 7 y 8	Semi-empírico
(He et al., 2021)	Dashahe Reservoir	China	2013 - 2018 (2 imagenes/año	Landsat 8	Machine Learning
(Mohsen et al., 2021)	Lake Burullus	Egypt	2010 - 2013	Landsat 7	Semi-empírico

Autores	Área de estudio	País	Período de estudio	Satélite	Método
(Arias-Rodriguez et al., 2021)	Five lakes	Mexico	2012 - 2018	Landsat 8	Machine Learning
(Dallosch & Creed, 2021)	Lakes	United States and Sweden	1984 - 2016	Landsat 5, 7 y 8	Machine Learning
(F. Zhang et al., 2021)	Guanting Reservoir	China	1985 -2019	Landsat 5, 7 y 8	Semi-empírico
(X. Zhao et al., 2021)	Taihu Lake	China	2017	Landsat 8	Machine Learning
(H. Yang et al., 2022)	Baiyangdian lake	China	Julio 2019 - sept 2019	Landsat 8	Machine Learning
(H. Zhang et al., 2022)	Dongping Lake	China	2013 - 2018	Landsat 8	Machine Learning
(Abdelal et al., 2022)	King Talal Dam	Jordan	2018 - 2019	Landsat 8	Semi-empírico
(Meng et al., 2022)	Shanmei Reservoir	China	2020 - 2022	Landsat 8-9	Semi-empírico
(Guo et al., 2022)	Lake Simcoe	Canada	1984 - 2020	Landsat 5, 7 y 8	Machine Learning
(Markogianni et al., 2022)	50 lakes	Greece	2013 - 2016 y 2018	Landsat 7 y 8	Semi-empírico
(Pahlevan et al., 2022)	Global	Global	Sin información	Landsat 8	Machine Learning
(Mushtaq et al., 2022)	Wular Lake	India	Octubre 2018	Landsat 8	Semi-empírico
(Tanner et al., 2022)	Utah Lake	United States	1984 - 2021	Landsat 5, 7 y 8	Semi-empírico
(Guo et al., 2023)	Lake Simcoe	Canada	2013 - 2019	Landsat 8	Machine Learning
(Arias-Rodriguez et al., 2023)	Global	Global	2021 - 2022	Landsat 8	Machine Learning
(Y. Yang et al., 2023)	Lake Dianchi	China	1998 - 2020	Landsat 5 y 8	Machine Learning
(Villota-González et al., 2023)	Cajititlán and Zapotlán lakes	Mexico	2013 - 2023	Landsat 8	Machine Learning
(Chegoonian et al., 2023)	Buffalo Pound Lake	Canada	2014 - 2020	Landsat 8	Machine Learning
(Jakovljevic et al., 2023)	main water bodies	Serbia	1984 - 2021	Landsat 5, 7 y 8	Machine Learning

Autores	Área de estudio	País	Período de estudio	Satélite	Método
(Barreneche et al., 2023)	Continental water bodies	Uruguay	2004 - 2020	Landsat 5, 7 y 8	Semi-empírico
(J. Wang & Chen, 2024)	Erhai Lake	China	2013 - 2021	Landsat 8	Machine Learning
(Tian et al., 2024)	Qianwu reservoir, Longjing reservoir and Nanshan reservoir	China	2021 - 2022	Landsat 7	Semi-empírico
(Yépez et al., 2024)	Laguna Grande de San Pedro de la Paz	Chile	2014 - 2022	Landsat 8	Semi-empírico
(Doña et al., 2014)	Albufera y Parque regional del Sureste	Spain	1985-2006	Landsat 5 y 7	empírico

- **Materia orgánica disuelta coloreada** (CDOM) (o "cromófora") es la porción coloreada del carbono orgánico disuelto total. Las fuentes de CDOM pueden ser autóctonas (es decir, fitoplancton, por ejemplo, plantas acuáticas en descomposición dentro de la masa de agua) o alóctonas (es decir, carbono terrestre, por ejemplo, plantas leñosas en descomposición en la cuenca) (Dörnhöfer & Oppelt, 2016). El CDOM es un indicador de teledetección (Tabla 1.6) cuantificable calculado como absorción en m^{-1} a una longitud de onda específica, a menudo 440 nm y se utiliza como sustituto del indicador del contenido de carbono de las masas de agua (Kutser, 2012). Altamente absorbente en el espectro visible, los niveles elevados de CDOM conducen a cuerpos de agua oscuros y estratificados con penetración de luz limitada (Topp et al., 2020).

Tabla 1.6: Artículos analizados que estudian el CDOM con teledetección.

Autores	Área de estudio	País	Período de estudio	Satélite	Método
(Concha & Schott, 2016)	Long Pond and Cranberry Pond	United States	3 fechas (2013, 2014, 2015)	Landsat 8	Semi-empírico
(Alcântara, Bernardo, et al., 2016)	Barra Bonita hydroelectric reservoir	Brazil	Mayo y octubre 2014	Landsat 8	Semi-empírico

Autores	Área de estudio	País	Período de estudio	Satélite	Método
(J. Chen et al., 2017)	Lake Huron	Canada-United States	2013	Landsat 5	Semi-empírico
(Coelho et al., 2017)	Marengo, Paus Branco and São Nicolau reservoirs	Brazil	2014-2015	Landsat 8	Semi-empírico
(J. Li et al., 2018)	Lake Huron	Canada-United States	2013 y 2015	Landsat8	Semi-analítico
(S. Martins et al., 2018)	Funil hydroeletric reservoir	Brazil	1995 - 2010	Landsat 5	Semi-empírico
(Olmanson et al., 2020)	10.000+ Minnesota lakes	United States	2015 - 2016	Landsat 8	Semi-empírico
(Koll-Egyed et al., 2021)	128 Southern lakes	Canada	2017 - 2019	Landsat 8	Semi-empírico
(Z. Cao et al., 2022)	Yunnan–Guizhou Plateau	China	2013 - 2022	Landsat 8 y 9	Machine Learning
(Pahlevan et al., 2022)	Global	Global	Sin información	Landsat 8	Machine Learning
(N. Cao et al., 2023)	Ebinur Lake	China	2014 - 2021	Landsat 8	Semi-analítico

- **Transparencia medida** con el disco de Secchi (SDD por sus siglas en inglés) Al igual que la turbidez, la transparencia se utiliza como medida relativa de claridad del agua. Fue desarrollada hace más de 150 años y cuantifica la profundidad máxima visible de un disco blanco y negro sumergido en un cuerpo de agua (Topp et al., 2020). Los estudios de la claridad del agua mediante sensores remotos utilizan casi universalmente longitudes de onda y proporciones de bandas que incluyen el espectro rojo de alguna manera (Tabla 1.7). La reflectancia en estas longitudes de onda explica las concentraciones totales de sedimento y clorofila, de modo que el aumento del brillo se asocia con una disminución de la claridad del agua. Desde hace mucho tiempo se reconoce que la claridad del agua es un indicador de la disponibilidad de nutrientes y las concentraciones de clorofila en las masas de agua, por lo que los estudios de teledetección lo utilizan con frecuencia como indicador del estado trófico general del lago (Dörnhöfer & Oppelt, 2016; Topp et al., 2020).

Tabla 1.7: Artículos analizados que estudian la transparencia con teledetección.

Autores	**Área de estudio**	**País**	**Período de estudio**	**Satélite**	**Método**
(Bonansea et al., 2015)	Río Tercero reservoir	Argentina	2003-2010	Landsat 5	empírico
(Chao Rodríguez et al., 2013)	Lake Arreo	Spain	2000-2012	Landsat 5	empírico
(Hicks et al., 2013a)	34 lakes	New Zealand	2000-2009	Landsat 5	Semi-empírico
(Mancino et al., 2009)	Monticchio lakes	Italy	2001	Landsat 5	empírico
(He et al., 2021)	Dashahe Reservoir	China	2013-2018 (2 imag/año)	Landsat 8	Machine Learning
(Masocha et al., 2018)	two reservoirs	Zimbabwe	jun-13	Landsat 8	Semi-empírico
(Guo et al., 2023)	Lake Simcoe	Canada	2013-2019	Landsat 8	Machine Learning
(Arias-Rodriguez et al., 2021)	Five lakes	Mexico	2012-2018	Landsat 8	Machine Learning
(Arias-Rodriguez et al., 2023)	Global	Global	2021-2022	Landsat 8	Machine Learning
(Lehmann et al., 2019)	23 lakes in Rotorua Lakes Region	New Zealand	1999 - 2018	Landsat 7 y Landsat 8	empírico
(Zeng et al., 2023)	4 Yunnan Plateau lakes	China	ene 2013 - ago 2022	Landsat 8	empírico
(Zeng et al., 2023)	4 Yunnan Plateau lakes	China	ene 2013 - ago 2022	Landsat 8	Machine Learning
(Deutsch et al., 2022)	lakes across southern	Canada	2017 - 2020	Landsat 8	empírico
(Deutsch et al., 2021)	lakes across southern	Canada	2013 - 2019	Landsat 8	Semi-empírico
(Y. Zhang et al., 2021)	various lakes	China	2016 - 2018	Landsat 5, 7 y 8	Semi-empírico
(Cui et al., 2022)	Chaohu Lake, Shengjin Lake, and Jiaogang Lake	China	2013 - 2019	Landsat 8	Machine Learning

Autores	Área de estudio	País	Período de estudio	Satélite	Método
(M. Chen et al., 2022)	Honghu Lake	China	1987 - 2020	Landsat 5, 7 y 8	Semi-analítico
(C. Zhao et al., 2022)	Hulun Lake	China	2010 - 2020	Landsat 5, 7 y 8	Semi-empírico
(Lu et al., 2023)	107 lakes and reservoirs in Yangtze Plain	China	1984 - 2020	Landsat 5, 7 y 8	Semi-empírico
(Song et al., 2020)	2759 lakes	China	2013 - 2018	Landsat 8	Semi-empírico
(Nascimento Silva et al., 2017)	Reservoir of Tocantins river	Brazil	2007 - 2014	Landsat 7	Machine Learning
(Rodrigues et al., 2017)	Nav reservoir	Brazil	2014 -2016	Landsat 8	Semi-analítico
(Ren et al., 2018)	Three Gorges and Dongting Lake	China	2013 - 2017	Landsat 8	Semi-empírico
(Maciel et al., 2023)	300+ water bodies	global	1985 - 2022	Landsat 5, 7 y 8	Machine Learning
(Papoutsa et al., 2014)	four different Case-2 waters	Cyprus and Greece	2010	Landsat 5	Semi-empírico
(Rubin et al., 2021)	Several lakes	United States	1984 - 2017	Landsat 5, 7 y 8	Machine Learning
(Q. Wang et al., 2022)	Several lakes	United States, canada and Mexico	1990–2019	Landsat 5, 7 y 8	Semi-empírico
(Tao et al., 2022)	10.814 lakes	China	1984 - 2018	Landsat 5, 7 y 8	empírico
(Somasundaram et al., 2021)	550 reservoirs	Sri Lanka	2013 - 2020	Landsat 8	Semi-analítico
(Markogianni et al., 2022)	50 lakes	Greece	2013 - 2016 y 2018	Landsat 7 y 8	Semi-empírico
(Mushtaq et al., 2022)	Wular Lake	India	oct-18	Landsat 8	Semi-empírico
(Song et al., 2022)	Global	Global	1984 - 2020	Landsat 5, 7 y 8	Semi-empírico
(F. Yang et al., 2023)	Honghu Lake	China	2000-2021	Landsat 5, 7 y 8	Semi-empírico
(Setiawan et al., 2019)	Lake Maninjau	Indonesia	1987 - 2018	Landsat 7	Semi-empírico

Autores	Área de estudio	País	Período de estudio	Satélite	Método
(Domínguez Gómez et al., 2009)	Parque Regional Sureste	Spain	1984 -2000	Landsat 7	empírico
(Doña et al., 2014)	Albufera y Parque regional del Sureste	Spain	1985-2006	Landsat 5 y 7	empírico

- La **Temperatura superficial** del agua en general está vinculada a los flujos de calor y energía y regula la estratificación térmica. Por lo tanto, los cambios en la temperatura del agua afectan las funciones ecosistémicas de las masas de agua y generan cambios en la composición de especies y la concentración de oxígeno. La teledetección proporciona información espacial sobre la temperatura radiométrica de la superficie (Tabla 1.8) que puede indicar la temperatura epilímnica; Sin embargo, dependiendo de la velocidad del viento, la temperatura de la superficie muy delgada (o skin surface) tiende a ser más fría que la capa superior de 50 cm de la columna de agua (Dörnhöfer & Oppelt, 2016).

Tabla 1.8: Artículos analizados que estudian la temperatura superficial del agua con teledetección.

Autores	Área de estudio	País	Período de estudio	Satélite	Método
(Bonansea et al., 2015)	Río Tercero reservoir	Argentina	2003-2010	Landsat 5	empírico
(Chao Rodríguez et al., 2013)	Lake Arreo	Spain	2000-2012	Landsat 5	empírico
(Simon et al., 2014b)	Lake Bariousses, Lake Bimont	France	2006-2013	Landsat 5	Semi-analítico
(Mohsen et al., 2021)	Lake Burullus	Egypt	2010-2013	Landsat 7	Semi-empírico
(Lamaro et al., 2013)	Río Tercero	Argentina	2000-2006	Landsat 7	Semi-analítico
(Wermuth et al., 2022)	Pampulha reservoir	Brazil	2013-2020	Landsat 8	Semi-analítico

Autores	Área de estudio	País	Período de estudio	Satélite	Método
(Y. Huang et al., 2015)	Alaska lakes	United States	2013	Landsat 8	empírico
(Tavares et al., 2019)	Lake Mangueira	Brazil	Not reported	Landsat 7	empírico
(Prats et al., 2018)	442 inland water bodies	France	1999–2016	Landsat 5 and 7	Semi-analítico
(Kong et al., 2024)	Poyang Lake	China	2020 -2021	Landsat 8	Semi-analítico
(Kramer et al., 2023)	Itaipu Reservoir	Brazil	2015-2017	Landsat 8	Semi-analítico
(Y. Huang et al., 2017)	Arctic Lakes	United States	2013	Landsat 8	Semi-analítico

1.1.4. Métodos para modelar los parámetros de calidad de agua

Los modelos que relacionan las cualidades ópticas de un cuerpo de agua y su concentración de componentes ópticamente activos con la calidad del agua se denominan comúnmente algoritmos bio-ópticos (Topp et al., 2020). En aguas continentales, estos modelos pueden clasificarse como empíricos, semi-empíricos, semi-analíticos o basados en aprendizaje automático (Dörnhöfer & Oppelt, 2016; Mouw et al., 2015; Topp et al., 2020).

- **Métodos empíricos:** constituyen el enfoque más comúnmente utilizado en la teledetección de aguas continentales. Implica ajustar una regresión lineal estándar entre valores de la banda espectral y mediciones de calidad del agua *in situ* que coincidan temporalmente, a menudo generando múltiples modelos y eligiendo el mejor ajuste mediante la comparación de métricas de error. Una limitación inherente de este enfoque es que debido a la variabilidad espectral que generan las variaciones en la composición atmosférica y el agua en la observación de los parámetros de calidad de agua, no es posible generalizar los resultados a grandes escalas espaciales y temporales. Por lo tanto, los modelos empíricos se limitan a predicciones confiables únicamente dentro del rango y la configuración de los datos de entrada (Dörnhöfer & Oppelt, 2016; Topp et al., 2020). (Matthews, 2011) proporcionó una revisión exhaustiva de los algoritmos empíricos y en el **Anexo 1** se listan los modelos empíricos recopilados durante la revisión bibliográfica de esta tesis.

- **Métodos semi-empíricos:** a diferencia de los puramente empíricos, utilizan valores de índices espectrales de múltiples bandas con alguna base en las propiedades físicas del parámetro a estudiar. Estos modelos se centran en gran medida en la medición de la claridad del agua, chl-a, cianobacterias y TSS. Al igual que los índices de vegetación terrestre (por ejemplo, el NDVI), están diseñados para mejorar las propiedades espectrales con las que medir los parámetros de calidad de agua y al mismo tiempo reducir el ruido de parámetros ópticos extraños. Existen múltiples índices utilizados en este método (J. Wang & Chen, 2024), como son el índice de clorofila (X. Zhao et al., 2021) y el Índice de clorofila en la vegetación (Raymond Hunt et al., 2011). Debido a su base en propiedades físicas, los modelos semi - empíricos son más generalizables que los enfoques puramente empíricos. Sin embargo, requieren mediciones de longitudes de onda específicas que capturen características de absorción y picos de dispersión, lo que restringe su aplicabilidad a sensores con centros de banda adecuadamente ubicados y resolución espectral suficiente (Topp et al., 2020).
- **Métodos semi-analíticos:** se basan en la física e implican parametrización basada en las propiedades ópticas inherentes (PIO) del agua y la atmósfera. Las PIO de un cuerpo de agua determinado se modelan en coordinación con propiedades ópticas aparentes (incluidas las condiciones de iluminación, la orientación del sensor y el campo de visión) para construir valores teóricos de absorción y retrodispersión que luego se pueden descomponer mediante una ecuación inversa para estimar los componentes de la calidad del agua ópticamente activos. Como resultado, los modelos semianalíticos, que incorporan mediciones *in situ* para parametrizar la ecuación inversa, son la forma principal de algoritmos basados en la física desarrollados para la obtención de parámetros de calidad de agua con sensores remotos (Dörnhöfer & Oppelt, 2016; Topp et al., 2020). Existen modelos semi-analiticos ampliamente utilizados como el propuesto por (Jimenez-Munoz et al., 2009) para estudiar la temperatura superficial, el Shallow Water Bio-optical Properties (SBOP) algorithm para estudiar CDOM (J. Li et al., 2018), el quasi-analytical algorithm (QAA) para obtener transparencia del agua (M. Chen et al., 2022; Rodrigues et al., 2017), entre otros.

- **Métodos basados en aprendizaje automáticos:** Si bien son inherentemente empíricas, las técnicas de aprendizaje automático (o machine Learning) se analizan por separado debido a su complejidad computacional y su capacidad para manejar relaciones no lineales (Topp et al., 2020). Los algoritmos de aprendizaje automáticos más utilizados en estudios de calidad de agua son redes neuronales artificiales (RNA) (He et al., 2021; F. Yang et al., 2023; X. Zhao et al., 2021), random forests (RF) (Adusei et al., 2021; Arias-Rodriguez et al., 2023; Z. Cao et al., 2022; Rubin et al., 2021; J. Wang & Chen, 2024; Y. Yang et al., 2023), extreme gradient boosting (J. Wang & Chen, 2024), multilayer perceptron regressor (MLP) (Arias-Rodriguez et al., 2023; Zeng et al., 2023) and support vector machines (SVM) (Adusei et al., 2021; Arias-Rodriguez et al., 2023; Z. Cao et al., 2022; Peterson et al., 2020; J. Wang & Chen, 2024; L. Wang et al., 2020; Y. Yang et al., 2023; Zeng et al., 2023). Al igual que con los modelos empíricos tradicionales, los enfoques de aprendizaje automático solo son aplicables dentro del rango y la configuración de los datos utilizados para entrenar un modelo determinado. Sin embargo, a diferencia de los modelos empíricos tradicionales, la mayoría de los modelos de aprendizaje automático utilizan el aprendizaje iterativo para reducir el error general y maximizar el ajuste del modelo (Topp et al., 2020).

(Odermatt et al., 2012) recopiló una serie de algoritmos publicados desde el 2006 al 2011 y en el **Anexo 1** se presentan los modelos obtenidos por múltiples autores para los diferentes parámetros de calidad de agua, así como sus errores y sus aplicaciones.

1.1.5. Factores externos e internos que influyen en la calidad de las masas de agua continentales

Se considera que la calidad del agua superficial continental está influenciada por una amplia gama de factores antropogénicos y naturales, como el uso del suelo y las variaciones topográficas y climáticas, así como las características morfométricas de las masas de agua. Comprender el estado de la calidad del agua superficial e identificar los factores clave que influyen es importante para establecer políticas para la gestión sostenible de los recursos hídricos (You et al., 2019).

Factores topográficos

Las áreas de mayor elevación pueden tener temperaturas más frías y menos impacto humano, mientras que las pendientes pronunciadas pueden aumentar la escorrentía y la erosión, transportando sedimentos y contaminantes a los cuerpos de agua. La topografía se ha considerado un factor que influye en la calidad de las aguas superficiales continentales, por ejemplo, (Pratt & Chang, 2012) encontraron que los arroyos con una elevación media más baja generalmente tenían una mayor concentración de nitrógeno nitrato, mientras que la pendiente media exhibía una correlación positiva con los sólidos totales.

Un elemento clave que influye directamente en la temperatura superficial del agua es la temperatura del aire, que a su vez depende de la latitud, longitud y altitud (Livingstone et al., 1999; Ptak et al., 2018).

Factores climáticos

La temperatura del aire se relaciona directamente con la temperatura superficial de la masa del agua, la cual afecta la solubilidad de los gases en el agua (como el oxígeno), la velocidad de los procesos biológicos y la prevalencia de ciertos contaminantes. La Precipitación influye en el volumen de agua, los patrones de escorrentía y la dilución o concentración de contaminantes. (Fukushima et al., 2000) encontró que la demanda química de oxígeno y la transparencia en el agua del lago Kasumigaura, el segundo lago más grande de Japón, se deterioraba con el aumento de la temperatura del aire. Además, observaron que una mayor precipitación conducía a una alta concentración de nitrógeno, probablemente inducida tanto por la escorrentía superficial que tenía una alta concentración de nitrógeno como por la reducción de los tiempos de residencia del agua del lago.

Uso y cobertura del suelo

Las áreas urbanas contribuyen a la contaminación del agua a través de escorrentías que contienen aceites, metales pesados y otros contaminantes de carreteras y edificios, mientras que las zonas agrícolas pueden introducir fertilizantes, pesticidas y sedimentos en los cuerpos de agua. Por su parte la deforestación y las prácticas de gestión forestal afectan las tasas de erosión y la carga de sedimentos en los cuerpos de agua.

Las concentraciones de contaminantes en los cuerpos de agua están correlacionadas positivamente con la agricultura y el uso del suelo urbano, pero negativamente con los tipos de cobertura de vegetación natural. Por ejemplo, el uso de la tierra agrícola y urbano se considera el factor principal para la concentración de nitrógeno en el agua en los cuerpos de agua superficiales (Morrice et al., 2008).

Características morfométricas del cuerpo de agua

Los cuerpos de agua más grandes y profundos pueden tener temperaturas más estables y menor susceptibilidad a la contaminación en comparación con los más pequeños y menos profundos. Las masas de agua poco profundas responden más rápidamente al cambio climático, dado que la profundidad del agua tiene una fuerte influencia en las temperaturas máximas del agua. Cuanto menos profundo es el lago, más estrechamente se acoplan la temperatura del aire y del agua. Para los lagos menos profundos, la tasa de calentamiento es significativamente mayor. Esto significa que las fluctuaciones estacionales en estas condiciones son más pronunciadas (Mooij et al., 2008). En consecuencia, en los lagos poco profundos el impacto de la radiación estacional y durante todo el año es mucho más fuerte que en los lagos más profundos. Además, en el caso de lagos no regulados, el nivel del agua es un buen indicador del efecto del cambio climático porque muestra la dinámica entre la entrada y salida de agua en el sistema (Adrian et al., 2009).

Además de la profundidad, la superficie de los lagos también tiene una influencia importante en la temperatura superficial del agua. La temperatura del aire tiene un efecto directo sobre la temperatura del agua porque impulsa la transferencia de calor entre la atmósfera y el agua. Según la investigación de (Magee & Wu, 2017), cuanto mayor es la superficie, mayor es la mezcla del viento. La mezcla del viento es un mecanismo de transferencia de calor y puede aumentar el efecto de la mezcla vertical (Rueda et al., 2009). Se ha demostrado que el tamaño del lago influye en la magnitud del enfriamiento y calentamiento diurno (Woolway et al., 2016). Cuanto mayor es la superficie, mayor es la interfaz agua-aire y más propensa es la temperatura superficial a la evaporación (Peng et al., 2022).

1.2. Estado de la cuestión

En los últimos años, la evaluación de la calidad del agua con teledetección se ha convertido en una tarea crucial en el monitoreo y la gestión ambiental. La disponibilidad de plataformas satelitales equipadas con sensores avanzados ha revolucionado la capacidad para observar, medir y analizar diversos parámetros que influyen en la calidad del agua en diversos entornos acuáticos. Esta integración de técnicas de teledetección con métodos tradicionales de monitoreo *in situ* ofrece conocimientos incomparables sobre la naturaleza dinámica de los cuerpos de agua, facilitando la toma de decisiones oportuna para la gestión de recursos, el control de la contaminación y la preservación de los ecosistemas.

El estado del arte en teledetección de la calidad del agua abarca un amplio espectro de metodologías, que van desde la detección de propiedades físicas como la temperatura y la turbidez hasta la estimación de constituyentes químicos como la clorofila-a y la materia orgánica disuelta. Estas técnicas aprovechan las firmas espectrales únicas del agua y sus componentes para recuperar información valiosa con alta resolución espacial y temporal. Además, los avances en los algoritmos de procesamiento de datos y los enfoques de aprendizaje automático han mejorado la precisión y eficiencia de la evaluación de la calidad del agua a partir de datos de teledetección, lo que permite un monitoreo integral a escala regional y global.

En el análisis de la cuestión que se presenta a continuación, se profundiza de forma integral en las diversas tecnologías de detección remota, técnicas de análisis de datos y los diversos parámetros que se estudian, todo ello enfocado en las aplicaciones en la evaluación de la calidad del agua (Figura 1-1). Esta exploración tiene como objetivo vislumbrar los desafíos, oportunidades y direcciones futuras en el aprovechamiento de la teledetección para la gestión eficaz de los recursos hídricos y la salvaguardia de los ecosistemas acuáticos.

Figura 1-1: Enfoque de análisis de la literatura sobre calidad de agua en masas de agua continentales.

El procedimiento seguido para desarrollar el estado de la cuestión se observa en la Figura 1-2.

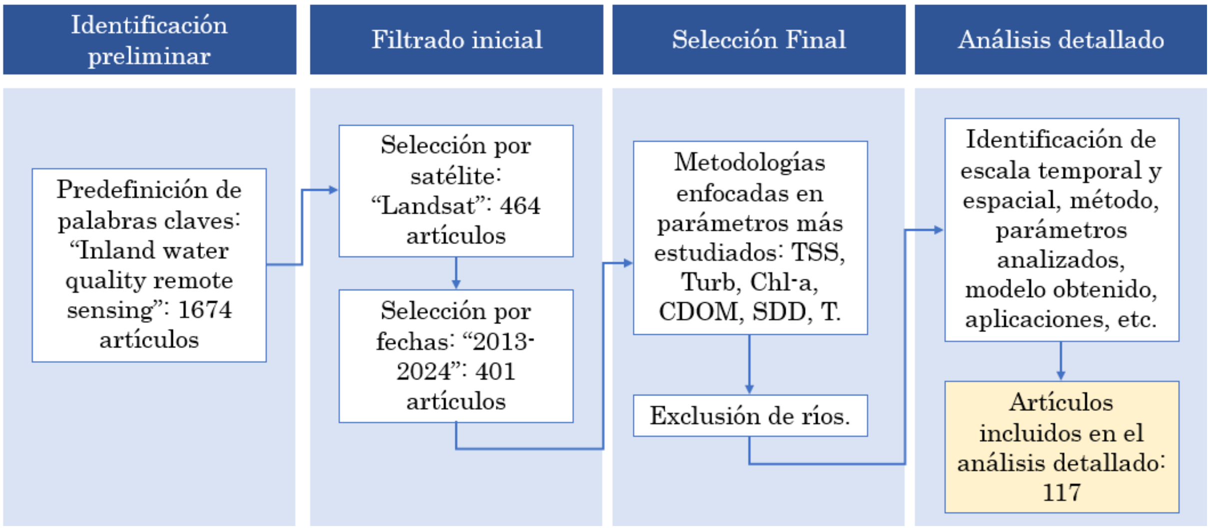

Figura 1-2: Procedimiento de búsqueda y selección de literatura en este estudio.

Se realizó una identificación preliminar donde se definieron las palabras clave y se llevó a cabo una búsqueda bibliográfica exhaustiva de artículos en Web of Science empleando los términos "inland water quality" y "remote sensing". Se recopilaron en total 1674 artículos que cubren todo el mundo con un mayor porcentaje en Norte América, China y Europa. (Figura 1-3). El número de publicaciones ha ido creciendo espectacularmente desde la introducción de la teledetección en los años 1970 con un incremento aún mayor en la última década (Figura 1-4).

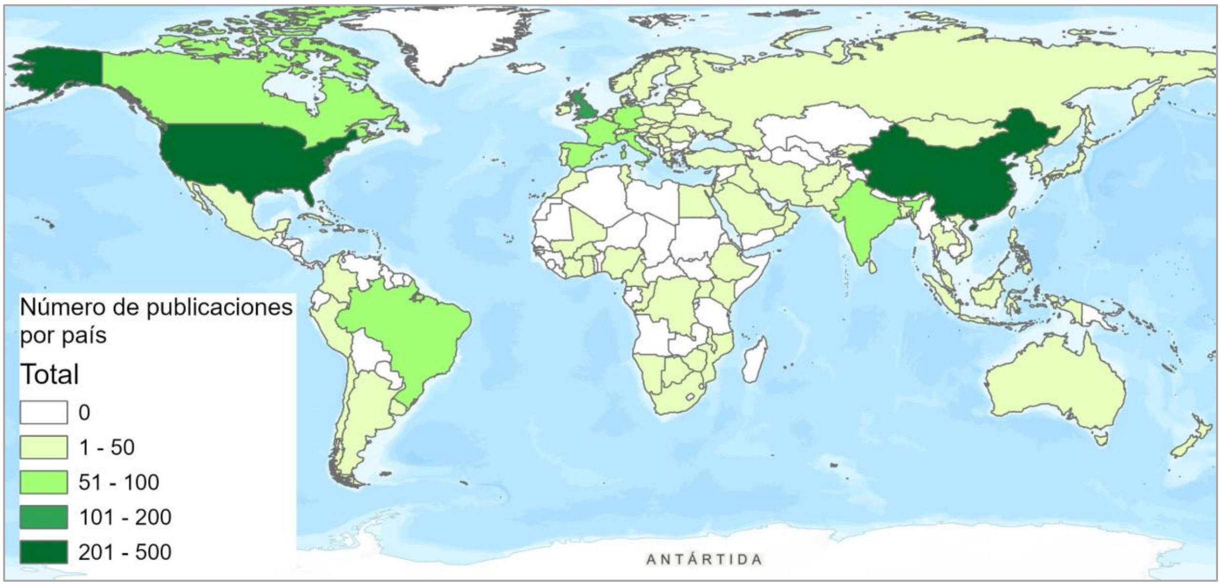

Figura 1-3: Mapa con la distribución de los artículos publicados en el panorama global con las palabras clave "Inland water quality remote sensing".

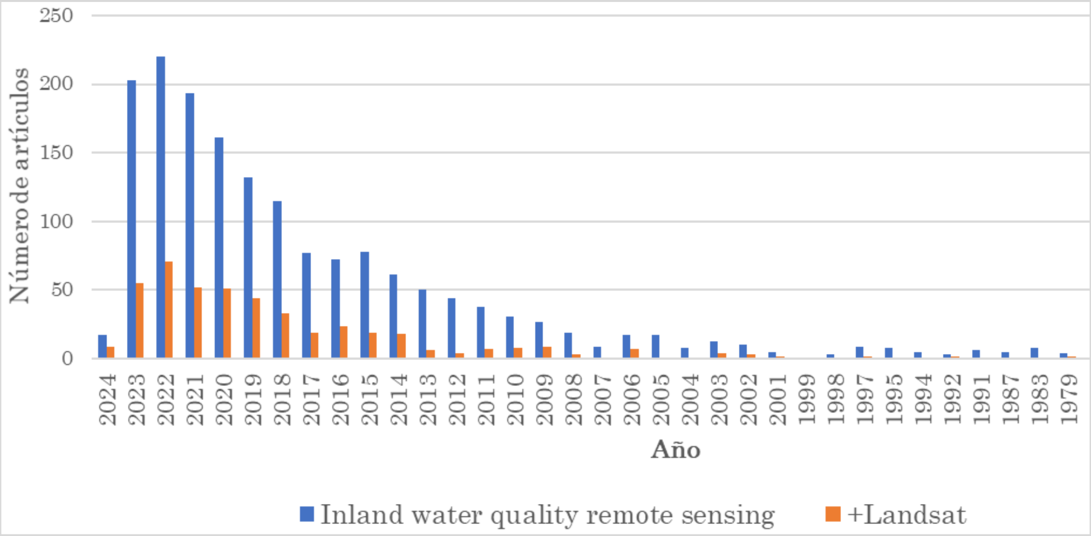

Figura 1-4: Artículos publicados por año.

Posteriormente, se llevó a cabo un filtrado con la palabra clave "Landsat" para analizar solo aquellos artículos que utilizaran este satélite, dado que, entre los satelites utilizados, Landsat tiene la mayor resolución espacial y el mayor periodo de funcionamiento (capítulo 1.1.1), por lo que se convierte en una gran herramienta para estudiar la dinámica de las masas de agua en la península Ibérica, una oportunidad que no existe con otros satélites debido a la resolución espacial y la longitud de la serie a estudiar. Se obtiene un resultado de 464 publicaciones, que además se filtró con los artículos publicados desde el año 2013 con un total de 401 publicaciones.

De estos últimos, se analizaron los títulos, las palabras clave y los resúmenes con el objetivo de llevar a cabo una selección final de los artículos en los que evaluar las metodologías, técnicas y enfoques utilizados. Se analizaron únicamente las publicaciones que estudian los parámetros de calidad de agua mencionados en el capítulo 0. La exclusión de los estudios en ríos y aguas costeras (fundamentales para el desarrollo de métodos de teledetección de la calidad de las aguas continentales) ha permitido centrarse mejor en las aplicaciones de la teledetección de lagos, y estuarios y en cómo esas aplicaciones han cambiado con el tiempo.

Cada uno de los 117 artículos del subconjunto final (Anexo 1), se leyó para analizar las tendencias generales en la escala espacial, temporal, metodología y aplicaciones según los criterios que se describen en la Tabla 1.9.

Tabla 1.9: Criterios de análisis detallado de la literatura seleccionada

Criterio	Descripción
Área de estudio	Masas de agua estudiadas y el país donde se encuentran.
Período de estudio	Las fechas en las que se elaboró el estudio. Se determinan desde la fecha de la primera imagen hasta la fecha de la imagen final.
Parámetro de calidad de agua	Los parámetros de calidad del agua incluidos en el estudio (capítulo 1.1.3).
Satélite	Landsat 4, 5, 7, 8 y/o 9.
Método	Método para obtener el modelo: Empírico, semi- empírico, analítico o Machine Learning.
Bandas	Bandas espectrales utilizadas en el modelo final.
Modelo obtenido	La ecuación obtenida que relaciona los datos de campo con la imagen Landsat (en caso de método empírico o semi- empírico) o el modelo semi – analítico (capítulo 0).
Errores	Error de validación del modelo.
Aplicación	El análisis y el uso que hace del parámetro de calidad de agua obtenido.

Los métodos más utilizados para modelar los parámetros son el método semi – empírico con un 46% de los artículos revisados, seguido por métodos de aprendizaje automático con un 23%, empíricos con un 16% y semi – analíticos con un 15% (Figura 1-5). En la Figura 1-6 se observa que los métodos empírico y semi - analítico se han utilizado constantemente en el período analizado, mientras que el aprendizaje automático (o machine Learning) ha tenido un importante repunte desde el año 2020 y el método semi – empírico ha ido en aumento hasta el año 2022.

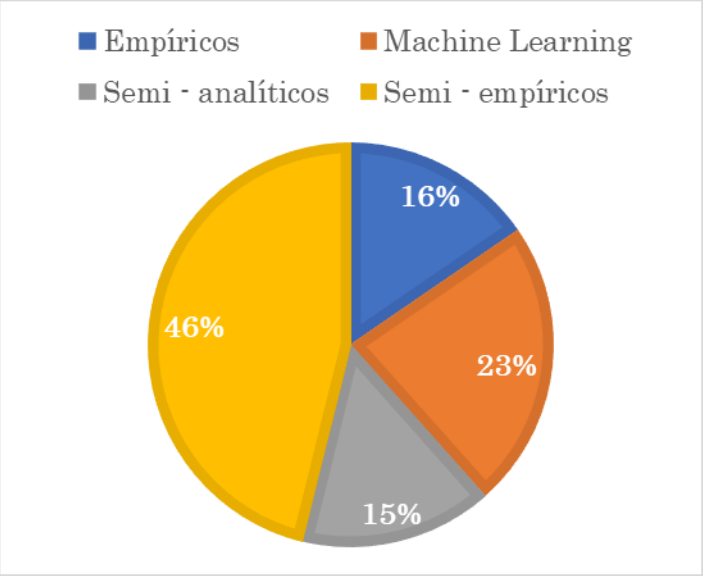

Figura 1-5: Clasificación de la literatura analizada según los métodos.

Asimismo, el parámetro más estudiado es la concentración de clorofila-a con un 28% de las publicaciones analizadas seguido por la transparencia medida con el disco de Secchi con un 21% (Figura 1-7), que ha ido en aumento en los últimos años (Figura 1-8). El parámetro menos estudiado es el fósforo total.

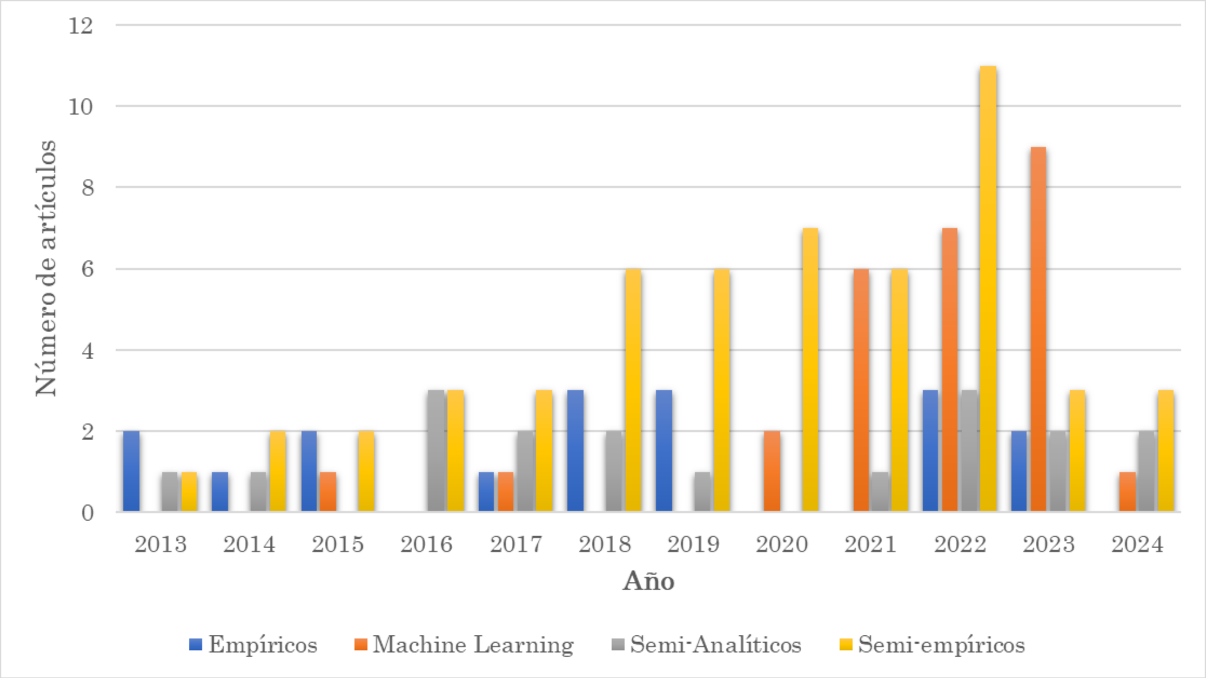

Figura 1-6: Evolución de los métodos utilizados en la literatura analizada a lo largo de los años.

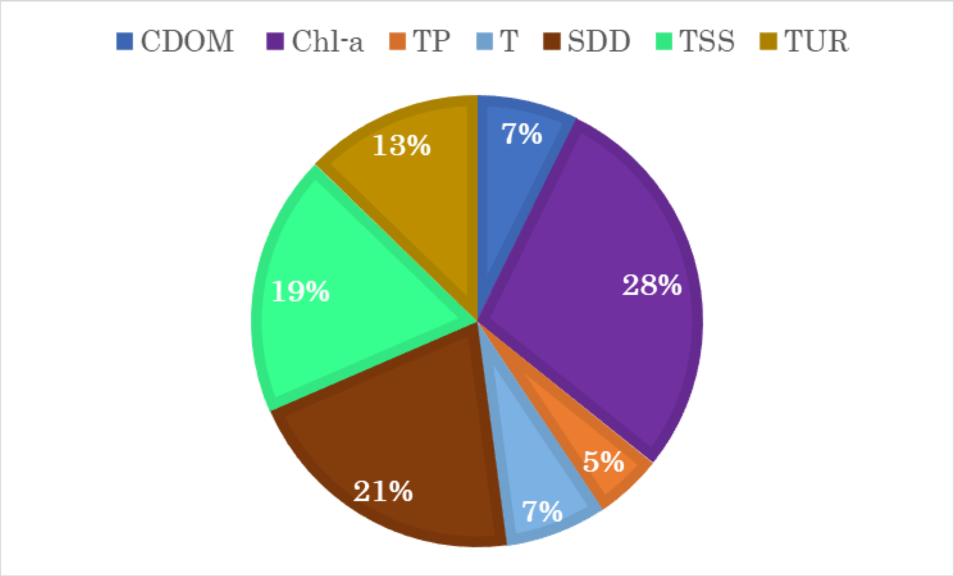

Figura 1-7: Clasificación de la literatura analizada según los parámetros estudiados.

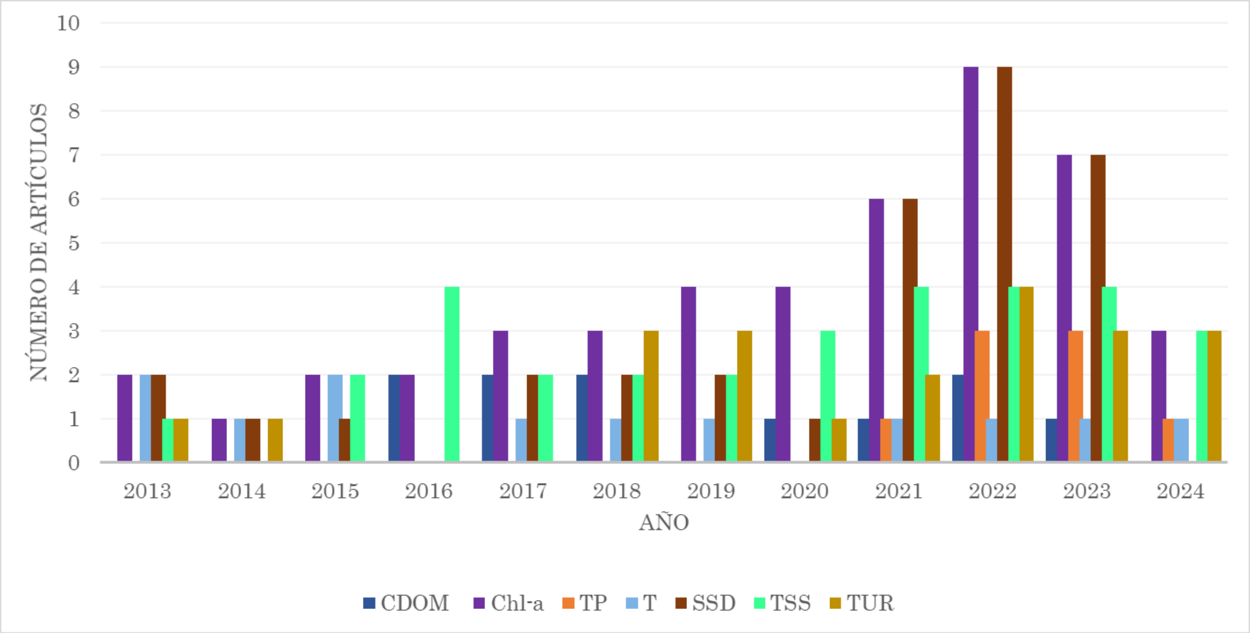

Figura 1-8: Evolución del número de artículos a lo largo de los años según los parámetros.

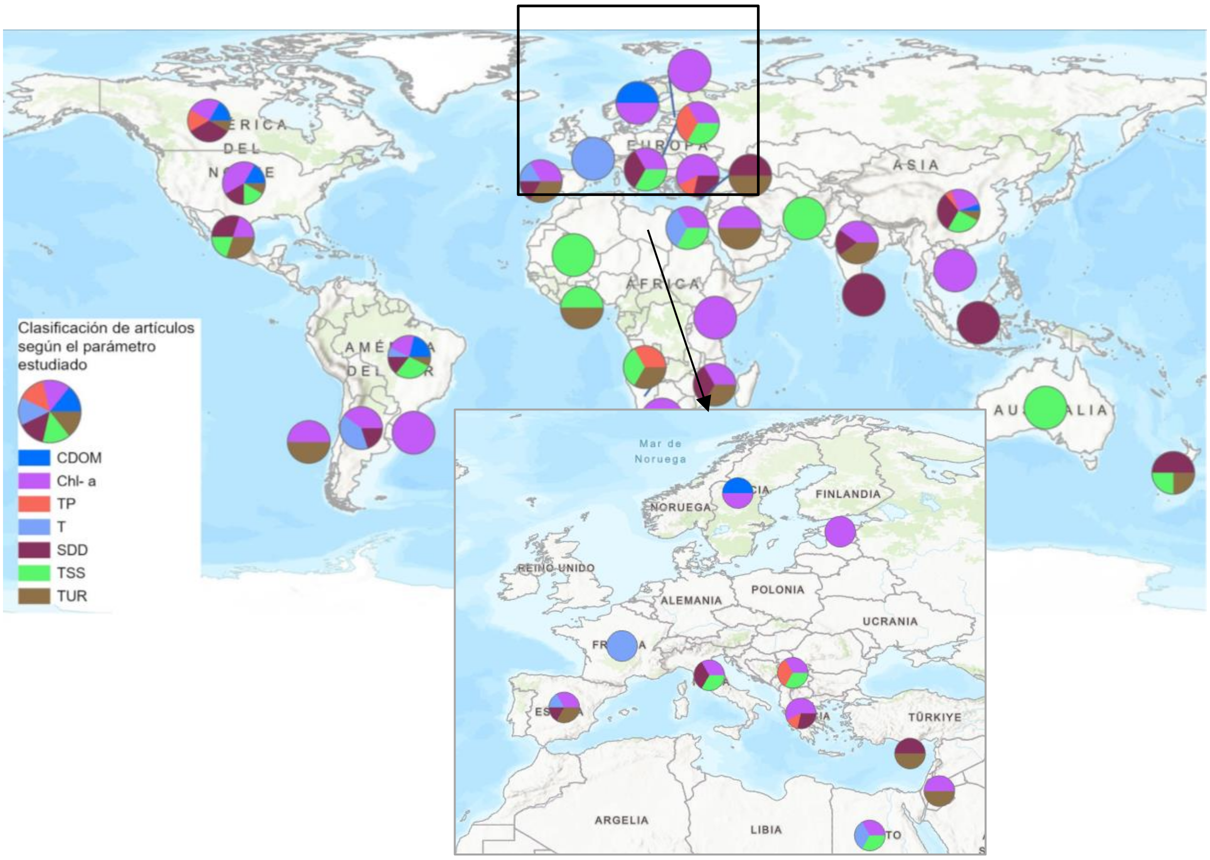

Figura 1-9: Distribución mundial de las zonas de estudio de los artículos analizados clasificados según los parámetros estudiados.

En general, el parámetro más estudiado a nivel mundial es la clorofila, excepto en zonas del oeste de África y Australia donde se estudian más los sólidos en suspensión, y en el sur de Asia donde se estudia más la transparencia. En España, se han estudiado la Clorofila -a, la turbidez, la transparencia y la temperatura superficial (Figura 1-9).

Cada uno de los 117 artículos resultantes se clasificó posteriormente según su aplicación en una de las categorías que se describen a continuación

- **Puramente técnicos:** El propósito del artículo es presentar y validar un nuevo modelo o metodología. Los resultados consisten en validación del modelo y métricas de error.
- **Técnicos con alguna aplicación ambiental:** el artículo trata predominantemente de desarrollo y validación de métodos, pero incluye algunos análisis sobre el resultado del modelo propuesto ya sea espacial o temporalmente.
- **Ambientales sobre análisis de tendencias**: El propósito del artículo es examinar patrones espaciotemporales y/o tendencias en la calidad del agua dentro del área de estudio. Se presentan los resultados de la validación del modelo, pero la mayor parte de los resultados y la discusión se centra en el análisis de tendencias espaciales o temporales.
- **Puramente ambientales:** Los resultados y la discusión se centran en la dinámica espaciotemporal de la calidad del agua, así como en los impulsores y/o impactos del cambio en la calidad del agua.

Según la clasificación realizada, se observa que la mayoría de las publicaciones tienen resultados técnicos con alguna aplicación ambiental con un 47%, seguidos por puramente técnicos con un 33%, mientras que solo el 18% están más enfocados en análisis ambientales sobre tendencias y el 2% son puramente ambientales (Figura 1-10 y Figura 1-11). Este patrón se debe a que es más probable que las publicaciones con la palabra clave "remote sensing" se enfoquen sobre desarrollo de métodos y en comunicar los avances dentro de la comunidad de teledetección, con quizás menos alcance para hidrólogos, ecólogos y otros científicos que no se centran inherentemente en la teledetección.

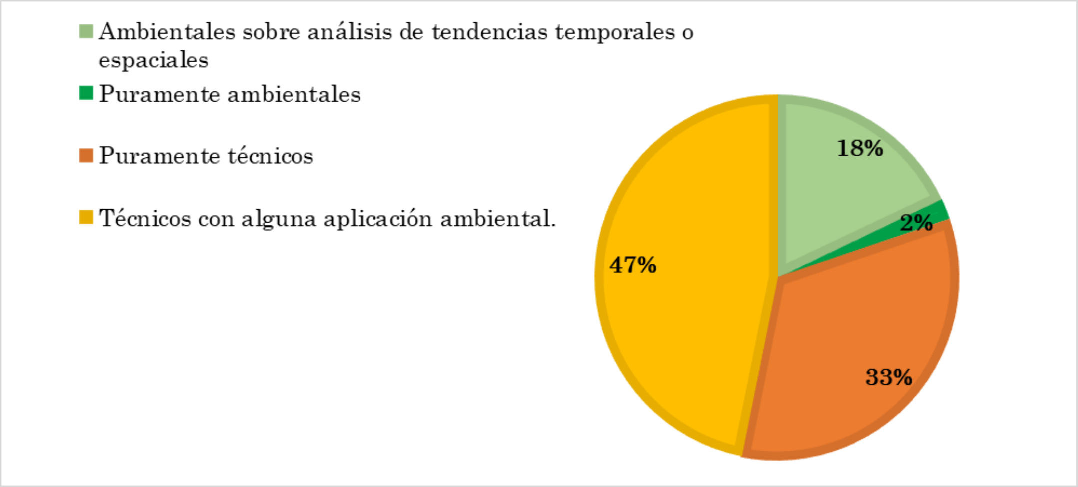

Figura 1-10: Clasificación de la literatura analizada según su aplicación.

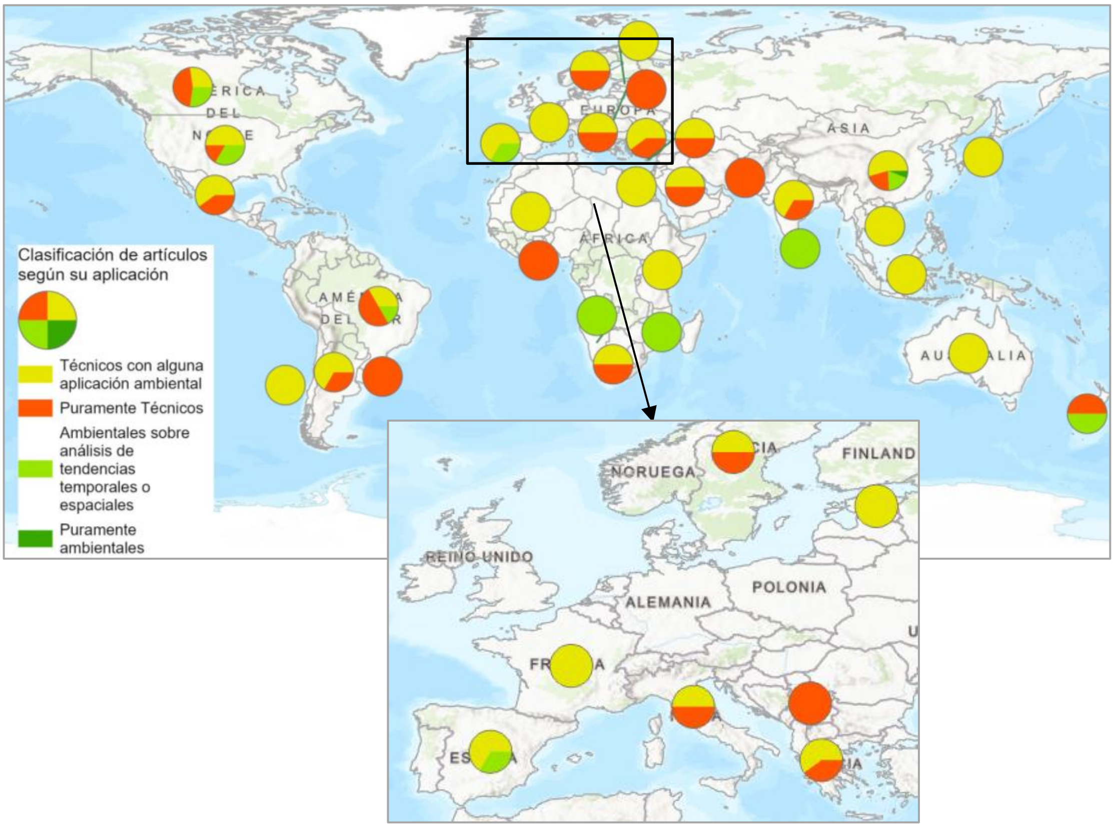

Figura 1-11: Distribución mundial de las zonas de estudio de los artículos analizados clasificados según su aplicación.

1.3. Justificación

Como se ha indicado, los cuerpos de agua continentales superficiales, que abarcan ríos, embalses, lagos y humedales, son componentes esenciales del medio ambiente y desempeñan funciones diversas y vitales en el funcionamiento de los ecosistemas y el bienestar humano: (1) sirven como hábitat para una gran variedad de especies de plantas y animales, fomentando una rica biodiversidad y apoyando procesos ecológicos (Moss, 2012); (2) brindan servicios ecosistémicos cruciales, como la purificación del agua, la regulación de inundaciones y la moderación del clima, lo que beneficia tanto a los ecosistemas naturales como a las sociedades humanas (Williamson et al., 2009); (3) son fuentes primarias de agua dulce, que sustentan la producción agrícola, la industria y las poblaciones urbanas en todo el mundo (Stendera et al., 2012); (4) tienen un significado cultural y brindan oportunidades para la recreación y el turismo. Reconocer la importancia de los cuerpos de agua continentales e implementar medidas efectivas de gestión y conservación es esencial para salvaguardar la biodiversidad, garantizar la seguridad hídrica y promover el desarrollo sostenible frente a los desafíos ambientales (Dörnhöfer & Oppelt, 2016). Sin embargo, la explotación antropogénica y múltiples factores estresantes como son la eutrofización, los contaminantes orgánicos e inorgánicos, las alteraciones morfológicas y los efectos del cambio climático, como la acidificación o el aumento de la temperatura del agua, amenazan las funciones ecológicas de las aguas continentales en todo el mundo (Dörnhöfer & Oppelt, 2016; Stendera et al., 2012).

Actualmente, existe el objetivo común de mejorar el estado ecológico de las masas de agua continentales a nivel mundial gracias a directivas y acuerdos nacionales e internacionales como son la Ley de Agua Limpia de Estados Unidos promulgada en 1972 y destinada a regular la contaminación del agua y mantener los estándares de calidad del agua para ríos, lagos y otros cuerpos de agua (Copeland, 2016); la Directiva Marco del Agua de la Unión Europea adoptada en 2000 con el objetivo de lograr un buen estado ecológico y químico de las aguas superficiales y subterráneas en todos los estados miembros (EC, 2000); Los Objetivos de Desarrollo Sostenible (ODS) de las Naciones Unidas, específicamente el Objetivo 6 que es garantizar la disponibilidad y la gestión sostenible del agua y el saneamiento para todos, e incluye objetivos relacionados con la mejora de la calidad del agua, la reducción de la contaminación, la protección de los ecosistemas de agua dulce y la mejora de la eficiencia en el uso del agua(Naciones Unidas, 2018); el acuerdo sobre la calidad del agua de los Grandes Lagos entre Canadá y Estados Unidos destinado a proteger y restaurar la calidad del agua de los Grandes Lagos (US EPA, 2012); la Convención de Ramsar sobre los Humedales centrado en la conservación y el uso sostenible de los humedales a través de la cooperación internacional(Ramsar, 1971), entre otros.

Para esto, es necesaria la identificación de factores estresantes y la implementación de estrategias de gestión sostenible respaldadas por un seguimiento más o menos frecuente (Dekker & Hestir, 2012; Dörnhöfer & Oppelt, 2016). El seguimiento a largo plazo de la calidad del agua en las masas de agua continentales superficiales es primordial por varias razones. En primer lugar, proporciona datos esenciales para evaluar la salud de los ecosistemas acuáticos y detectar cambios a lo largo del tiempo, lo que permite una intervención temprana en respuesta a la contaminación, la degradación del hábitat u otros factores estresantes como el cambio climático (Chu et al., 2018). Los conjuntos de datos a largo plazo permiten a los científicos y formuladores de políticas identificar tendencias, establecer condiciones de referencia y evaluar la efectividad de las estrategias de gestión destinadas a preservar la calidad del agua y la integridad de los ecosistemas (Hestir et al., 2015). En general, los esfuerzos encaminados al monitoreo son esenciales para proteger y gestionar las masas de agua continentales superficiales, garantizar su continuo suministro de servicios ecosistémicos vitales y apoyar el bienestar humano (Blanchet et al., 2022; Chu et al., 2018; Dekker & Hestir, 2012).

El uso de sensores remotos representa una herramienta eficaz y cada vez más utilizada para estudiar la calidad de las masas de agua continentales. La teledetección ofrece varias ventajas para la evaluación de la calidad del agua, incluida su capacidad para proporcionar una cobertura a gran escala, alta resolución espacial y muestreo temporal frecuente (Q. Chen et al., 2004; Williamson et al., 2009). Al capturar datos de plataformas satelitales, aéreas o de vehículos aéreos no tripulados (UAV), los sensores remotos pueden observar y monitorear cuerpos de agua con una mínima perturbación y en áreas remotas o inaccesibles. Estos sensores miden varios parámetros, incluida la temperatura del agua (Bonansea et al., 2015; Chao Rodríguez et al., 2013; Lamaro et al., 2013; Mohsen et al., 2021; Simon et al., 2014a; Wermuth et al., 2022), la turbidez (Arias-Rodriguez et al., 2021; Dave et al., 2019; Hicks et al., 2013a; Meng et al., 2022; Surisetty et al., 2018; Yépez et al., 2024), la concentración de clorofila a (Kutser et al., 2016; Mancino et al., 2009; Masocha et al., 2018; Peterson et al., 2020; Tebbs et al., 2013; Villota-González et al., 2023), la materia orgánica disuelta (J. Chen et al., 2017; Concha & Schott, 2016; Kutser, 2012; S. Martins et al., 2018; Pahlevan et al., 2022) y los sedimentos suspendidos (Adusei et al., 2021; Alcântara, Curtarelli, et al., 2016; Ghirardi et al., 2023; Lobo et al., 2015; Pahlevan et al., 2022; Shahzad et al., 2018; Sun et al., 2024), mediante el análisis de las firmas espectrales únicas del agua y sus constituyentes. Además, la teledetección permite la detección de patrones espaciales y temporales en la calidad del agua, lo que facilita la identificación de fuentes de contaminación, el seguimiento de la proliferación de algas y la evaluación de la salud de los ecosistemas (Dekker & Hestir, 2012; Dörnhöfer & Oppelt, 2016; Malthus et al., 2012). Al integrar datos de teledetección con mediciones terrestres y técnicas avanzadas de análisis de datos, como algoritmos de aprendizaje automático, los investigadores y gestores de los recursos hídricos pueden obtener información valiosa sobre la dinámica de la calidad de las aguas continentales, ayudando a la toma de decisiones informadas y a la implementación de medidas eficaces, estrategias de gestión para preservar y proteger estos valiosos recursos (Malthus et al., 2012; Mouw et al., 2015; Topp et al., 2020; Zandaryaa, 2018).

Aunque la teledetección ofrece una de las herramientas más completas espacial y temporalmente para observar la calidad de las aguas, por una variedad de razones, los investigadores y administradores hoy todavía enfrentan muchos desafíos para su uso (Malthus et al., 2012; Mouw et al., 2015; Topp et al., 2020). Entre estos desafíos, los más destacables son: (1) que no existe un método estandarizado para la corrección atmosférica para aplicaciones de calidad de aguas continentales, lo que genera un elemento de incertidumbre en las estimaciones de la calidad del agua, dado que los métodos más rigurosos de corrección atmosférica implican el uso de modelos de transferencia radiativa y pueden proporcionar mejores resultados, pero son complicados de implementar y requieren datos de entrada que no siempre están disponibles, mientras que las técnicas de corrección radiométrica simples (por ejemplo, Dark object subtraction (DOS)) se basan estrictamente en imágenes y no requieren mediciones de campo *in situ*, pero son insuficientes para proporcionar una corrección atmosférica absoluta (Kloiber et al., 2002); (2) que es necesario que se pongan a disposición metodologías para obtener parámetros de calidad del agua continentales que permitan estudiar su variabilidad a nivel regional, nacional y mundial, aunque la parametrización de algoritmos se complica por la variabilidad de las propiedades ópticas inherentes de este tipo de ecosistemas, especialmente en ecosistemas como los existentes en la península Ibérica; y (3) analizar los factores antropogénicos y naturales que pueden influir en el estado de la calidad del agua superficial en las masas de agua mediterráneas existentes en la península ibérica.

1.4. Objetivos

Con todo lo dicho, se plantea como objetivo general para esta tesis estudiar la calidad de agua en masas de agua continentales a partir de datos de teledetección en la península Ibérica teniendo en cuenta su tamaño y su variabilidad estacional y a largo plazo. Este objetivo se desarrollará en los siguientes objetivos específicos: (1) identificar y evaluar sensores remotos y productos derivados que permitan estudiar la calidad de las masas de agua en este contexto; (2) analizar la variación a nivel espacio – temporal de la calidad de agua a partir de determinados parámetros; y (3) estudiar la influencia de factores geográficos sobre determinados parámetros de calidad de agua.

2. Metodología

A continuación, se presenta la metodología propuesta para monitorear y analizar la calidad en las masas de agua continentales de la península ibérica.

2.1. Datos de entrada

2.1.1. Imágenes de satélite

Descarga de las imágenes Landsat colección 2 Nivel 2 que incluye productos científicos de temperatura superficial y reflectancia de superficie a nivel global (Malakar et al., 2018; Masek et al., 2006a; Zanter, 2021), de la página EROS Earth Explorer (https://earthexplorer.usgs.gov).

2.1.2. Datos de campo

- **Reflectancia del agua:** las mediciones de campo de la reflectancia del agua (Ra) se utilizan para evaluar la corrección atmosférica de los productos Landsat. Las mediciones se llevaron a cabo utilizando un espectrorradiómetro de campo portátil de Analytical Spectral Devices (ASD), que mide la cantidad de energía reflejada por el agua en diferentes longitudes de onda, en 38 puntos de las lagunas del Parque Regional del Sureste (PRSE) en Madrid, los días 3 y 31 de julio del 2000, durante el trabajo de tesis doctoral desarrollado por (Domínguez Gómez et al., 2002). Los resultados están disponibles como reflectancia del agua en porcentaje (%) en función de la longitud de onda de 350 a 1000 nm.
- **La transparencia del agua** (SDD) expresada mediante el valor de la profundidad del disco de Secchi (DS). Los valores de DS se obtuvieron de diferentes conjuntos de datos: (1) mediciones realizadas el 13 de agosto de 1992 en 16 localidades de las lagunas Las Madres, El Campillo y El Porcal en el PRSE en Madrid (Domínguez et al., 1997); (2) mediciones realizadas el 29 de octubre de 1997 en 18 localidades de las lagunas El Campillo y El Porcal en el PRSE (Domínguez Gómez & Peña, 1999); (3) mediciones realizadas los días 3 y 4 de julio de 2000 en las lagunas Las Madres, El Campillo y El Porcal en el PRSE en 38 puntos (Domínguez Gómez et al., 2002); (4) mediciones realizadas el 31 de julio de 2000 en 13 localidades de

las lagunas Las Madres, El Campillo y El Porcal (Domínguez Gómez et al., 2002); (5) y datos in situ mensuales recopilados por el Dr. Miguel Álvarez Cobelas desde septiembre de 1991 hasta diciembre de 2013 en la laguna de Las Madres (Alvarez-Cobelas et al., 2000).

- **Temperatura superficial del agua** en la península ibérica proporcionados por: (1) el Ministerio para la Transición Ecológica y el Reto Demográfico (MITECO) en España, medidos en campo entre 1994 y 2020 en un total de 46.086 puntos que proporcionan la temperatura de la superficie en grados Celsius en 677 masas de agua; y (2) el Sistema Nacional de Información sobre recursos hídricos de Portugal con un total de 2254 datos desde 1981 hasta 2022. Estos datos se utilizarán para validar las series temporales de temperatura de la superficie del agua de Landsat.

2.2. Procesamiento de las Imágenes

2.2.1. Corrección atmosférica

Se utilizaron las imágenes Landsat del producto de la colección 2 Nivel 2 atmosféricamente corregidas, dado que para llevar a cabo su corrección se ha aplicado la cadena de corrección atmosférica Landsat Ecosystem Disturbance Adaptive Processing System (LEDAPS) (Claverie et al., 2015; Maiersperger et al., 2013; Masek et al., 2006b; Nazeer et al., 2014) que es un método riguroso y que ha sido utilizado con éxito por múltiples autores (Sima et al., 2013; Somasundaram et al., 2021; Song et al., 2020; Tanner et al., 2022; Tao et al., 2022; Q. Wang et al., 2022; F. Yang et al., 2023; Yin et al., 2022; Y. Zhang et al., 2021).

2.2.2. Extracción de masas de agua

Se utilizaron dos métodos para delimitar las masas de agua de las características terrestres circundantes de las imágenes Landsat: (1) aplicación de un umbral a partir del Índice de diferencia de agua normalizada (NDWI) (McFeeters, 1996); (2) Clasificación de la banda de calidad (QA_PIXEL) proporcionada por el producto de Landsat.

2.3. Modelado y validación de Variables

Inicialmente, se identificaron los parámetros clave de calidad del agua a modelar. En este caso, entre los parámetros de calidad de agua más estudiados con teledetección (apartado 2.1) y dados los datos de campo disponibles, se estudiaron dos parámetros: la transparencia del agua y la temperatura superficial del agua.

Posteriormente, en el caso de la transparencia del agua se desarrollaron modelos de regresión que relacionan los valores de reflectancia de las diferentes bandas de las imágenes Landsat con las mediciones de campo.

Finalmente, se validó el modelo obtenido utilizando un conjunto de datos diferentes de mediciones de campo para garantizar su precisión y solidez. Las métricas estadísticas utilizadas son: el coeficiente de correlación (R^2), el error cuadrático medio (RMSE) y el error absoluto medio (MAE) (Baughman & Conaway, 2021; Z. Cao et al., 2018; Schaeffer, Seegers, et al., 2018).

2.4. Construcción de series temporales

Para el caso del parámetro de transparencia del agua, se aplicó el modelo obtenido y validado a las bandas espectrales seleccionadas para obtener los valores del parámetro estudiado para todos los píxeles y en todas las fechas con imágenes disponibles, y se llevó a cabo la composición de series temporales de imágenes o construcción de cubos de datos utilizando el enfoque de apilamiento de capas. En el caso de la temperatura se utilizaron directamente las imágenes de temperatura descargadas.

Posteriormente, se llevó a cabo la imputación o rellenado de datos que consiste en obtener los datos faltantes en la serie temporal. Se utilizaron tres métodos diferentes: interpolación lineal (Ponkina et al., 2021), la imputación multivariada por ecuaciones encadenadas (MICE) (Van Buuren and Groothuis-Oudshoorn, 2011) y el método de imputación de valores perdidos estacionalmente descompuestos (SEADEC) (Moritz and Bartz-Beielstein, 2016). Finalmente se aplicó el método de suavizado Whittaker (Whittaker, 1922) para reducir el ruido y resaltar tendencias significativas en los datos.

2.5. Validación de la Serie con datos de Campo

Para el caso del parámetro de temperatura superficial del agua, se llevó a cabo la validación una vez construida la serie de tiempo o el cubo de imágenes para evaluar el desempeño de la metodología de procesamiento utilizada debido a la falta de imágenes durante el período estudiado. Para esto, se compararon los datos de series de tiempo procesadas con las mediciones de campo utilizando el R^2, el RMSE y el error porcentual absoluto medio (MAPE) para evaluar la precisión.

2.6. Análisis de series espacio -temporales

Una vez construidas y validadas las series de tiempo de los parámetros de transparencia y temperatura superficial del agua, se procede a analizar los cambios temporales y espaciales de las variables. Para esto, se utilizaron diferentes métodos:

2.6.1. Diagrama de Hovmöller

Permite visualizar la variación temporal y espacial de los parámetros de calidad del agua a lo largo de un transecto particular o en todo el cuerpo de agua a lo largo del tiempo (HovmÖller, 1949). El diagrama de Hovmöller es una representación gráfica utilizada en meteorología, climatología y oceanografía para mostrar la evolución de una variable a lo largo del tiempo y la latitud (o longitud) a lo largo de una ruta o región específica. Es particularmente útil para visualizar la propagación de fenómenos atmosféricos u oceánicos, como sistemas meteorológicos, patrones climáticos o corrientes oceánicas, a lo largo de una trayectoria o coordenada geográfica particular (Sverdrup et al., 2017).

Consta de una cuadrícula bidimensional, donde un eje representa el tiempo y el otro eje representa la latitud (o longitud). La variable de interés, se traza como un gráfico de contorno o codificado por colores en esta cuadrícula. Cada fila o columna de la cuadrícula corresponde a una latitud (o longitud) específica a lo largo del camino o región de interés, mientras que cada columna o fila representa un período de tiempo específico. Esto permite visualizar cómo la variable de interés varía tanto espacial como temporalmente a lo largo de la trayectoria o coordenada geográfica elegida. Al examinar la evolución de la variable en el tiempo y el espacio, se pueden identificar patrones, tendencias e interacciones entre diferentes regiones o períodos de tiempo (Weeks et al., 2012).

2.6.2. Anomalías o de-mained:

Para analizar las desviaciones temporales de los valores de los parámetros de calidad de agua a lo largo del tiempo y el espacio, se calculan las anomalías como la resta de la media de toda la serie temporal de cada punto (o píxel) (Godah et al., 2018).

2.6.3. Análisis empírico de función ortogonal (EOF):

Para caracterizar la variabilidad de los valores de los parámetros de calidad derivados de las imágenes satelitales, se realizó un EOF en el conjunto de datos durante toda la serie temporal. El análisis EOF es una técnica estadística que permite descomponer los datos de series temporales en modos ortogonales de variabilidad, lo que ayuda a identificar patrones y tendencias dominantes en los parámetros de calidad del agua. Proporciona información sobre la estructura subyacente de los datos y ayuda a descubrir características o tendencias importantes que pueden no ser evidentes a partir de una simple inspección o análisis visual. Se utiliza ampliamente en diversos campos, incluidos la meteorología, la oceanografía, la ciencia climática y la teledetección, para identificar e interpretar patrones espaciales o temporales en conjuntos de datos complejos (Z. Chen et al., 2015).

Para llevar a cabo el análisis EOF se debe (Weeks et al., 2012): (1) preparar los datos como una matriz, donde cada fila representa una ubicación espacial o un punto temporal, y cada columna representa una variable u observación; (2) normalizar los datos para eliminar cualquier sesgo o diferencia de escala entre las variables, lo que asegura que cada variable contribuya por igual al análisis; (3) calcular la matriz de covarianza del conjunto de datos que cuantifica las relaciones entre pares de variables y proporciona información sobre la variabilidad y covariabilidad dentro del conjunto de datos; (4) la matriz de covarianza luego se descompone en sus vectores propios y valores propios. Los vectores propios representan los patrones espaciales o temporales de variabilidad dentro del conjunto de datos, mientras que los valores propios indican la cantidad de varianza explicada por cada vector propio; (5) obtener los vectores propios, también conocidos como modos EOF o componentes principales, representan los patrones dominantes de variabilidad dentro del conjunto de datos. Cada modo EOF describe un patrón espacial o temporal que es ortogonal (no correlacionado) con los otros modos y captura una cierta cantidad de variación en los datos; (6) obtener las puntuaciones EOF: son los coeficientes que expresan la contribución de cada modo EOF a cada ubicación espacial o punto temporal en el conjunto de datos. Estas puntuaciones se pueden utilizar para reconstruir el conjunto de datos original o para analizar la distribución espacial o temporal de la variabilidad asociada con cada modo EOF; (7) Finalmente, los modos y puntuaciones del EOF se interpretan para comprender los patrones dominantes de variabilidad dentro del conjunto de datos. Esto puede implicar identificar patrones espaciales o temporales, evaluar la coherencia espacial o la evolución temporal de estos patrones y relacionarlos con procesos físicos o fenómenos de interés.

2.6.4. Tendencias

Identificación de patrones significativos en los datos de calidad del agua a lo largo del tiempo a partir de la regresión lineal. Implica ajustar una ecuación lineal a los datos, donde la variable independiente representa el tiempo y la variable dependiente representa los valores observados. La pendiente de la línea de regresión indica la magnitud y dirección de la tendencia a lo largo del tiempo (Mahmoudi, Mohammadi, and Daneshmand, 2019; Wang et al., 2021).

2.6.5. Isotermas

Las isotermas o líneas de temperatura constante se utilizan para comprender la dinámica espacial y temporal de la temperatura superficial del agua en la península ibérica. Su cálculo y análisis se ha llevado cabo según lo propuesto por R. Wang et al., (2021).

2.7. Estado trófico

A partir del indicador clave del estado trófico como es la profundidad del disco de Secchi obtenido a partir de los datos de teledetección, se lleva a cabo la clasificación de los cuerpos de agua en diferentes estados tróficos (oligotrófico, mesotrófico, eutrófico o hipertrófico) según los criterios de la OCDE (Organización para la Cooperación y el Desarrollo Económico) y se analiza la evolución del estado trófico a lo largo del tiempo para monitorear los cambios e identificar posibles tendencias de eutrofización u oligotrofización.

3. Resultados

3.1. Artículo 1: Assessment of Landsat 5 Images Atmospherically Corrected with LEDAPS in Water Quality Time Series

A continuación, se reproduce el artículo 1 publicado (https://doi.org/10.1080/07038992.2019.1674136)

CANADIAN JOURNAL OF REMOTE SENSING
2019, VOL. 45, NO. 5, 691–706
https://doi.org/10.1080/07038992.2019.1674136

Taylor & Francis
Taylor & Francis Group

Assessment of Landsat 5 Images Atmospherically Corrected with LEDAPS in Water Quality Time Series

Carolina Echavarría-Caballero[a], José Antonio Domínguez-Gómez[b], Concepción González-García[a], and María Jesús García-García[a]

[a]Universidad Politécnica de Madrid, E.T.S. Ingeniería de Montes, Forestal y del Medio Natural, Spain; [b]Crop Research Institute, Praha, Czech Republic

ABSTRACT
The main objective of this work is to assess and use Landsat TM5 for the inventory and study of the evolution of water quality in gravel pit ponds within the natural park, Parque Regional del Sureste (PRSE), from 1984 to 2011. First, the normalized difference water index (NDWI) was applied to 230 Landsat TM5 images to distinguish water and non-water information. Next, the surface reflectance derived from Landsat TM5 images atmospherically corrected with the Landsat Ecosystem Disturbance Adaptive Processing System (LEDAPS) was compared to water-leaving reflectance measured in the field, showing a significant overestimation of surface reflectance derived from Landsat data. Thus, a new regression equation was proposed linking the *in situ* Secchi depth (SD) measurements to surface reflectance measured by Landsat 5. This regression was validated and subsequently applied to every image, providing an SD value for each pixel in the time series. Finally, the retrieved SD values were used to compute the trophic state of water bodies according to the Organization for Economic Co-operation and Development (OECD) classification. The results show an increase in the surface area of water bodies in the PRSE from 1984 to 2006, as well as an improvement in their water quality.

RÉSUMÉ
Le principal objectif de ce travail est d’utiliser des images Landsat-5 TM pour l’inventaire et l’étude de l’évolution de la qualité de l’eau dans les gravières au sein d’un parc naturel « *Parque Regional del Sureste* » (PRSE) de 1984 à 2011. Afin d’y parvenir, dans un premier temps, le *Normalized Difference Water Index* (NDWI) a été appliqué à 230 images Landsat-5 TM disponibles afin de distinguer les surfaces d’eau. Ensuite, la réflectance au sol de l’eau dérivée des images Landsat-5 TM (atmosphériquement corrigées avec LEDAPS) a été comparée à la réflectance de l’eau mesurée in situ, montrant une surestimation significative de la mesure satellitaire. Ainsi, une nouvelle équation de régression avec les mesures in situ de profondeur du disque de Secchi (DS) et la réflectance mesurée dans les bandes de Landsat a été récupérée, validée et appliquée à chaque image, fournissant une valeur du DS pour chaque pixel sur la série temporelle. Enfin, les valeurs récupérées de DS sont utilisées pour calculer l’état trophique des plans d’eau selon la classification OCDE. Les résultats montrent la croissance de la dimension des plans d’eau au sein du PRSE entre 1984 et 2006 et une amélioration de la qualité de l’eau des gravières durant la même période.

ARTICLE HISTORY
Received 15 March 2019
Accepted 21 September 2019

Introduction

Since the 1960s, Madrid has experienced an urban expansion that increases its needs for raw material from surrounding areas, such as the low-lying basin at the junction of the Jarama and Manzanares river (Madrid basin). During the next 3 decades, open-pit mining activity resulted in an environmental deterioration characterized by the disappearance of cover vegetation, as well as the appearance of bare soil areas and many gravel pit ponds due to the rise of the phreatic level resulting from dredging activities (Puche Riart et al. 2012). These artificial ponds, when abandoned, turned into wetland ecosystems with established aquatic fauna and flora (Domínguez and Peña 1999). A new ecosystem was generated, and given the necessity to protect it, the natural park Parque Regional del Sureste (PRSE) was established in 1994 (Comunidad de Madrid 1994). This natural park

CONTACT María Jesús García-García ✉ mariajesus.garcia.garcia@upm.es 🖃 Universidad Politécnica de Madrid, E.T.S. Ingeniería de Montes, Forestal y del Medio Natural, Spain

covers an area of 300 km^2 belonging to 18 municipalities, and the vegetation is composed mainly of helophytes. In accordance with regulations, the management and action plans of the PRSE should be reviewed every 4 years and should include a census of existing wetlands (Comunidad de Madrid 1990).

The first inventory of water bodies in the PRSE was performed in 1997 and defined 123 wetlands: 115 which were a result of human activity (111 due to mining extraction, 2 due to dams, one due to an irrigation reservoir and one due to a well), and 8 which were of natural origin (Asociación Ecologista del Jarama "El Soto" 2001). The second inventory was carried out in 2002 and identified 103 wetlands using remote-sensing images. The main difference between both inventories is that the first inventory was done only with field sampling, while the second inventory included remote-sensing techniques in addition to field sampling. Since the 1980s, there has been a high level of interest in the gravel pit ponds in the PRSE, which have consequently been widely studied through field campaigns (Alvarez 1991; Alvarez et al. 2000; Alvarez et al. 1987).

The methods used to delimitate and subsequently inventory bodies of water from remote-sensing imagery are generally divided into 2 categories: single-band and multi-band methods (Xu 2006). The single-band method involves choosing a band from a multispectral image and determining a threshold for the band to discriminate water from land (Domínguez et al. 2009; Frazier and Page 2000). One multi-band method is the band-ratio of the reflectance from 2 multispectral bands. Typically, reflectance taken in the visible wavelength range (VIS) is divided by that taken in the near infrared (NIR) wavelength range.

The most used band-ratio methods are the normalized difference water index (NDWI) (Liu et al. 2016; Oyama et al. 2015; Wang et al. 2018a) proposed by McFeeters (1996) and the Modified NDWI (MNDWI) (Xu 2006). The NDWI maximize water reflectance by using green wavelengths and minimize the low reflectance of NIR characteristic of water features, as explained by Khattab and Merkel (2014), while in MNDWI the mid-infrared (MIR) band is used instead of the NIR (Ogilvie et al. 2018).

Among the different parameters used to study water quality, transparency is an essential lake property (Domínguez et al. 2009; Dörnhöfer and Oppelt 2016; Soria et al. 2017b; Qi et al. 2017) because it gives a general view of all the water components and the interactions between them. The Secchi disk is considered the oldest and simplest optical instrument used to measure transparency, also referred to as turbidity, of ocean and lake waters because it acts as a rough proxy for water transparency by directly detecting changes in the visible underwater light field (Harvey et al. 2019). In inland water, the transparency is measured with a black-and-white disk with a typical diameter of about 30 cm that is lowered into a body of water until it can no longer be viewed by an observer (Lee et al. 2015; Wernand 2010). Secchi depth (SD) is widely used to study aspects of water quality, such as its trophic state (Vollenweider and Kerekes 1982) and ecological status in the European Communities (European Commission 2000).

Eutrophication is the most important worldwide environmental issue regarding reservoirs as well as many other types of aquatic ecosystems. It is responsible for water quality degradation and severe restrictions on water uses because nutrient enrichment can lead to highly undesirable changes in ecosystem structure and function (Padedda et al. 2017; Smith et al. 1999). To evaluate the nutrient load in water bodies and subsequently classify their trophic states, several biological indicators (chlorophyll-a and algal density) and physicochemical indicators (concentration of total phosphorus and SD) are used. The trophic classifications of lakes have a long history, from the use of the trophic state index (TSI) (Carlson 1977) to the use of trophic status categories set by the OECD probability distribution diagrams (Giardino et al. 2001; Smith et al. 1999; Vollenweider 1968; Vollenweider and Kerekes 1982; Wetzel 2001). The OECD method evaluates the probability distribution of 5 trophic classes (ultra-oligotrophic, oligotrophic, mesotrophic, eutrophic or hypertrophic) based on the mean annual concentrations of total phosphorus and chlorophyll-a (Chl-a), the peak concentration of Chl-a and the mean annual value of SD transparency.

Remote sensing has already been used for quite some time in water quality and eutrophication studies. For example, predictive regression equations were developed to monitor the spatial variation of trophic zones by SD and Chl-a concentration in U.S. lakes (Verdin 1985). In another case, Landsat TM5 was used to retrieve Seston dry weight, Chl-a and SD values in a Dutch lake (Dekker and Peters 1993). Similarly, integration of remote-sensing data (Landsat TM5 and SPOT-HRV), *in situ* data and water quality models was performed for the assessment of suspended matter concentrations in lakes in the Netherlands (Dekker et al. 2001). In the United States, the use of satellite images to estimate water quality from predicted SD measurements in 730 of

Michigan's 11,000 inland lakes was investigated (Fuller et al. 2004). Meanwhile, in China, a model was derived for the retrieval of suspended sediment (SS) concentrations from Landsat TM images and *in situ* data based on studies of Lake Taihu (Guang et al. 2006). In Japan, a method was developed for using Landsat TM5 data on a eutrophic lake to map Chl-a and non-phytoplankton SS distributions (Oyama et al. 2009). The spatial patterns in water quality in Lake Beysehir in Turkey were studied using Landsat TM5 images and field data of SS, turbidity, SD, and Chl-a (Nas et al. 2010). Additionally, an evaluation of the Landsat archive for mapping changes in Colored dissolved organic matter (CDOM) in Swedish lakes over the last 30 years has been made (Kutser 2012). In another example, an algorithm has been developed to relate *in situ* Chl-a measurements and remotely sensed Chl-a in U.S. lakes in Maine and New Hampshire (Boucher et al. 2018). Additionally, an assessment of the trophic states of large inland water bodies distributed around the world was carried out using Moderate Resolution Imaging Spectroradiometer (MODIS) data by comparing the remote data with concurrent *in situ* measurements (Wang et al. 2018b). In Finland, the use of 33 years of Landsat data for reconstructing seasonal patterns of Chl-a concentration was analyzed using field measurements (Maeda et al. 2019).

In Spain, remote-sensing techniques have been used to estimate water quality variables such as Chl-a, total suspended particles and water transparency (Caballero et al. 2018; Chao Rodriguez et al. 2014; Domínguez and Peña 1999; Domínguez et al. 2009; Domínguez et al. 2017; Doña et al. 2014, 2015; López and Caselles 1990; Soria et al. 2017a, 2017b). These algorithms allow determination of water eutrophic and ecological states (Domínguez et al. 2011a; Pereira et al. 2017; Serrano et al. 1997).

Atmospheric correction is the first and essential step in the development of water analysis algorithms from remote-sensing data (Yongzhen et al. 2017). Ideally, it should remove the radiance contribution of the atmosphere to calculate water-leaving radiances, which can be used to determine water quality parameters such as the SD transparency. The atmosphere may contribute about 90% of the radiance measured by a satellite sensor, and in water areas this contribution could be even higher, especially in the blue bands (Wang 2010; Warren et al. 2019). The performance of atmospheric correction is therefore key to ensuring quality in geophysical variables retrieved from remote sensing of reflectance for monitoring water quality, given the high absorption and low scattering properties of water bodies (Mouw et al. 2015; Pahlevan et al. 2017; Palmer et al. 2015; Qin et al. 2017; Wang and Jiang 2018).

The most-used atmospheric correction methods are: relative (image-to-image) normalization by applying regression models to targets that have stable reflectance over time to normalize multitemporal images to a single reference scene (Kloiber et al. 2002; Olmanson et al. 2008); the image-based dark object subtraction (DOS) model, which assumes that some pixels within the image are in complete shadow and that their radiances measured at the satellite are only due to atmospheric scattering (Boucher et al. 2018; Chavez 1996; Giardino et al. 2001; Matthews et al. 2010); COST-DOS, which applies DOS but in which the value of the atmospheric transmittance along the path from the ground to the sensor (TAUz) from the cosine of the solar zenith angle (Brivio et al. 2001; Hicks et al. 2013; Song et al. 2001); the Gilabert method, which is applicable to Landsat-TM data and requires only inputs that are commonly available and the presence in the imaged scenes of some dark surfaces in TM bands 1 (blue) and 3 (red) (Gilabert et al. 1994); the fast line-of-sight atmospheric analysis of hypercubes (FLAASH), a physical method which attempts to model the atmospheric effects by solving a radiative transfer equation (Adler-Golden et al. 1999; Wang et al. 2018a); and the Second Simulation of the Satellite Signal in the Solar Spectrum correction scheme (6S), which can accurately simulate the atmosphere along the path from the Sun to the target (surface) and then to the sensor (Bernardo et al. 2017; Chao Rodriguez et al. 2014; Matthews et al. 2010; Ren et al. 2018; Vermote et al. 1997).

The most rigorous methods of atmospheric correction involve the use of radiative transfer models and may provide better results, but they are complicated to implement and require input data that are not always available. On the other hand, simple radiometric correction techniques, such as dark pixel subtraction and Sun angle correction, are strictly image-based and do not require *in situ* field measurements, but are insufficient to provide an absolute atmospheric correction (Kloiber et al. 2002).

In 2012, the United States Geological Survey (USGS) Earth Resources Observation and Science (EROS) Center released a global land surface reflectance (SR) coverage from the Landsat archives using the atmospheric correction chain Landsat Ecosystem Disturbance Adaptive Processing System (LEDAPS) (Claverie et al. 2015; Masek et al. 2006). Some researchers have evaluated the performance of

LEDAPS on Landsat SR products by comparisons with field spectrometers as well as other sensors (such as MODIS and the Aerosol Robotic Network [AERONET]) in bare soil and vegetated areas. The results indicate similarity between LEDAPS and alternative data products in longer wavelengths over areas with no adjacent water, while less reliable performance was observed in shorter wavelengths and sparsely vegetated areas (Claverie et al. 2015; Maiersperger et al. 2013; Nazeer et al. 2014).

On the basis of the above, the Landsat SR has not been widely evaluated for the purposes of water studies. The main objective of this work is thus to assess the use of Landsat TM5 images that have been atmospherically corrected with LEDAPS developed by the USGS in studying water quality time series through SD using water-leaving reflectance measured in the field.

Study area

The study is focused in the PRSE, which covers an area of 300 km^2 belonging to 18 municipalities located in the southwestern region of the Madrid community (Figure 1).

The PRSE is characterized by the presence of 2 fundamental lithological domains: the Neogene Tertiary and the Quaternary. It is included in the Tajo basin, specifically in the sub-basin belonging to the Jarama River, which is the main watercourse in the Park and runs in the north-south direction (Mostaza-Colado et al. 2018; Roblas and García 1997).

As a consequence of the appearance of the wetlands, flora consisting mainly of helophytes has developed. In the existing helophyte vegetation, the presence of reeds (Phragmites australis) stands out, sometimes accompanied by bulrushes (Typha spp.) and rushes (Scirpus holoschoenus). Finally, the presence of repopulations with various native species (alders, poplars, elms, etc.), as well as more exotic species (tree of paradise, weeping willow tree) in the restored gravel pits is common (Roblas and García 1997).

The climate in the study area is classified as Mediterranean temperate-continental, with temperate winters and warm, dry summers. The average temperature is 13.8 °C and the average rainfall is 440 mm/year (Mostaza-Colado et al. 2018).

Data

Landsat 5 images

The images used correspond to the Landsat SR data product (Masek et al. 2006) of Landsat TM5 which

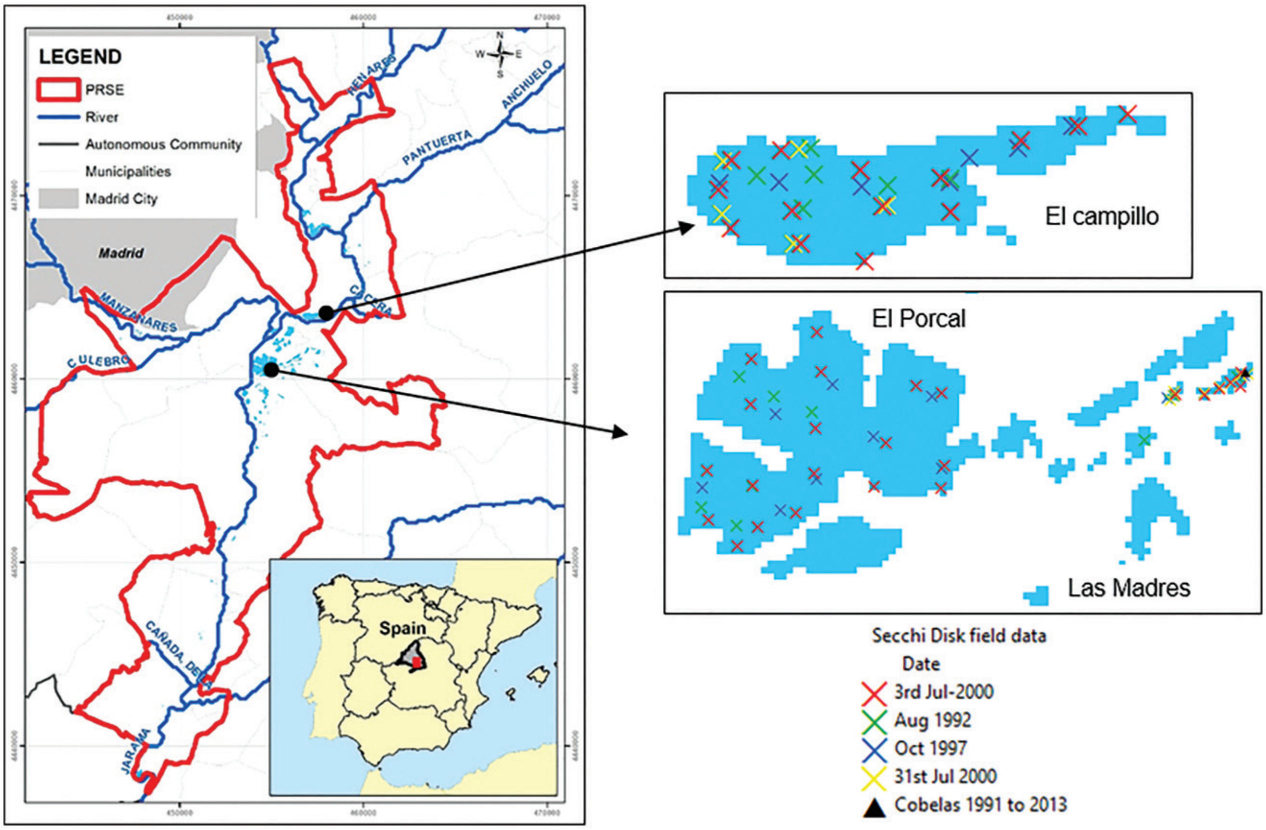

Figure 1. Study area location and distribution of SD field data.

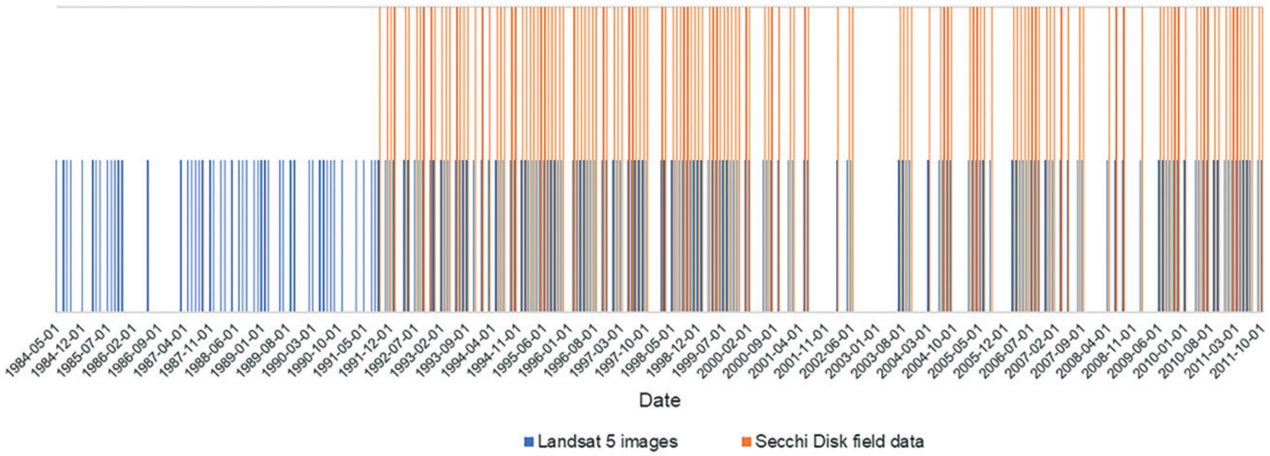

Figure 2. Temporal distribution of Landsat images and SD field data.

have been atmospherically corrected with LEDAPS by the USGS, available on EarthExplorer (https://earthexplorer.usgs.gov). The Landsat SR data product is generated at a 30-meter spatial resolution on a Universal Transverse Mercator (UTM) and the default file format is GeoTIFF. The data type is 16-bit signed integer, the range is -2000–16000, with a valid range of 0–10000 and a scale factor of 0.0001 for all bands.

The area under consideration corresponds to scene Path 201 and Row 32. A total of 452 images, acquired from the years 1984 to 2011, were downloaded from the USGS website and visually verified to dismiss any image with clouds, shadows or any kind of errors over the study area. Only cloud-free images in the study were used, so 230 Landsat scenes were selected (blue in Figure 2) for this work.

In general, there are at least 4 images per year, with cases such as the year 1995 where there is an image for each month and exceptions such as in 1986 and 2002 where there is only one image for each year. In total 148 images (blue and red in Figure 2), which is 64% of the images, coincide with at least one field point.

Reflectance field data

As detailed below, in this work field measurements of water reflectance (R_a) are used to assess the LEDAPS atmospheric correction, given that *in situ* data collected from hand-held devices and shipborne spectrometers may be considered free from atmospheric effects since the path from sensor to observation surface is negligible (Warren et al. 2019).

The measurements were carried out using an Analytical Spectral Devices (ASD) portable field spectroradiometer, which measures the amount of energy reflected from water over different wavelengths. Measurements were taken outside of the water body with a Field of View (FOV) of 23° at a short distance from the water surface in order to avoid atmospheric effects, in 38 locations on July 3rd and 31st of 2000, during doctoral thesis work developed by Domínguez (2002). The results are available as water reflectance in percentage (%) as a function of wavelength from 350 to 1000 nm.

The continuous reflectance values are transformed into discrete values in order to compare them with the pixel values from the Landsat SR images using the calibration model presented by the National Aeronautics and Space Administration (NASA) (NASA (National Aeronautics and Space Administration) 2001).

SD field data

The water transparency expressed by the SD value was measured using a white and black disk with a diameter of about 30 cm, which was lowered into a water body until it was no longer viewable by an observer. The SD values (Figures 1 and 2) were obtained from different datasets: measurements carried out on August 13th, 1992 at 16 locations in Las Madres, El Campillo and El Porcal ponds (Domínguez et al. 1997), represented by the green points in Figure 1; measurements carried out on October 29th, 1997 at 18 locations in El Campillo and El Porcal ponds (Domínguez and Peña 1999), represented by the blue points in Figure 1; measurements carried out on July 3rd and 4th, 2000 in Las Madres, El Campillo and El Porcal ponds (Domínguez 2002) at 38 locations, represented by the red points in Figure 1; measurements carried out on July 31st, 2000 at 13 locations in Las Madres, El Campillo and El Porcal ponds (Domínguez 2002), represented by the yellow

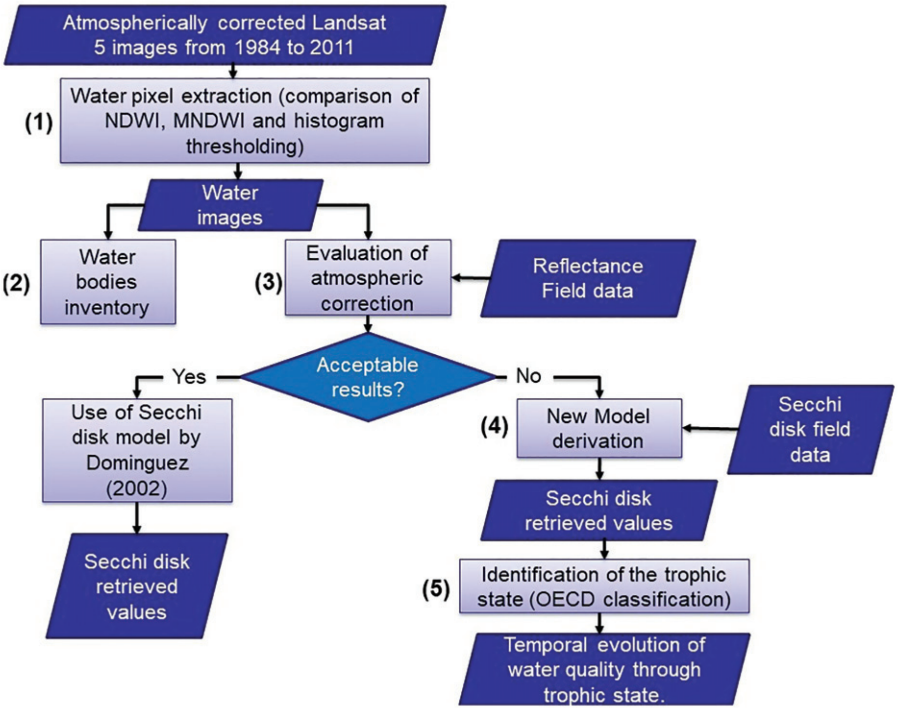

Figure 3. Flow chart of the research process.

points in Figure 1; and *in situ* data collected by Dr. Miguel Alvarez Cobelas from September 1991 to December 2013 at the buoy in Las Madres pond (Alvarez et al. 2000), indicated by the black point in Figure 1.

Methods

As the first step, the water pixel identification method to distinguish water and non-water information was developed by comparing the NDWI, the MNDWI and the histogram thresholding, and subsequently applying the best method, which was found to be NDWI, to every available Landsat TM5 in the area under consideration (scene Path 201 and Row 32) from the years 1984 to 2011 (Figure 3(1)).

Second, once the images were classified in such a way that only water information is present in the images (water images), the inventory of water bodies was carried out (Figure 3(2)).

Third, using the water images (step 1) to certify that only water pixels were used, the evaluation of the atmospheric correction was developed, where the reflectance measured in the Landsat bands was compared with available water spectral reflectance measured in the field (Figure 3(3)). The evaluation shows an overestimation of the Landsat reflectance values. Thus, the fourth step corresponds to the development of a new regression equation with the SD *in situ* measurements and reflectance measured in the sensor bands (Figure 3(4)).

Fifth, the SD model developed in this research was applied to every image in order to assign each pixel an SD transparency value, and subsequently used to obtain the trophic state using OECD Probability Distribution Diagrams (Figure 3(5)).

The whole procedure was carried out with a Python script developed for this work and called FWLandsat5.

Water pixel extraction

Detecting bodies of water and accurately delineating them from their surroundings was the first step for monitoring the pit ponds. Various methods are currently in use to distinguish water from non-water surfaces for water pixel extraction, which function by analyzing and discerning spectral features. The method used in this study is among the most common approaches.

First, the NDWI was applied. Areas covered with water produced positive values, while areas with vegetation or soil tended to have zero or negative values (McFeeters 1996).

$$\mathrm{NDWI} = \frac{Band\ 2 - Band\ 4}{Band\ 2\ +\ Band\ 4} \qquad [1]$$

Second, the MNDWI was applied, in which water features had positive values while built-up land, bare

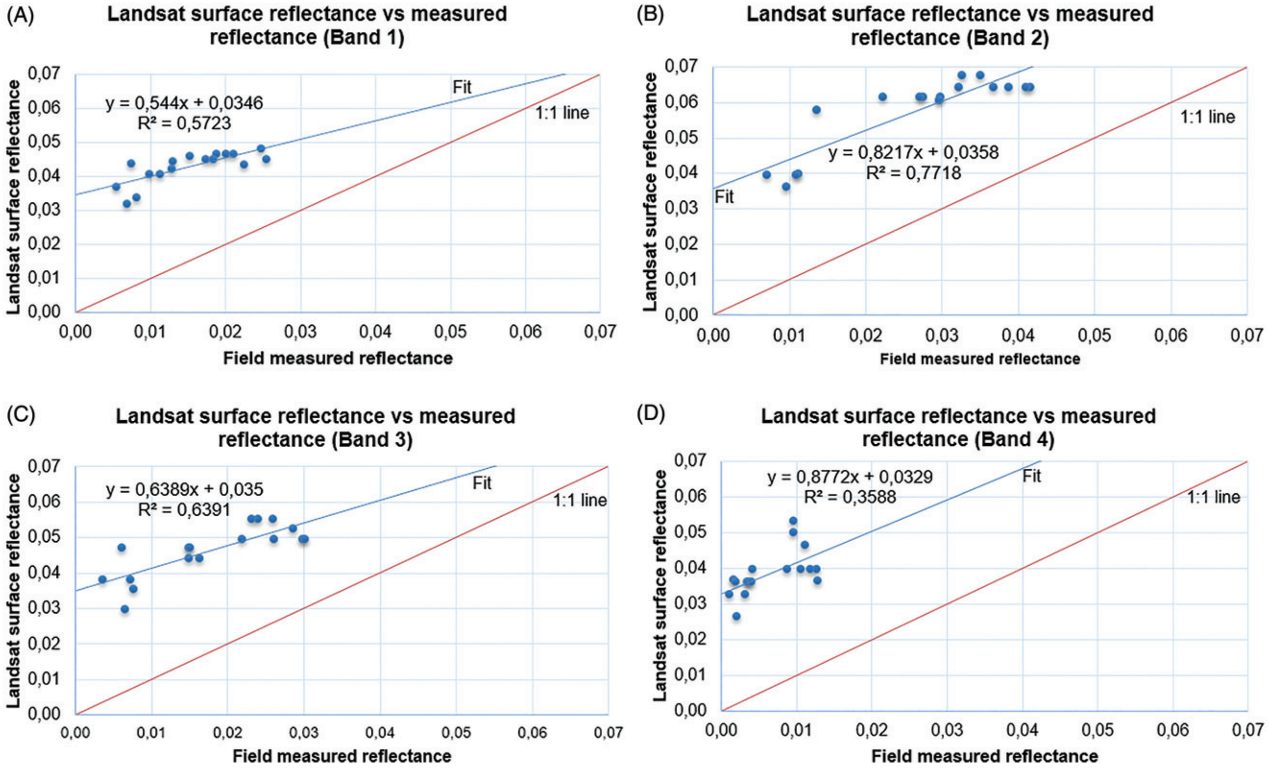

Figure 4. Landsat SR versus measured reflectance.

soil and vegetation had negative values (Xu 2006).

$$\text{MNDWI} = \frac{Band\ 2 - Band\ 5}{Band\ 2\ +\ Band\ 5} \qquad [2]$$

Third, using the histogram thresholding method based on the NIR band, the Landsat 5 scenes were visually analyzed to obtain a threshold. All pixels with reflectance in band 4 below that threshold corresponded to water or shadows (Domínguez and Peña 1999).

Once the 3 methods were applied, the results of water pixel extraction were visually analyzed. Given the dynamic conditions that occur in the study area, where some bodies of water may disappear completely in some seasons, the method that offered optimal results was chosen through the following criteria: (a) minimization of the number of errors, i.e., less confusion of water pixels with shadows and vegetation; (b) verification of the fit between the result and the field data, that is, sampling locations in the bodies of water should fall in areas classified as water by the analysis method.

Finally, to certify that only open water pixels were obtained in order to use the Secchi disk, only water bodies greater than 2 pixels were selected. The frequency of water bodies of 2 or fewer pixels with doubtful classification (which could be shadows or vegetation), was very high compared with the frequency of doubtful water bodies of 3 or more pixels, and furthermore, most of them were mapped in the inventory made in 2002. The areas belonging to river and mountain zones were also discarded, given that the water bodies under consideration are located only in the flat area.

Once the water/land pixel discrimination for each Landsat scene was done, the number and area of water bodies were computed.

Evaluation of atmospheric correction LEDAPS with reflectance field data

In order to assess the suitability of the Landsat SR images corrected with LEDAPS software by the USGS for water quality studies, a comparison was made between the reflectance values measured in the field and the water reflectance measured in the sensor bands. In this study, because the *in situ* measurements were mostly from optically complex waters where the water depth may change over a very short distance, the satellite SR from the pixel of the Landsat images closest to the corresponding *in situ* site was used for analysis.

The scatter plots between *in situ* SR measurements and satellite matchup SR (Figure 4) show that the Landsat SR has a large deviation from the 1:1 line due to the significantly overestimated Landsat SR.

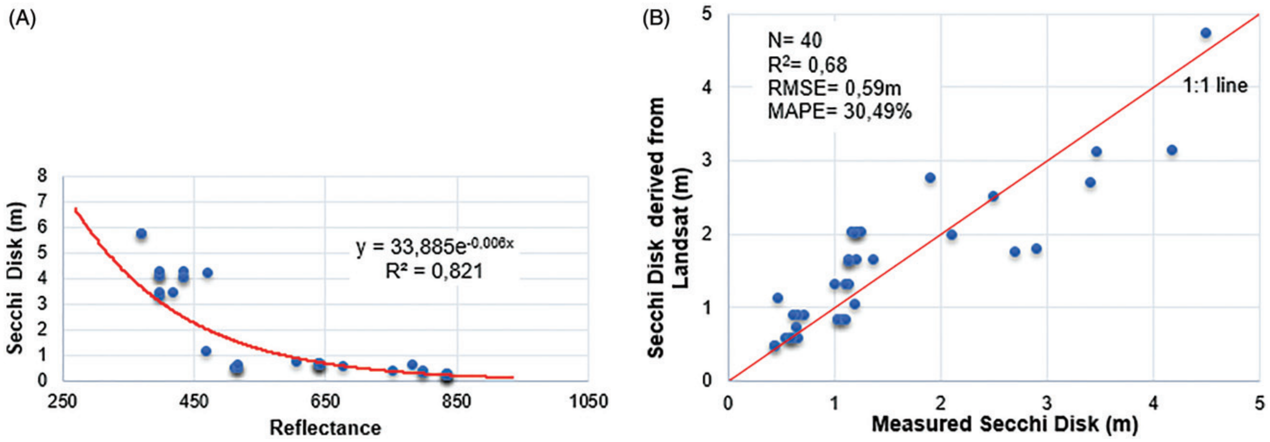

Figure 5. (A) Relationship between SD and Landsat SR band 2 (520-600 nm); (B) Relationship between SD measured in the field and calculated SD values.

Additionally, there are small R^2 values for bands 1 and 4.

Based on the results of the comparison between the Landsat SR data product and the reflectance field data, it was not possible to apply the models previously developed for the study area (Domínguez et al. 2009), given the overestimation of the Landsat SR. Thus, a new regression equation with the SD *in situ* measurements and the reflectance measured in the sensor bands must be obtained and validated.

Secchi depth modeling

Model development

Estimates of SD based on Landsat imagery were obtained using a regression model for establishing an empirical relationship with the water reflectance measured in one or multiple sensor bands. In this case, the number of field sites was determined using common statistical sampling strategies (Domínguez et al. 2009).

$$N = \left(\frac{z_c \sigma}{\varepsilon}\right)^2 \quad [3]$$

$$N = \left(\frac{1.96 \times 3}{1}\right)^2 = 34.5744 \quad [4]$$

where, N is the number of samples. z_c the confidence coefficient ($z_c = 1.96$ for a confidence interval of 95%). ε the error of estimation (1 cm according to Domínguez et al. (2009)). σ the estimated variance (3 cm estimated by Domínguez et al. (2009) from analysis of a long SD measurement series in different reservoirs).

To fit the model, the number of samples had to be greater than 35. On the other hand, the analysis of the diffuse attenuation coefficient (Kd)—i.e., the gradual loss of light with depth—for each band allowed us to choose the band between 520 nm and 600 nm (green band) because it had a smaller Kd and consequently the highest light penetration (Domínguez et al. 2009).

Thus, a total of 40 points were selected to calculate the new empirical relationship between SD and the water reflectance measured in the sensor green band (Figure 5(A)).

Model validation

Assessing the accuracy of the calculated remote-sensing SD required *in situ* measurements contemporary to image acquisition, since lake conditions may change rapidly. Calculated SD values were compared with measured SD values other than those used in the model derivation. The obtained algorithm was then applied to the second group of data reserved for testing and results, and the results were compared with the SD field data.

The metrics used to perform statistical analysis included the determination coefficient (R^2), the root-mean-square error (RMSE) and the mean absolute percentage error (MAPE) (Cao et al. 2018). The RMSE was equal to 0.59 m and reflects the difference between the predicted values and the true (measured) values, where smaller RMSEs indicate higher evaluation accuracies. The MAPE equal was to 30.49% and is a measure of the prediction accuracy of a forecasting method. The MAPE expresses accuracy as a percentage, where smaller MAPEs indicate better modeling results.

The relation of SD and calculated SD values (Figure 5(B)) exhibits the smallest biases from the *in situ* data, with a linear slope close to 1:1 line and $R^2 = 0.68$, which presents a good correlation degree of the coupled data in the modeling.

Once validated, the regression equation was then applied to every image, providing an SD value for each pixel. To apply the regression equation a Python language script called FWLandsat5 was developed to automate image processing.

Temporal evolution of water quality

For identification of the trophic state of pit ponds within the PRSE, the probability (in per cent) of a trophic state was calculated using OECD Probability Distribution Diagrams using the SD annual mean (Giardino et al. 2001).

Having evaluated the accuracy of the obtained SD values for the entire population of water bodies for the period from 1985 to 2011, the annual mean SD map was computed as the mean of all the resulting thematic maps in the same year. Next, each annual mean SD was obtained for every water body and was subsequently used to determine the trophic status category. Finally, the percentage of water bodies in each trophic status category for each year was computed.

Results

The most suitable method for water pixel extraction

Once the water bodies had been identified by means of the NDWI, MNDWI and histogram thresholding methods, an accuracy assessment was carried out by comparing the identified water bodies to data collected in the field.

The NDWI method was capable of extracting more water body-related information, while MNDWI mistakenly extracted some small shadows and errors in the images, which presents a limitation for the extraction of small water bodies. Given that NDWI generated more accurate results, this method was applied to every available image.

Inventory of water bodies in the natural park from 1984 to 2011

The number of water bodies assessed ranged from 29 in ~1987 to ~150 in ~2001. The total surface area covered by water bodies (Figure 6) increased during the period from 1984 to 2006, covering up to 350 hectares. Afterwards, the area decreased to 260 hectares, which still represents almost twice the area covered in 1984.

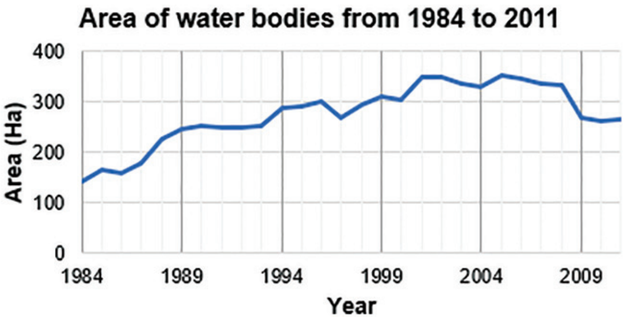

Figure 6. Area of water bodies over the studied time series.

The appearance of new water bodies since 1994 has been observed in the nominated Zone of Ordered Exploitation of Natural Resources, which is the area constituted by lands with lower ecological quality and located on the right bank of the Jarama river below the confluence of the Manzanares and Jarama rivers.

Result of evaluation of atmospheric correction LEDAPS with reflectance field data

The Landsat SR results differed from the measurements taken in the field. For example, in the case of band 2, when the reflectance measured in the field was 0.04, the Landsat SR was 0.06. For band 4, when the measured reflectance was 0.01, the Landsat SR ranged from 0.04 to 0.05 (Figure 4).

Obtained SD model

The empirical relationship between the measured SD and its corresponding reflectance value in the green band of Landsat 5 was found to be:

$$y = 33.885e^{-0.006x}, \qquad [5]$$

$$R^2 = 0.821$$

where y is the SD in meters and x corresponds to the Landsat 5 SR corrected with LEDAPS, which usually ranges from 0 to 10000. The validation of the SD model showed an R2 equal to 0.68, an RMSE equal to 0.59 m and a MAPE equal to 30.49%.

SD thematic maps

The algorithm previously developed and validated for the estimation of SD was applied to every available Landsat SR image in the time series. Because of the huge number of Landsat images and therefore SD maps, equivalent to 230 maps, Figure 7 presents only 6 dates for the pit ponds located in the central region of the study area, where El Campillo, Las Madres and El Porcal are situated.

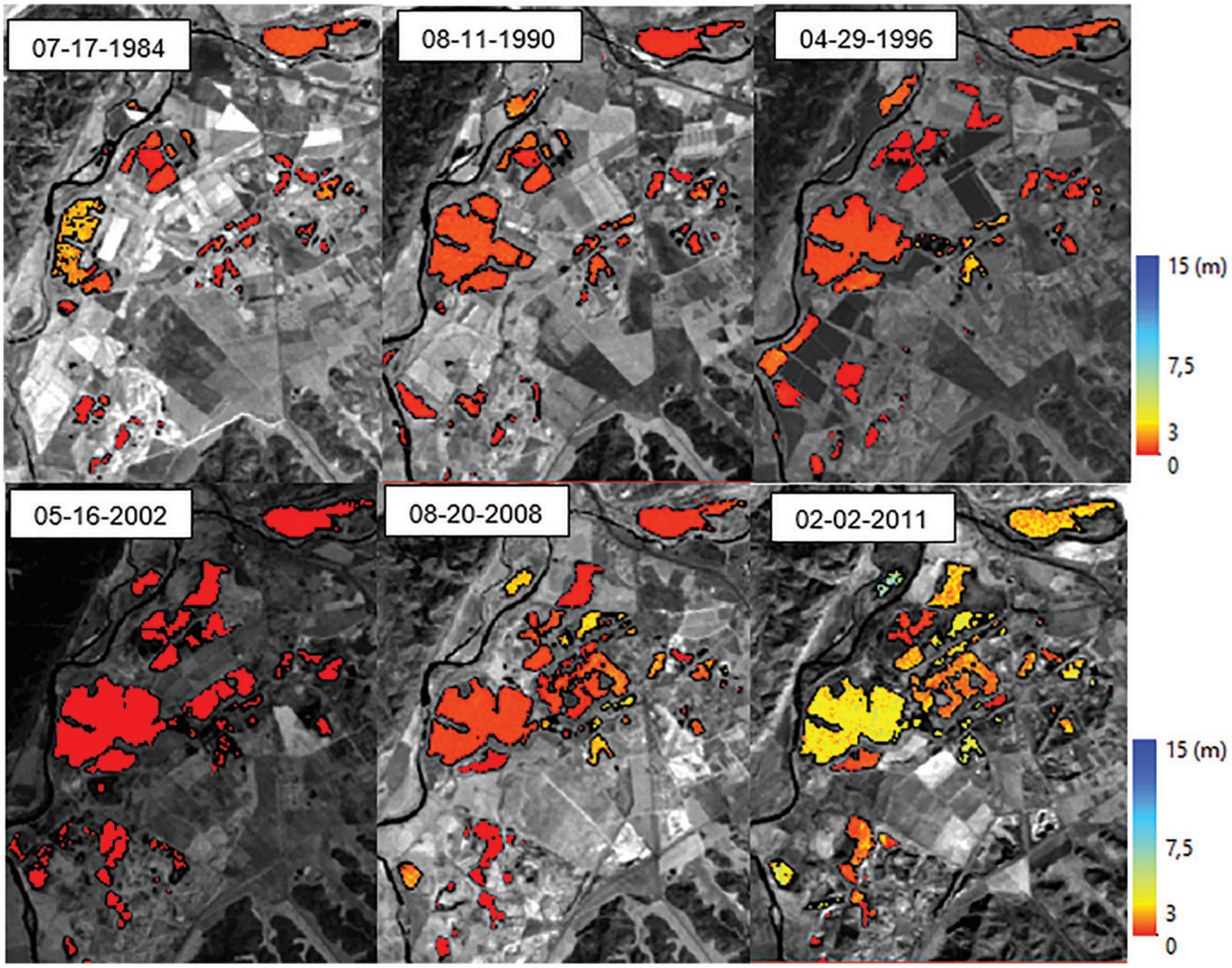

Figure 7. Thematic maps of SD for some pit ponds in the central area of PRSE, on 6 different dates.

Temporal evolution of water quality

The water quality of pit ponds within the PRSE improved over the studied time series according to their SD (Figure 8). In 1984, almost all water bodies were classified as hypereutrophic (98.3%). There is a noticeable improvement over the years, such that that in 2010 and 2011 the number of water bodies in a hypereutrophic state has been almost halved.

In 2010, water bodies classified as oligotrophic appeared for the first time. In 2011, which was the final year of the study period, 60% of the water bodies were hypereutrophic, 30.7% were eutrophic and 9.3% were mesotrophic.

Discussion

To study the evolution of the water quality of the well ponds within the PRSE using the Landsat TM5 images, it is essential to identify the water information in these images. Since these bodies of water come from the historical activity of open mining, the study area is highly dynamic. Water table fluctuations produce considerable size changes or even the disappearance of some ponds. Therefore, a method that works in this condition needed to be identified.

The NDWI is capable of extracting more water body-related information with fewer mistakes due to small shadows and errors in the images. Limitations of the selected method are associated with the fact that it relies only on spectral feature analysis; terrain shadows with spectral characteristics extremely similar to those of water cannot be eliminated completely. In addition, the inherent spatial resolution of the Landsat 5 imagery prevents detection and extraction of very small water bodies (Duru 2017). To account for these limitations, a comparison with the water bodies inventory made in 2002 was done, and only water bodies greater than 2 pixels were selected. The majority of water bodies mapped in this inventory were 3 or more pixels.

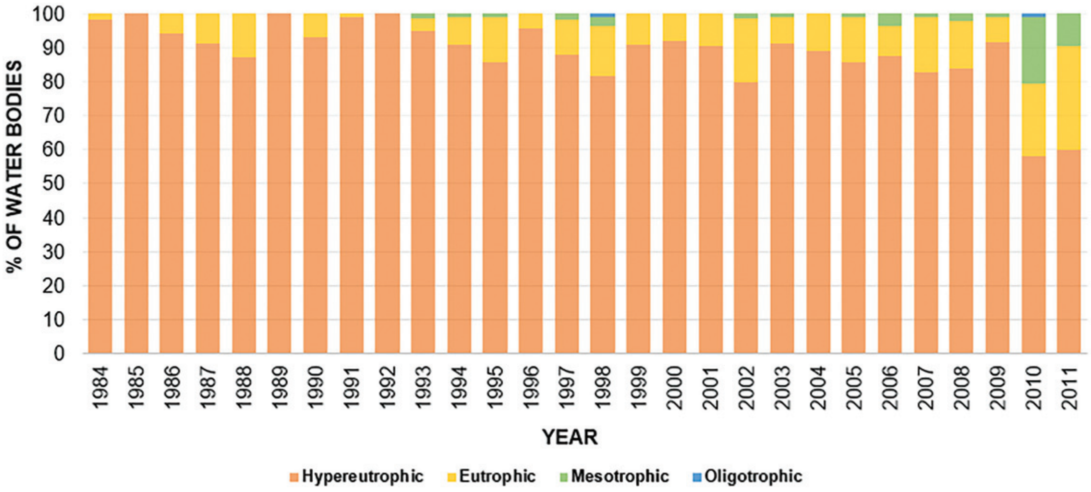

Figure 8. OECD classification of water bodies trophic state (according to their SD) from 1984 to 2011.

Applying this method over the whole time period (1984–2011) allowed the number and area of water bodies obtained in this research to be compared with predictive models to represent the temporal evolution of water bodies and their area changes in the twentieth century, as carried out by Domínguez et al. (2011b) using a small number of dates (8 dates).

Those models explain the generation of gravel pits ponds between 1955 and 1975 and the rapid increase in the number of water bodies and their area. In addition, those models were generated based on the premise of the law that created the PRSE, which stated that new pit ponds could not appear.

The present work contrasts the models created based on the nonappearance of water bodies through the gravel extraction with the reality (Figure 9), which indicates that more water bodies have appeared than expected or stipulated by law. We can also see that the dynamics of appearance and disappearance of water bodies in a short time is very high.

The analysis of the temporality of the appearance of the gravel pits ponds will be addressed in successive studies since it requires an environmental and sociocultural evaluation between 1975 and 2011 in the study area, which exceeds the scope of this research.

On the other hand, the results of the comparison between Landsat SR data product (images LEDAPS corrected) and reflectance field data show significant overestimation in the Landsat SR. These discrepancies were found also by Claverie et al. (2015) for Landsat 5 and 7 sensors, where the blue band used for aerosol optical thickness (AOT) retrieval in LEDAPS shows a high level of uncertainty for low values. The images show consistent SR for all spectral bands except for the blue band, which is known to have the greatest atmospheric sensitivity (Vermote and Kotchenova 2008). High uncertainty is observed over high latitudes and over tropical regions in the visible bands, for which SR is usually lower and the atmospheric effects are more pronounced.

These deviations have also been shown for U.S. sites by Maiersperger et al. (2013), and slightly impact the uncertainty of low green band values. Results consistently indicated similarity between LEDAPS and alternative data products in longer wavelengths over vegetated areas with no adjacent water, while less reliable performance was observed in shorter wavelengths and sparsely vegetated areas.

Typical values of remote sensing reflectance over water bodies are generally on the order of 1% for visible bands and much lower in the NIR spectral region. Thus, even small overestimations such as those present in our results (0.06 over 0.04) must be considered when inferring optical and biophysical parameters of the observed water body from the remote sensor (Warren et al. 2019).

Despite the overestimation detected in the visible and NIR bands, the LEDAPS atmospheric correction approach has been applied to the historic Landsat Thematic Mapper archive (available since 1982) (Ju et al. 2012) because it is a rigorous method that involves the use of radiative transfer models, which are complicated to implement and require input data that are not always available. In our research, we had enough SD *in situ* measurements to obtain a model that relates SD and Landsat SR, but we did not have the ancillary data needed to develop a rigorous atmospheric correction. Thus, we decided to use the corrected images and to develop a new model for SD, similar to the methodology followed by Masek et al. (2006).

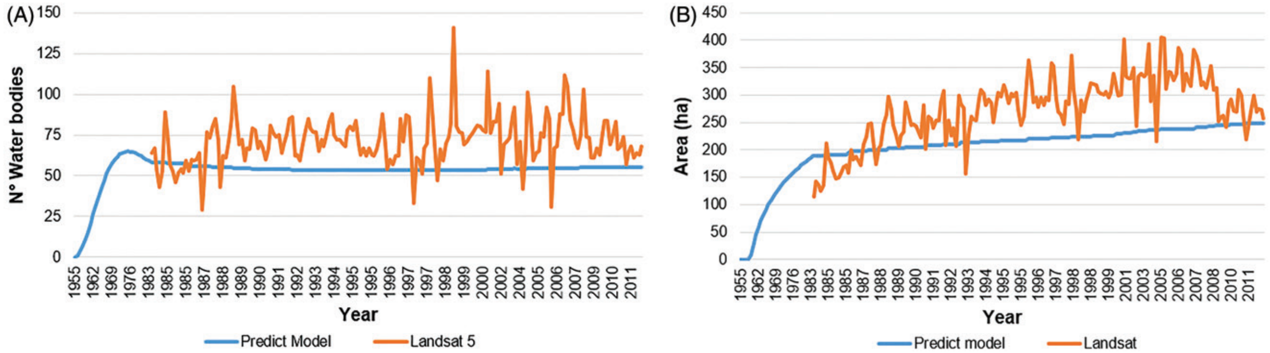

Figure 9. Monitoring the gravel pit ponds. (A) Number of water bodies; (B) Area composed by water bodies.

Our results showed that the equation proposed in this study presents acceptable results in SD estimation from different combinations of TM bands (1–4), which supports the hypothesis that *in situ* measurements of SD are highly correlated with band reflectance values.

These results seem to agree with other authors who have reported a large range of model performances, with R^2 varying from 0.4 to 0.94 (Chao Rodriguez et al. 2014; Giardino et al. 2001; Hicks et al. 2013; Olmanson et al. 2008; Soria et al. 2017b; Wang et al. 2006). Some of these accuracies are higher than those obtained in our study, which was 0.68. Nonetheless, it should be noted that in some of the previous studies reporting high model accuracies, models were developed to assess the spatial variability of SD within lakes but did not account for temporal variability.

Regarding water quality, it seems that the declaration of the PRSE in 1994 has been effective and has had a positive impact on its evolution over the years (Figure 8). However, a period of stagnation was observed between 1989 and 2009, coinciding with the appearance of numerous bodies of water in the exploitation area. Once the area of water bodies was stabilized after 2009 (Figure 6), the water quality increased significantly in the study area. Although it seems that the relationship between water quality and the creation of pit ponds in the PRSE is evident, there are several environmental factors that have great influence. Thus, it is necessary to expand the investigation of the dynamics that have occurred in these water bodies.

Conclusion

The main goal of this work was to assess the use of Landsat TM5 images which have been atmospherically corrected with LEDAPS developed by the USGS for studying water quality time series through SD, using water-leaving reflectance measured in the field. The USGS provides images with good atmospheric and geometric correction to users, in such a way that they can develop research based on the time series from TM5 images for long periods, in our case from 1984 to 2011. At first, our time series was formed by 452 images, although only 230 images were cloud-free images usable. Therefore, approximately 51% of the available images were used. Although, the atmospheric correction developed by the USGS has been robust and evaluated by several authors in vegetation and soil covers showing satisfactory results, in this study is observed that it does not fit well in case of water covers. It is worth expanding the investigation so that the Landsat TM5 images with this correction can be used in water studies.

The evaluation of different techniques for water pixel extraction allowed us to determine that NDWI is the most effective spectral index for the separation of water pixels from non-water types of ground cover. The study of the gravel pit ponds time series generated from LEDAPS atmospheric correction allowed us to identify the appearance and disappearance of gravel pit ponds over time.

The availability of good radiometric field data, which can be considered free from atmospheric effects since the path from the sensor to the observation surface is negligible, allowed us to evaluate new atmospheric correction methods applied to TM5 images in the optical range, including LEDAPS. The main challenge of water bodies is that their reflectance values are very low, and their reflectance maximum values range from 1% to 5%. This is why the overestimation of the water bodies reflectance obtained with generic atmospheric corrections like LEDAPS must be considered when inferring optical and biophysical parameters. Two possible solutions were available to us: LEDAPS could be adapted to water bodies, which means to adapt the corrected images to the already algorithms developed for the study area by other authors; or to develop an algorithm which could be adapted to LEDAPS. We decided to select the second solution since the proposed methodology allows easy application of LEDAPS images in other water bodies with similar characteristics.

Finally, our aim was achieved given that we have assessed LEDAPS atmospheric correction for water bodies, and we propose a solution for using LEDAPS atmospheric correction for studying permanent and temporal water bodies. We have generated 2 time series: number/area of gravel pit ponds and water quality using SD as a parameter of the water quality. The results of the study of these time series will be published soon, to allow water and PRSE managers to understand the behavior in the non-protected and protected areas where the gravel pit ponds are located. Also, this information will be useful for many managers to understand the behavior not only of these artificial water bodies, but also water bodies with similar conditions around the world.

References

Adler-Golden, S.M., Matthew, M.W., Bernstein, L.S., Levine, R.Y., Berk, A., Richtsmeier, S.C., Acharya, P.K., et al. 1999. “Atmospheric correction for shortwave spectral imagery based on MODTRAN4.” *Imaging Spectrometry V*, Vol. 3753: pp. 61–69.

Alvarez, M. 1991. “Optical Limnology of a Hypertrophic Gravel-Pit Lake.” *Internationale Revue Der Gesamten Hydrobiologie Und Hydrographie*, Vol. 76(No. 2): pp. 213–223.

Álvarez-Cobelas, M., Rubio, A., Arauzo, M., Alarcón, P., and Alario, V. 1987. “Morfometría y geoquímica de una laguna de gravera.” *Limnetica*, Vol. 3: pp. 91–95.

Álvarez-Cobelas, M., Riolobos, P., Himi, Y., Sánchez-Carrillo, S., García-Avilés, J., Hidalgo, J. 2000. *Estudio físico-químico de los ambientes estancados del Parque Regional del Sureste de la Comunidad de Madrid.* Centro de Investigaciones Ambientales de la Comunidad de Madrid “Fernando González Bernáldez”. Madrid.

Asociación Ecologista del Jarama “El Soto”. 2001. *Guía de humedales del Parque Regional del Sureste*. Mejorada del Campo: Asociación Ecologista del Jarama “El Soto”.

Bernardo, N., Watanabe, F., Rodrigues, T., and Alcântara, E. 2017. “Atmospheric correction issues for retrieving total suspended matter concentrations in inland waters using OLI/Landsat-8 image.” *Advances in Space Research*, Vol. 59(No. 9): pp. 2335–2348. doi:10.1016/j.asr.2017.02.017.

Boucher, J., Weathers, K., Norouzi, H., and Steele, B. 2018. “Assessing the effectiveness of Landsat 8 chlorophyll a retrieval algorithms for regional freshwater monitoring.” *Ecological Applications*, Vol. 28(No. 4): pp. 1044–1054. doi:10.1002/eap.1708.

Brivio, P., Giardino, C., and Zilioli, E. 2001. “Validation of satellite data for quality assurance in lake monitoring applications.” *Science of the Total Environment*, Vol. 268(No. 1–3): pp. 3–18. doi:10.1016/S0048-9697(00)00693-8.

Caballero, I., Steinmetz, F., and Navarro, G. 2018. “Evaluation of the first year of operational sentinel-2A data for retrieval of suspended solids in Medium- to high-Turbidity Waters.” *Remote Sensing*, Vol. 10(No. 7): pp. 982. doi:10.3390/rs10070982.

Cao, Z., Duan, H., Song, Q., Shen, M., Ma, R., and Liu, D. 2018. “Evaluation of the sensitivity of China’s next-generation ocean satellite sensor MWI onboard the Tiangong-2 space lab over inland waters.” *International Journal of Applied Earth Observation and Geoinformation*, Vol. 71: pp. 109–120. doi:10.1016/j.jag.2018.05.012.

Carlson, R. 1977. “A trophic State Index for lakes.” *Limnology and Oceanography*, Vol. 22(No. 2): pp. 361–369. doi:10.4319/lo.1977.22.2.0361.

Chao Rodriguez, Y., el Anjoumi, A., Domínguez Gómez, J.A., Rodríguez Pérez, D., and Rico, E. 2014. “Using Landsat image time series to study a small water body in Northern Spain.” *Environmental Monitoring and Assessment*, Vol. 186(No. 6): pp. 3511–3522. doi:10.1007/s10661-014-3634-8.

Chavez, P.S. 1996. “Image Based atmospheric corrections.” *Revisited and Improved. Photogrammetric Engineering and Remote Sensing*, Vol. 62(No. 9): pp. 1025–1036.

Claverie, M., Vermote, E.F., Franch, B., and Masek, J.G. 2015. “Evaluation of the Landsat-5 TM and Landsat-7 ETM + surface reflectance products.” *Remote Sensing of Environment*, Vol. 169: pp. 390–403. doi:10.1016/j.rse.2015.08.030.

Comunidad de Madrid. 1990. “Ley 7/1990, de 28 de junio, de Protección de Embalses y Zonas Húmedas de la Comunidad Autónoma de Madrid.” *Boletìn Oficial Del Estado (Boe) Num*, Vol. 234: pp. 28349–28352.

Comunidad de Madrid. 1994. *Ley 6/1994, de 28 de junio, sobre el Parque Regional en torno a los ejes de los cursos bajos de los ríos Manzanares y Jarama* Boletìn Oficial del Estado (BOE) num. 206, 29/aug/1994, pp. 27312–27333. Available at: https://www.boe.es/buscar/doc.php?id=BOE-A-1994-19704

Dekker, A.G., and Peters, S. 1993. “The use of the Thematic Mapper for the analysis of eutrophic lakes: a case study in the Netherlands.” *International Journal of Remote Sensing*, Vol. 14(No. 5): pp. 799–821. doi:10.1080/01431169308904379.

Dekker, A.G., Vos, R.J., and Peters, S. 2001. “Comparison of remote sensing data, model results and in situ data for total suspended matter (TSM) in the southern Frisian lakes.” *Science of the Total Environment*, Vol. 268(No. 1–3): pp. 197–214. doi:10.1016/S0048-9697(00)00679-3.

Domínguez, J. A. 2002. *Estudio de Calidad del Agua de lagunas de gravera mediante teledetección*. Alcalá de Henares: Universidad de Alcalá.

Domínguez, J.A., Alonso Alonso, C., and Alonso García, A. 2011a. “Remote sensing as a tool for monitoring water quality parameters for Mediterranean Lakes of European Union water framework directive (WFD) and as a system of surveillance of cyanobacterial harmful algae blooms (SCyanoHABs).” *Environmental Monitoring and Assessment*, Vol. 181(No. 1–4): pp. 317–334. doi:10.1007/s10661-010-1831-7.

Domínguez, J.A., Chuvieco Salinero, E., and Sastre Merlín, A. 2009. “Monitoring transparency in inland water bodies using multiespectral images.” *International Journal of Remote Sensing*, Vol. 30(No. 6): pp. 1567–1586. doi:10.1080/01431160802513811.

Domínguez, J. A., Marcos, C., Chao, Y., Delgado, G., and Rodriguez, D. 2011b. *Estudio de aguas continentales mediante teledetección*. Madrid: UNED. ISBN: 978-84-362-6376-3.

Domínguez, J.A., and Peña, R. 1999. “Trophic state assessment in two gravel pits (El Campillo & Porcal) using airborne imagery.” *Limnética*, Vol. 16: pp. 107–112.

Domínguez, J.A., Peña, R., and Sastre, A. 1997. Detección de cambios en los humedales del rìo Jarama entre 1988 y 1992 y evaluaciòn del estado tròfico de las lagunas del Campillo, El Porcal y las Madres en 1992 mediante imàgenes Landsat TM. Santiago de Compostela., Universidad Santiago de Compostela- Asociación Española de Teledetección, pp. 339–351.

Domínguez, J. A., Vargas, J., Navarro, E., and Martín, A. 2017. *Seguimiento de la Calidad del Agua del embalse de Picadas mediante imágenes Landsat 8 (Septiembre 2015-Diciembre 2016)*. In Proceedings book of XVII Congreso de la Asociación Española de Teledetección. Nuevas plataformas y sensores de Teledetección. Aplicados a la gestión del agua, la agricultura y el medio ambiente. Ed. Universidad Politécnica de Valencia. ISBN: 978 84 9048 650 4.

Doña, C., Sánchez, J.M., Caselles, V., Domínguez, J.A., and Camacho, A. 2014. “Empirical Relationships for Monitoring Water Quality of Lakes and Reservoirs Through Multispectral Images.” *IEEE Journal of Selected Topics in Applied Earth Observations and Remote Sensing*, Vol. 7(No. 5): pp. 1632–1641.

Doña, C., Chang, N.-B., Caselles, V., Sánchez, J.M., Camacho, A., Delegido, J., Vannah, B.W., et al. 2015. “Integrated satellite data fusion and mining for monitoring lake water quality status of the Albufera de Valencia in Spain.” *Journal of Environmental Management*, Vol. 151: pp. 416–426. doi:10.1016/j.jenvman.2014.12.003.

Dörnhöfer, K., and Oppelt, N. 2016. “Remote sensing for lake research and monitoring – Recent advances.” *Ecological Indicators*, Vol. 64: pp. 105–122. doi:10.1016/j.ecolind.2015.12.009.

Duru, U. 2017. “Shoreline change assessment using multi-temporal satellite images: a case study of Lake Sapanca, NW Turkey.” *Environmental Monitoring and Assessment*, Vol. 189(No. 8): pp. 385. doi:10.1007/s10661-017-6112-2.

European Commission, 2000. “European Parliament and of the Council of 23 October 2000 establishing a framework for Community action in the field of water policy.” *Official Journal of the European Communities*, Vol. L 327: pp. 1–73.

Frazier, P.S., and Page, K.J. 2000. “Water body detection and delineation with Landsat TM data.” *Photogramm Eng Remote Sensing*, Vol. 66(No. 12): pp. 1461–1467.

Fuller, L., Aichele, S., and Minnerick, R. 2004. Predicting Water Quality by Relating Secchi-Disk Transparency and Chlorophyll a Measurements to Satellite Imagery for Michigan Inland Lakes, August 2002. U.S. Geological Survery Scientific Investigations Report 2004–5086.

Giardino, C., Pepe, M., Brivio, P.A., Ghezzi, P., and Zilioli, E. 2001. “Detecting chlorophyll, Secchi disk depth and surface temperature in a sub-alpine lake using Landsat imagery.” *Science of the Total Environment*, Vol. 268(No. 1-3): pp. 19–29. doi:10.1016/S0048-9697(00)00692-6.

Gilabert, M.A., Conese, C., and Maselli, F. 1994. “An atmospheric correction method for the automatic retrieval of surface reflectance from TM images.” *International Journal of Remote Sensing*, Vol. 15(No. 10): pp. 2065–2086. doi:10.1080/01431169408954228.

Guang, J., Yuchun, W., and Jiazhu, H. 2006. “A model for the retrieval of suspended sediment concentrations in Taihu Lake from TM images.” *Journal of Geographical Sciences*, Vol. 16(No. 4): pp. 458–464. doi:10.1007/s11442-006-0409-3.

Harvey, E.T., Walve, J., Andersson, A., Karlson, B., and Kratzer, S. 2019. “The Effect of Optical Properties on Secchi Depth and Implications for Eutrophication Management.” *Frontiers in Marine Science*, Vol. 5(No. 496). doi:10.3389/fmars.2018.00496.

Hicks, B.J., Stichbury, G.A., Brabyn, L.K., Allan, M.G., and Ashraf, S. 2013. “Hindcasting water clarity from Landsat satellite images of unmonitored shallow lakes in the Waikato region, New Zealand.” *Environmental Monitoring and Assessment*, Vol. 185(No. 9): pp. 7245–7261. doi:10.1007/s10661-013-3098-2.

Ju, J., Roy, D.P., Vermote, E., Masek, J., and Kovalskyy, V. 2012. “Continental-scale validation of MODIS-based and LEDAPS Landsat ETM + atmospheric correction methods.” *Remote Sensing of Environment*, Vol. 122: pp. 175–184. doi:10.1016/j.rse.2011.12.025.

Khattab, M.F.O., and Merkel, B.J. 2014. “Application of Landsat 5 and Landsat 7 images data for water quality mapping in Mosul Dam Lake, Northern Iraq.” *Arabian Journal of Geosciences*, Vol. 7. doi:10.1007/s12517-013-1026-y.

Kloiber, S.M., Bauer, M.E., Brezonik, P.L., and Olmanson, L.G. 2002. “A procedure for regional lake water clarity assessment using Landsat multispectral data.” *Remote Sensing of Environment*, Vol. 82(No. 1): pp. 38–47. doi:10.1016/S0034-4257(02)00022-6.

Kutser, T. 2012. “The possibility of using the Landsat image archive for monitoring long time trends in coloured dissolved organic matter concentration in lake waters.” *Remote Sensing of Environment*, Vol. 123: pp. 334–338. doi:10.1016/j.rse.2012.04.004.

Lee, Z., Shang, S., Hu, C., Du, K., Weidemann, A., Hou, W., Lin, J., et al. 2015. “Secchi disk depth: A new theory and mechanistic model for underwater visibility.” *Remote Sensing of Environment*, Vol. 169: pp. 139–149. doi:10.1016/j.rse.2015.08.002.

Liu, Z., Yao, Z., and Wang, R. 2016. “Assessing methods of identifying open water bodies using Landsat 8 OLI imagery.” *Environmental Earth Sciences*, Vol. 75(No. 873). doi:10.1007/s12665-016-5686-2.

López, M.J., and Caselles, V. 1990. “A multi-temporal study of chlorophyll-a concentration in the Albufera lagoon of Valencia, Spain, using Thematic Mapper data.” *International Journal of Remote Sensing*, Vol. 11: pp. 301–311. doi:10.1080/01431169008955021.

Maeda, E.E., Lisboa, F., Kaikkonen, L., Kallio, K., Koponen, S., Brotas, V., Kuikka, S., et al. 2019. “Temporal patterns of phytoplankton phenology across high latitude lakes unveiled by long-term time series of satellite data." *Remote Sensing of Environment*, Vol. 221: pp. 609–620. doi:10.1016/j.rse.2018.12.006.

Maiersperger, T.K., Scaramuzza, P.L., Leigh, L., Shrestha, S., Gallo, K.P., Jenkerson, C.B., and Dwyer, J.L. 2013. "Characterizing LEDAPS surface reflectance products by comparisons with AERONET, field spectrometer, and MODIS data." *Remote Sensing of Environment*, Vol. 136: pp. 1–13. doi:10.1016/j.rse.2013.04.007.

Masek, J.G., Vermote, E.F., Saleous, N.E., Wolfe, R., Hall, F.G., Huemmrich, K.F., Gao, F., Kutler, J., and Lim, T.-K. 2006. "A Landsat surface reflectance dataset for North America, 1990-2000." *IEEE Geoscience and Remote Sensing Letters*, Vol. 3(No. 1): pp. 68–72. doi:10.1109/LGRS.2005.857030.

Matthews, M.W., Bernard, S., and Winter, K. 2010. "Remote sensing of cyanobacteria-dominant algal blooms and water quality parameters in Zeekoevlei, a small hypertrophic lake, using MERIS." *Remote Sensing of Environment*, Vol. 114(No. 9): pp. 2070–2087. doi:10.1016/j.rse.2010.04.013.

McFeeters, S.K. 1996. "The use of Normalized Difference Water Index (NDWI) in the delineation of open water features." *International Journal of Remote Sensing*, Vol. 17(No. 7): pp. 1425–1432. doi:10.1080/01431169608948714.

Mostaza-Colado, D., Carreño-Conde, F., Rasines-Ladero, R., and Iepure, S. 2018. "Hydrogeochemical characterization of a shallow alluvial aquifer: 1 baseline for groundwater quality assessment and resource management." *Science of the Total Environment*, Vol. 639: pp. 1110–1125. doi:10.1016/j.scitotenv.2018.05.236.

Mouw, C.B., Greb, S., Aurin, D., DiGiacomo, P.M., Lee, Z., Twardowski, M., Binding, C., et al. 2015. "Aquatic color radiometry remote sensing of coastal and inland waters: Challenges and recommendations for future satellite missions." *Remote Sensing of Environment*, Vol. 160: pp. 15–30. doi:10.1016/j.rse.2015.02.001.

Nas, B., Ekercin, S., Karabörk, H., Berktay, A., and Mulla, D.J. 2010. "An Application of Landsat-5TM Image Data for Water Quality Mapping in Lake Beysehir, Turkey." *Water, Air, and Soil Pollution*, Vol. 212(No. 1–4): pp. 183–197. doi doi:10.1007/s11270-010-0331-2.

NASA (National Aeronautics and Space Administration). 2001. *Landsat 7 Science Data Users Handbook*. Retrieved from http://ltpwww.gsfc.nasa.gov/IAS/handbook/handbook_toc.html.

Nazeer, M., Nichol, J.E., and Yung, Y.-K. 2014. "Evaluation of atmospheric correction models and Landsat surface reflectance product in an urban coastal environment." *International Journal of Remote Sensing*, Vol. 35(No. 16): pp. 6271–6291. doi:10.1080/01431161.2014.951742.

Ogilvie, A., Belaud, G., Massuel, S., Mulligan, M., Le Goulven, P., and Calvez, R. 2018. "Surface water monitoring in small water bodies: potential and limits of multi-sensor Landsat time series." *Hydrology and Earth System Sciences*, Vol. 22(No. 8): pp. 4349–4380. doi:10.5194/hess-22-4349-2018.

Olmanson, L.G., Bauer, M.E., and Brezonik, P.L. 2008. "A 20-year Landsat water clarity census of Minnesota's 10,000 lakes." *Remote Sensing of Environment*, Vol. 112(No. 11): pp. 4086–4097. doi:10.1016/j.rse.2007.12.013.

Oyama, Y., Matsushita, B., and Fukushima, T. 2015. "Distinguishing surface cyanobacterial blooms and aquatic macrophytes using Landsat/TM and ETM + shortwave infrared bands." *Remote Sensing of Environment*, Vol. 157: pp. 35–47. doi:10.1016/j.rse.2014.04.031.

Oyama, Y., Matsushita, B., Fukushima, T., Matsushige, K., and Imai, A. 2009. "Application of spectral decomposition algorithm for mapping water quality in a turbid lake (Lake Kasumigaura, Japan) from Landsat TM data." *ISPRS Journal of Photogrammetry and Remote Sensing*, Vol. 64(No. 1): pp. 73–85. doi:10.1016/j.isprsjprs.2008.04.005.

Padedda, B.M., Sechi, N., Lai, G.G., Mariani, M.A., Pulina, S., Sarria, M., Satta, C.T., Virdis, T., Buscarinu, P., and Lugliè, A. 2017. "Consequences of eutrophication in the management of water resources in Mediterranean reservoirs: A case study of Lake Cedrino (Sardinia, Italy)." *Global Ecology and Conservation*, Vol. 12: pp. 21–35. doi:10.1016/j.gecco.2017.08.004.

Pahlevan, N., Sarkar, S., Franz, B.A., Balasubramanian, S.V., and He, J. 2017. "Sentinel-2 MultiSpectral Instrument (MSI) data processing for aquatic science applications: Demonstrations and validations." *Remote Sensing of Environment*, Vol. 201: pp. 47–56. doi:10.1016/j.rse.2017.08.033.

Palmer, S.C., Kutser, T., and Hunter, P.D. 2015. "Remote sensing of inland waters: Challenges, progress and future directions." *Remote Sensing of Environment*, Vol. 157: pp. 1–8. doi:10.1016/j.rse.2014.09.021.

Pereira, M. 2017. Objectives and first results of ESAQS project (Ecological Status of Aquatic Systems with Sentinel satellites. In Proceedings book of XVII Congreso de la Asociación Española de Teledetección. Nuevas plataformas y sensores de Teledetección. Aplicados a la gestión del agua, la agricultura y el medio ambiente. Ed. Universidad Politécnica de Valencia. ISBN: 978 84 9048 650 4.

Puche Riart, O., Mazadiego Martínez, L.F., Jordá Bordehore, L., and Hervás, A.M. 2012. "La minería en la comunidad de Madrid." *Madrid Histórico*, Vol. 40: pp. 32–47.

Qi, J., Chen, J., Lafortezza, R., and Lin, Z. 2017. "Remote sensing for ecosystem sustainability. *Reference Module in Earth Systems and Environmental Sciences." Comprehensive Remote Sensing*, Vol. 9: pp. 186–201. doi:10.1016/B978-0-12-409548-9.10428-2.

Qin, P., Simis, S.G., and Tilstone, G.H. 2017. "Radiometric validation of atmospheric correction for MERIS in the Baltic Sea based on continuous observations from ships and AERONET-OC." *Remote Sensing of Environment*, Vol. 200: pp. 263–280. doi:10.1016/j.rse.2017.08.024.

Ren, J., Zheng, Z., Li, Y., Lv, G., Wang, Q., Lyu, H., Huang, C., et al. 2018. "Remote observation of water clarity patterns in Three Gorges Reservoir and Dongting Lake of China and their probable linkage to the Three Gorges Dam based on Landsat 8 imagery." *Science of the Total Environment*, Vol. 625: pp. 1554–1566. doi:10.1016/j.scitotenv.2018.01.036.

Roblas, N., and García, J. 1997. *Valoración ambiental y caracterización de los ecosistemas acuáticos leníticos del*

Parque Regional en torno a los ejes de los cursos bajos de los ríos Manzanares y Jarama, Madrid: Consejería de Medio Ambiente y Desarrollo Regional.

Serrano, P., Camacho, A., Vicente, E., and Peña, R. 1997. “Estudio por teledetección de la evolución del estado trófico de tres embalses del ámbito de la Confederación Hidrográfica del Júcar en el periodo estival de los años 1994 y 1995.” *Limnetica*, Vol. 13(No. 1): pp. 5–14.

Smith, V.H., Tilman, G.D., and Nekola, J.C. 1999. “Eutrophication: Impacts of excess nutrient inputs on freshwater, marine, and terrestrial ecosystems.” *Environmental Pollution*, Vol. 100(No. 1–3): pp. 179–196. doi:10.1016/S0269-7491(99)00091-3.

Song, C., Woodcock, C.E., Seto, K.C., Lenney, M.P., and Macomber, S.A. 2001. “Classification and change detection using landsat TM data: When and how to correct atmospheric effects?” *Remote Sensing of Environment*, Vol. 75(No. 2): pp. 230–244. doi:10.1016/S0034-4257(00)00169-3.

Soria, X., Delegido, J., Urrego, E. P., Pereira-Sandoval, M., Vicente, E., Ruíz-Verdú, A., Soria, J., Peña, R., Tenjo, C., and Moreno, J. 2017a. Validación de algoritmos para la estimacion de la Clorofila-a con Sentinel-2 en la Albufera de Valencia. In Proceedings book of XVII Congreso de la Asociación Española de Teledetección. Nuevas plataformas y sensores de Teledetección. Aplicados a la gestión del agua, la agricultura y el medio ambiente. Ed. Universidad Politécnica de Valencia. ISBN: 978 84 9048 650 4.

Soria, X., Vicente, E., Durán, C., Soria, J. M., and Peña, R. 2017b. Uso de imágenes Landsat-8 para la estimación de la *profundidad del disco de Secchi en aguas continentales.* In Proceedings book of XVII Congreso de la Asociación Española de Teledetección. Nuevas plataformas y sensores de Teledetección. Aplicados a la gestión del agua, la agricultura y el medio ambiente. Ed. Universidad Politécnica de Valencia. ISBN: 978 84 9048 650 4.

Verdin, J.P. 1985. “Monitoring water quality conditions in large western reservoir with Landsat imagery.” *Photogrammetric Engineering and Remote Sensing*, Vol. 51: pp. 343–353.

Vermote, E.F., and Kotchenova, S. 2008. “Atmospheric correction for the monitoring of land surfaces.” *Journal of Geophysycal Research*, Vol. 113(No. D23S90).

Vermote, E.F., Tanré, D., Deuzé, J.L., Herman, M., and Morcrette, J.J. 1997. “Second Simulation of the Satellite Signal in the Solar Spectrum, 6S: An Overview.” *IEEE Transactions on Geoscience and Remote Sensing*, Vol. 35(No. 3):pp. 35. doi:10.1109/36.581987.

Vollenweider, R. A. 1968. Scientific fundamentals of the eutrophication of lakes and flowing waters, with particular reference to nitrogen and phosphorus as factors in eutrophication. Paris Organisation for Economic Co-operation and Development (OECD). Paris. Report Num.: DAS/CSI/62.27. pp. 61

Vollenweider, R. A., and Kerekes, J. J. 1982. *Eutrophication of Waters. Monitoring, Assessment and Control.* Paris: Organization for Economic Co-operation and Development (OECD). 156 p.

Wang, M. 2010. *Atmospheric correction for Remotely-Sensed Ocean-Colour products*. Silver Spring, MD: NOAA/NESDIS Center for Satellite Applications and Research.

Wang, X., Gong, Z., and Pu, R. 2018b. “Estimation of chlorophyll a content in inland turbidity waters using WorldView-2 imagery: a case study of the Guanting Reservoir, Beijing, China.” *Environmental Monitoring and Assessment*, Vol. 190(No. 10): pp. 620. doi:10.1007/s10661-018-6978-7.

Wang, F., Han, L., Kung, H.-T., and Van Arsdale, R. 2006. “Applications of Landsat-5 TM imagery in assessing and mapping water quality in Reelfoot Lake, Tennessee.” *International Journal of Remote Sensing*, Vol. 27(No. 23): pp. 5269–5283. doi:10.1080/01431160500191704.

Wang, M., and Jiang, L. 2018. “Atmospheric Correction Using the Information From the Short Blue Band.” *IEEE Transactions on Geoscience and Remote Sensing*, Vol. 56(No. 10): pp. 6224–6227. doi:10.1109/TGRS.2018.2833839.

Wang, S., Li, J., Zhang, B., Spyrakos, E., Tyler, A.N., Shen, Q., Zhang, F., et al. 2018a. “Trophic state assessment of global inland waters using a MODIS-derived Forel-Ule index.” *Remote Sensing of Environment*, Vol. 217: pp. 444–460. doi:10.1016/j.rse.2018.08.026.

Warren, M.A., Simis, S.G.H., Martinez-Vicente, V., Poser, K., Bresciani, M., Alikas, K., Spyrakos, E., et al. 2019. “Assessment of atmospheric correction algorithms for the Sentinel-2A MultiSpectral Imager over coastal and inland waters.” *Remote Sensing of Environment*, Vol. 225: pp. 267–289. doi:10.1016/j.rse.2019.03.018.

Wernand, M.R. 2010. “On the history of the Secchi disk.” *Journal European Optical Society*, Vol. 5(No. 100135): pp. 2–6. doi:10.2971/jeos.2010.10013s.

Wetzel, R. 2001. *Limnology*. 3rd ed. New York: Elsevier Inc. ISBN: 9780127447605.

Xu, H. 2006. “Modification of normalized difference water index (NDWI) to enhance open water features in remotely sensed imagery.” *International Journal of Remote Sensing*, Vol. 27(No. 14): pp. 3025–3033. doi:10.1080/01431160600589179.

Yongzhen, F., Li, W., Gatebe, C., Jamet, C., Zibordi, G., Schroeder, T., and Stamnes, K. et al. 2017. “Atmospheric correction over coastal waters using multilayer neural networks.” *Remote Sensing of Environment*, Vol. 199: pp. 218–240.

3.2. Artículo 2: Water quality spatial-temporal analysis of gravel pit ponds in the southeast regional park Madrid (Spain) from 1984 to 2009.

A continuación, se reproduce el artículo 2 publicado https://doi.org/10.1080/10106049.2022.2037736.

GEOCARTO INTERNATIONAL
https://doi.org/10.1080/10106049.2022.2037736

Taylor & Francis
Taylor & Francis Group

Water quality spatial-temporal analysis of gravel pit ponds in the southeast regional park Madrid (Spain) from 1984 to 2009.

Carolina Echavarría-Caballero[a], José Antonio Domínguez-Gómez[b], Concepción González-García[a] and María Jesús García-García[a]

[a]Universidad Politécnica de Madrid, E.T.S. Ingeniería de Montes, Forestal y del Medio Natural, Madrid, Spain; [b]GIS and Remote Sensing Lab, Institute of Agri-Food Research and Development (IMIDA), Murcia, Spain

ABSTRACT

We used a time series of Secchi disk values retrieved from Landsat 5 images to study temporal and spatial patterns of water quality across gravel pit ponds located in Madrid, Spain from 1984 to 2009. There is a seasonal behavior in the water quality, with higher values of Secchi disks in autumn and winter (December–February) and lower values in summer (July–August), which can be explained by the relationship between Secchi disk values and temperature and solar radiation. We found that the 1994 administrative declaration of the regional park has had a positive impact on the water quality. The trophic state of the studied pit ponds has slowly improved, though the ponds have not reached the oligotrophic state.

ARTICLE HISTORY
Received 28 October 2021
Accepted 30 January 2022

KEYWORDS
Inland water; Secchi depth; transparency; spatial–temporal series; gravel pit pond

Introduction

Sand and gravel are fundamental to the development of the urban and industrial economy (construction, civil works, and infrastructure) (Mollema and Antonellini 2016; Søndergaard et al. 2018; U.S. Geological Survey 2015). The most intensely exploited deposits are typically very close to large cities, which are the main consuming centers of these materials (Vucic et al. 2019). Spain (along with Italy) had the highest rates of urban growth of the future European Union in the 1960s. During that decade and the next, nine of the twelve European urban agglomerations with the most growth were Spanish, with Madrid taking the lead (Díaz and Araujo 2017). This activity has resulted in the generation of gravel ponds due to the rise of the phreatic level when dredging was carried out. When abandoned, these ponds and artificial lakes became wetland ecosystems with established aquatic fauna and flora (Domínguez Gómez and Peña 1999). This phenomenon is common across the world. For example, in Maine, USA, 34 active and former gravel pits cover 26% of the aquifer surface (Peckenham et al. 2009); in the Netherlands, 500 gravel pit lakes give this country the highest production of gravel and sand per surface area of

CONTACT María Jesús García-García mariajesus.garcia.garcia@upm.es

all countries (Mollema et al. 2015); in Italy, the gravel pit lakes along the coast near Ravenna increased the open water surface in the catchment by 6% from 1972 to 2012, and the excavation is not yet finished (Mollema et al. 2012); in Nottinghamshire, UK, gravel pits exploited between 1929 and 1967 became the Attenborough Nature Reserve and received the designation of a Site of Special Scientific Interest (SSSI) (Andrews 1990).

In recent years, interest in protecting the environment that hosts this type of extractive activity has increased. This is the case in Madrid. In 1994, the declaration of the regional park 'Parque Regional del Sureste' (PRSE) (Ley 6/1994, Spain) was made in order to protect the area of the Manzanares and Jarama rivers' confluence, including the gravel pit ponds, against all kinds of negative environmental impacts.

The gravel pit ponds are peculiar water bodies. They are young compared to most natural lakes, given that they are less than one hundred years old; dynamic due to their origin; and difficult to access because they are on private property. As a result, it has not been possible to investigate long-term environmental concerns for these ponds, and they have not been studied in detail compared to other types of natural and man-made lakes (Vucic et al. 2019). Thus, it is necessary to study gravel pit lakes' water quality, their aquatic ecosystem function, and the effects of environmental changes (Mollema and Antonellini 2016). Such research is important both due to its ecological importance and because this type of wetland will continue to be generated in metropolitan areas such as Madrid, given that urban development is continuous.

Since the 1980s, there has been a high level of interest in the gravel pit ponds in the PRSE, which have consequently been widely studied through field campaigns (Álvarez-Cobelas 1991; Álvarez-Cobelas et al. 1987; Álvarez-Cobelas 2000). However, the conservation status of the lentic ecosystems located in the PRSE has not been periodically monitored. Such monitoring is essential because the role of wetland ecosystems, as well as how that role will change with increasing pressure from human activity and climate change, require significant study (Álvarez-Cobelas et al. 2019).

Several national and international directives address these problems and aim to improve the ecological state of inland waters. In EU Member States, the Water Framework Directive (WFD) was intended to unify water management efforts in the European Union. Since its approval, the European Communities have the responsibility of monitoring the water quality of their waterbodies (EC 2000). However, for a comprehensive understanding of lake ecology, integrative, frequent, and consistent long-term monitoring approaches are required (Hestir et al. 2015; Seelen et al. 2021). Understanding the temporal trends and spatial distributions of water quality is essential for maintaining the health of aquatic ecosystems and ensuring the safety of water (Blanchet et al. 2022; Chu et al. 2018). To this end, spatio-temporal modeling for water quality has produced considerable advances over the last few decades (Kim et al. 2017; Kim et al. 2015; Liu et al. 2021; Seers and Shears 2015; Weeks et al. 2012; Yoder et al. 2002).

Remote sensing is a highly useful tool to achieve this aim. Global mapping satellite missions make systematic measurements over years or decades, providing a time series of consistently measured data to assess system conditions, identify changes and understand processes for an important suite of biophysical variables. Even if monitoring is generally performed using field data, remote sensing can play a key role as it offers the opportunity to extend monitoring at low cost (Devlin et al. 2015; el Serafy et al., 2021) and examine the spatial and temporal variability of water quality data (Boucher et al. 2018; Chao Rodríguez et al. 2014; Domínguez Gómez et al. 2009; Hicks et al. 2013; Li et al. 2021; Lobo et al. 2021; López-Andreu et al. 2021; Maeda et al. 2019; Nas et al. 2010; Paltsev and Creed 2021; Wang et al. 2021).

In a previous study, transparency measured by Secchi disk (SD) values was obtained for the PRSE water bodies from 1984 to 2009 using a regression equation that relates field data and the reflectance of the Landsat 5 image. This method produced a spatial–temporal series of SD data (Echavarría-Caballero et al. 2019).

These time series can be approached by predictive modeling (Delasalles et al. 2019) or exploratory analysis (Cressie and Wikle 2015). In the latter case, methods such as the Hovmöller diagram, anomalies analysis, and the empirical orthogonal function (EOF) have a long history of being used in remote sensing to study atmospheric phenomena (Hannachi et al. 2007; Liew et al. 2010; Persson 2017). More recently, they have been used in water studies (Beltrán-Abaunza et al. 2017; Bracher et al. 2020; Weeks et al. 2012; Yoder et al. 2002)

Spatial–temporal SD data provides an opportunity to better understand the behavior of water quality in gravel pit ponds. Therefore, the aim of our research is to carry out statistical analysis in order to assess the spatial and temporal patterns of water quality using time series of SD data retrieved from Landsat 5 images. In particular, we aimed to (1) detect changes and magnitudes of the differences in water transparency in space and time; (2) characterize the seasonal behavior of SD; and (3) determine the dominant modes of variation and identify the physical drivers that influence the spatio-temporal patterns of water transparency.

Study area

The study focuses on the PRSE (Figure 1), which covers an area of 300 km^2 in 18 municipalities located in the southwestern part of the Madrid region (Spain). The area includes the lower course of the Jarama River, specifically from Coslada to Aranjuez-Ciempozuelos.

The PRSE is characterized by the presence of two fundamental lithological domains: the Neogene Tertiary and the Quaternary. It is included in the Tajo basin, specifically in the sub-basin belonging to the Jarama River. This river is the main watercourse in the park and runs in the north–south direction (Moreno & García-Avilés, 1997; Mostaza-Colado et al. 2018). The flora includes primarily helophyte vegetation, especially reeds (*Phragmites australis*), accompanied by bulrushes (*Typha spp.*), rushes (*Scirpus holoschoenus*), and repopulations of native species such as alders, poplars, and elms, as well as more exotic species such as tree of paradise and weeping willow (Moreno & García-Avilés, 1997). The climate in the study area is classified as Mediterranean temperate-continental, with temperate winters and warm, dry summers. The average temperature is 13.8 °C and the average rainfall is 440 mm/year (Mostaza-Colado et al. 2018).

In the environment of the PRSE, water is the omnipresent and dominant natural element. Rivers and lakes have shaped the territory of the park and support a large number of species. In the PRSE, a total of 123 wetlands have been inventoried, occupying more than 400 hectares. To develop the current research, we selected four gravel pit ponds: Picón de los Conejos, Campillo, Porcal, and Soto de las Cuevas. We applied three selection criteria, choosing water bodies (1) with sufficient size to be analyzed according to the spatial resolution of the Landsat 5 images; (2) that are distributed throughout the study area and (3) that belong to areas with different environmental classifications (degraded zones for regeneration, conservation areas and orderly exploitation of natural resources zones). The water bodies developed by gravel extraction, which are the subject of this study, will be named as gravel pit ponds, gravel pit lakes, water bodies, or lakes.

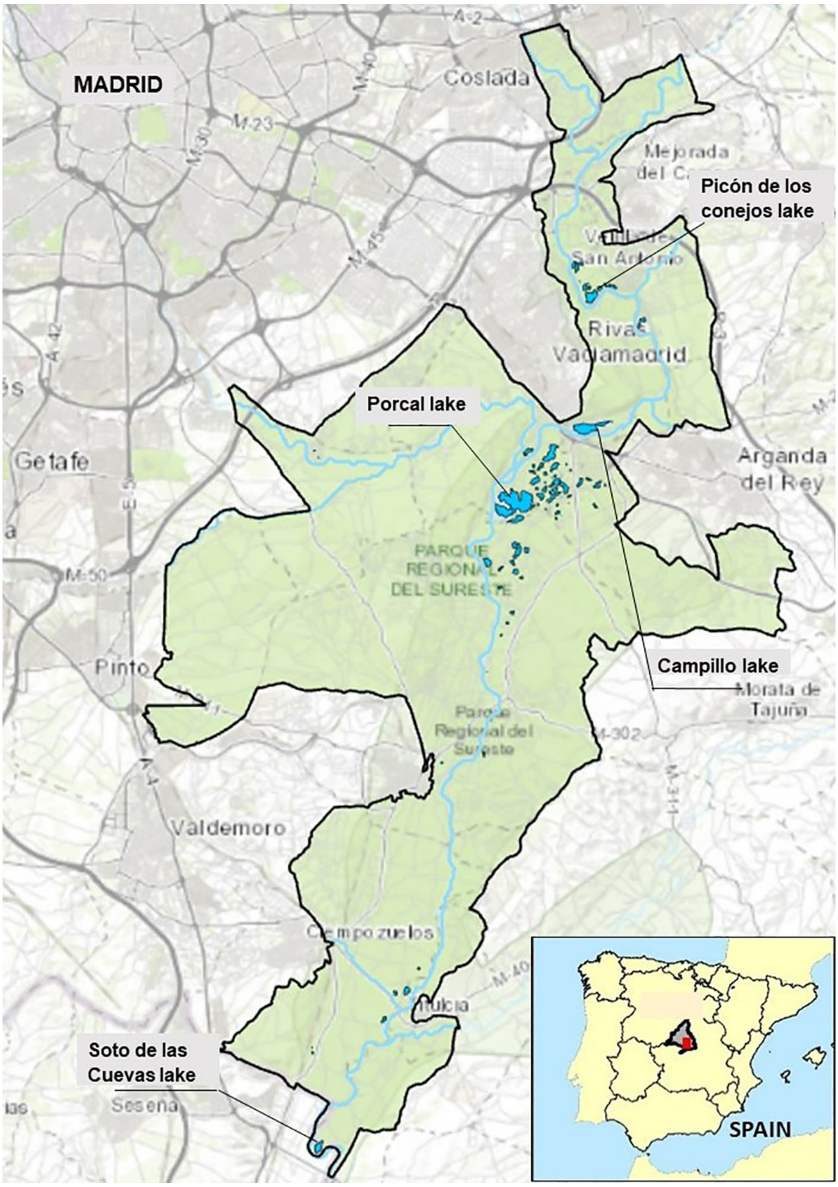

Figure 1. Study area, including gravel pit ponds (bright blue) and the boundary of the PRSE (black).

Picón de los Conejos gravel pit pond

The Picón de los Conejos gravel pit pond complex originated in 1991 and comprises four water bodies. It underwent multiple transformations until 1994, when it stabilized in its current form (Figure 2). For the purposes of the present study, the analysis of water quality in this pond has been carried out since 1994.

According to the environmental park zoning developed in the Planning and Management Plan in Protected Natural Areas (Decreto 27/1999 of February 11th, Madrid), the Picón de los Conejos gravel pit pond complex is located in zone C, which corresponds to the degraded zones for regeneration classification. It has been included in

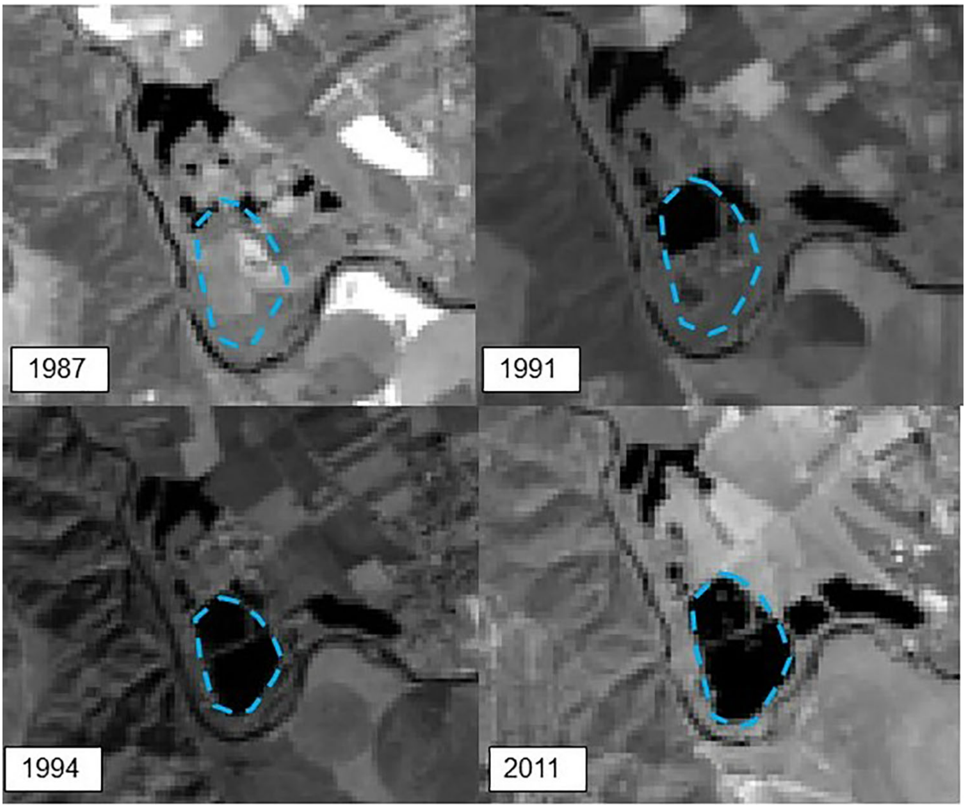

Figure 2. Picón de los Conejos lake development from 1987 to 2011, with the assumed shape in this study (light blue dashed line).

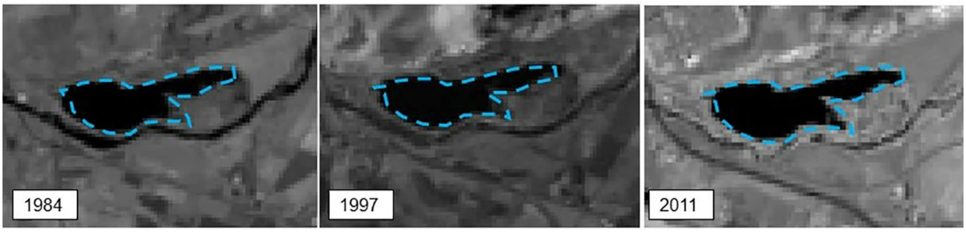

Figure 3. Campillo lake development from 1984 to 2011, with the assumed shape in this study (light blue dashed line).

the 'cataloged wetlands' by the Madrid regional government given its unique landscape, fauna, botany, hydrological, ecological, or geological characteristics (Comunidad de Madrid 2020).

Campillo gravel pit pond

As this lake maintained its extension throughout the study period, its water quality is evaluated from 1984 to 2009 (Figure 3). According to the zoning of the regional park, the Campillo lake is located in zone B, which is conservation zone. It has been included in the 'cataloged wetlands' by the Madrid regional government.

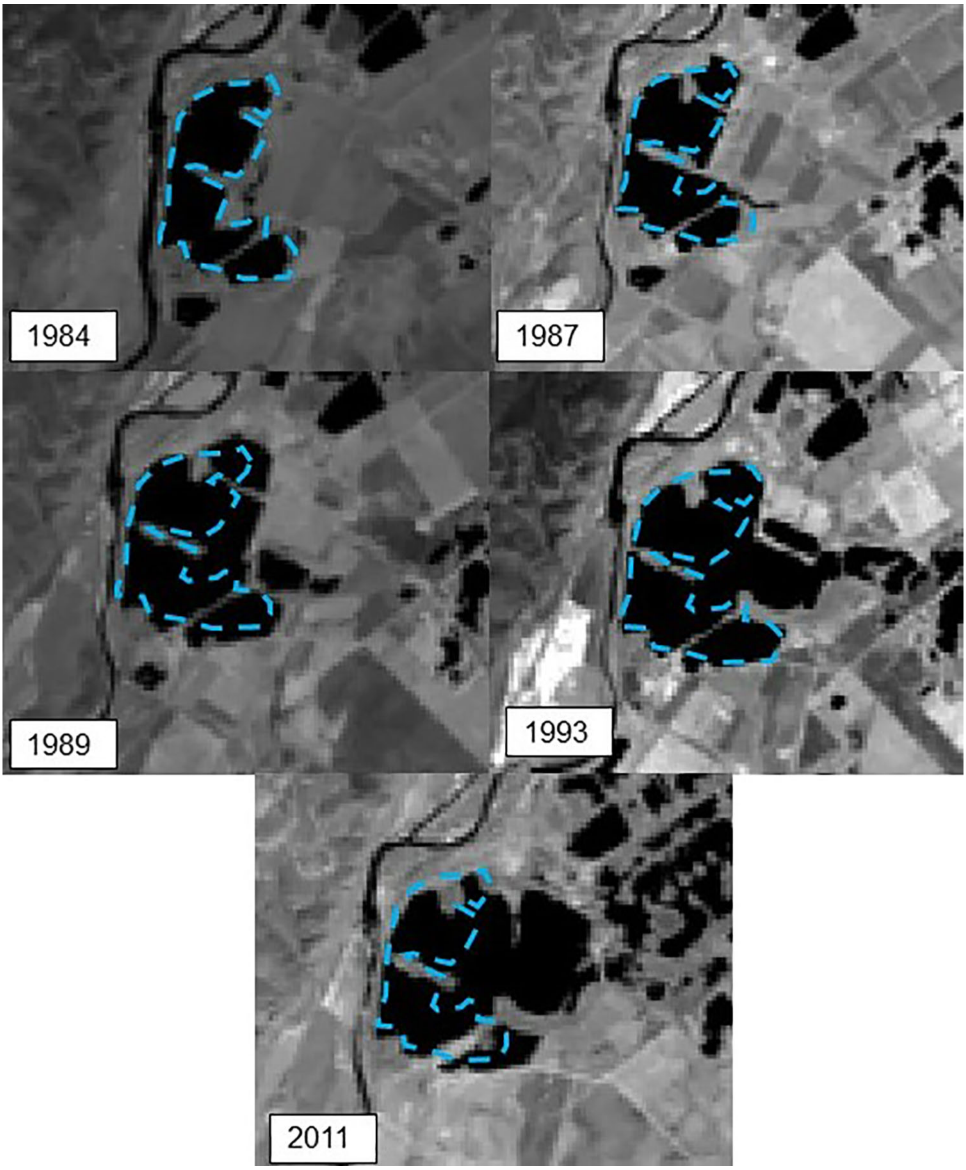

Figure 4. Porcal lake development from 1984 to 2011, with the assumed shape in this research (light blue dashed line).

The Porcal gravel pit pond

The Porcal lake has undergone changes throughout the time series of the present study (from 1984 to 2011). Therefore, the water quality study of this water body is only carried out in the area formed since 1984 (dashed blue line in Figure 4). Porcal lake is located in zone D, orderly exploitation of natural resources, according to the zoning of the regional park.

Soto de las Cuevas

Soto de las Cuevas lake was partially formed in 1984, but it was not until 1991 that it reached its current form (Figure 5). Therefore, the water quality study of this lake has

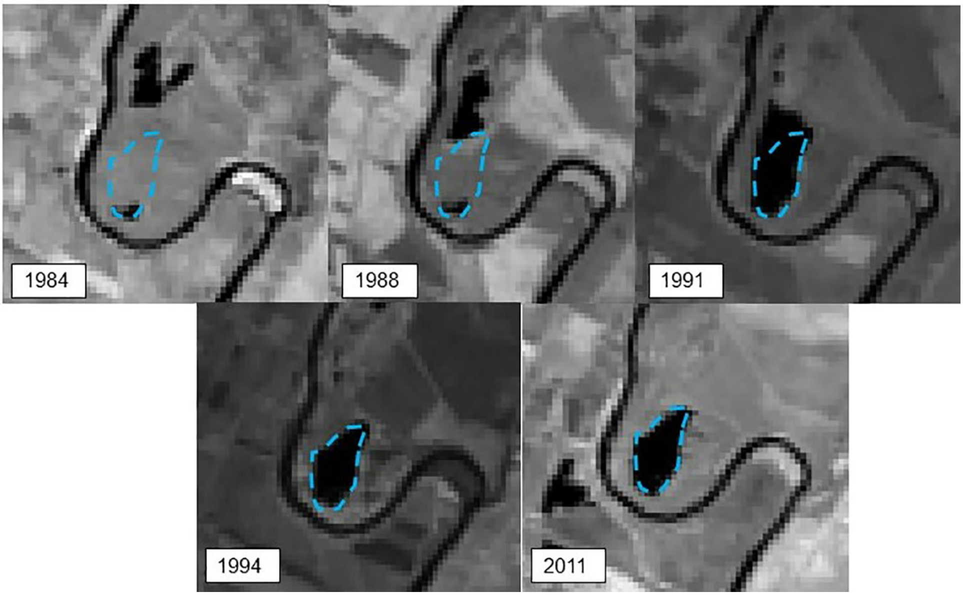

Figure 5. Soto de las Cuevas lake development from 1984 to 2011, with the assumed shape in this research (light blue dashed line).

been carried out since 1991. According to the zoning of the regional park, the Soto de las Cuevas lake is located in zone B, conservation area, and it is included in the 'cataloged wetlands' by the Madrid regional government.

Materials and methods

We analyzed the spatial and temporal water quality behavior of the gravel pit ponds through the retrieved SD values obtained from Landsat 5 satellite images and field data from 1984 to 2009 (Echavarría-Caballero et al. 2019).

One SD value per month was selected; despite having an image every 16 days (corresponding to the satellite revisit time), many of these images were covered by clouds and therefore no SD value was available.

The methodological process (Figure 6) includes the following phases: data preparation to fill in missing SD values, construction of the Hovmöller diagram, anomaly analysis, and EOF analysis. In the data preparation phase, once the monthly SD data has been sorted by date, the missing data is filled in and the monthly spatial–temporal data series of the SD is constructed for each studied water body. In the second phase, the Hovmöller diagram is prepared from the monthly spatial–temporal SD series to study the spatial and temporal evolution for each lake. In the third phase, the anomalies of the SD are calculated corresponding to the variation of each monthly data with respect to the mean of the entire series for each point; for each SD value, the mean over the whole time series at that point is subtracted from the SD. Then, the anomalies of the SD are analyzed at a spatial and temporal level, calculating the multiannual mean for each month. Finally, in the fourth phase, the EOF analysis is performed from the anomalies.

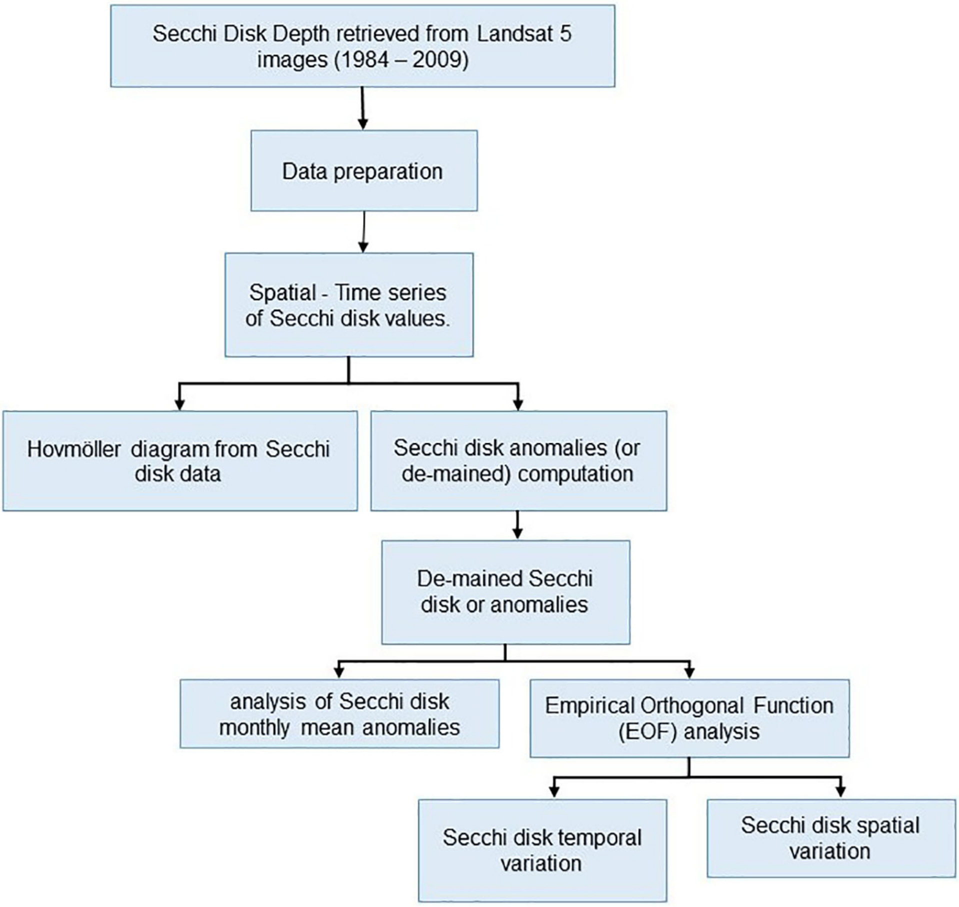

Figure 6. Flow chart of the research process.

Input data

In order to evaluate the spatial and temporal variations of water quality in the PRSE, the input data are the SD values since 1984 to 2011. These values were retrieved in a previous study (Echavarría-Caballero et al. 2019) from Landsat 5 images atmospherically corrected by the USGS with software LEDAPS.

The first step of the process of obtaining the SD values was the water pixel identification method to distinguish water and non-water information. In this step, we applied the normalized difference water index (NDWI) to every available Landsat 5 image in the area under consideration. Dynamic conditions in the study area can lead to misidentified water pixels; some bodies of water may disappear completely in some seasons, and water pixels can be confused with shadows and vegetation. Therefore, we took several steps to verify the water pixels. First, we tested the fit between the result classification and the field data—that is, sampling locations in the bodies of water should fall in areas classified as water by the analysis method. Second, to certify that only open water pixels were obtained, only water bodies greater than two pixels were selected. This step was appropriate because dubious water bodies (i.e. water bodies that could be shadows or vegetation) of two or fewer pixels occurred far more frequently than dubious water bodies of three or

Table 1. Evaluated MICE library methods.

Name	Description	RMSE
cart	**Classification and regression trees**	**0,48**
midastouch	Weighted predictive mean matching	0,49
pmm	Predictive mean matching	0,55

more pixels. Third, areas belonging to river and mountain zones were also discarded to dismiss shadows, given that the water bodies under consideration are located only in flat areas. Fourth, only water pixels in the whole period (1984 to 2011) were selected—that is, pixels that are classified as water 100% of the time (light blue dashed lines in Figures 2–5).

Then, we developed a new regression equation and validated it with the SD in situ measurements and reflectance measured in the sensor bands. Finally, the SD model developed was applied to every water image (images classified so that only water information is present in the images to certify that only water pixels were used) in order to assign each pixel an SD transparency value.

Data preparation

Given that spatial–temporal series assume that there is no gap in the data, missing data were filled prior to the analysis. In the first place, to complete isolated missing values, simple interpolation methods were used since there are no significant differences from the values obtained with other more complex methods such as regression (Mukadi and González-García 2021). In the interpolation method, a missing SD value at time t was completed with the mean of the data immediately before and after it (at times $t-1$ and $t+1$). Missing contiguous data values were completed with the average of the previous and subsequent years. The remaining missing data were filled in with the library multivariate imputation by chained equations (MICE) in R (van Buuren and Groothuis-Oudshoorn 2011).

To validate the results of the MICE method, we used the field data of Las Madres lake (also located in the PRSE) obtained by Álvarez-Cobelas et al. (2019) since there is monthly data since 1991. Some data were randomly eliminated in order to be completed with the different MICE methods. Then, the root-mean-square error (RMSE) (Table 1) was obtained. Finally, the method with the lowest RMSE was selected and used to complete the data for the Picón de los Conejos, Campillo, Porcal, and Soto de las Cuevas pit ponds.

Hovmöller diagram from SD data

Once the monthly spatial–temporal series of SD data were completed, longitude–time Hovmöller diagrams were generated to represent the temporal evolution of water transparency in each pit pond from May 1984 to December 2009. The Hovmöller diagram averages all the depth values of the SD in meters in a single column of longitude or latitude and places them on an axis. The other axis represents time.

SD anomalies (or de-meaned) computation

In order to analyze the temporal variations of the SD values, the anomalies are calculated as the subtraction of the mean of the entire time series of each point (or pixel) from each

SD value (Godah et al. 2018; Hannachi et al. 2007):

$$SDA_m(t) = SD_m(t) - \mu_m \tag{1}$$

where $SDA_m(t)$ corresponds to the SD anomaly at point m and time t $(1 \ldots n)$; $SD_m(t)$ is the SD value at point m and time t; and μ_m is the mean of the SDs of each series, i.e. the mean of the SDs at point m. It is calculated as follows:

$$\mu_m = \frac{\sum_{i=1}^{n} SD_m}{n} \tag{2}$$

where n is the number of dates to study, which is equivalent to the length of the time series.

Subsequently, we analyzed the SD anomalies. We calculated the multiannual monthly average of the anomalies at each point ($SDA\mu_m(x)$) for the months x = 1, 2, 3, … 12, as well as the multi-year monthly average of all the points $SDA\mu(x)$:

$$SDA\mu_m(x) = \frac{\sum_{i=1}^{n} SDA_m(x)}{n} \tag{3}$$

$$SDA\mu(x) = \frac{\sum_{i=1}^{n} SDA(x)}{n} \tag{4}$$

Empirical orthogonal function (EOF) analysis

To characterize the variability of the satellite-derived SD values, an EOF was performed on the SD data set over the entire time series (1984 to 2009). EOF analysis is a statistical technique used to decompose the spatial and temporal variability of time series data sets into a few independent dominant modes. Each mode represents a certain percentage of the total variance of the data set (Figure 7) (Chen et al. 2015; Weeks et al. 2012).

The EOF analysis was carried out with the anomalies of the SD (i.e. the variations of each value of the SD with respect to the mean of each point).

The data supporting the findings of this study are available from the corresponding author upon reasonable request.

Results and discussion

Hovmöller diagram from SD data

In the Hovmöller diagrams (Figure 8), the SD values are plotted for each east–west coordinate (on the horizontal axis) and time (on the vertical axis). The red lines located on the maps represent the minimum and maximum x coordinates, which is the area covered by the Hovmöller diagram.

Since the Hovmöller diagrams graphically represent the mean of all the pixels in the gravel pit pond for each east–west coordinate, it is difficult to distinguish any definite spatial pattern of the SD values in such small water bodies. However, the variations of the SD values over time are clearly observed. In general terms, the transparency of the water pit ponds has improved compared to the initial study period.

In the case of Campillo lake (Figure 8c), SD values less than 0.5 meters are observed between 1985 and 1994, followed by values between 0.5 and 1 meter in 1994 to 1998, and values above 1 meter after 1998. However, between 2007 and 2009, the SE values are again below 1 meter. In the case of Picón de los Conejos lake (Figure 8a), SD values of

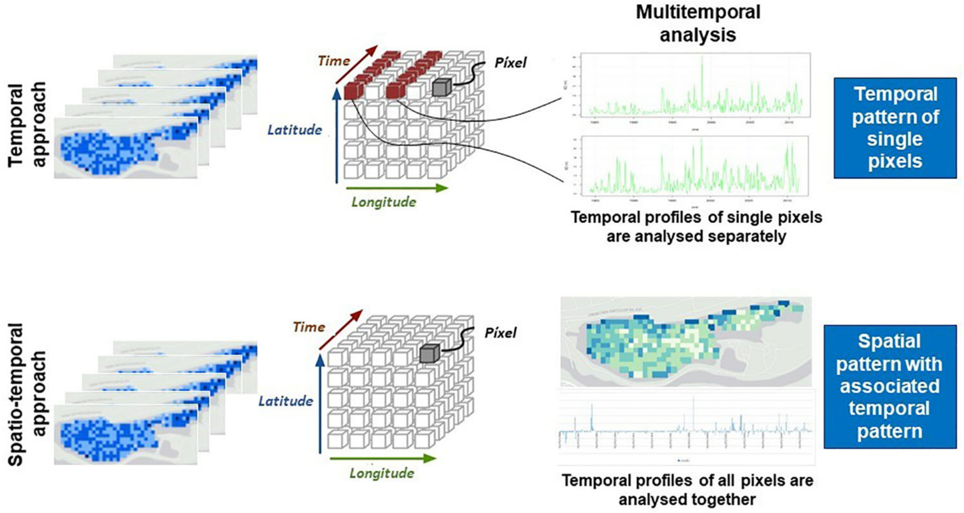

Figure 7. Overview of the time series analysis of variables using the temporal and spatio-temporal approaches.

less than 1 meter are observed not only from 1994 to 1999, but also in 2004 and from 2007 to 2009. In Porcal lake (Figure 8b) SD values of less than 1 meter are observed during the whole study period. Finally, in Soto de las Cuevas lake (Figure 8d), a period of low transparency (less than 1 meter) is observed from 1991 to 1994 and another from 2007 to 2009.

It is also visible that for the Campillo, Picón de los Conejos and Soto de las Cuevas lakes, the declaration of the regional park in 1994 had a positive impact on the water quality (Figures 8 and 9), since the SD values have increased. Nevertheless, Porcal lake shows the possible impact of anthropic activities since it is located in the area of orderly exploitation of natural resources according to the PRSE zoning.

The trophic OECD classifications of lakes are as follows: hypertrophic, with annual mean SD values less than 0.75 meters; eutrophic, with SD values between 0.75 and 1.5 meters; mesotrophic, with SD values between 1.5 and 3 meters; and oligotrophic, with SD values greater than 3 meters (Giardino et al. 2001; OCDE 1982). The annual SD mean value reveals how the trophic state of pit ponds in the PRSE has changed over the years (Figure 9). Porcal lake has been classified as hypertrophic or eutrophic during the whole study period. Picón de los Conejos was mesotrophic from 1999 to 2009 except in 2001, when the trophic state was hypertrophic and eutrophic. Campillo lake has fluctuated between hypertrophic (1984–1985; 1987; 1989–1992), eutrophic (1986; 1988; 1993–1996; 1998–2000; 2005–2007) and mesotrophic (1997; 2001–2004; 2008–2009) states. Finally, Soto de las Cuevas has been classified as mesotrophic since 1996 except the period from 2006 to 2008, when the trophic state was hypertrophic and eutrophic.

According to mean SD (Figure 9), the water quality in the studied pit ponds has improved slowly since the area was declared as protected in 1994, although the ponds have not reached the oligotrophic state. There is no significant difference between the SD values of the water bodies, although Porcal has improved the least. This outcome agrees with Shevenell et al. (1999), who concluded that water quality in some pits may improve with time once exploitation ends. Given that little is known about the development of these lake ecosystems following extraction activities, further research is necessary to confirm this tendency.

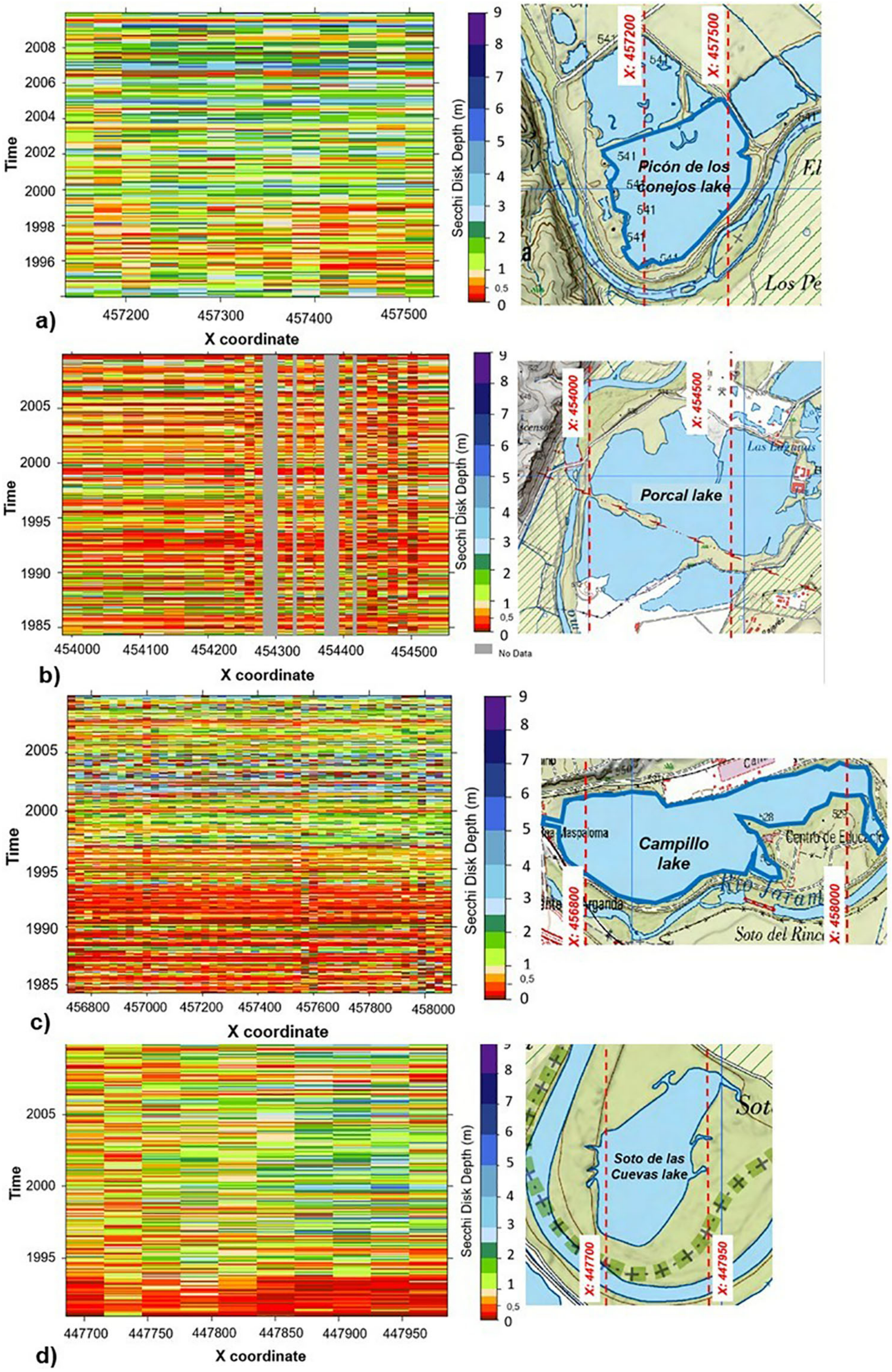

Figure 8. Hovmöller diagrams for (a) Picón de los Conejos; (b) Porcal; (c) Campillo and (d) Soto de las Cuevas lakes.

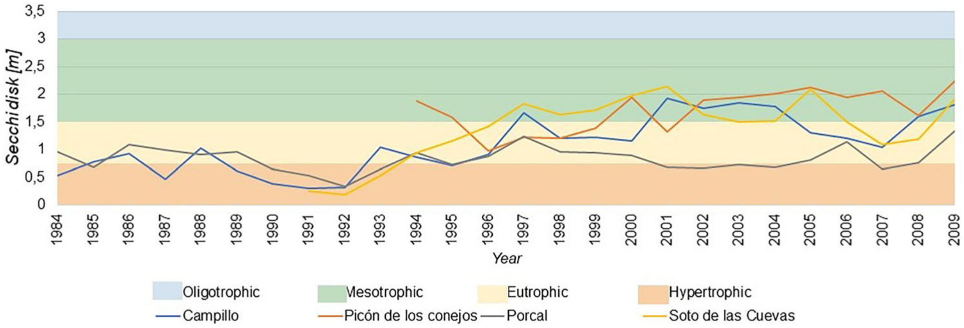

Figure 9. Secchi disk annual means for each gravel pit pond and trophic OECD classifications.

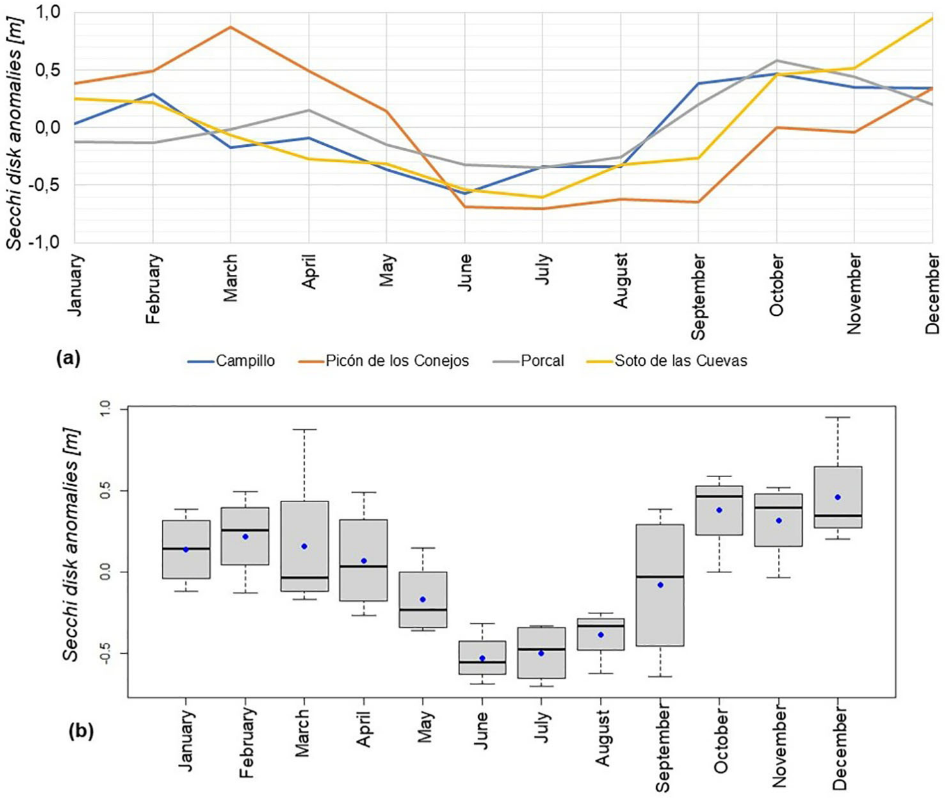

Figure 10. (a) Monthly evolution of Secchi disk anomalies; b) box plot with the mean (blue points), minimum, maximum, median, first quartile, and third quartile.

These findings are relevant as they become a right tool for decision-makers to guarantee that administrative protection figures are effective to assure the sustainable management of these ecosystems. Also, this research provides the necessary data to program and plan improvement actions to comply with the Water Framework Directive (EC 2000), which requires that all water bodies must achieve good ecological status and have not been carried out in PRSE.

Monthly analysis of Secchi disk anomalies

The analysis of multi-year monthly mean anomalies of the SD values of all points (Figure 10a) allows two periods to be distinguished: a peak in autumn and winter (September–February) when the SD values are greater than the mean and a period in summer (May–August) when the SD values are lower than the mean. These results agree with Castagna et al. (2015), Naumenko (2008), Rodrigo et al. (2015), and Ziauddin et al. (2013), who concluded that when the water becomes warmer, the water transparency decreases. This trend primarily reflects the level of development of biological communities and charophyte biomass, given that the photosynthetically active radiation reaches its maximum during the warmest months.

The seasonal behavior of the water bodies has little dispersion in the months of January, June, July, and August (Figure 10b). This behavior, similar in the different studied pit ponds, can be explained by the relationship between SD and temperature, given that SD is affected by two primary factors: the lake algae and suspended particulate matter (Pal & Chakraborty, 2014). These results are of great interest for the ecological management of gravel pit ponds or artificial pit ponds. Moreover, they are in agreement with other investigations such as those of lake Ladoga (Naumenko 2008) or Indian floodplain wetlands (Ziauddin et al. 2013), where equivalent results were obtained despite very different environmental conditions. The same type of environmental behavior is also observed in the case of the small shallow basin created and flooded with groundwater in a reserve area in Albufera de Valencia Natural park under the scope of a restoration program (Rodrigo et al. 2015). Global radiation and temperature increase from December to June, with maximum values in July and minimum values in December (Agencia Estatal de Meteorología de España 2017). This behavior is completely inverse to that of the SD values, where the values are lowest in July–August and highest in December–January (Figure 11).

The multiannual monthly average for each pixel shows the same seasonal trends. For example, in the Campillo water pit pond, the abrupt changes occur in May and September (Figure 12). During this period, temperatures rise from 15 °C to 20 °C and solar radiation from 2,000 to 2,500 10 KJ/m^2. After September, temperatures fall below 20 °C and radiation decreases below 2,000 10 KJ/m^2 (Figure 11). No particular spatial pattern is observed.

Magnitude of change

We analyzed the magnitude or breadth of change of the SD for each pixel (Figure 13) calculated as the difference between the minimum and maximum SD values throughout the time series studied. It was observed that in Picón de los Conejos (Figure 13a) and Soto de las Cuevas (Figure 13d), pixels with a breadth of change between 5.7 and 8 meters are very frequent. In contrast, in Porcal lake (Figure 13b), there are no pixels with this amplitude, whereas the most frequent amplitudes are less than 4.6 meters. In the case of Campillo (Figure 13c), in areas whose depth is about 20 meters, the amplitude of the change in SD is less than 5.7 meters.

In general terms, in Porcal lake there are small fluctuations (i.e. in small ranges), while in practically the whole area of Soto de las Cuevas, Picón de los Conejos, and in specific places in Campillo there are extreme variations of more than 5.7 meters. It can be inferred that this is related to the depth of the lake, since fluctuations are smaller in deeper areas.

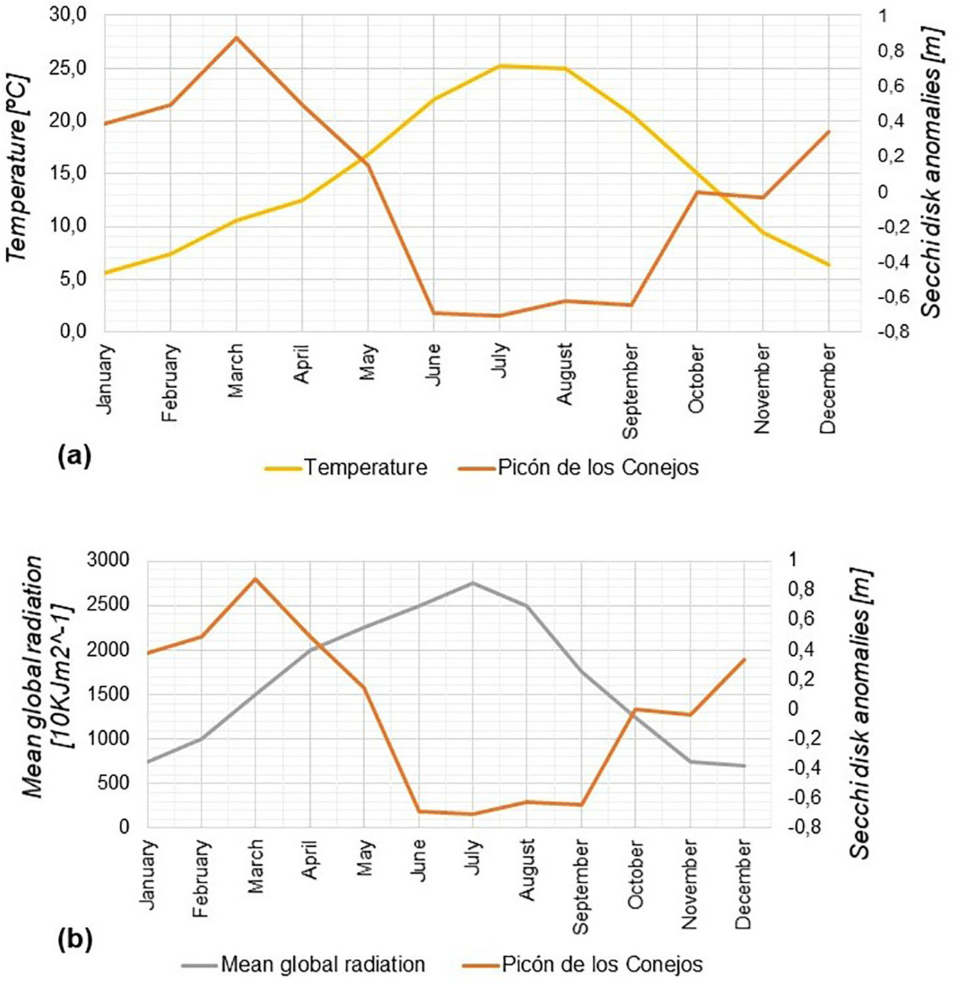

Figure 11. Monthly evolution of Secchi disk Picón de los Conejos anomalies compared with (a) air temperature and (b) global radiation.

The behavior of Picón de los Conejos and Porcal lakes is different. These water bodies present fluctuations distributed over their entire surface, as well as very widespread spatial patterns of variability. This may be due to human intervention. Quality recovery actions are being carried out in Picón de los Conejos, while the exploitation of aggregates continues in Porcal.

Water quality variation in the studied time period

In the EOF anomalies analysis, Mode 1 explains 59.4%, 70.4%, 77.8%, and 82.6% of the spatial and temporal variability of the series for the Campillo, Picón de los Conejos, Porcal, and Soto de las Cuevas lakes, respectively.

Figure 14 shows the coefficients of each pixel for Mode 1 since this mode explains a large percentage of the variability for each water pit pond. The values that most influence the Mode 1 behavior are shown in dark blue. It can be inferred that the deeper areas have the most influence on the behavior of the time series, while the shallower areas (edges) have the least influence.

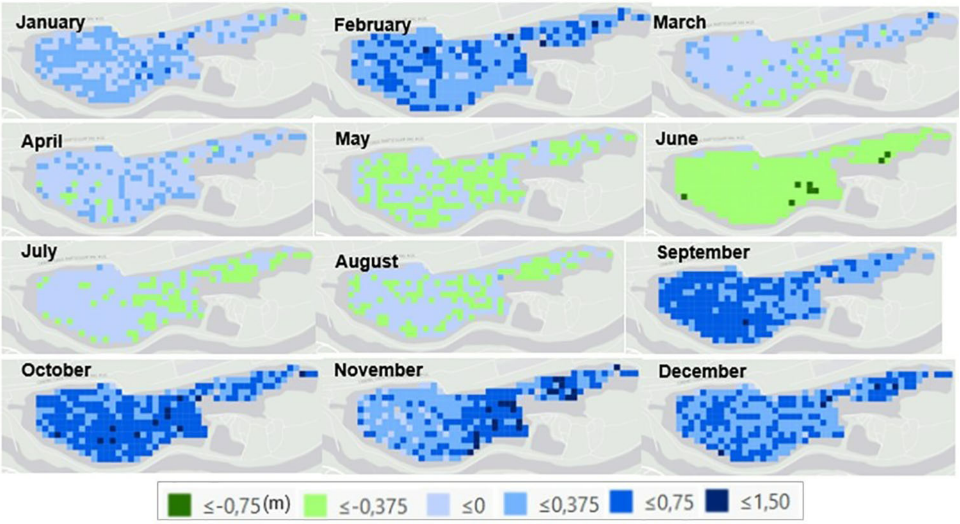

Figure 12. Monthly spatial evolution of Secchi disk anomalies in the Campillo water pit pond.

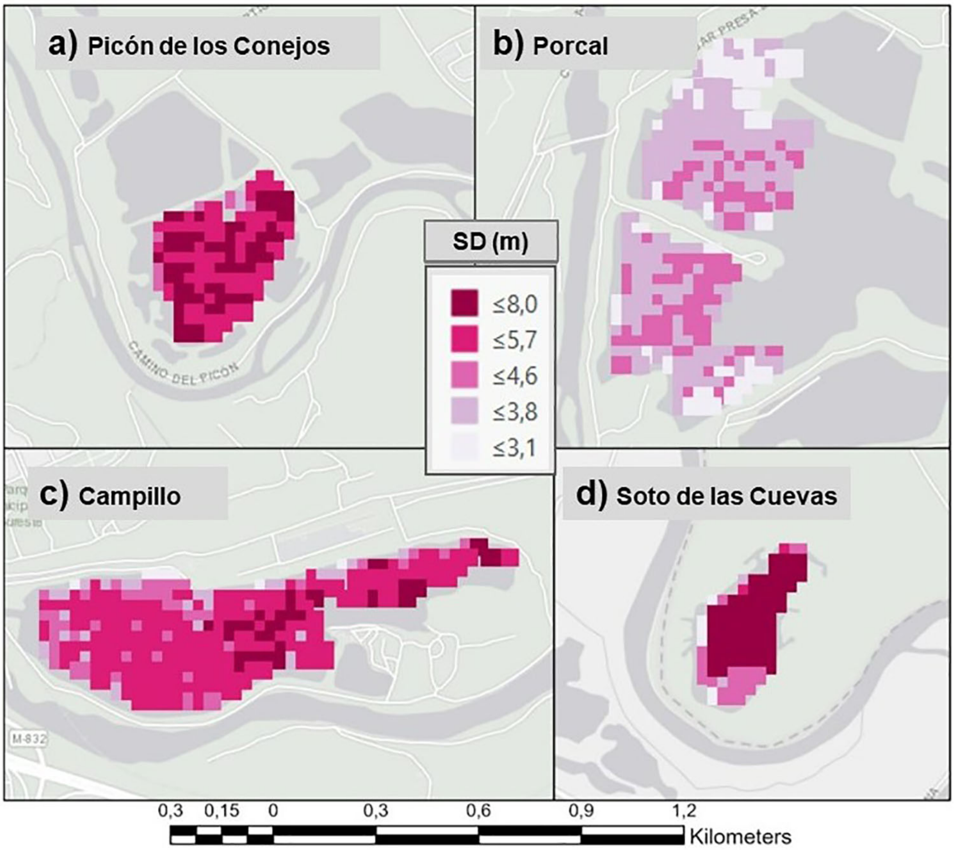

Figure 13. Magnitude of change of the Secchi disk for each pixel throughout the studied time series (1984–2009) for (a) Picón de los Conejos; (b) Porcal; (c) Campillo and (d) Soto de las Cuevas lakes.

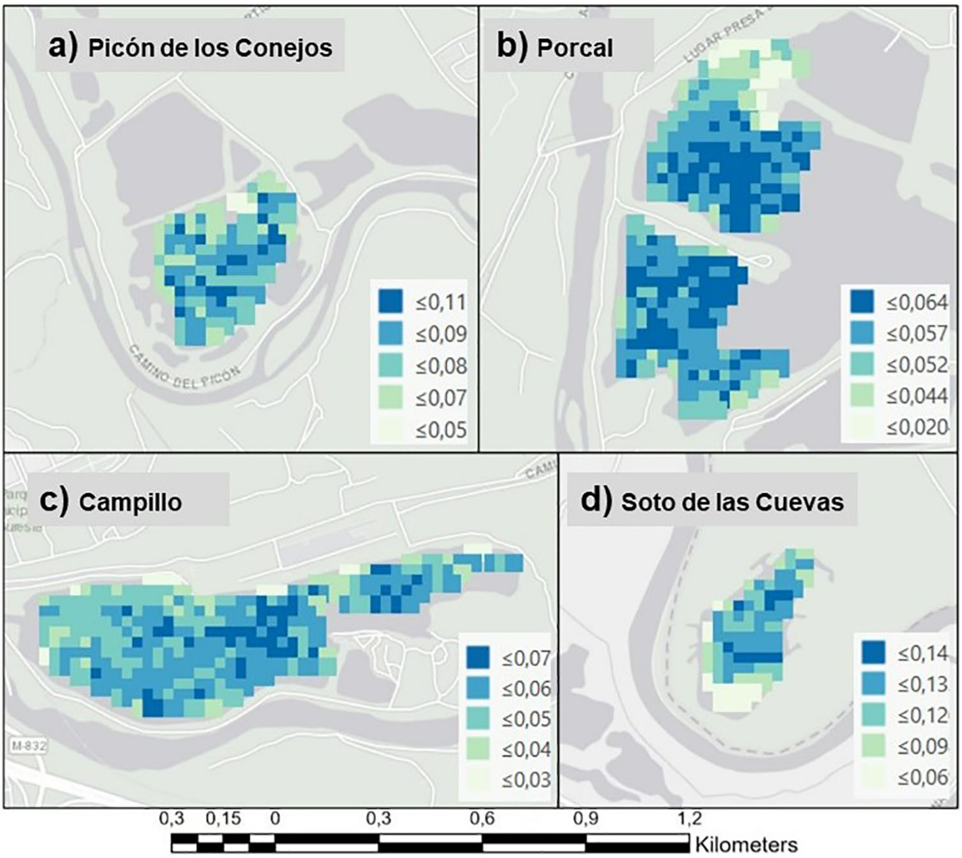

Figure 14. Mode 1 spatial variability of EOF analysis for (a) Picón de los Conejos; (b) Porcal; (c) Campillo and (d) Soto de las Cuevas lakes.

The pixels that most influence the behavior of the water pit ponds, which are in deeper areas and have a greater range of variation (Figure 13), are those that determine the general behavior of the lake. The geometry of the water pit ponds can condition their ecological evolution; as explained by Søndergaard et al. (2018), lakes with a large hypolimnion (deep area) are usually less susceptible to eutrophication than fully mixed shallow lakes. Moreover, Castagna et al. (2015) showed that lakes with a larger depth and volume generally have a lower tendency toward eutrophication.

In addition, we analyzed the temporal behavior associated with the spatial pattern (Figure 15). In this case, the bars represent the coefficient of each date for Mode 1, which explains a large percentage of the variability; the largest values represent dates that have had a greater influence on the Mode 1 behavior. In the cases of Picón de los Conejos (Figure 15a) and Porcal (Figure 15b), Mode 1 is explained—or, more fundamentally, influenced—by what has happened in recent years (larger bars), possibly reflecting human intervention in these pit ponds. On the other hand, for Campillo (Figure 15c) and Soto de las Cuevas (Figure 15d), the influence is distributed throughout the entire series with no apparent trends.

In the Porcal and Soto de las Cuevas lakes, punctual events happen throughout the series that further condition the evolution of the water pit ponds, but a seasonal temporal pattern is not observed. Therefore, the autocorrelation function (ACF) is analyzed to determine if there is any temporal pattern.

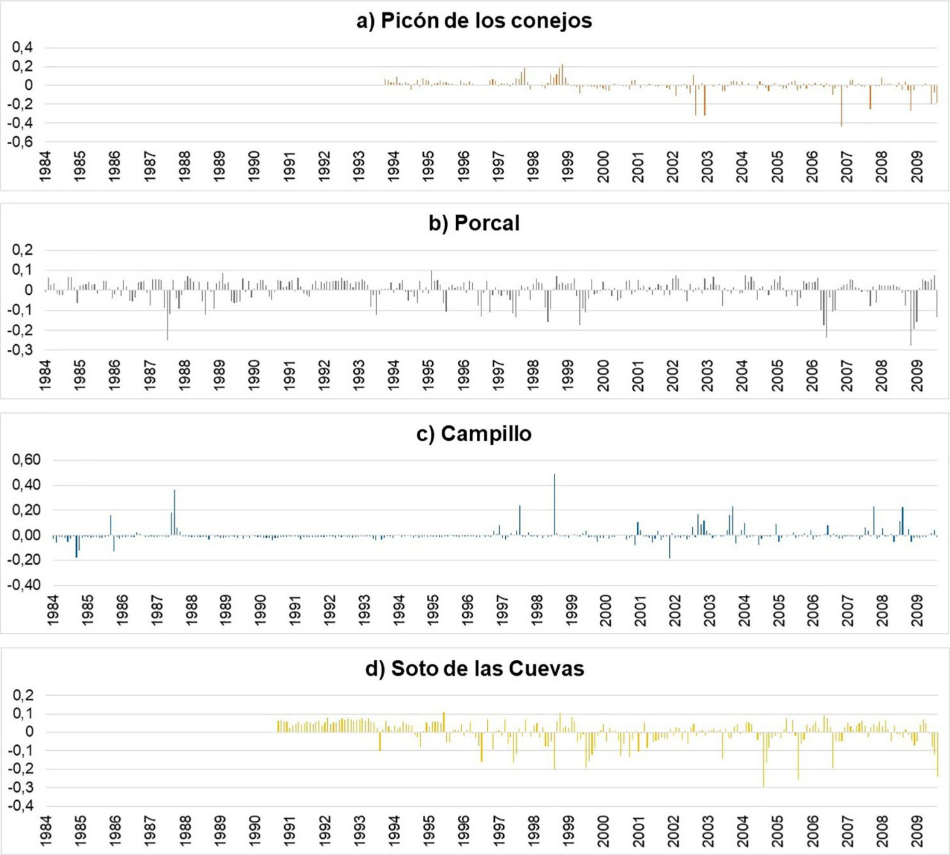

Figure 15. Mode 1 temporal variation of EOF analysis for (a) Picón de los Conejos; (b) Porcal; (c) Campillo and (d) Soto de las Cuevas lakes; the date where the year is located corresponds to May 1 for each year.

Figure 16 shows the Mode 1 autocorrelations for each studied gravel pit pond. In the case of Campillo (Figure 16c), the autocorrelations indicate a small autocorrelation around 12 and 40 lags. In Picón de los Conejos (Figure 16a), a small autocorrelation is visible in lags 10, 24, and 33. Therefore, it can be deduced that a behavior pattern is not observed in the series after 12 months. In the case of Porcal (Figure 16b) and Soto de las Cuevas (Figure 16d), the values of the SD show temporal variation with seasonality.

Practical applications

In this study, we analyzed the temporal trends and spatial distributions of water quality in water pit ponds in the PRSE by using long-term time series of water transparency retrieved by remote sensing. This technique allows the monitoring of the quality of water bodies according to the WFD (EC 2000) at low cost compared with field campaigns. As most of these water bodies are located on private lands and are therefore inaccessible, this methodology makes long-term monitoring possible. Therefore, we can also evaluate the impact of administrative and territorial planning actions, such as the 1994 declaration of a regional park.

In addition, this research has allowed us to understand whether gravel pit ponds can be compared to natural lakes in terms of seasonal behavior and the physical drivers that

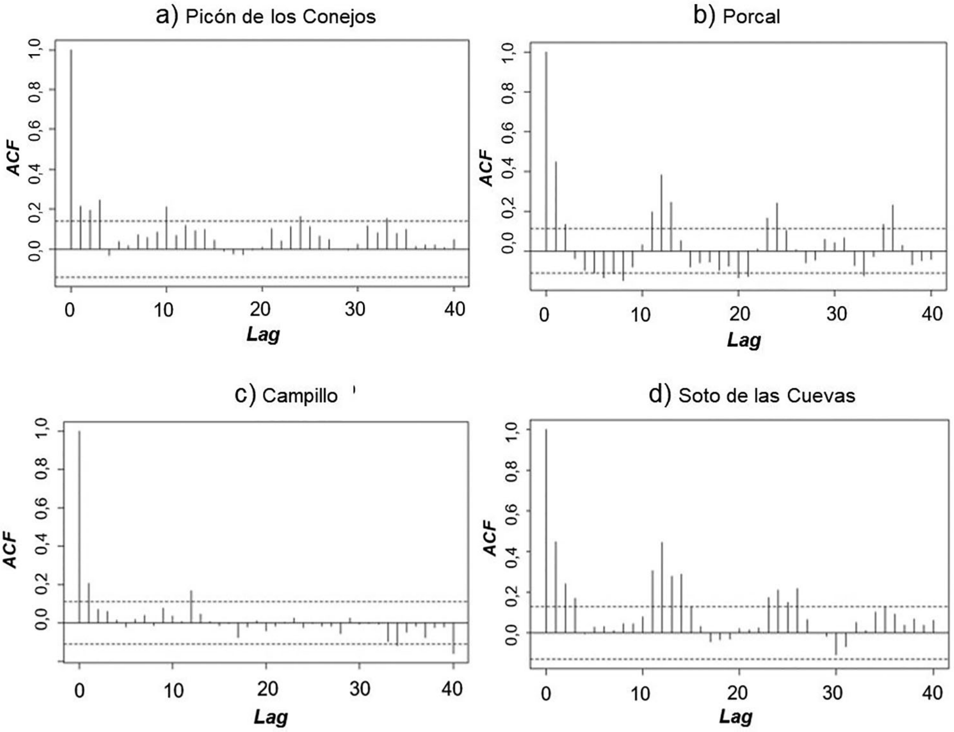

Figure 16. Autocorrelation function of temporal variation mode 1. (a) Picón de los Conejos; (b) Porcal; (c) Campillo and (d) Soto de las Cuevas lakes.

influence transparency, as well as to assess their ecological evolution. The environmental changes in relation to climate change can also be studied and analyzed. Therefore, this methodology is an excellent tool to support decision-making about land use practice restrictions according to the Planning and Management Plan in Protected Natural Areas of PRSE or the remedial actions to be carried out for the environmental improvement and sustainability of these ecosystems.

It is very important to have a reliable, accessible, and low-cost tool for the environmental monitoring and management of areas affected by mining activity, which remain active for many years in the metropolitan areas of large, growing cities around the world. In the case of Madrid and also in other Spanish cities, the environmental concern for this type of space is relevant (Vucic et al. 2019) due to the scarcity of aquatic ecosystems, their high environmental value, and the social importance they acquire in highly populated areas (Seelen et al. 2021).

The development of satellites with increasing spatial and temporal precision offers an enormous opportunity, which we can take advantage of by adopting the proposed methodology.

Conclusions

In this study, we examined the temporal and spatial patterns of water quality using the parameter of transparency in the Campillo, Picón de los Conejos, Porcal, and Soto de las Cuevas gravel pit ponds in the PRSE in a period of 25 years (1984–2009) using time series from Landsat 5 images.

This study highlights seasonal behavior in the water quality, with higher Secchi disk values in autumn and winter (December–February) and lower values in summer (July–August). This behavior can be explained by the relationship between SD and temperature and solar radiation.

We also used Hovmöller diagrams and the SD annual mean to show that the declaration of the Regional park in 1994 has had a positive impact on the quality of the water, since the values of the SD have increased in Campillo, Picón de los Conejos, and Soto de las Cuevas pit ponds. In contrast, the Porcal pit pond showed uniform SD values throughout the study period; this pond has been impacted by anthropic activities since it is located in the area of orderly exploitation of natural resources, according to the PRSE zoning. Furthermore, transparency (measured as SD depth) has improved compared to the initial study period in the four studied pit ponds. Also, the trophic state of the studied pit ponds has slowly improved, though it has not reached the oligotrophic state: Campillo, Picón de los Conejos, and Soto de las Cuevas have been between the eutrophic and mesotrophic states, while Porcal has been eutrophic.

According to the EOF analysis, the pixels that most influence the behavior of the pit ponds are in deeper areas and have a greater range of variation. This suggests that the geometry of the pit ponds can condition their ecological evolution. Concerning the temporal variation, in the case of Picón de los Conejos and Porcal, the variability has been more fundamentally influenced by recent developments. On the other hand, for Soto de las Cuevas and Campillo, the influence is distributed throughout the entire series without apparent trends.

This methodology elucidates the behavior of the transparency and water quality of gravel pit ponds in spatial and temporal terms. Therefore, it can be used to evaluate how previously implemented strategies have affected water quality and the ponds' subsequent evolution toward sustainable ecosystems.

Furthermore, this methodology can be replicated with different satellite platforms, including the ESA's new Copernicus program. Potential future applications include (i) identifying and quantifying future changes in water quality as a result of land use practice changes or other environmental changes such as climate change and (ii) comparing the obtained SD time series with levels of gravel extraction or environmental variables such as temperature or precipitation. This will allow a better understanding of the evolution of these artificial ecosystems, allowing better medium- and long-term management.

Acknowledgments

We thank to Dr. Álvarez Cobelas for providing Secchi disk field data. This research did not receive any specific grant from funding agencies in the public, commercial, or not-for-profit sectors. There are no relevant financial or non-financial competing interests to report.

Disclosure statement

No potential conflict of interest was reported by the authors.

References

Agencia Estatal de Meteorología de España. 2017. Informe de radiación solar. https://www.bing.com/search?q=Agencia+Estatal+de+Meteorolog%C3%ADa+de+Espa%C3%B1a.+(2017).+Informe+de+radiaci%C3%B3n+solar.+Madrid&cvid=60ab20a244d74436813cfd9e0d10aef7&aqs=edge.69i57.259j0j4&pglt=2083&FORM=ANAB01&PC=LGTS.

Álvarez-Cobelas M, Rubio A, Arauzo M, Alarcón P, Limnética VA. 1987. Morfometria y composición química de una laguna de gravera. Limnetica.Net. http://www.limnetica.net/documentos/limnetica/limnetica-3-1-p-91.pdf.

Álvarez-Cobelas M. 1991. Optical limnology of a hypertrophic gravel-pit lake. Int Revue Ges Hydrobiol Hydrogr. 76(2):213–223. https://doi.org/10.1002/iroh.19910760206.

Álvarez-Cobelas M, Rojo C, Benavent-Corai J. 2019. Long-term phytoplankton dynamics in a complex temporal realm. Sci Rep. 9(1):15967. https://doi.org/10.1038/s41598-019-52333-z.

Álvarez-Cobelas M. 2000. *Estudio físico-químico de los ambientes estancados del Parque Regional del Sureste de la Comunidad de Madrid*. Centro de Investigaciones Ambientales de la Comunidad de Madrid "Fernando González Bernáldez."

Andrews J. 1990. Principles of restoration of gravel pits for wildlife. Br Wildlife. 2(2):80–88. https://doi.org/10.1016/0006-3207(92)91240-s.

Beltrán-Abaunza JM, Kratzer S, Höglander H. 2017. Using MERIS data to assess the spatial and temporal variability of phytoplankton in coastal areas. Int J Remote Sens. 38(7):2004–2028. https://doi.org/10.1080/01431161.2016.1249307.

Blanchet CC, Arzel C, Davranche A, Kahilainen KK, Secondi J, Taipale S, Lindberg H, Loehr J, Manninen-Johansen S, Sundell J, et al. 2022. Ecology and extent of freshwater browning – What we know and what should be studied next in the context of global change. Sci Total Environ. 812:152420. https://doi.org/10.1016/J.SCITOTENV.2021.152420.

Boucher J, Weathers KC, Norouzi H, Steele B. 2018. Assessing the effectiveness of Landsat 8 chlorophyll a retrieval algorithms for regional freshwater monitoring. Ecol Appl. 28(4):1044–1054. https://doi.org/10.1002/eap.1708

Bracher A, Xi H, Dinter T, Mangin A, Strass V, von Appen WJ, Wiegmann S. 2020. High resolution water column phytoplankton composition across the Atlantic ocean from ship-towed vertical undulating radiometry. Front Mar Sci. 7:235. https://doi.org/10.3389/fmars.2020.00235

Castagna SED, de Luca DA, Lasagna M. 2015. Eutrophication of piedmont quarry lakes (North-Western Italy): hydrogeological factors, evaluation of trophic levels and management strategies. J Environ Assess Pol Manag. 17(04):1550036. https://doi.org/10.1142/S1464333215500362

Chao Rodríguez Y, el Anjoumi A, Domínguez Gómez JA, Rodríguez Pérez D, Rico E. 2014. Using Landsat image time series to study a small water body in Northern Spain. Environ Monit Assess. 186(6): 3511–3522. https://doi.org/10.1007/s10661-014-3634-8

Chen Z, Zhang SR, Coster AJ, Fang G. 2015. EOF analysis and modeling of GPS TEC climatology over North America. J Geophys Res Space Phys. 120(4):3118–3129. https://doi.org/10.1002/2014JA020837

Chu HJ, Kong SJ, Chang CH. 2018. Spatio-temporal water quality mapping from satellite images using geographically and temporally weighted regression. Int J Appl Earth Obs Geoinf. 65:1–11. https://doi.org/10.1016/J.JAG.2017.10.001

Comunidad de Madrid. 2020. *Plan de Actuación sobre Humedales Catalogados de la Comunidad de Madrid. Madrid* – Bing. https://www.bing.com/search?q=Plan+de+Actuaci%C3%B3n+sobre+Humedales+Catalogados+de+la+Comunidad+de+Madrid.+Madrid&qs=n&form=QBRE&msbsrank=0_0__0&sp=-1&pq=plan+de+actuaci%C3%B3n+sobre+humedales+catalogados+de+la+comunidad+de+madrid.+madrid&sc=0-79&sk=&cvid=1790048BAEA54D62B99D5E207A1741E4.

Cressie N, Wikle C. 2015. *Statistics for spatio-temporal data*. https://books.google.com/books?hl=es&lr=&id=4L_dCgAAQBAJ&oi=fnd&pg=PP1&ots=idWU3BNn0-&sig=itYykh_C0wyLAKxBD5PUlXtyuR8.

Delasalles E, Ziat A, Denoyer L, Gallinari P. 2019. Spatio-temporal neural networks for space-time data modeling and relation discovery. Knowl Inf Syst. 61(3):1241–1267. https://doi.org/10.1007/S10115-018-1291-X/TABLES/5

Devlin MJ, Petus C, da Silva E, Tracey D, Wolff NH, Waterhouse J, Brodie J. 2015. Water quality and river plume monitoring in the Great Barrier Reef: an overview of methods based on ocean colour satellite data. Remote Sens. 7(10):12909–12941. https://doi.org/10.3390/RS71012909

Díaz JMC, Araujo JM. 2017. Historic urbanization process in Spain (1746–2013): from the fall of the American empire to the real estate bubble. J Urban Hist. 43(1):33–52. https://doi.org/10.1177/0096144215583481

Domínguez Gómez JA, Chuvieco Salinero E, Sastre Merlín A. 2009. Monitoring transparency in inland water bodies using multispectral images. Int J Remote Sens. 30(6):1567–1586. https://doi.org/10.1080/01431160802513811

Domínguez Gómez JA, Peña R. 1999. Trophic state assessment in two gravel pits (El Campillo & El Porcal) using airborne imagery. Limnetica.16(1).

EC. 2000. Directive 2000/60/EC of the European Parliament and of the Council of 23 October 2000 establishing a framework for Community action in the field of water policy. Off J Eur Parliam. :1–73.

Echavarría-Caballero C, Domínguez-Gómez JA, González-García C, García-García MJ. 2019. Assessment of Landsat 5 images atmospherically corrected with LEDAPS in water quality time series. Can J Remote Sens. 45(5):691–706. https://doi.org/10.1080/07038992.2019.1674136

el Serafy GYH, Schaeffer BA, Neely MB, Spinosa A, Odermatt D, Weathers KC, Baracchini T, Bouffard D, Carvalho L, Conmy RN, et al. 2021. Integrating inland and coastal water quality data for actionable knowledge. Remote Sens. 13(15):2899. https://doi.org/10.3390/RS13152899

Giardino C, Pepe M, Brivio PA, Ghezzi P, Zilioli E. 2001. Detecting chlorophyll, Secchi disk depth and surface temperature in a sub-alpine lake using Landsat imagery. Sci Total Environ. 268(1–3):19–29. https://doi.org/10.1016/S0048-9697(00)00692-6

Godah W, Szelachowska M, Krynski J. 2018. Application of the PCA/EOF method for the analysis and modelling of temporal variations of geoid heights over Poland. Acta Geod Geophys. 53(1):93–105. https://doi.org/10.1007/s40328-017-0206-8

Hannachi A, Jolliffe IT, Stephenson DB. 2007. Empirical orthogonal functions and related techniques in atmospheric science: a review. Int J Climatol. 27(9):1119–1152. https://doi.org/10.1002/joc.1499

Hestir EL, Brando VE, Bresciani M, Giardino C, Matta E, Villa P, Dekker AG. 2015. Measuring freshwater aquatic ecosystems: the need for a hyperspectral global mapping satellite mission. Remote Sens Environ. 167:181–195. https://doi.org/10.1016/j.rse.2015.05.023

Hicks BJ, Stichbury GA, Brabyn LK, Allan MG, Ashraf S. 2013. Hindcasting water clarity from Landsat satellite images of unmonitored shallow lakes in the Waikato region. New Zealand Environ Monit Assess. 185(9):7245–7261. https://doi.org/10.1007/s10661-013-3098-2

Kim SE, Seo IW, Choi SY. 2017. Assessment of water quality variation of a monitoring network using exploratory factor analysis and empirical orthogonal function. Environ Modell Software. 94:21–35. https://doi.org/10.1016/j.envsoft.2017.03.035

Kim SH, Yang CS, Ouchi K. 2015. Spatio-temporal patterns of Secchi depth in the waters around the Korean Peninsula using MODIS data. Estuarine Coastal Shelf Sci. 164:172–182. https://doi.org/10.1016/j.ecss.2015.07.003

Li X, Yang C, Zhang H, Wang P, Tang J, Tian Y, Zhang Q. 2021. Identification of abandoned Jujube fields using multi-temporal high-resolution imagery and machine learning. Remote Sens. 13(4):801. https://doi.org/10.3390/rs13040801

Liew SC, Chia AS, Kwoh LK. 2010. Spatio-temporal variability of precipitation in Southeast Asia analyzed using the empirical orthogonal function (EOF) technique. International Geoscience and Remote Sensing Symposium (IGARSS), 4701–4704.

Liu D, Yu SJ, Xiao QT, Qi TC, Duan HT. 2021. Satellite estimation of dissolved organic carbon in eutrophic Lake Taihu, China. REMOTE Sens Environ. 264:112572. https://doi.org/10.1016/j.rse.2021.112572

Lobo F, de L, Nagel GW, Maciel DA, de Carvalho LAS, Martins VS, Barbosa CCF, de Moraes Novo EML. 2021. Algaemap: algae bloom monitoring application for inland waters in Latin America. Remote Sens. 13(15):2874. https://doi.org/10.3390/RS13152874

López-Andreu FJ, Erena M, Dominguez-Gómez JA, López-Morales JA. 2021. Sentinel-2 images and machine learning as tool for monitoring of the common agricultural policy: Calasparra rice as a case study. Agronomy. 11(4):621. https://doi.org/10.3390/AGRONOMY11040621

Maeda EE, Lisboa F, Kaikkonen L, Kallio K, Koponen S, Brotas V, Kuikka S. 2019. Temporal patterns of phytoplankton phenology across high latitude lakes unveiled by long-term time series of satellite data. Remote Sens Environ. 221:609–620. https://doi.org/10.1016/j.rse.2018.12.006

Mollema P, Antonellini M, Gabbianelli G, Laghi M, Marconi V, Minchio A. 2012. Climate and water budget change of a Mediterranean coastal watershed, Ravenna, Italy. Environ Earth Sci. 65(1):257–276. https://doi.org/10.1007/s12665-011-1088-7

Mollema P, Antonellini M. 2016. Water and (bio)chemical cycling in gravel pit lakes: a review and outlook. Earth-Sci Rev. 159:247–270. https://doi.org/10.1016/j.earscirev.2016.05.006

Mollema P, Stuyfzand P, Juhász-Holterman MHA, van Diepenbeek PMJA, Antonellini M. 2015. Metal accumulation in an artificially recharged gravel pit lake used for drinking water supply. J Geochem Explor. 150:35–51. https://doi.org/10.1016/j.gexplo.2014.12.004

Moreno N, García-Avilés J. 1997. *Valoración ambiental y caracterización de los ecosistemas acuáticos leníticos del Parque Regional en torno a los ejes de los cursos bajos de los ríos*. https://www.researchgate.net/profile/Javier-Garcia-Aviles/publication/297387060_Valoracion_ambiental_y_caracterizacion_de_los_ecosistemas_acuaticos_leniticos_del_Parque_Regional_en_torno_a_los_ejes_de_los_cursos_bajos_de_los_rios_Manzanares_y_Jarama/links/56deb0c408ae46f1e9a0e3eb/Valoracion-ambiental-y-caracterizacion-de-los-ecosistemas-acuaticos-leniticos-del-Parque-Regional-en-torno-a-los-ejes-de-los-cursos-bajos-de-los-rios-Manzanares-y-Jarama.pdf.

Mostaza-Colado D, Carreño-Conde F, Rasines-Ladero R, Iepure S. 2018. Hydrogeochemical characterization of a shallow alluvial aquifer: 1 baseline for groundwater quality assessment and resource management. Sci Total Environ. 639:1110–1125. https://doi.org/10.1016/j.scitotenv.2018.05.236

Mukadi PM, González-García C. 2021. Time series analysis of climatic variables in peninsular spain. trends and forecasting models for data between 20th and 21st centuries. Climate 2021. 9(7):119. https://doi.org/10.3390/CLI9070119

Nas B, Ekercin S, Karabörk H, Berktay A, Mulla DJ. 2010. An application of landsat-5TM image data for water quality mapping in Lake Beysehir, Turkey. Water Air Soil Pollut. 212(1–4):183–197. https://doi.org/10.1007/s11270-010-0331-2

Naumenko MA. 2008. Seasonality and trends in the Secchi disk transparency of Lake Ladoga. Hydrobiologia. 599(1):59–65. https://doi.org/10.1007/s10750-007-9198-7

OCDE. 1982. OECD: eutrophication of waters. monitoring, assessment and control. 154pp Paris: organisation for economic co-operation and development 1982. Int Revue Der Gesamten Hydrobiol Und Hydrograph. 69(2):200.

Pal S, Chakraborty K. 2014. Importance of some physical and chemical characteristics of water bodies in relation to the incidence of zooplanktons: a review. Indian Journal of Social and Natural Sciences. 3: 102–116.

Paltsev A, Creed IF. 2021. Are northern lakes in relatively intact temperate forests showing signs of increasing phytoplankton biomass? Ecosystems. https://doi.org/10.1007/s10021-021-00684-y

Peckenham JM, Thornton T, Whalen B. 2009. Sand and gravel mining: effects on ground water resources in Hancock county, Maine, USA. Environ Geol. 56(6):1103–1114.

Persson A. 2017. The story of the Hovmöller diagram: an (almost) eyewitness account. Bull Am Meteorol Soc. 98(5):949–957.

Rodrigo M, Rojo C, Segura M, Alonso-Guillén J, Martín M, Vera P. 2015. The role of charophytes in a Mediterranean pond created for restoration purposes. Elsevier. https://www.sciencedirect.com/science/article/pii/S0304377014000692.

Seelen LMS, Teurlincx S, Bruinsma J, Huijsmans TMF, van Donk E, Lürling M, de Senerpont Domis LN. 2021. The value of novel ecosystems: disclosing the ecological quality of quarry lakes. Sci Total Environ. 769:144294.

Seers BM, Shears NT. 2015. Spatio-temporal patterns in coastal turbidity – long-term trends and drivers of variation across an estuarine-open coast gradient. Estuarine Coastal Shelf Sci. 154:137–151. https://doi.org/10.1016/j.ecss.2014.12.018

Shevenell L, Connors KA, Henry CD. 1999. Controls on pit lake water quality at sixteen open-pit mines in Nevada. Appl Geochem. 14(5):669–687. https://doi.org/10.1016/S0883-2927(98)00091-2

Søndergaard M, Lauridsen TL, Johansson LS, Jeppesen E. 2018. Gravel pit lakes in Denmark: chemical and biological state. Sci Total Environ. 612:9–17. https://doi.org/10.1016/j.scitotenv.2017.08.163

U.S. Geological Survey. 2015. Mineral commodity summaries 2015 mineral commodity summaries 2015. US Geological Survey. http://www.usgs.gov/pubprod%0Ahttps://minerals.usgs.gov/minerals/pubs/commodity/phosphate_rock/mcs-2015-phosp.pdf.

van Buuren S, Groothuis-Oudshoorn K. 2011. mice: multivariate imputation by chained equations in R. J Stat Soft. 45(3):1–67. https://doi.org/10.18637/jss.v045.i03

Vucic JM, Cohen RS, Gray DK, Murdoch AD, Shuvo A, Sharma S. 2019. Young gravel-pit lakes along Canada's Dempster highway: how do they compare with natural lakes? Arctic Antarctic Alpine Res. 51(1):25–39. https://doi.org/10.1080/15230430.2019.1565854

Wang R, Yan X, Niu Z, Chen W. 2021. Long-term changes in inland water surface temperature across china based on remote sensing data. J Hydrometeorol. 22(2):523–532. https://doi.org/10.1175/JHM-D-20-0104.1

Weeks S, Werdell PJ, Schaffelke B, Canto M, Lee Z, Wilding JG, Feldman GC. 2012. Satellite-derived photic depth on the Great Barrier Reef: spatio-temporal patterns of water clarity. Remote Sensing. 4(12):3781–3795. https://doi.org/10.3390/rs4123781

Yoder JA, Schollaert SE, O'Reilly JE. 2002. Climatological phytoplankton chlorophyll and sea surface temperature patterns in continental shelf and slope waters off the northeast U.S. coast. Limnol Oceanogr. 47(3):672–682. https://doi.org/10.4319/lo.2002.47.3.0672

Ziauddin G, Chakraborty SK, Jaiswar AK, Bhaumik U. 2013. Productivity study in relation to temperature and transparency in the euphotic zone of selected tropical freshwater floodplain wetlands of West Bengal. *N Save Nature to Survive* (Vol. 7, Issue 4). https://www.researchgate.net/publication/280832042.

3.3. Artículo 3: Warming inland water in peninsular Spain revealed by Landsat 5 analysis

A continuación, se reproduce el artículo 3 publicado: https://doi.org/10.1080/10106049.2024.2371923.

GEOCARTO INTERNATIONAL
https://doi.org/10.1080/10106049.2024.2371923

Taylor & Francis
Taylor & Francis Group

Warming inland water in peninsular Spain revealed by landsat 5 analysis

Carolina Echavarría-Caballero[a], José Antonio Domínguez-Gómez[b], Concepción González-García[a], Raquel Domínguez-Perez[a] and María Jesús García-García[a]

[a]Universidad Politécnica de Madrid, E.T.S. Ingeniería de Montes, Forestal y del Medio Natural, Madrid, Spain; [b]Universidad Politécnica de Madrid, E.T.S. Ingeniería de Topografía, Geodesia y Cartografía, Madrid, Spain

ABSTRACT

Lakes and reservoirs provide habitat for a wide range of species and are essential components of numerous ecosystems. In Spain, these water bodies are particularly important and sensitive, so studying the impact of climate change critical for their long-term management and maintenance. This study aims to identify warming trends in these water bodies and determine whether they vary by season or geographical location by processing time series data of surface temperatures from Landsat 5 images to identify changes in the surface temperature of lakes and reservoirs between 1994 and 2011. This analysis revealed that 87% of water bodies exhibit a warming trend, with an average increase in water surface temperature of +0.037 °C per year. The Ebro and Guadalquivir depressions exhibited the highest temperature increases. However, temperature changes vary across the peninsula, generally associated with air surface temperatures, and are influenced by altitude in the mountain areas and Atlantic winds in the west depressions. The trends indicate a seasonal pattern: in summer, the number of water bodies with high temperatures increases, while in autumn there are more lakes and reservoirs with intermediate temperatures. In winter and spring, the number of water bodies with low temperatures decreases and they are located further north. The influence of factors such as climate and local conditions should be investigated to better understand the warming of these water bodies.

ARTICLE HISTORY
Received 23 January 2024
Accepted 19 June 2024

KEYWORDS
Inland water; surface temperature; spatial–temporal series; Landsat

Introduction

Inland waters provide habitat for a wide range of species, and they are essential components in the hydrological, nutrient and carbon cycles (Moss 2012; Dörnhöfer and Oppelt 2016) but their ecological functions are threatened by eutrophication, inorganic and organic contaminants, morphological alterations, and overexploitation, especially in arid or semi-arid regions (Klein et al. 2014) such as Spain (Brönmark and Hansson 2002).

CONTACT María Jesús García-García mariajesus.garcia.garcia@upm.es

The problem is getting worse as climate change rapidly warms lakes around the world (Schneider and Hook 2010) and impacts many physical, chemical and bioecological processes resulting in changes in species composition (Armstrong et al. 2021), oxygen concentration (Dekker and Hestir 2012; Dörnhöfer and Oppelt 2016), and acidification, etc. (Brönmark and Hansson 2002). In this context, consistent and frequent temperature data for inland waters is particularly important because water temperature is one of the most direct indicators of climate change in these ecosystems (Schneider et al. 2009). This is why it is so important to have a good knowledge of inland water temperature dynamics, especially considering its continuity, completeness and time horizons (Zhu et al. 2022a).

Although efforts are being made to model the temperature of inland water bodies worldwide (Piccolroaz et al. 2024), integrative, regular and consistent long-term monitoring approaches are necessary for a comprehensive understanding of lake ecology (Dekker and Hestir 2012; Hestir et al. 2015). Many researchers have compared the long-term changes in water surface temperature (WST) in different parts of Europe (Dokulil 2014; Lieberherr and Wunderle 2018; Dokulil et al. 2021; Stefanidis et al. 2022) and the world (Schneider et al. 2009; Schneider and Hook 2010, 2012; O'Reilly et al. 2015; Piccolroaz et al. 2020; Woolway et al. 2020), showing that water temperature has increased over time but warming rates depend on a combination of geographic coordinates, elevation, climate, and local characteristics. Therefore, studies should be adapted to the local geographical conditions. Most monitoring programs are data field-based but extensive, systematic extensive water temperature data is historically lacking because it is labor-, cost-, and time-intensive, so it is difficult to capture.

In Spain, all studies of WST are limited to the few water bodies and locations for which long-term temperature records are available. Consequently, these studies focus on the analysis of a few water bodies. Serra et al. (2020) analyzed water temperature changes in Lake Banyoles over the past four decades; Ramos-Fuertes et al. (2020) studied the thermal response of Sanabria Lake to global change; and Chao Rodríguez et al. (2014) obtained water surface temperatures of Arreo lake in the north of Spain from 2001 to 2011 using Landsat 5 data. Due to the variation in characteristics of individual inland water surface temperature and their responses to climate change across, it is not clear how inland water bodies in Spain have responded to climate change in the past. There is no assessment of the temporal and spatial variation characteristics of water surface temperature using a consistent method on a national scale.

In this regard, remote sensing can provide tailored solutions for this type of regional study, so it has become an important tool in water quality research and monitoring given its frequency and global coverage (Baughman and Conaway 2021).

Many studies have showed that thermal infrared (TIR) remote sensing data, available only from a restricted number of sensors, can be used to obtain surface temperature and analyze time series to detect global trends in lake surface temperature with respect to climate warming (Alcântara et al. 2010; Schneider and Hook 2010, 2012; Politi et al. 2012; Chao Rodríguez et al. 2014; Huang et al. 2015; Tavares et al. 2019; Wang et al. 2021).

Most continental water bodies in medium-sized arid regions, such as Spain, are not large, so a sensor that combines good spatial and temporal resolution is particularly valuable. Landsat is a better tool than other satellites for studying the dynamics of water bodies due to its spatial resolution and the length of the series to be studied. In 2017, the Earth Resources Observation and Science (EROS) Center released archived Landsat imagery that had been rigorously processed and radiometrically calibrated to provide remote sensing scientists with a common and consistent dataset, including Landsat Level-2 Surface Temperature (LST).

However, LST has not been widely used in water studies despite its suitable spatial resolution (Schaeffer et al. 2018; Duan et al. 2020; Baughman and Conaway 2021). So, an effort has to be made to propose and validate a Landsat water surface temperature (LWST) processing methodology to water applications fitted suitable for the geographic conditions of each region.

Therefore, the main objective of this paper is to study the long term changes in inland water surface temperature in Spain from 1994 to 2011, through the analysis of temporal trend and spatial pattern over time by using remote sensing to answer questions such as: Is there a warming trend on the surface of continental water bodies in Spain? Are there seasonal or geographical variations in this trend? The answers to these questions provide scientific support for the management of wetland ecosystems with the advantages of large research scope and high spatial–temporal resolution of temperature data.

Materials and methods

First, Landsat surface temperature (LST) images were processed by removing non-valid values according to the quality band, masking the water pixels, and creating empty images to replace the missing images. The time series composition was done by the layer stacking approach. It was then interpolated to fill in the missed values, smoothed to remove outliers, and converted to Celsius. Second, LWST time series were validated with field data to assess the degree of agreement once the data processing methodology had been applied. Finally, if a successful validation was obtained, trend and isotherm analyses would be carried out to study the long-term changes in WST (Figure 1).

Study area

For lake selection, a minimum surface area of 50 hectares was established. This threshold helps prevent adjacency errors in the NIR region caused by nearby land surfaces and bottom reflectance during sensor acquisitions (Zibordi et al. 2014; Arias-Rodriguez et al. 2023). Additionally, this area size ensures an adequate number of pixels can be retrieved from image acquisition, based on the sensor's spatial resolution of 30 × 30 meters, which will serve as the source of radiometric data. Thus, the size was determined according to the following criteria: (1) each water body must have at least three pixels on each side, (2) *in situ* data points must be at least one pixel away from the edge, to avoid land proximity influence, and (3) Each water body should have a safety margin to account for seasonal fluctuations of the water surface. This was obtained by comparing the Ministry for the Ecological Transition and the Demographic Challenge (MITECO) boundaries with high-resolution images from Google Maps.

Then, an initial selection of inland waters in Spain with an area larger than 50 ha was done using the inland water boundaries from cartography supplied by the MITECO, water bodies with elongated shapes, e.g. dammed rivers, were excluded because their variability could affect the results. This was done using the elongation ratio equation (Re), which is the relationship between the area and the square of the length (Sukristiyanti et al. 2018). The preliminary selection yielded 325 water bodies, including 53 lakes (18 artificial, 23 natural and 12 heavily modified) and 272 reservoirs, all of them located in mainland Spain (Figure 2).

Input data

Landsat surface temperature data

The Landsat water surface temperature (LWST) data was obtained from the USGS Landsat surface temperature (LST) provisional product with a spatial resolution of 30

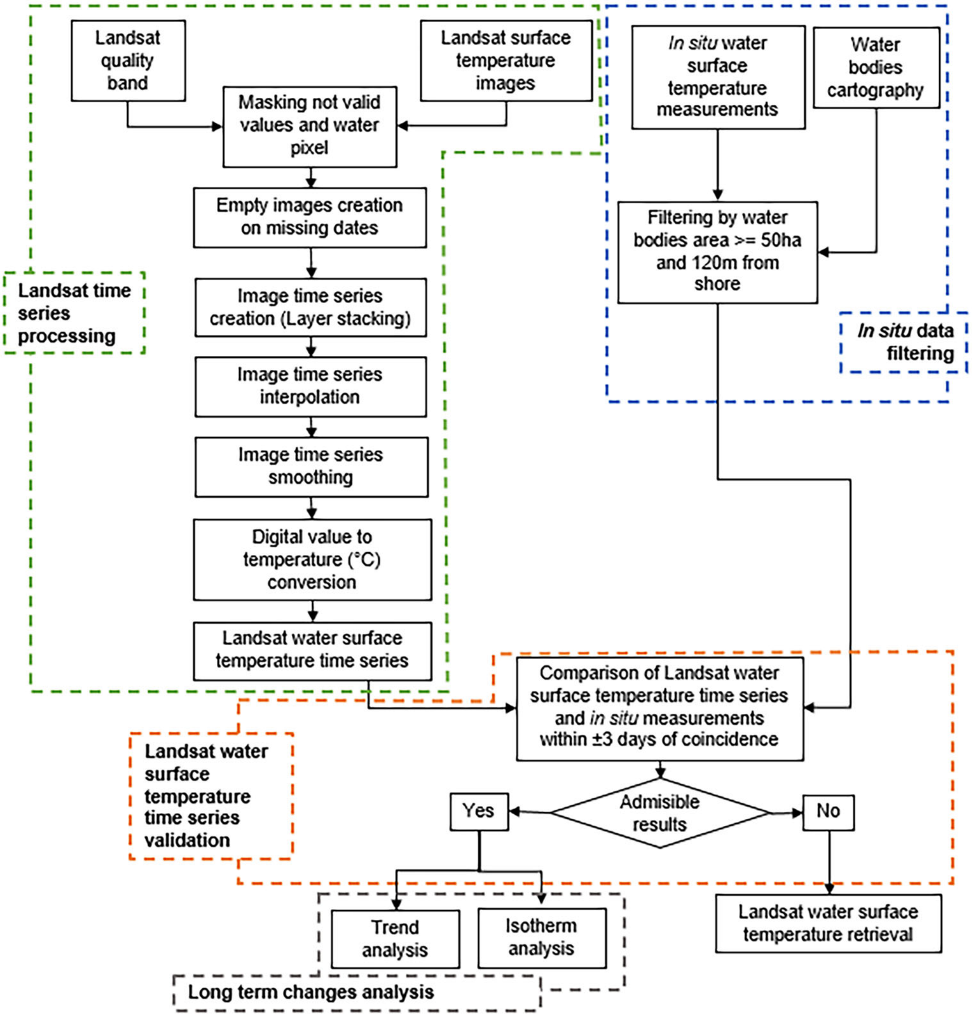

Figure 1. Flow chart of the research process.

meters and a temporal resolution of 16 days. The LST was derived using Landsat 5 Thematic Mapper (TM), North American Regional Reanalysis (NARR) weather data, the Moderate Resolution Atmospheric Transmission (MODTRAN) model, and ASTER emissivity data (Malakar et al. 2018; Zanter 2021).

All the available LST data for peninsular Spain, 11,481 images in total, were downloaded from 1994 to 2011. Landsat 5 collection 2 level 2 scenes were downloaded in bulk from the EROS Earth Explorer website (https://earthexplorer.usgs.gov). Every image package included twelve output raster layers. The raster layers used in this research are surface temperature (ST) and pixel quality assessment (PIXELQA), which assigns each pixel a condition (clear terrain, water terrain, cloud shadow, or snow/ice) based on spectral information and confidence level (low, medium, and high).

Water surface temperature in situ measurements for landsat data validation

The water surface temperature data measured in the field provided by MITECO will be used to validate the Landsat water surface temperature time series. A total of 46,086

COLOR Online / B&W in Print

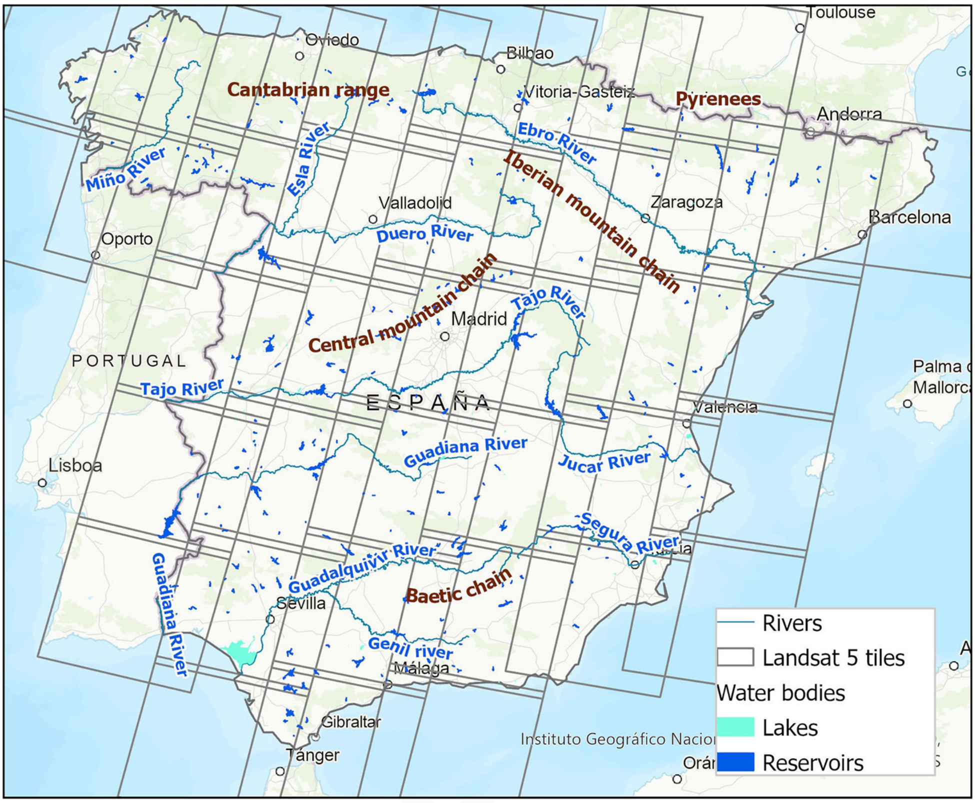

Figure 2. Location of the studied water bodies.

points providing surface temperature in degrees Celsius in 677 water bodies were obtained between 1994 and 2020.

Sampling was confined to water bodies with a surface area greater than or equal to 50 ha because smaller water bodies could not be studied with Landsat due to the image pixel size. In total, 36,105 sampling data points were preliminarily selected. Finally, only sampling points located more than 120 meters from the shore were selected by using the inland water boundaries from cartography supplied by MITECO because, although the surface temperature product has a spatial resolution of 30 meters, the original thermal band is 100 meters. In this way, the ground effect is removed as the pixel is resampled. The sampling data used for validation are 3,032 (Figure 3 and Table 1), located in 70 water bodies, of which 17 are lakes and 53 are reservoirs.

Landsat water surface temperature time series processing

Data filtering

LST images were masked to null values according to the quality band (QA_PIXEL) to obtain standard values without clouds. Then, empty images were created to get images for missing dates and construct image data cubes representing evenly spaced time series associated to spatially aligned pixels. The water boundary was obtained based on quality band (QA_PIXEL) by using the 'water with low sets' class, which is used for masking surface temperature images.

COLOR Online / B&W in Print

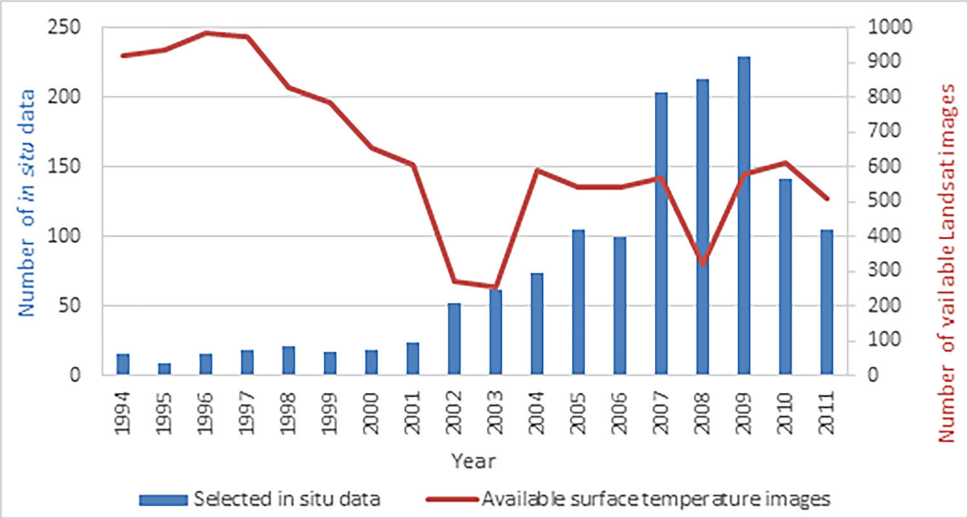

Figure 3. Available Landsat images and selected in situ surface temperature data per year.

Table 1. Number of selected *in situ* points for every filtering process.

Filtering process	Number of *in situ* data	Number of water bodies
Initial	46086	677
In water bodies with surface area ≥ 50 ha	36105	432
Located more than 120 m from the shore	3032	70

COLOR Online / B&W in Print

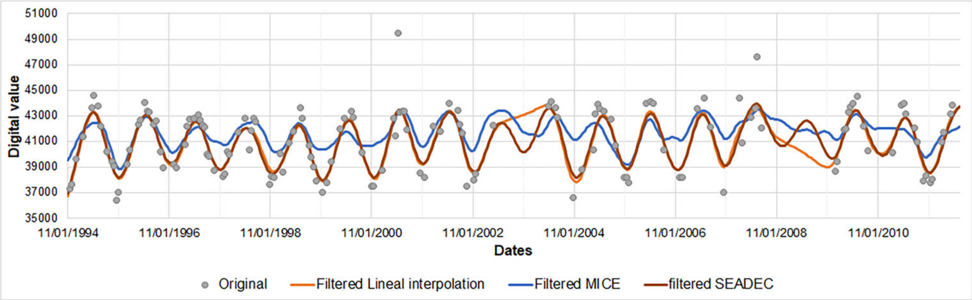

Figure 4. Comparison of imputation methods: Example with filtered time series.

Time series creation

Subsequently, the LST image time series composition or data cube construction was carried out using the layer stacking approach. The imputation of missing values was carried out with the linear interpolation method. Three imputation methods were tested to determine which one was the most accurate and the least computationally expensive: lineal interpolation (Ponkina et al. 2021), the Multivariate Imputation by Chained Equations (MICE) (van Buuren and Groothuis-Oudshoorn 2011) and the Seasonally Decomposed Missing Value Imputation method (SEADEC) (Moritz and Bartz-Beielstein 2016) (Figure 4). By visual inspection, MICE was the least reliable method and linear interpolation and SEADEC got similar results with differences only in periods with more missing data (years 2002, 2003 and 2008). To quantify the difference between the linear interpolation and SEADEC methods, the general trend was calculated and compared (see the section

'Water Surface Temperature Trend Analysis') for five water bodies with varying trend levels distributed across the study area. The results showed a mean difference value of 0.0007 between the two methods. Consequently, the linear interpolation method was selected because the SEADEC method is computationally more expensive, especially considering the amount of data involved.

Then, smoothing with the Whittaker filter to eliminate outliers was done (Figure 5). The Whittaker smoother (Whittaker 1922) is a penalized least squares algorithm that minimizes fitting error and penalizes the roughness of the smooth curve. It can effectively balance the fidelity of the original time series and roughness of the fitted time series (Kong et al. 2019; Zeng et al. 2020; Liu et al. 2022).

Conversion to celsius

Finally, given that LWST images are in scaled Kelvin values (SKV), it is necessary to convert them to degrees Celsius ($T(^{\circ}C)$) to compare them with the field values. The following equations were used (Zanter 2021):

$$T(^{\circ}K) = SKV \ * \ 0.00341802 + 149 \tag{1}$$

$$T(^{\circ}C) = T(^{\circ}K) - 273.15 \tag{2}$$

At the end of the processing, a time series of water surface temperature was obtained for each water body for each available Landsat tile, so the tile with the most valid data was selected. Then, pixels that were classified as water throughout the whole time series were selected. Finally, 325 time series were obtained, given that water bodies with dry periods were discarded.

Landsat water surface temperature time series validation with in situ data

Because there was a lack of images during the studied period and the time series will be used to analyze long-term changes, they were validated to assess the performance of the processing methodology. So, the filtered *in situ* temperature measures for a three-day window of coincidence with the Landsat images were compared. A three-day time window was selected because there is a negative correlation between accuracy and the length of the time window (Zeng et al. 2023) and three-day windows have proven to be sufficient in previous studies (Schaeffer et al. 2018). The agreement was quantified by using the Pearson correlation coefficient and p-value to consider whether the correlation was statistically significant (Schaeffer, Seegers, et al. 2018; Baughman and Conaway 2021).

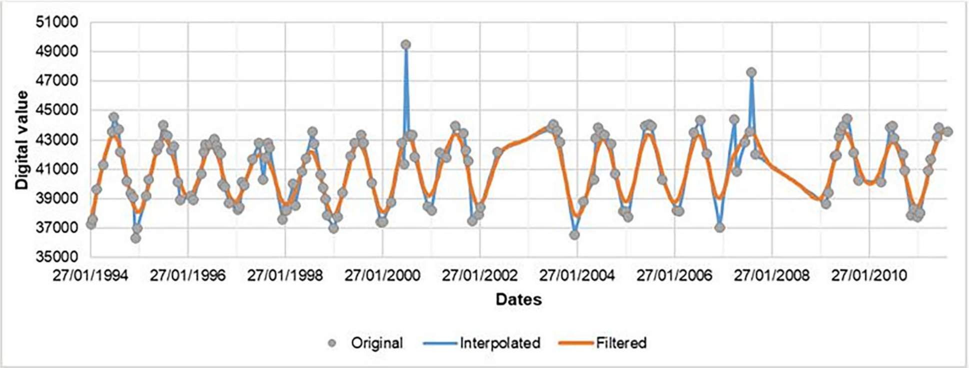

Figure 5. Interpolation and filtering process example.

Water surface temperature trend analysis

Once the image data cube evenly representing the time series of water surface temperature had been obtained for every water body in the study, the general trend for each spatially aligned pixel from 1994 to 2011 was obtained. The trend analysis was done by fitting a linear least-square regression model as a function of time (Mahmoudi et al. 2019; Wang et al. 2021). The slope of the line indicates the positive or negative direction of the trend. The F test of the ANOVA regression was used to test the null hypothesis that the slope (regression coefficient) is null. Considering an alpha level of 0.1, if the p-value of the F-test statistic is less than the selected alpha level, the null hypothesis can be rejected (Wanishsakpong and McNeil 2016; Chambers 2017; Mahmoudi et al. 2019).

A p-value and slope were obtained for every pixel from each water body, and the average of all pixels with significative slope within each water body was calculated and analyzed.

To compare the trends in water surface temperature with the surrounding air temperatures, daily mean data from all stations available at the Spanish State Meteorological Agency (AEMET) were downloaded, the trends were calculated by fitting a linear regression, and the resulting trend values were interpolated using the Inverse Distance Weighting (IDW) method (Tanır Kayıkçı and Zengin Kazancı 2016).

To quantify the rate of increase, the mean WST for each water body was determined, and the annual mean was calculated only for water bodies with a significant trend. The difference for each year was then calculated to obtain the mean difference.

Isotherm analysis

The spatial variation in the WST over time was studied with an isotherm-based method tested in the research of Wang et al. (2021). A total of three isotherms were created: 10 °C, 20 °C and 25 °C. A raster was created in the GIS software (ArcGIS Pro 3.1.2) by interpolating the mean WST of all studied water bodies every 16 days, so the calculated raster represents the hypothetical WST for each pixel, assuming all pixels represent water. To dismiss errors, none of the natural water bodies were included because of their high degree of variability. Finally, three different isotherms were calculated for each raster. If more than one isotherm was created for one temperature value, the longest isotherm was selected to calculate X (Longitude or East) and Y (Latitude or North) coordinates of its central point and the total length of the curve.

Once the central coordinates and length of the longest isotherms of temperatures 10 °C, 20 °C and 25 °C were obtained the seasonal behavior and the interannual changes or long-term trends were analyzed. To detect the long-term trend an analytical adjustment by regression was made by adjusting linear regression models as a function of time, confirming the significance of the slope of the straight line (Mahmoudi et al. 2019; Wang et al. 2021).

The data supporting the findings of this study are available from the corresponding author upon reasonable request.

Results and discussion

Landsat water surface temperature time series validation

After the Landsat time series processing, the time series were validated with a three-day window match-up for *in situ* points. Only data points with three or more

COLOR Online / B&W in Print

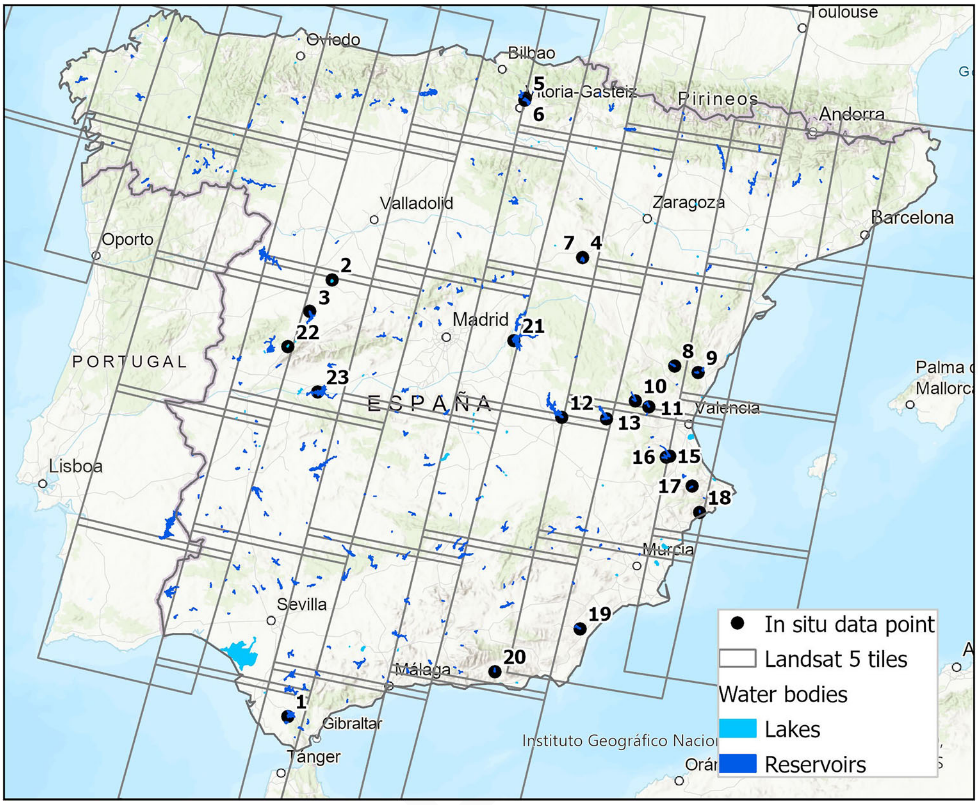

Figure 6. Location of in situ data point coincident with landsat water surface temperature time series in a three-day window. The in situ identifier corresponds to Table 2.

coincidences were selected to compute the Pearson correlation coefficient. Finally, 341 coincidences were obtained in 23 *in situ* points in 20 inland water bodies (Figure 6). The Pearson correlation coefficient ranged from 0.60 to 0.98 with all p-values less than 0.1. In 87% of the cases, the p values were less than 0.05 (Table 2), which indicates a sufficiently significant correlation. This supports the use of remote sensing data in the analyses carried out.

The lack of images between 2002 and 2003 and in 2008 affects the LWST time series behavior, especially because the non-available images correspond to winter periods (Figure 7). Despite the underestimation of LWST in 2002, 2003, and 2008 with respect to in situ values, the accuracy obtained is acceptable.

The overall performance of the time series processing methodology of the LST product was achieved for all points with a Pearson correlation coefficient and significative ($p < 0.1$) in all cases. If there is a correlation between LWST time series and *in situ* surface temperature, the LWST time series could be sufficient for determining historical seasonal trends and assessing the inter-annual variability of water bodies. This is similar to results in previous studies in which authors concluded, that due to the high performance in open water pixels, Landsat satellite time series can supplement traditional *in situ* sampling by providing data for most water bodies for an extended period (Schaeffer et al. 2018; Duan et al. 2020; Baughman and Conaway 2021).

Table 2. Summary of agreement between landsat water surface temperature time series and *in situ* water temperature.

Id	Water body name	Field point code	Tiles	# of coincident data	Pearson	P-value
1	Barbate reservoir	AA00000750	201035	7	0,98	0,00
2	Riolobos reservoir	DURIO1	202031	5	0,93	0,02
3	Santa Teresa reservoir	DUTER1	202032	5	0,92	0,03
4	La Tranquera reservoir	EB00000553	200031	17	0,65	0,00
5	Ullivarri-Gamboa reservoir	EB00000827	201030	14	0,76	0,00
6	Ullivarri-Gamboa reservoir	EB00000829	201030	14	0,65	0,05
7	La Tranquera reservoir	EB0553-FQ	200031	5	0,97	0,01
8	Arenós reservoir	JU06140034	199032	9	0,75	0,02
9	Sichar reservoir	JU06150028	198032	10	0,98	0,00
10	Benagéber reservoir	JU06660017	199032	7	0,65	0,09
11	Loriguilla reservoir	JU06660020	199032	9	0,67	0,05
12	Alarcón reservoir	JU06910006	200032	9	0,82	0,01
13	Contreras reservoir	JU06930008	199033	14	0,63	0,02
14	Tous reservoir	JU07460013	199033	16	0,60	0,01
15	Escalona reservoir	JU07690008	199033	61	0,63	0,00
16	Escalona reservoir	JU07690041	199033	18	0,67	0,00
17	Beniarrés reservoir	JU08210023	198033	19	0,96	0,00
18	Amadorio reservoir	JU08470015	198033	14	0,97	0,00
19	Cuevas de Almanzora reservoir	MA1014B001	199034	9	0,94	0,00
20	Benínar reservoir	MA1043B006	200034	21	0,96	0,00
21	Buendía reservoir	TA56201002	200032	38	0,63	0,00
22	Baños reservoir	TACC576996	202032	9	0,81	0,01
23	Valdecañas reservoir	TACC652014	202032	11	0,85	0,00

Water surface temperature trend analysis

To determine whether the slope was significant linear least-square regression was done for all the water surface temperature time series for all pixels in every water body.

Most pixels, 70.13%, have a statistically significant positive trend ($p < 0.1$), 5.66% have a statistically significant negative trend, and 24.21% have no significant trend. The average of all pixels with a significant slope was 0.0072, which means that the WST increased in the 18-year study period, from 1994 to 2011. The mean significant slope for all pixels in each water body shows that 87% of water bodies have a positive mean slope (Figure 8). This means that the temperature has increased in those water bodies during the study period.

This is consistent with trends in the temperature of inland water bodies in other countries around the world. Wang et al. (2021) concluded that the temperature of lakes in China has shown an upward trend from 2000 to 2010; Schneider et al. (2009) found that lakes in California and Nevada (North America) had a rapid warming trend from 1991 to 2008; Aranda et al. (2021) analyzed monthly, seasonal and annual surface temperature trends in 14 Chilean lakes between 2000 and 2016 period with the results showing that 12 of them presented a statistically significant increase in surface temperature; Dokulil (2014) found that most inland waters in Europe showed a warming trend between 1960 and 2010; and Schneider and Hook (2010, 2012) concluded that the surface temperatures of 169 of the largest inland water bodies worldwide have been increasing with the greatest warming in the middle and high latitudes of the Northern Hemisphere, and particularly in Northern Europe.

The results presented in this paper show that this warming trend represents an average of +0.037 °C per year in water bodies with a significant trend, which means a total of +0.592 °C over the entire study period. These results are consistent with those obtained by O'Reilly et al. (2015) for the whole world (+0.034 °C per year) and by Woolway et al. (2020a) for Europe (+0.035 °C per year). However, they are much higher than those of Virdis et al. (2020) for Sardinia (+0.01 °C per year), and considerably lower than those

COLOR Online / B&W in Print

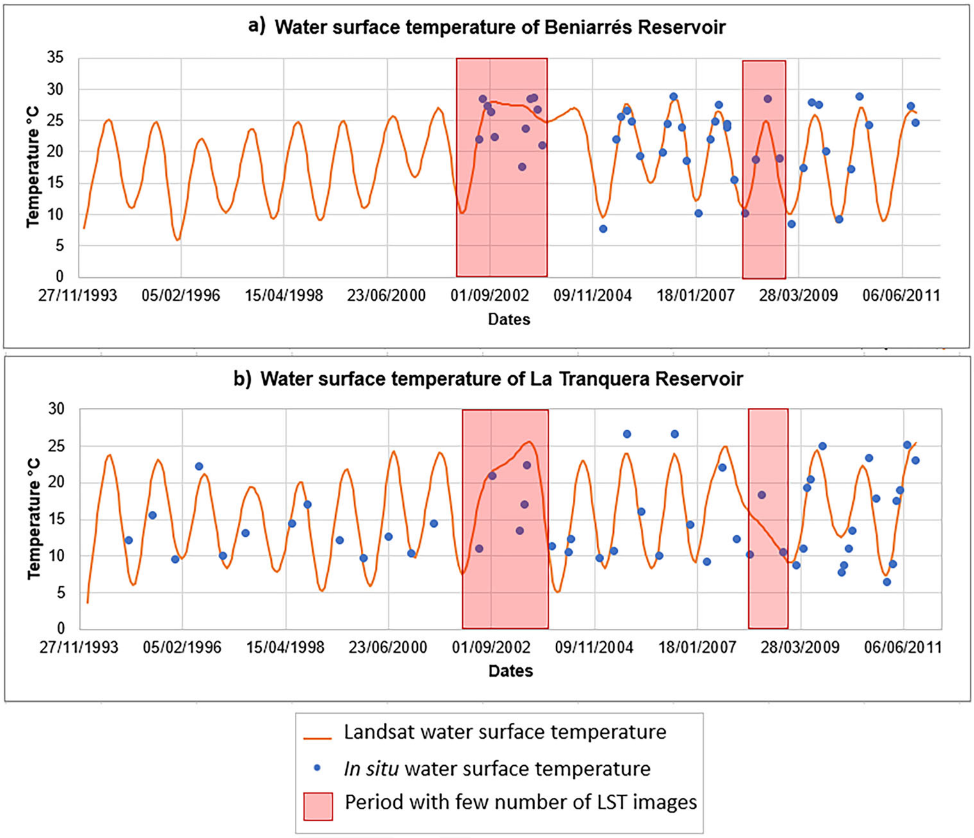

Figure 7. Landsat and in situ water surface temperature time series. (a) Beniarrés reservoir, point code: JU08210023, slope: 0.0053 (p 0.03) and (b) La tranquera reservoir, point code: EB00000553, slope: 0.0071 (p 0.002).

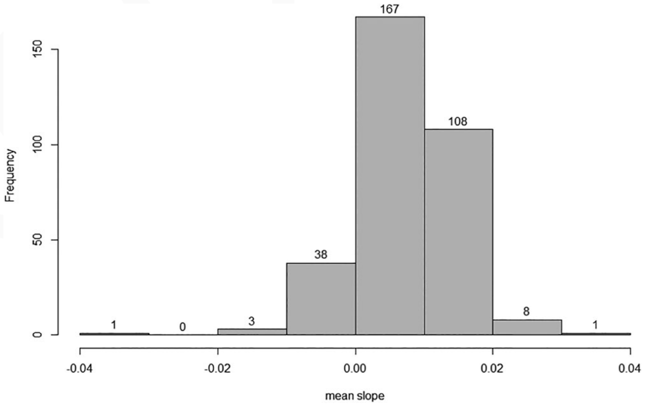

Figure 8. Mean of significant slope for each water body.

estimated by Schneider and Hook (2010) for Eastern Europe (+0.06 °C per year). The differences can be explained by the high spatial variability that WST trends can present as well as variations in the study periods. For example, Sardinia is a small island in the central Mediterranean Sea, and its climatic conditions are very different from those of the Iberian Peninsula.

In this study area, the WST trend distribution (Figure 9) is highly irregular due to its complicated orography and the diversity of climatic regions.

There is a pronounced warming trend in the water bodies of the Ebro River depression, located in the southern part of the Pyrenees. The warming trends in the Guadalquivir River basin are somewhat more variable and dispersed (Figure 9). These depressions are situated at altitudes of 200 and 100 meters, respectively, and feature a 'continentalized Mediterranean with warm summers' climate in the first one, and a 'warm inland Mediterranean' climate in the second, with both areas partial exhibiting an 'arid Mediterranean' climate (Instituto Geográfico Nacional, no date).

On the other hand, there are also elevated warming trends in high-altitude areas, such as the Montes de León (between the Miño and Esla rivers), as well as in the Cantabrian Range and the Central Mountain Chain in the middle part of the peninsula (see Figure s 2 and 9). These areas have altitudes ranging from 2,188 to 2,650 m above sea level (ASL), so water bodies that are geographically very close may experience different climates, e.g. a 'subhumid continentalized Mediterranean' climate, a 'mountain' climate, or a 'transitional oceanic' climate.

The trends are less pronounced on the northern plateau, which is situated at an altitude of 750 m ASL and experiences a 'continentalized Mediterranean with cold winters' climate. In contrast, the WST trends in water bodies on the southern plateau of the peninsula are much more varied. This region, with a slightly lower altitude (600 m ASL), falls within the 'continentalized Mediterranean with warm summers' and 'Mediterranean inland warm' climate zones. Here, water bodies exhibit a wide range of warming trends,

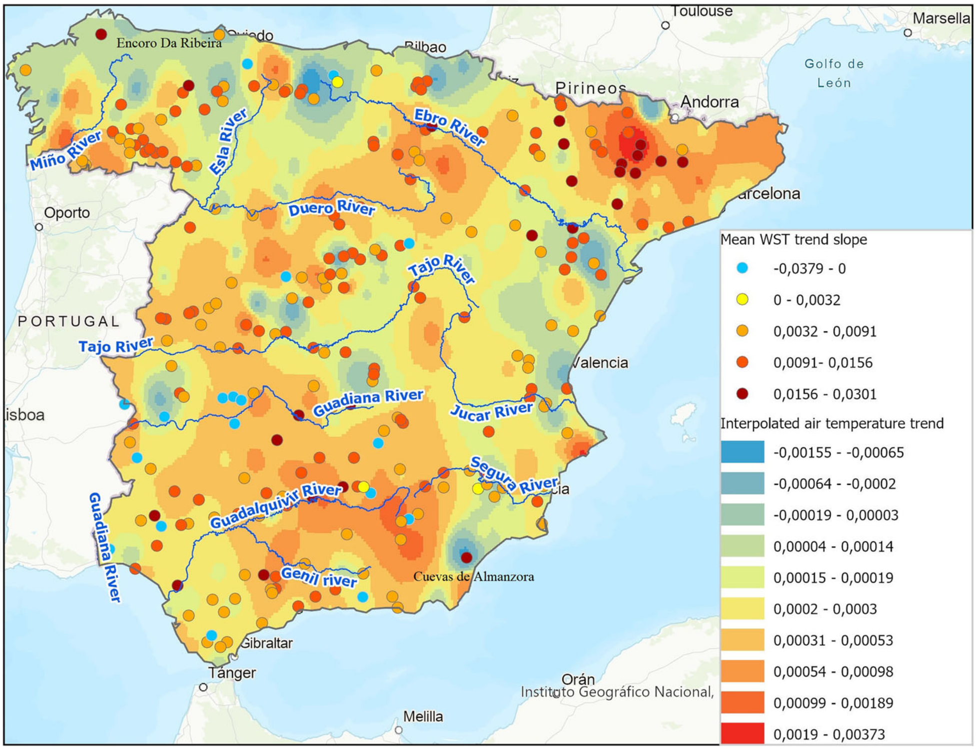

Figure 9. Daily mean air temperature trend interpolation (hatch) in peninsular Spain and significative WST mean slope for each water body (points). Only water bodies with more than 60% of pixels with significant slope are shown.

some of which show a significant tendency to warm, some a moderate trend, and a few with hardly any tendency at all.

The results indicate a clear warming trend in the water masses of these areas. While this trend cannot be directly attributed to altitude or climate alone, it is likely to be influenced by a combination of climatic and other factors. These include local characteristics (O'Reilly et al. 2015), altitude and geographical position (Stefanidis et al. 2022), and solar radiation (Woolway et al. 2020).

Generally, the WST trend spatial patterns and air temperature trends coincide (Schneider and Hook 2010; Woolway et al. 2020; Wang et al. 2021). Our results show this relationship, particularly in the Ebro and Guadalquivir river depressions. However, there are zones where water bodies appear to warm more than the surrounding air (Austin and Colman 2007; Schneider and Hook 2010; O'Reilly et al. 2015). In Spain, this effect is observed at several locations across the study area. In some cases, an inverse relationship occurs; water bodies with high warming tendencies are situated in environments with negative air temperature trends. Examples of this include the Cuevas de Almanzora reservoir in the Southeast and the Encoro Da Ribeira reservoir in the Northwest of the peninsula, and several water bodies south of the Ebro River (Figure 9). This local variability could be explained by the greater influence of several combined elements in the so-called atmospheric circulation modes (Hernández et al. 2015) or by some other element, such as a strong altitudinal gradient (Sánchez et al. 2022) resulting from the complex peninsular orography.

The most significant warming trends were observed in the southern part of the peninsula trends become less pronounced in the central plateau to the north. However, there are strong warming trends further north, in the Northeastern (Pyrenees) and Northwest (Galicia) (Figure 10). The coastal influence is evident in both air temperature and WST trends on the East–West axis (Figures 9 and 10). In the East, the Mediterranean Sea appears to soften the warming trend that is occurring in the interior areas, but to the west is a cluster of water bodies with negative trends, indicating a cooling between 1994 and 2011, which may be due to the influence of fresh and humid Atlantic winds that penetrate the area through the Guadiana and Tajo depressions (García Vega and García de Pedraza 1991) (Figure 10).

This outcome agrees with the global findings revealing increased warming in water bodies in temperate regions of the Northern Hemisphere (Schneider and Hook 2010; Piccolroaz et al. 2020), increasing warming trends in the southwest northeastern Europe (Lieberherr and Wunderle 2018), and in Mediterranean lakes (Virdis et al. 2020).

However, more research is needed to fully understand the warming processes in the Iberian Peninsula water bodies, because, although they seem to be influenced by global factors such as the increasing trend in air temperature associated with climate change (del Río et al. 2011; Ríos-Cornejo et al. 2015), there are other more local influences such as geomorphology, elevation, and climate that need to be analyzed.

Isotherm analysis

Seasonal variation

Low temperatures occur in the Iberian Peninsula at latitudes above 4,350,000 N, meaning the water bodies in Andalusia maintain temperatures above 10 °C throughout the year. During spring, between February and June, the 10 °C isotherm move from the water bodies located in the peninsular center to those located further north, gradually disappearing (Figure 11b). There is a western movement at the end of spring and during the

COLOR Online / B&W in Print

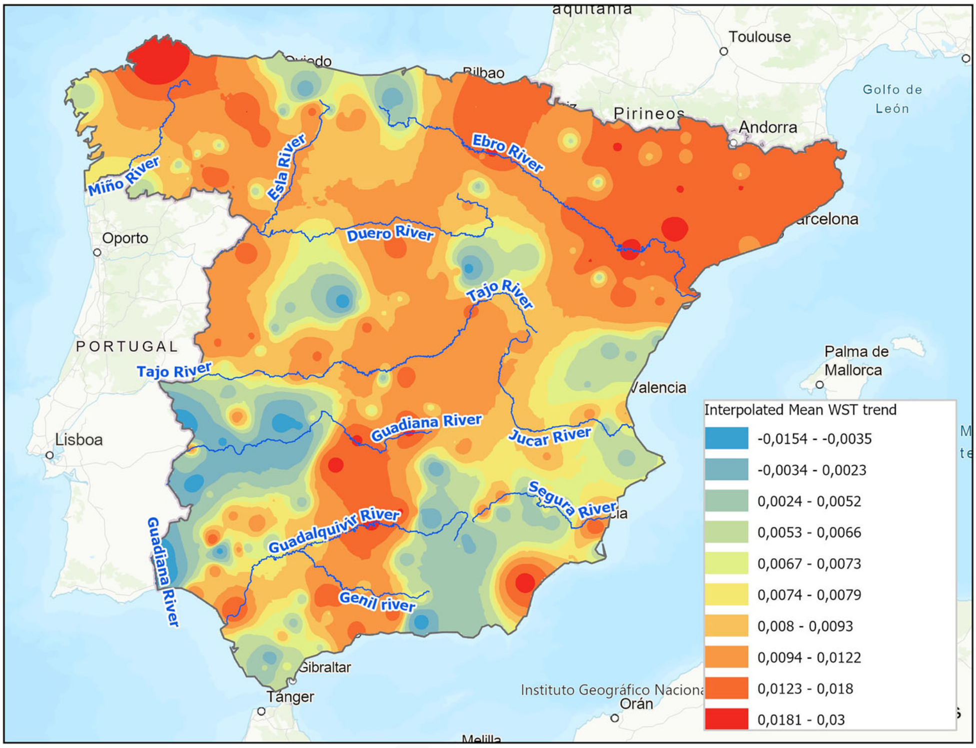

Figure 10. Interpolated mean WST trend in peninsular Spain with IDW method.

autumn. On the other hand, the number of water bodies with10 °C or lower temperatures increases between October and March, after which temperatures rise until June, when no water bodies in the Iberian Peninsula have 10 °C or less (zero length of the 10 °C isotherm, Figure 11c).

This WST seasonal spatial pattern may be closely related to air temperature (Cobelas and García-Morato, 2021), but it is even more strongly associated with land surface temperature (LST). On the peninsula, land surface warming begins in April in the East and decreases between September and October. Temperatures decrease earlier in the Northwest (Khorchani et al. 2018).

The 25 °C isotherm generally appears stable in water bodies in the south and part of the center region of the peninsula until summer (June), after which they are further north, remaining stable at those latitudes until September. This displacement occurs because a range of higher temperatures affects the water bodies in these territories. In October, the reverse movement occurs, bringing temperatures of 25 °C back to the water bodies of the southern peninsula (Figure 11b). There are areas of the peninsula in which water temperatures reach 25 °C, even in the autumn months, e.g. November 2010 (Figure 12). However, during autumn, winter and spring very few water bodies on the peninsula reach 25 °C. Their number increases rapidly from June to August, when it decreases again until the end of October (length of the isotherm 25 °C in Figure 11c). The longitudinal movement of the 25° isotherm has a similar pattern of latitude, it increases in summer and rapidly decreases in early autumn (Figure 11a).

As previously mentioned, the warming of water bodies parallels that of the LST. The heat moves northeast through the Guadalquivir depression, reaching 25 °C WST in most

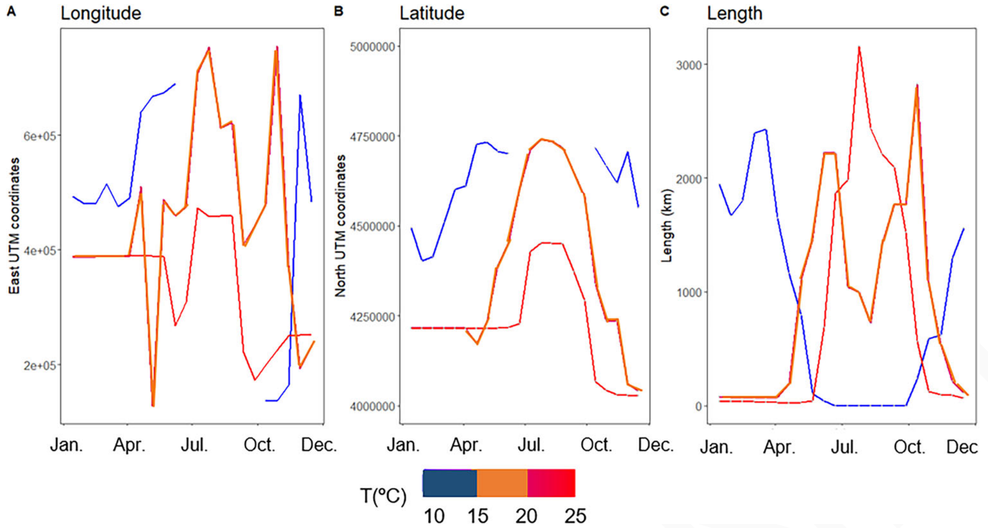

Figure 11. Seasonal changes in a) longitude of the midpoint, (b) latitude of the midpoint, (c) length of the isotherms 10 °C, 20 °C and 25 °C inland WST in Spain during year 2010.

of the peninsula, but not the Mediterranean and the Cantabrian coasts. The Ebro basin is characterized by a perpendicular pattern, that is warming towards the northwest from its mouth in the Mediterranean. This area has certain water bodies outside the pattern, influenced by the Pyrenees' orography.

Regarding intermediate temperatures (20 °C), the largest number of water bodies with this temperature occurs in the months of May and October, with a minimum in August coinciding with the greatest presence of water bodies at 25 °C. During the summer months, in which there are no water bodies at 10 °C, the 20 °C isotherm takes its place (Figure 11b) occupying positions further north than the 25 °C isotherm (July 2010, Figure 12).

The seasonal spatial distribution of the WST shows practically the same pattern in all seasons (Figure 12) – South–North gradient with localized areas of lower temperatures. In winter (01/14/2010 in Figure 12), the water bodies in the southern half of the peninsula have temperatures between 10 and 15 °C, while most in the northern half range between 5 and 10 °C. Two localized areas have water temperatures below 5 °C, influenced by the Pyrenees and Cantabrian mountain ranges and the Cantabrian Sea. A similar pattern occurs in spring, but with each area experiencing a WST higher range (04/20/2010 in Figure 12). The autumn shows a similar distribution (11/30/2010 in Figure 12), but in this case, the influence of the Betic System in the southeast of the peninsula is evident. In summer, almost all water bodies have temperatures of 25 °C or higher, with only a few having lower temperatures of about 20 °C. The areas with lower temperature ranges are practically the same in all seasons (<5 °C in Winter, <10° C in Spring and Autumn, <20 °C in Summer, see Figure 12).

There are significant spatial and seasonal differences in WST throughout peninsular Spain. This variability appears to be strongly related to air temperature or LST and its associated components such as vegetation cover (Khorchani et al. 2018), although the influence of other local components, such as those derived from the country's complex orography (altitude, slopes, very local microclimates, etc.) must also be considered (Sánchez et al. 2022). In some cases, the lakes of the peninsula show greater sensitivity to

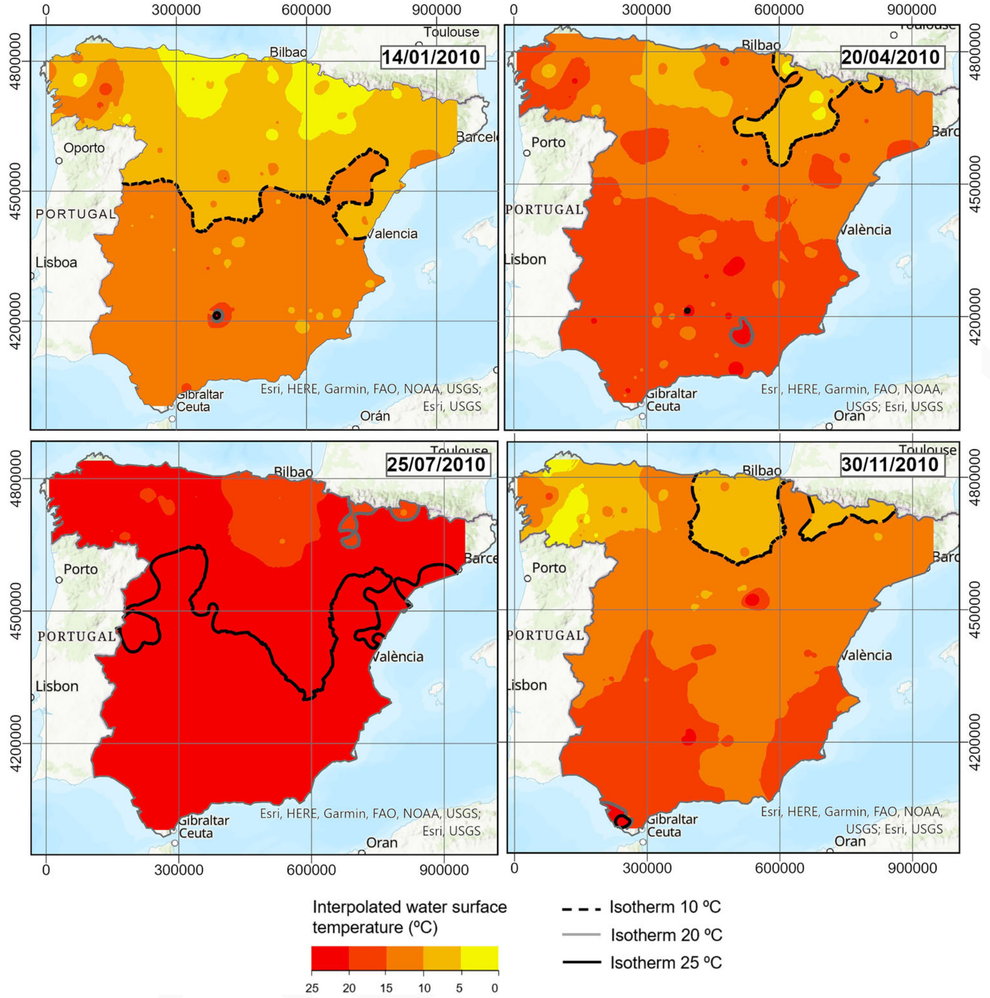

Figure 12. Location of the isotherms 10 °C, 20 °C and 25 °C inland WST in different seasons during the year 2010.

variations in atmospheric circulation modes (ACM) than to individual local meteorological variables (Hernández et al. 2015).

Long term tendencies

To study interannual changes by month in the 10 °C, 20 °C and 25 °C isotherms, the trend slope and p-value of longitude and latitude coordinates and length for each isotherm was analyzed for every month between 1994 and 2011 (Table 3). The results show that the 10 °C isotherm has a statistically significant ($p < 0.1$) negative trend slope in September, October and December for X-central coordinate (or longitude).

This suggests that over the studied years, the 10 °C isotherm has been shifting westward. Additionally, its central Y coordinate (latitude) shows a significant positive trend from December to February, while the isotherm is also becoming shorter. This implies that between 1994 and 2011, there were fewer water bodies with a temperature of 10 °C, and these bodies of water were located further north.

Table 3. Trend slope and p-value of longitude and latitude coordinates and length of isotherms 10°C, 20°C and 25°C for each month from 1994 to 2011.

Month	Slope Isotherm 10°C	p-value	Slope Isotherm 20°C	p-value	Slope Isotherm 25°C	p-value
Longitude						
January	−47.86206	0.98	−1544.549	0.67	−991.5659	0.64
February	−1903.188	0.54	143.6676	0.90	0	0.91
March	−2021.019	0.25	4686.336	0.15	453.5949	0.44
April	−605.9494	0.86	3988.531	0.11	2782.055	0.25
May	−3527.173	0.43	2287.408	0.31	6071.056	0.02*
June	0	0.74	−1641.126	0.34	2091.991	0.59
July	0	0.86	−1475	0.55	−998.4874	0.19
August	0	0.93	2057.775	0.37	281.6293	0.67
September	−12601.61	0.01*	−983.1453	0.39	−1418.796	0.61
October	−7685.64	0.05*	1943.151	0.16	−430.9965	0.83
November	−1572.138	0.78	−3712.518	0.29	−7730.225	0.09*
December	−5325.773	0.06*	−3741.66	0.23	−1783.632	0.59
Latitude						
January	9793.491	0.005*	−2685.004	0.18	−2938.565	0.28
February	9237.682	0.008*	1304.762	0.52	−2611.667	0.49
March	3640.95	0.14	1291.38	0.32	7636.204	0.11
April	−875.6807	0.28	690.4239	0.79	2933.916	0.34
May	−116.7445	0.45	804.7101	0.78	−1265.329	0.42
June	0	0.45	959.3492	0.34	−1808.512	0.21
July	0	0.93	−459.032	0.44	522.0772	0.85
August	0	0.52	699.2438	0.32	2322.054	0.19
September	−1068.291	0.37	2641.068	0.03*	3410.819	0.10*
October	0	1	3384.899	0.23	−1309.704	0.32
November	722.7777	0.55	311.2409	0.73	−4613.935	0.07*
December	7534.344	0.02*	−1253.506	0.63	−2189.86	0.38
Length						
January	−13.25814	0.35	−0.5007776	0.92	1.076808	0.38
February	−9.159196	0.56	9.300592	0.10*	0.7455181	0.70
March	−19.82289	0.12	1.308572	0.42	1.365169	0.28
April	−7.52237	0.42	−6.926845	0.57	−1.432626	0.57
May	1.009959	0.45	2.650647	0.88	−14.68862	0.05*
June	0	0.91	−14.79569	0.35	−9.68697	0.51
July	0	0.79	−6.954177	0.49	10.85281	0.31
August	0	0.68	−20.1464	0.01*	9.389652	0.10*
September	−4.609443	0.05*	−18.00391	0.14	8.977678	0.48
October	−15.42589	0.001*	−0.2185724	0.97	0.282008	0.97
November	−47.82879	0.001*	6.059229	0.63	−2.261955	0.52
December	−37.02459	0.009*	−1.693451	0.73	−2.243785	0.38

*Statistically significant p-value.

The 25 °C isotherm does not show clear a movement pattern. In May it moved eastward, in September it moved northward, and in November it moved to the south-west. What it does show is that in August, the month where the land surface temperature is highest in the Iberian Peninsula (Figure 12), the length of the 25 °C isotherm has a significant positive trend.

In contrast, the 20 °C isotherm shows few significant trends. At the end of summer (September), it tends to move northward. There is a significant trend for it to decrease in length in August, but there is little tendency for it to increase in length in February (Table 3).

This shows: (1) a greater northward trend and decreasing length temperatures of 10° C in winter and (2) at the end of summer, the 20° C isotherm tends to remain further north and its length decreases (3) the 25° C isotherm increased in length, which means that in 2011 there were more water bodies with a surface temperature of 25° C.

Illustrative months were selected to visualize the interannual movements and lengths of WST 10° C and 25° C isotherms, considering the months when each isotherm has significative trend in central coordinates or length (Table 3). Assuming December as the representative month of WST 10° C, the spatial changes from 1994 to 2011 were studied using the midpoint of the longest 10° C isotherm. As can be seen from Figures 13 and 15, the isotherm gradually shifted northward by approximately 4,625,000 North UTM (latitude) coordinate, until 2007, then it started to move southward about 4,375,000 N. In the longitude direction, the central point shows a cycle movement with no big movements, first westward about 400,000E before 1997, then gradually moved eastward by about 550,000 East UTM (longitude) coordinate and repeated the same movement to the coordinate 500,000 E in 2011. The length of the January 10° isotherm decreased from 2,400 km in 1994 to 1,900 km in 2011.

In the case of WST 25 °C, the length and midpoint of the longest August 25 °C isotherm were analyzed to study interannual movement (Figures 14 and 15). Although the central coordinate of the 25 °C isotherm did not move much to the north (from coordinate 4,400,000 N in 1994 to coordinate 4,500,000 N in 2011) or to the east (from coordinate 450,000E in 1994 to coordinate 460,000E in 2011), its length varies from 1,750 km in 1994 to 2,000 km in 2011.

Thus, while the 10 °C isotherm decreased in length and its central point moved towards the north of the peninsula above 4,625,000 N in 2011, the 25 °C isotherm increased in length and its central point has also moved towards the north, reaching 4,500,000 N in 2011.

The 20 °C isotherm exhibits a distribution pattern that combines characteristics of the previous ones. It shifts northward, though less pronouncedly than the 10 °C isotherm, while extending in length similarly to the 25 °C isotherm, folding within its zone of influence (slightly to the north-central area of the peninsula) (Figure 15).

In summary, by the end of the period from 1994 to 2011, an increasing number of water bodies had reached temperatures of 25 °C. However, this temperature is not reached

COLOR Online / B&W in Print

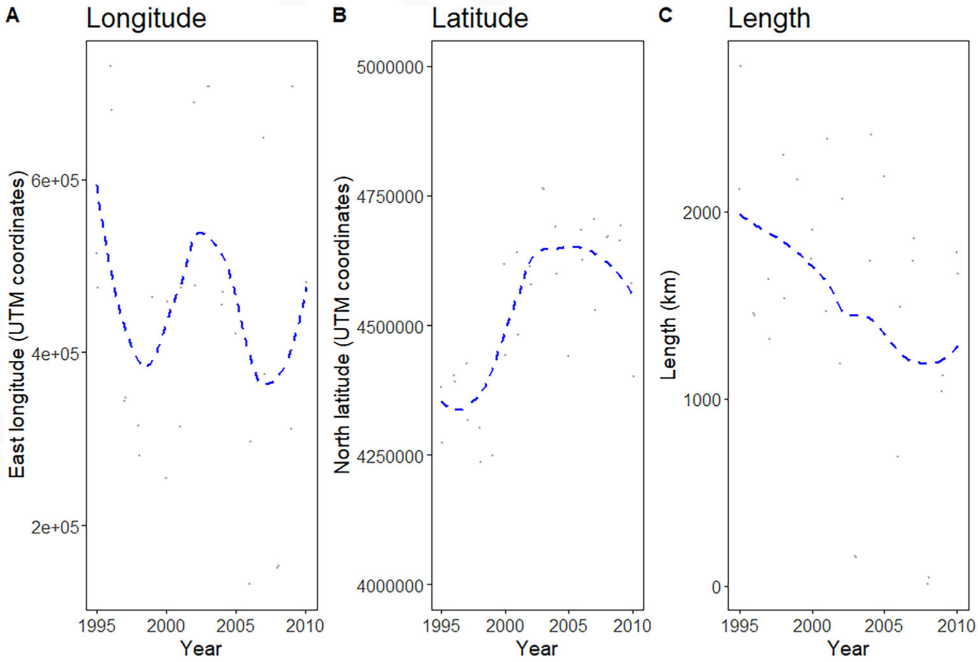

Figure 13. Interannual changes in a) longitude of the midpoint, (b) latitude of the midpoint, (c) length of isotherm 10 °C in Spain inland water bodies in December from 1994 to 2011.

COLOR Online / B&W in Print

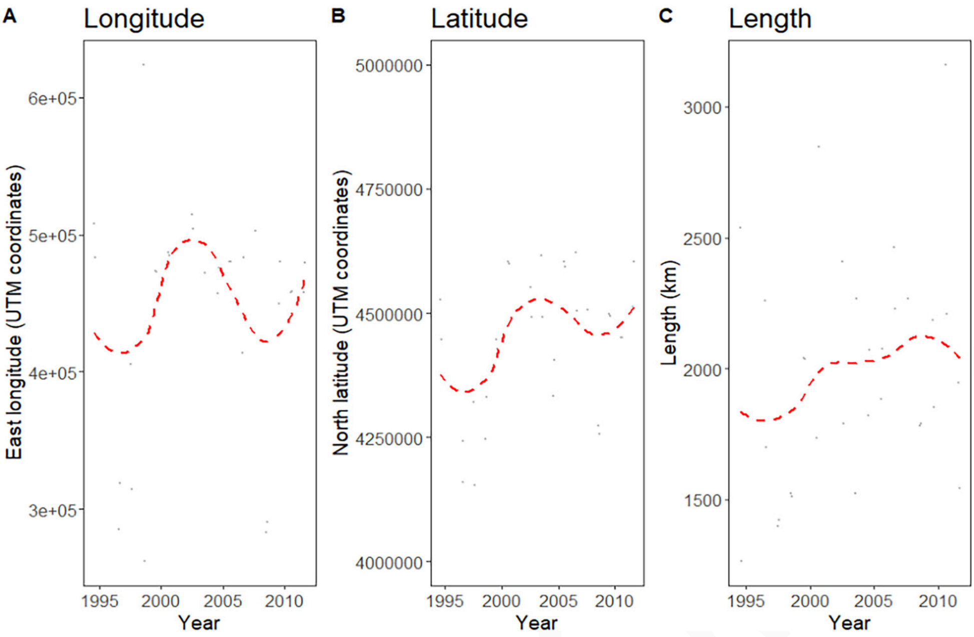

Figure 14. Interannual changes in a) longitude of the midpoint, (b) latitude of the midpoint, (c) length of isotherm 25 °C in Spain inland water bodies in August from 1994 to 2011.

by water bodies located in the northern region of the peninsula. As temperatures decline in autumn, there is also a growing prevalence of water bodies with relatively warm temperatures (20 °C) situated farther north that at the beginning of the period. During winter, there was a noticeable decrease in the number of water masses that cooled with temperatures dropping to 10 °C or below. Additionally, these cool water bodies were also positioned considerably farther north that in 1994.

The outcomes agree with several authors who studied interannual variations of WST and found that the most visible trend and pattern changes occurred during the coldest seasons. Niedrist et al. (2018) studied a 44-year time series of water temperature from a small mountain lake in Austria and observe a significant long-term warming trend. However, but this occurred only from August to December with a significant autumn/winter warming effect of lake water together with an increasing intensity of temperature fluctuations in this seasonally ice-covered mountain lake, suggesting that current broad scale estimates of climate change impacts on lakes, based on summer temperature measurements and surface layers, do not fully reflect the effect of climate change. Woolway et al. (2019) investigated the changes in annual minimum surface water temperature in eight European lakes (one in Ireland, five in the UK, one in Austria and one in Switzerland) and found that between 1973 and 2014, the annual minimum lake surface temperature had increased at an average rate of + 0.35 °C per decade, which is comparable to the rate of summer average lake surface temperature change during the same period (+ 0.32 °C per decade) As a result of the rapid warming of annual minimum lake surface temperatures, some of the lakes studied no longer reach important minimum winter surface temperature thresholds, with complex and significant potential implications for the lakes and the ecosystem services they provide. Öğlü et al. (2020) determined long-term trends and detected changes in the frequency of extreme events in the surface water temperature of Lake Peipsi in Russia between 1950 and 2018. Their results showed that,

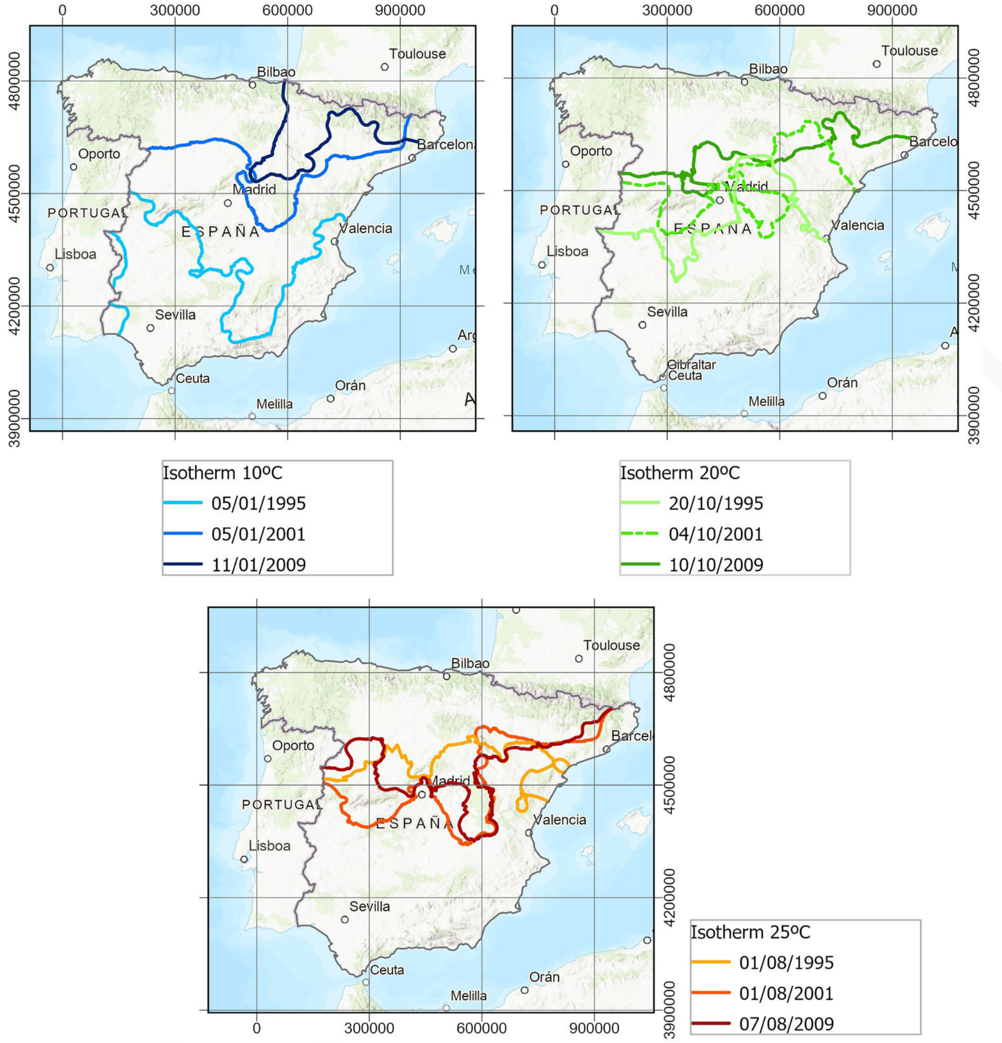

Figure 15. Location of the isotherms 10 °C, 20 °C and 25 °C WST in 1995, 2001 and 2009.

although the average surface temperature had not increased significantly on an annual basis since 1950, it rose rapidly in the winter season during the last decade. Aguilar-Lome et al. (2021) evaluated the space-temporal variation of the water surface temperature of Lake Titicaca in the Central Andes during the period 2000 to 2020 and found that there is a general increasing trend of the average LWST during the coldest time (winter) of the year. Huang et al. (2023) simulated lake surface water temperature between 1979 and 2018 for 91 large lakes across China. Most these lakes showed significant warming trends with a higher rate in winter and spring than in summer and autumn.

In the Mediterranean geographical setting, Virdis et al. (2020) examined 24 lakes on the island of Sardinia between 1999 and 2018. They observed a warming trend of 0.01 °C per year, predominantly occurring during winter. Conversely, there was a tendency towards cooling during the summer months.

These results are critical for the ecology of lakes and continental water bodies. For example, freshwater biodiversity can be negatively impacted because communities at sites with faster rates of warming had fewer gains in taxon richness, functional richness, and abundance (Haase et al. 2023). Regarding freshwater fauna, many fish species have limited capacity to disperse in response to new environmental conditions (Carosi et al. 2023), so their situation is likely to worsen, as rising temperatures could encourage an increase in invasive fish species (Woodward et al. 2010).

On the other hand, the increase in water temperature affects the growth of phytoplankton (Tewari 2022), and many species of cyanobacteria prefer warmer temperatures (Glibert 2020), with some thriving above 25 °C (Paerl and Huisman 2009). Additionally, the complex dynamics in the water column and between species can lead to nonlinear effects, so the results could be more severe than initially expected (Jöhnk et al. 2008; Griffith and Gobler 2020). From the periodic data obtained in this research, it is possible to derive models (Zhu et al. 2022b; Piccolroaz et al. 2024) that enable the daily study of temperature dynamics in these bodies of water and their evolution in the context of climate change.

Conclusions

This research shows that during the period from 1994 to 2011 there was an average warming of water bodies of +0.037 °C per year. This is similar in magnitude to that found in large areas of the world and Europe, but this trend is distributed variably across the entire peninsular territory.

Differences appear to be associated with air temperature and land surface temperature but, in certain areas, altitude has a greater influence, with the water bodies of the mountain Montes de León, Cantabrian Range, and Central Mountain Chain showing more pronounced trends. The influence of southwest–northeast Atlantic winds on the cooling of a group of water bodies in the Guadiana basin was also revealed.

The trends have not been fully explained, so the influence of factors such as climate and other local conditions such as elevation, geomorphology, winds, even vegetation cover, or their combination, must be studied.

Throughout the period from 1994 to 2011, the long-term warming trend differed according to the seasons. There was an increase in the number of water bodies with high temperatures during the summer, despite no geographical displacement on the peninsula. In autumn, there were more water bodies with intermediate temperatures and they were situated farther north than at the beginning of the period. During winter and spring, water bodies with cold temperatures were located further north and were less numerous.

Regarding the implemented methodology, it has been demonstrated that the Landsat 5 surface temperature product can be successfully applied to describe a historical series of temperature for continental water bodies in Spain.

This work has a temporal limitation, as it analyzes a relatively short time span to study the phenomenon of warming in inland water bodies. However, applying the developed methodology to other sensors will allow extending the study period, expanding it to the present. Clearly, other study field areas can benefit from the application of this methodology. However, there is potential for improvement by, e.g. combining data from different sources and interpolation processes to reduce data gaps and achieve a more robust and adjusted time series.

In the present era of global climate change, in which temperature plays an important role in freshwater bodies ecology, enhancing our comprehension of the warming mechanisms impacting these ecosystems is imperative. Continuous long-term monitoring, covering wide spatial and temporal scopes, is essential to safeguard their sustainability and ensure the continuity of the ecosystem services they offer.

In that regard, we aim for this paper to be a valuable and practical tool in achieving that goal.

Acknowledgments

We thank the ©Ministerio para la Transición Ecológica y el Reto Demográfico (MITECO) for providing us water surface temperature field data. This research did not receive any specific grant from funding agencies in the public, commercial, or not-for-profit sectors. There are no relevant financial or non-financial competing interests to report.

Disclosure statement

No potential conflict of interest was reported by the authors.

References

Aguilar-Lome J, Soca-Flores R, Gómez D. 2021. Evaluation of the Lake Titicaca's surface water temperature using LST MODIS time series (2000–2020). J South Am Earth Sci. 112:103609. doi: 10.1016/j.jsames.2021.103609.[Mismatch]

Q2 Q3 Q4 Q5 Alcântara EH, Stech JL, Lorenzzetti JA, Bonnet MP, Casamitjana X, Assireu AT, Novo EMLdM 2010. Remote sensing of water surface temperature and heat flux over a tropical hydroelectric reservoir. Remote Sens Environ. 114(11):2651–2665. doi: 10.1016/j.rse.2010.06.002.

Alvarez-Cobelas M, Rojo C. 2021. That twenty years is nothing for gravel-pit limnology. Limnetica. 40(1):169–187. doi: 10.23818/limn.40.12.

Aranda A, Rivera-Ruiz D, Rodríguez-López L, Pedreros P, Arumí-Ribera J, Morales-Salinas L, Fuentes-Jaque G, Urrutia R. 2021. Evidence of climate change based on lake surface temperature trends in south central Chile. Remote Sens. 13(22):4535. doi: 10.3390/rs13224535.

Arias-Rodriguez LF, Tüzün UF, Duan Z, Huang J, Tuo Y, Disse M. 2023. Global water quality of inland waters with harmonized landsat-8 and sentinel-2 using cloud-computed machine learning. Remote Sens. 15(5):1390. doi: 10.3390/RS15051390/S1.

Armstrong JB, Fullerton AH, Jordan CE, Ebersole JL, Bellmore JR, Arismendi I, Penaluna B, Reeves GH. 2021. The importance of warm habitat to the growth regime of cold-water fishes. Nat Clim Chang. 11(4):354–361. doi: 10.1038/s41558-021-00994-y.

Austin JA, Colman SM. 2007. Lake Superior summer water temperatures are increasing more rapidly than regional temperatures: a positive ice-albedo feedback. Geophys Res Lett. 34(6). doi: 10.1029/2006GL029021.

Q6 Baughman CA, Conaway JS. 2021. Comparison of historical water temperature measurements with Landsat analysis ready data provisional surface temperature estimates for the Yukon River in Alaska. Remote Sens. 13(12):2394. doi: 10.3390/rs13122394.

Bresciani M, Giardino C, Boschetti L. 2011. Multi-temporal assessment of bio-physical parameters in lakes Garda and Trasimeno from MODIS and MERIS. ItJRS. 43(3):49–62. doi: 10.5721/ItJRS20114334.

Brönmark C, Hansson LA. 2002. Environmental issues in lakes and ponds: current state and perspectives. Envir Conserv. 29(3):290–307. doi: 10.1017/S0376892902000218.

Carosi A, Lorenzoni F, Lorenzoni M. 2023. Synergistic effects of climate change and alien fish invasions in freshwater ecosystems: a review. Fishes. 8(10):486. doi: 10.3390/fishes8100486.

Chambers JM. 2017. Linear Models. Statistical Models in S. p. 95–144. doi: 10.1201/9780203738535-4.

Q7 Chao Rodríguez Y, el Anjoumi A, Domínguez Gómez JA, Rodríguez Pérez D, Rico E. 2014. Using Landsat image time series to study a small water body in Northern Spain. Environ Monit Assess. 186(6):3511–3522. Available at: doi: 10.1007/S10661-014-3634-8/FIGURES/11.

Dekker AG, Hestir EL. 2012. 'Evaluating the feasibility of systematic inland water quality monitoring with satellite remote sensing', *publications.csiro.au* [Preprint]. Available at: https://publications.csiro.au/rpr/download?pid=csiro:EP117441&dsid=DS10 (Accessed: 1 April 2023).

del Río S, Herrero L, Pinto-Gomes C, Penas A. 2011. Spatial analysis of mean temperature trends in Spain over the period 1961–2006. Global Planet Change. 78(1-2):65–75. doi: 10.1016/j.gloplacha.2011.05.012.

Dokulil MT. 2014. Impact of climate warming on European inland waters. IW. 4(1):27–40. doi: 10.5268/IW-4.1.705.

Dokulil MT, de Eyto E, Maberly SC, May L, Weyhenmeyer GA, Woolway RI. 2021. Increasing maximum lake surface temperature under climate change. Clim Change. 165(3-4):1–17. doi: 10.1007/S10584-021-03085-1/FIGURES/6.

Dörnhöfer K, Oppelt N. 2016. Remote sensing for lake research and monitoring – recent advances. Ecol Indic. 64:105–122. doi: 10.1016/j.ecolind.2015.12.009.

Duan SB, et al. 2020. Validation of Landsat land surface temperature product in the conterminous United States using in situ measurements from SURFRAD, ARM, and NDBC sites. Int J Digital Earth 14(5):640–660. doi: 10.1080/17538947.2020.1862319.

García Vega C, García de Pedraza L. 1991. 'Contrastes meteorológicos en la península ibérica: cuenca atlántica frente a zona mediterránea', *Repositorios AEMET* [Preprint]. https://repositorio.aemet.es/bitstream/20.500.11765/905/1/contrastes_cal92.pdf (Accessed: 1 June 2024).

Glibert PM. 2020. Harmful algae at the complex nexus of eutrophication and climate change. Harmful Algae. 91:101583. doi: 10.1016/J.HAL.2019.03.001.

Griffith AW, Gobler CJ. 2020. Harmful algal blooms: a climate change co-stressor in marine and freshwater ecosystems. Harmful Algae. 91:101590. doi: 10.1016/J.HAL.2019.03.008.

Haase P, Bowler DE, Baker NJ, Bonada N, Domisch S, Garcia Marquez JR, Heino J, Hering D, Jähnig SC, Schmidt-Kloiber A, et al. 2023. The recovery of European freshwater biodiversity has come to a halt. Nature. *2023* 620(7974):582–588. doi: 10.1038/s41586-023-06400-1.

Hernández A, Trigo RM, Pla-Rabes S, Valero-Garcés BL, Jerez S, Rico-Herrero M, Vega JC, Jambrina-Enríquez M, Giralt S. 2015. Sensitivity of two Iberian lakes to North Atlantic atmospheric circulation modes. Clim Dyn. 45(11-12):3403–3417. doi: 10.1007/S00382-015-2547-8/TABLES/5.

Hestir EL, Brando VE, Bresciani M, Giardino C, Matta E, Villa P, Dekker AG. 2015. Measuring freshwater aquatic ecosystems: the need for a hyperspectral global mapping satellite mission. Remote Sens Environ. 167:181–195. doi: 10.1016/j.rse.2015.05.023.

Huang L, Wang X, Yan Y, Jin L, Yang K, Chen A, Zheng R, Ottlé C, Wang C, Cui Y, et al. 2023. Attribution of lake surface water temperature change in large lakes across China over past four decades. JGR Atmospheres. 128(21): e2022JD038465. doi: 10.1029/2022JD038465.

Huang Y, et al. 2015. Analysis of water temperature variability of Arctic lakes using Landsat-8 data. International Geoscience and Remote Sensing Symposium (IGARSS), 2015-November, pp. 2501–2503. doi: 10.1109/IGARSS.2015.7326318.

Instituto Geográfico Nacional. (no date) *El clima en España*. https://www.ign.es/espmap/mapas_clima_bach/pdf/Clima_Mapa_1_2texto.pdf. (Accessed: 1 June 2024).

Jöhnk KD, Huisman JEF, Sharples J, Sommeijer BEN, Visser PM, Stroom JM. 2008. Summer heatwaves promote blooms of harmful cyanobacteria. Global Change Biol. 14(3):495–512. doi: 10.1111/j.1365-2486.2007.01510.x.

Khorchani M, Martin-Hernandez N, Vicente-Serrano SM, Azorin-Molina C, Garcia M, Domínguez-Duran M^{a}A, Reig F, Peña-Gallardo M, Domínguez-Castro F. 2018. Average annual and seasonal Land Surface Temperature, Spanish Peninsular. J Maps. 14(2):465–475. doi: 10.1080/17445647.2018.1500316.

Klein I, Dietz AJ, Gessner U, Galayeva A, Myrzakhmetov A, Kuenzer C. 2014. Evaluation of seasonal water body extents in Central Asia over the past 27 years derived from medium-resolution remote sensing data. Int J Appl Earth Obs Geoinf. 26(1):335–349. doi: 10.1016/j.jag.2013.08.004.

Kong D, Zhang Y, Gu X, Wang D. 2019. A robust method for reconstructing global MODIS EVI time series on the Google Earth Engine. ISPRS J Photogramm Remote Sens. 155:13–24. doi: 10.1016/j.isprsjprs.2019.06.014.

Lieberherr G, Wunderle S. 2018. Lake surface water temperature derived from 35 years of AVHRR sensor data for European lakes. Remote Sens. 10(7):990. doi: 10.3390/rs10070990.

Liu X, et al. 2022. A method for reconstructing NDVI time-series based on envelope detection and the Savitzky-Golay filter. 15(1):553–584. Available at: doi: 10.1080/17538947.2022.2044397.

Mahmoudi P, Mohammadi, ·M, Daneshmand ·H. 2019. Investigating the trend of average changes of annual temperatures in Iran. Int J Environ Sci Technol. 16(2):1079–1092. doi: 10.1007/s13762-018-1664-4.

Malakar NK, Hulley GC, Hook SJ, Laraby K, Cook M, Schott JR. 2018. An operational land surface temperature product for landsat thermal data: methodology and validation. IEEE Trans Geosci Remote Sens. 56(10):5717–5735. doi: 10.1109/TGRS.2018.2824828.

Moritz S, Bartz-Beielstein T. 2016. imputeTS: time Series Missing Value Imputation in R. *R package version 1.7* [Preprint].

Moss B. 2012. Cogs in the endless machine: lakes, climate change and nutrient cycles: a review. Sci Total Environ. 434:130–142. doi: 10.1016/J.SCITOTENV.2011.07.069.

Niedrist GH, Psenner R, Sommaruga R. 2018. Climate warming increases vertical and seasonal water temperature differences and inter-annual variability in a mountain lake. Clim Change. 151(3-4):473–490. doi: 10.1007/S10584-018-2328-6/FIGURES/5.

Öğlü B, Möls T, Kaart T, Cremona F, Kangur K. 2020. Parameterization of surface water temperature and long-term trends in Europe's fourth largest lake shows recent and rapid warming in winter. Limnologica. 82:125777. doi: 10.1016/j.limno.2020.125777.

O'Reilly CM, Sharma S, Gray DK, Hampton SE, Read JS, Rowley RJ, Schneider P, Lenters JD, McIntyre PB, Kraemer BM, et al. 2015. Rapid and highly variable warming of lake surface waters around the globe. Geophys Res Lett. 42(24):10,773–10,781. doi: 10.1002/2015GL066235.

Paerl HW, Huisman J. 2009. Climate change: a catalyst for global expansion of harmful cyanobacterial blooms. Environ Microbiol Rep. 1(1):27–37. doi: 10.1111/J.1758-2229.2008.00004.X.

Piccolroaz S, Woolway RI, Merchant CJ. 2020. Global reconstruction of twentieth century lake surface water temperature reveals different warming trends depending on the climatic zone. Clim Change. 160(3):427–442. doi: 10.1007/s10584-020-02663-z.

Piccolroaz S, Zhu S, Ladwig R, Carrea L, Oliver S, Piotrowski AP, Ptak M, Shinohara R, Sojka M, Woolway RI, et al. 2024. Lake water temperature modeling in an era of climate change: data sources, models, and future prospects. Rev Geophys. 62(1):e2023RG000816. doi: 10.1029/2023RG000816.

Politi E, Cutler MEJ, Rowan JS. 2012. Using the NOAA advanced very high resolution radiometer to characterise temporal and spatial trends in water temperature of large European lakes. Remote Sens Environ. 126:1–11. doi: 10.1016/j.rse.2012.08.004.

Ponkina E, Illiger P, Krotova O, Bondarovich A. 2021. Do ARMA models provide better gap filling in time series of soil temperature and soil moisture? The case of arable land in the Kulunda Steppe, Russia. Land. 10(6):579. doi: 10.3390/land10060579.

Pour HK, Rontu L, Duguay C, Eerola K, Kourzeneva E. 2014. Impact of satellite-based lake surface observations on the initial state of HIRLAM. Part II: analysis of lake surface temperature and ice cover. Tellus A: Dynamic Meteorol Oceanogr. 66(1):21395. doi: 10.3402/tellusa.v66.21395.

Prats J, Reynaud N, Rebière D, Peroux T, Tormos T, Danis P-A. 2018. LakeSST: lake skin surface temperature in French inland water bodies for 1999-2016 from Landsat archives. Earth Syst Sci Data. 10(2):727–743. doi: 10.5194/essd-10-727-2018.

Ramos-Fuentes A, Palau A, Armengol J, Casasola A, Rodríguez A, Dolz J, Vega JC. 2020. Thermal response of Sanabria Lake to global change (NW Spain). Limnetica. 39(1):455–468. doi: 10.23818/limn.39.29.

Ríos-Cornejo D, Penas Á, Álvarez-Esteban R, del Río S. 2015. Links between teleconnection patterns and mean temperature in Spain. Theor Appl Climatol. 122(1-2):1–18. doi: 10.1007/S00704-014-1256-2/TABLES/2.

Sánchez DE, García CC, Cantos AJO. 2022. Spatiotemporal changes in frost indicators in Southeastern Spain (1950–2020): influence of the East Atlantic Index (EA). J Appl Meteorol Climatol. 61(9):1305–1327. doi: 10.1175/JAMC-D-21-0064.1.

Schaeffer BA, Iiames J, et al. 2018. An initial validation of Landsat 5 and 7 derived surface water temperature for U.S. lakes, reservoirs, and estuaries. Int J Remote Sens. 39(22):7789–7805. doi: 10.1080/01431161.2018.1471545.

Schneider P, Hook SJ. 2010. Space observations of inland water bodies show rapid surface warming since 1985. Geophys Res Lett. 37(22). doi: 10.1029/2010GL045059.

Schneider P, Hook SJ, Radocinski RG, Corlett GK, Hulley GC, Schladow SG, Steissberg TE. 2009. Satellite observations indicate rapid warming trend for lakes in California and Nevada. Geophys Res Lett. 36(22). doi: 10.1029/2009GL040846.

Schneider P, Hook SJ. 2012. Global trends in lake temperatures observed from space. International Geoscience and Remote Sensing Symposium (IGARSS), pp. 5258–5261. doi: 10.1109/IGARSS.2012.6352423.

Seegers BN, Stumpf RP, Schaeffer BA, Loftin KA, Werdell PJ. 2018. Performance metrics for the assessment of satellite data products: an ocean color case study. Opt Express. 26(6):7404–7422. doi: 10.1364/OE.26.007404.

Serra T, Pascual J, Brunet R, Colomer J. 2020. The mixing regime and turbidity of Lake Banyoles (NE Spain): response to climate change. Water. 12(6):1621. doi: 10.3390/w12061621.

Sima S, Ahmadalipour A, Tajrishy M. 2013. Mapping surface temperature in a hyper-saline lake and investigating the effect of temperature distribution on the lake evaporation. Remote Sens Environ. 136:374–385. doi: 10.1016/j.rse.2013.05.014.

Simon RN, Tormos T, Danis PA. 2014. Retrieving water surface temperature from archive LANDSAT thermal infrared data: application of the mono-channel atmospheric correction algorithm over two freshwater reservoirs. Int J Appl Earth Obs Geoinf. 30(1):247–250. doi: 10.1016/j.jag.2014.01.005.

Stefanidis K, Varlas G, Papaioannou G, Papadopoulos A, Dimitriou E. 2022. Trends of lake temperature, mixing depth and ice cover thickness of European lakes during the last four decades. Sci Total Environ. 830:154709. doi: 10.1016/J.SCITOTENV.2022.154709.

Sukristiyanti S, Maria R, Lestiana H. 2018. Watershed-based morphometric analysis: a review. IOP Conf Ser: Earth Environ Sci. 118(1):012028. doi: 10.1088/1755-1315/118/1/012028.

Tanır Kayıkçı E, Zengin Kazancı S. 2016. Comparison of regression-based and combined versions of Inverse Distance Weighted methods for spatial interpolation of daily mean temperature data. Arab J Geosci. 9(17):1–10. doi: 10.1007/S12517-016-2723-0/FIGURES/7.

Tavares MH, Cunha AHF, Motta-Marques D, Ruhoff AL, Cavalcanti JR, Fragoso CR, Jr., Martín Bravo J, Munar AM, Fan FM, Rodrigues LHR, et al. 2019. Comparison of methods to estimate lake-surface-water temperature using Landsat 7 ETM + and MODIS imagery: case study of a large shallow subtropical lake in Southern Brazil. Water. 11(1):168. doi: 10.3390/w11010168.

Tewari K. 2022. A review of climate change impact studies on harmful algal blooms. Phycology. 2(2):244–253. doi: 10.3390/phycology2020013.

van Buuren S, Groothuis-Oudshoorn K. 2011. mice: multivariate imputation by chained equations in R. J Stat Softw. 45(3):1–67. doi: 10.18637/jss.v045.i03.

Virdis SGP, Soodcharoen N, Lugliè A, Padedda BM. 2020. Estimation of satellite-derived lake water surface temperatures in the western Mediterranean: integrating multi-source, multi-resolution imagery and a long-term field dataset using a time series approach. Sci Total Environ. 707:135567. doi: 10.1016/J.SCITOTENV.2019.135567.

Wang R, Yan X, Niu Z, Chen W. 2021. Long-term changes in inland water surface temperature across china based on remote sensing data. J Hydrometeorol. 22(2):523–532. doi: 10.1175/JHM-D-20-0104.1.

Wanishsakpong W, McNeil N. 2016. Modelling of daily maximum temperatures over Australia from 1970 to 2012. Meteorol Appl. 23(1):115–122. doi: 10.1002/met.1536.

Whittaker ET. 1922. On a New Method of Graduation. Proc Edinburgh Math Soc. 41[Preprint]:63–75. doi: 10.1017/S0013091500077853.

Woodward G, Perkins DM, Brown LE. 2010. Climate change and freshwater ecosystems: impacts across multiple levels of organization. Philos Trans R Soc Lond B Biol Sci. 365(1549):2093–2106. doi: 10.1098/RSTB.2010.0055.

Woolway RI, Kraemer BM, Lenters JD, Merchant CJ, O'Reilly CM, Sharma S. 2020. Global lake responses to climate change. Nat Rev Earth Environ. 1(8):388–403. doi: 10.1038/s43017-020-0067-5.

Woolway RI, Weyhenmeyer GA, Schmid M, Dokulil MT, de Eyto E, Maberly SC, May L, Merchant CJ. 2019. Substantial increase in minimum lake surface temperatures under climate change. Clim Change. 155(1):81–94. doi: 10.1007/s10584-019-02465-y.

Zanter K. 2021. LSDS-1618 Landsat 4-7 Collection 2 (C2) Level 2 Science Product (L2SP) Guide.

Zeng L, Wardlow BD, Xiang D, Hu S, Li D. 2020. A review of vegetation phenological metrics extraction using time-series, multispectral satellite data. Remote Sens Environ. 237:111511. doi: 10.1016/j.rse.2019.111511.

Zeng W, Xu K, Cheng S, Zhao L, Yang K. 2023. Regional remote sensing of lake water transparency based on google earth engine: performance of empirical algorithm and machine learning. App Sci (Switzerland). 13(6):4007. doi: 10.3390/APP13064007/S1.

Zhu S, Luo Y, Graf R, Wrzesiński D, Sojka M, Sun B, Kong L, Ji Q, Luo W. 2022a. Reconstruction of long-term water temperature indicates significant warming in Polish rivers during 1966–2020. J Hydrol: Reg Stud. 44:101281. doi: 10.1016/j.ejrh.2022.101281.

Zibordi G, Kiselev V, Bulgarelli B. 2014. Simulation and analysis of adjacency effects in coastal waters: a case study. Appl Opt. 53(8):1523–1545. doi: 10.1364/AO.53.001523.

3.4. Análisis de la calidad del agua en Portugal

La estancia de investigación en la Universidad de Coímbra se planteó con el objetivo de añadir un enfoque multidisciplinar para complementar y hacer más eficiente el mapeo de parámetros de calidad del agua según la metodología presentada en los artículos anteriormente publicados (capítulos 3.1, 3.2 y 3.3), además de incluir datos de campo de Portugal y obtener una visión conjunta de la península Ibérica.

La metodología planteada durante la estancia está conformada por cuatro fases (Figura 3-1): La primera fase consiste en la selección, descarga y estructuración de los datos tomados en campo de parámetros de calidad de agua en Portugal a partir de la selección de cuerpos de agua a estudiar desde la cartografía de masas de agua; la segunda fase consiste en la selección del sensor de teledetección a utilizar, la descarga y el procesamiento de las imágenes para obtener series de tiempo del parámetro de calidad de agua a estudiar; la tercera fase es la validación con datos de campo de las series de tiempo del parámetro seleccionado calculado con teledetección; y finalmente la cuarta fase corresponde al análisis de la variabilidad espacial y temporal en Portugal del parámetro de calidad de agua estudiado.

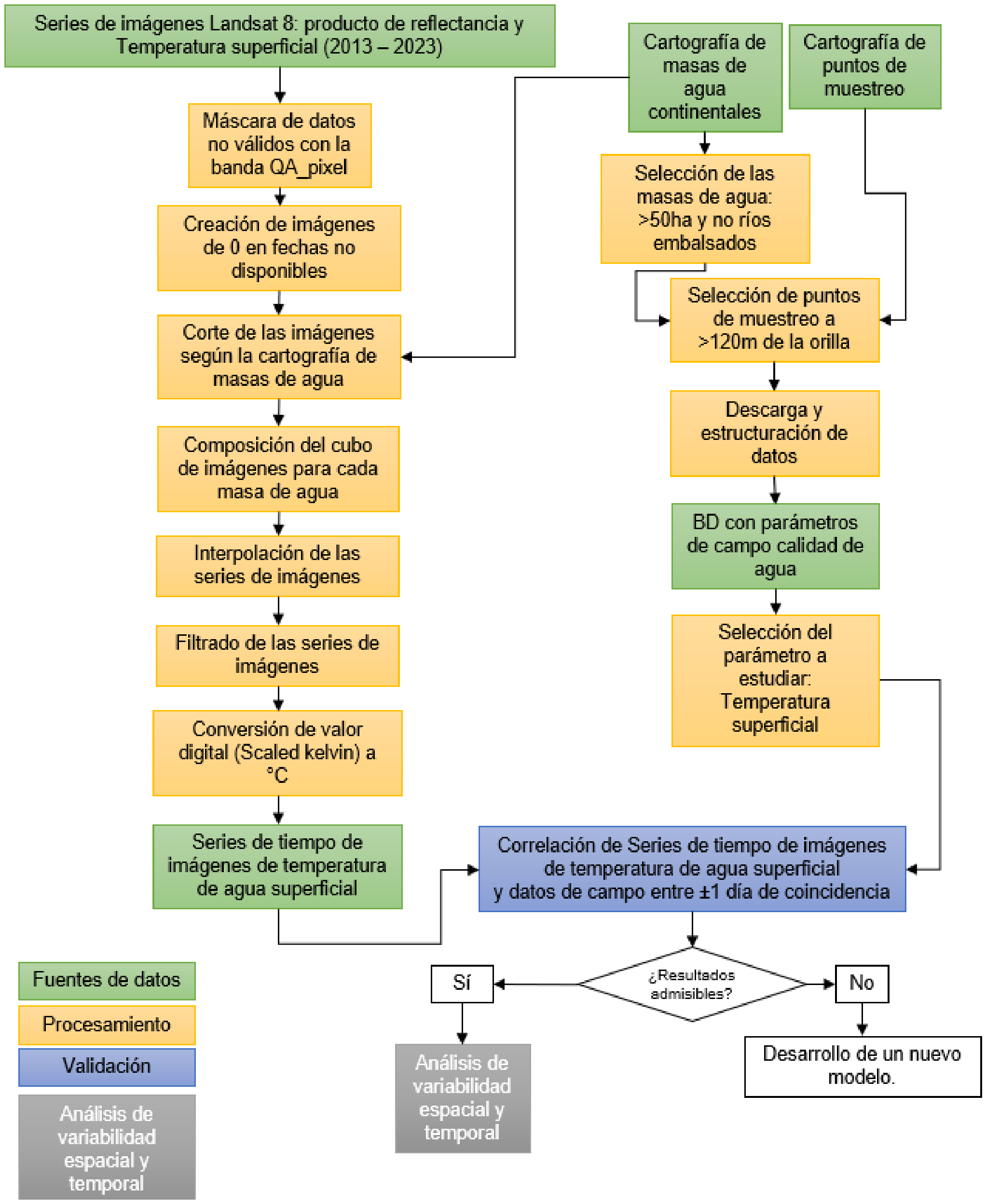

Figura 3-1: Flujograma de trabajo llevado a cabo durante la estancia en la Universidad de Coímbra.

3.4.1. Selección de las masas de agua y los puntos de muestreo

A partir de la cartografía de las masas de agua disponible en la página web https://inspire-geoportal.ec.europa.eu/srv/api/records/F8A32C30-7716-40D2-9095-920D17023056 se seleccionaron las masas de agua a estudiar con teledetección, teniendo en cuenta que estas deben tener una superficie suficiente debido al tamaño de los píxeles de la imagen. En este caso, se conocía de antemano que el trabajo se desarrollaría con Landsat dado que tiene mayor resolución espacial y el mayor periodo de funcionamiento, comparada con Sentinel 2 y 3 y MODIS. En total se seleccionaron 86 masas de agua a estudiar.

Posteriormente, a partir de la cartografía disponible en https://dados.gov.pt/es/datasets/rede-de-estacoes-de-qualidade-das-aguas-superficiais-ligacao-direta-ao-snirh-2/ se seleccionaron los puntos de muestreo que estaban ubicados lo suficientemente lejos de la orilla, para el caso de Landsat se seleccionó una distancia de 120m (máximo tamaño de píxel los diferentes sensores de Landsat. Ver Tabla 1.2) y que no estuviesen localizados en ríos embalsados. En total se seleccionaron **186** puntos de muestreo localizados **69** masas de agua (Tabla 3.1 y Figura 3-2).

Tabla 3.1: Proceso de selección de las masas de agua y puntos de muestreo.

Número puntos muestreo	**Número masas de agua**	**Filtro**
3763	148	
558	86	>50ha
210	82	> 120 m orilla
186	69	No ríos embalsados

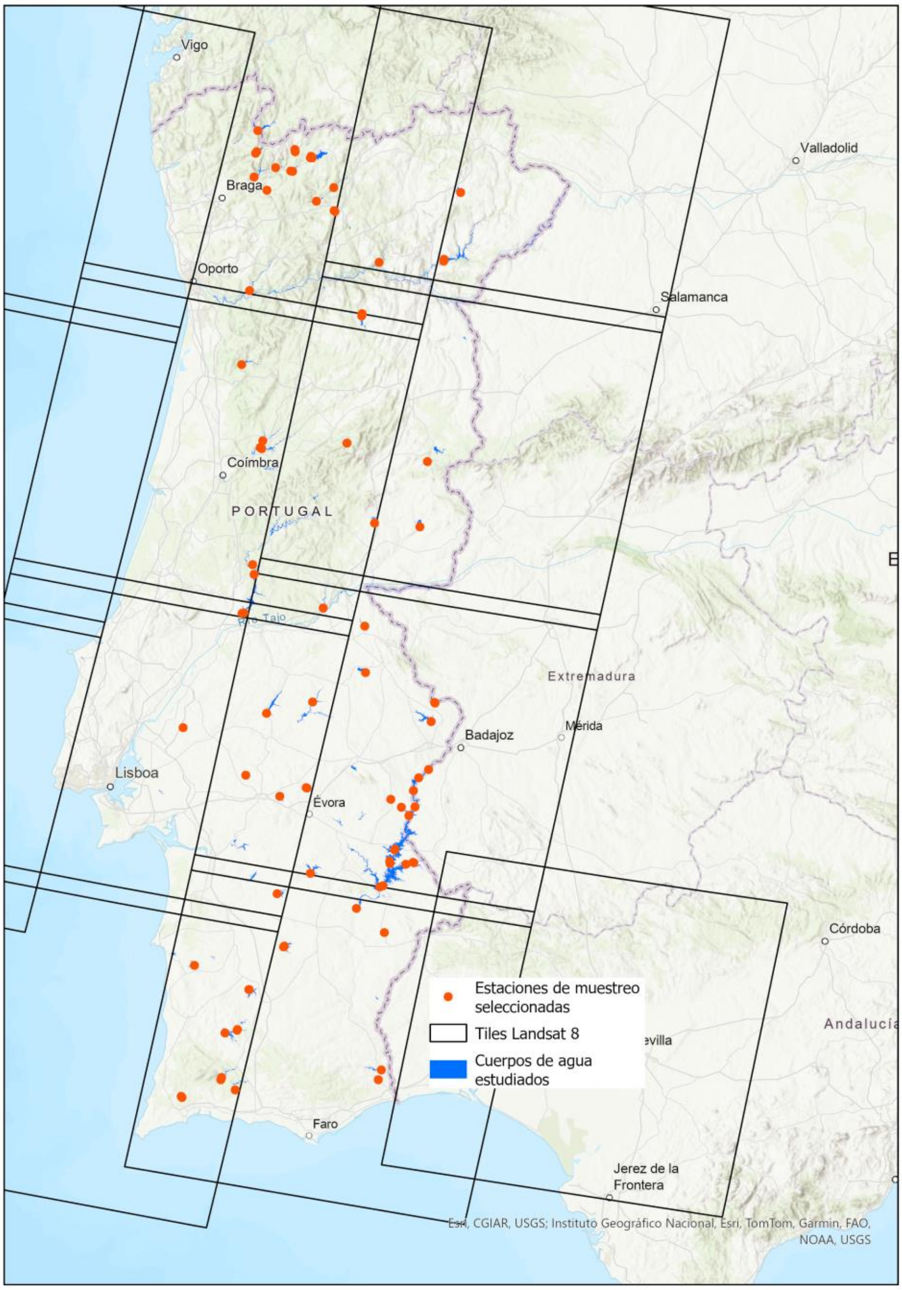

Figura 3-2: Localización de las estaciones de muestreo y las masas de agua estudiadas en Portugal.

Una vez seleccionadas las estaciones de muestreo, se descargaron los datos de campo de los parámetros de calidad de agua más estudiados con teledetección (capítulo 1.1.3) del Sistema Nacional de Información sobre recursos hídricos (https://snirh.apambiente.pt/). Se descargaron en total **95957** datos de todos los parámetros seleccionados disponibles desde el año 1981 hasta 2023, siendo el parámetro de temperatura el que más datos tiene con 71500 (Figura 3-3) en el período 2011 a 2022 (Figura 3-4).

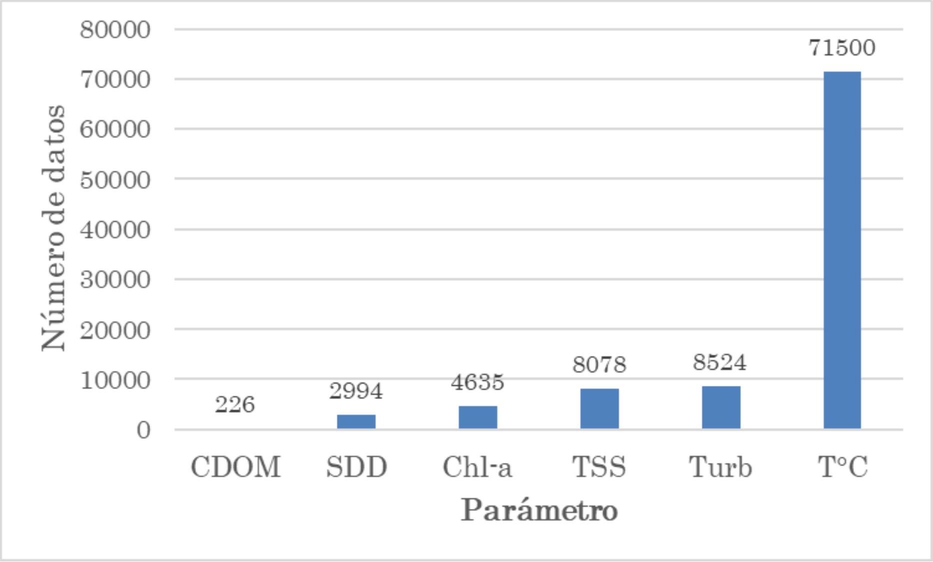

Figura 3-3: Número de datos de campo disponibles para cada parámetro de calidad de agua.

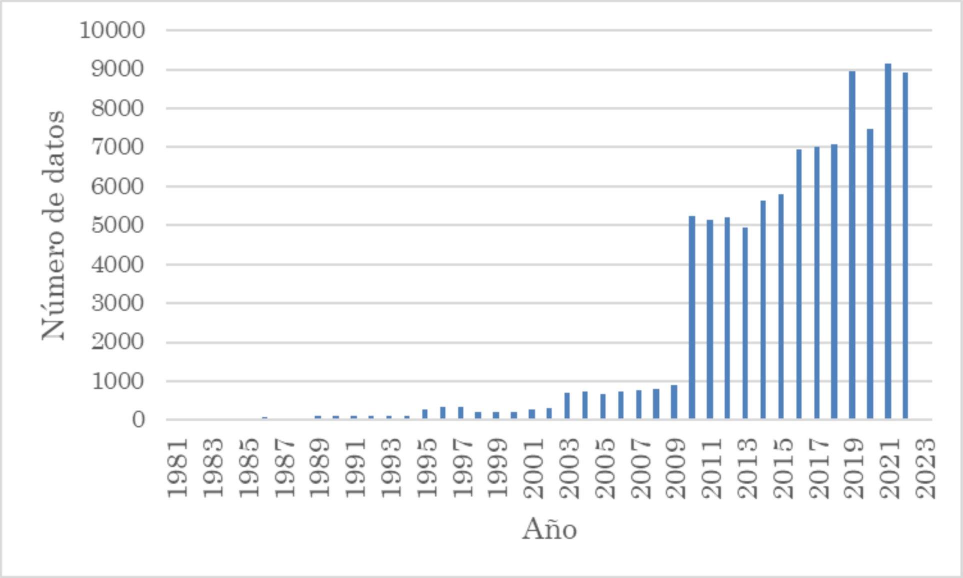

Figura 3-4: Número de datos de campo disponibles para cada año.

3.4.2. Análisis exploratorio de los datos de campo

De acuerdo con los datos de campo obtenidos, se llevó a cabo un análisis exploratorio de los datos de calidad de agua para Portugal (Tabla 3.2). Se observa que la temperatura superficial del agua, como es de esperar, es mayor en verano descendiendo en el otoño hasta obtener sus mínimos en invierno, con desviaciones estándar mayores en otoño y primavera. Para el caso de la turbidez y los sólidos en suspensión, los valores máximos se obtienen en invierno y los mínimos en verano.

Por el contrario, la clorofila alcanza sus mínimos durante el invierno y sus máximos en primavera. La transparencia, contrario a lo que se espera, es mayor en primavera y verano y mínima durante el invierno. Finalmente, el Carbono orgánico disuelto alcanza sus mínimos en invierno y sus máximos en verano.

Tabla 3.2: Análisis exploratorio de los datos de campo obtenidos.

Estación climática	Promedio	Máximo	Mínimo	Desviación estándar	Número de datos
Temperatura superficial (°C)					
Otoño	18,80	27,70	5,30	3,93	609
Primavera	15,61	29,40	2,60	3,95	469
Verano	23,37	33,50	8,50	2,76	802
Invierno	10,56	17,20	5,80	2,35	374
Total	**18,40**	**33,50**	**2,60**	**5,63**	**2254**
Turbidez (NTU)					
Otoño	4,8	152,9	0,1	9,1	1831
Primavera	5,5	516,7	0,2	18,1	1764
Verano	4,7	295,7	0,1	12,4	3255
Invierno	7,2	894	0,1	31,4	1674
Total	**5,4**	**894**	**0,1**	**18,4**	**8524**
Sólidos Totales en suspensión (mg/l)					
Otoño	8,1	698	0,1	23,5	2067
Primavera	7,8	218	0,1	14,7	1865
Verano	6,7	270	0,2	13,2	2528
Invierno	9,5	308	0,1	19,5	1618
Total	**7,9**	**698**	**0,1**	**18,0**	**8078**
Clorofila a (µg/l)					
Otoño	10,3	430	0,027	24,1	1233
Primavera	13,4	1100	0,07	46,4	1044
Verano	11,3	294	0,0028	25,0	1491
Invierno	8,4	390	0,07	27,0	867
Total	**10,9**	**1100**	**0,0028**	**31,3**	**4635**
Transparencia (m)					
Otoño	3,3	14	0,2	2,0	817
Primavera	3,5	10	0,1	2,1	641
Verano	3,5	11,4	0,2	2,0	1014
Invierno	3,1	9,5	0,18	1,9	522
Total	**3,4**	**14**	**0,1**	**2,0**	**2994**
Carbono orgánico disuelto (mg/l)					
Otoño	6,4	32	1	6,1	61
Primavera	5,9	25	1,2	4,3	48
Verano	6,7	30	0,3	4,8	78
Invierno	5,3	12	1	2,9	39
Total	**6,2**	**32**	**0,3**	**4,8**	**226**

Dado que el parámetro de calidad de agua con mayor número de datos de campo disponible es la temperatura superficial del agua con **2254** datos, se seleccionó este parámetro para analizar su comportamiento durante la estancia de investigación.

Se realizó un proceso de adecuación y homogeneización de los datos. Así, los datos de temperatura descargados de la web, obtenidos de las estaciones de muestreo se han relacionado con las imágenes del sensor TIRS del satélite Landsat 8 siguiendo la metodología estándar utilizada en los trabajos de teledetección cuando se usan datos procedentes de estaciones de muestreo o boyas (Dunn et al., 2024).

En la Figura 3-5 se observa que la mayor cantidad de datos de temperatura superficial se encuentra en la última década, por lo tanto, se ha seleccionado el satélite Landsat 8 para analizar inicialmente el comportamiento de este parámetro con teledetección.

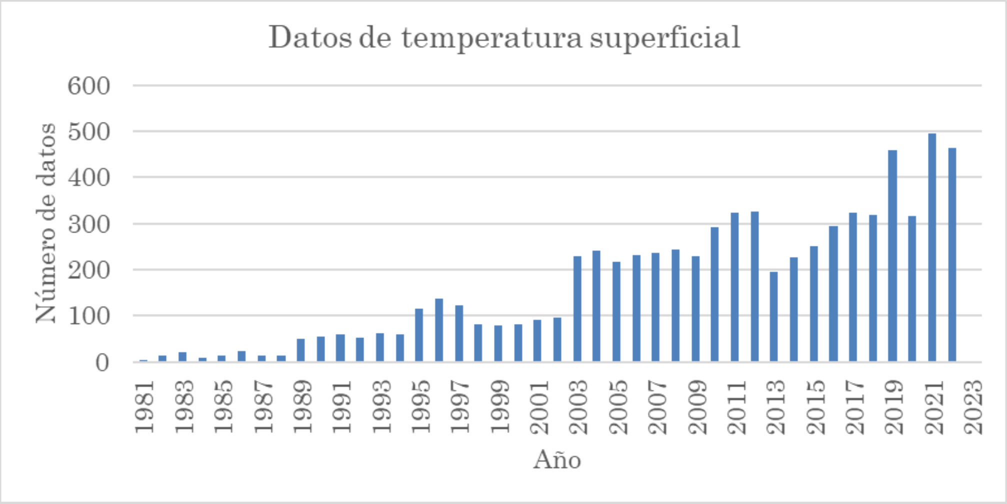

Figura 3-5: Número de datos de campo de temperatura superficial del agua disponibles para cada año.

3.4.3. Selección, descarga y procesamiento de imágenes de satélite

Como se menciona en el capítulo 3.3, en 2017, el Centro de Ciencia y Observación de Recursos Terrestres (EROS) publicó imágenes Landsat rigurosamente procesadas y calibradas radiométricamente para proporcionar a los científicos de teledetección un conjunto de datos común y consistente, entre ellos se incluye la temperatura superficial de nivel 2 del Landsat. Para esta estancia de investigación se utilizó este producto de Landsat para analizar el comportamiento de la temperatura superficial de las masas de agua en Portugal (Figura 3-6).

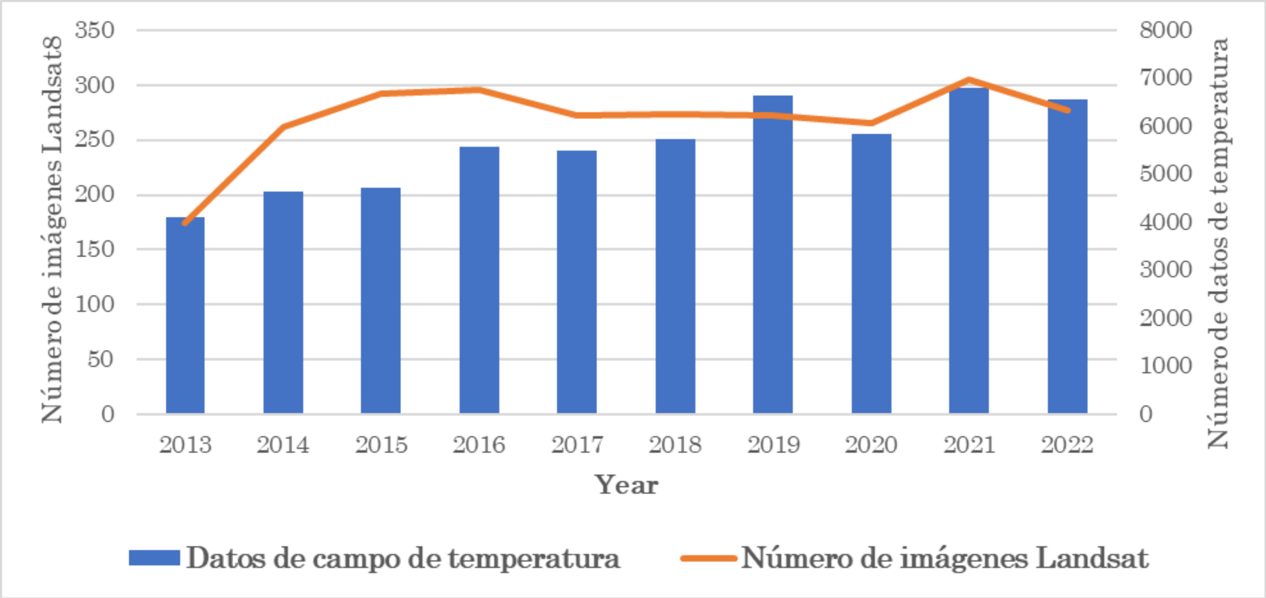

Figura 3-6: Número de datos de campo de temperatura superficial e imágenes de temperatura superficial de Landsat 8.

Inicialmente, se procesaron imágenes de temperatura superficial de Landsat 8 eliminando los valores no válidos según la banda de calidad y se seleccionaron los píxeles de agua, luego se crearon imágenes vacías para reemplazar las imágenes no disponibles y se llevó a cabo la composición del cubo de series de tiempo. Posteriormente, las series temporales se interpolaron para completar los valores faltantes, se suavizaron para eliminar los valores atípicos y los valores digitales se convirtieron a grados Centígrados (Figura 3-7).

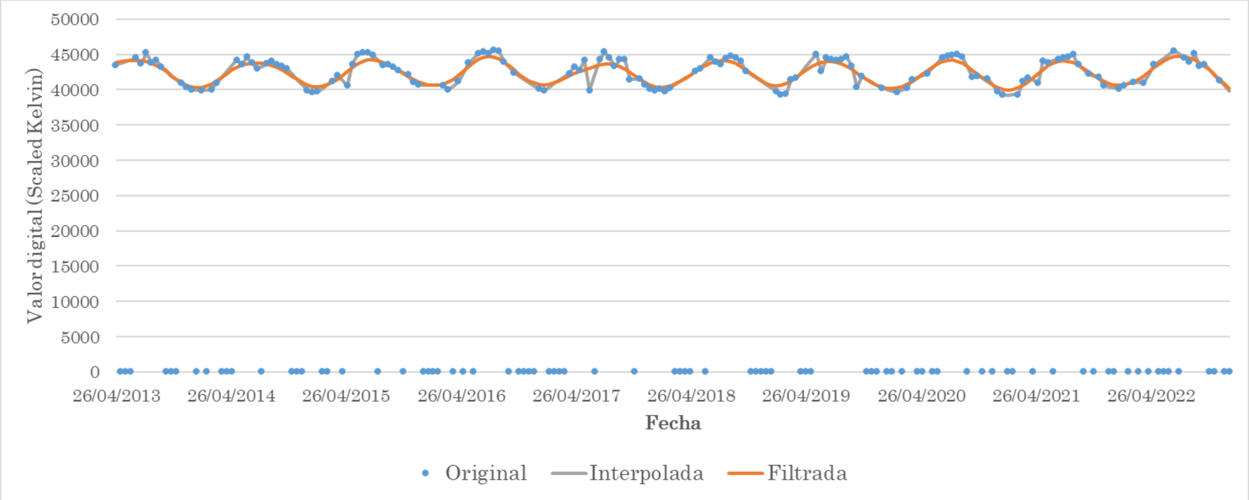

Figura 3-7: Serie de valores digitales procesados del producto de temperatura superficial de Landsat 8 en el punto de muestreo CAPTAÇÃO - CCHA (S) en el embalse PEDROGÃOARDILA.

3.4.4. Validación de las series de temperatura superficial de Landsat 8

Posteriormente, se validaron las series temporales de la temperatura superficial del agua de Landsat 8 con datos de campo para evaluar el grado de ajuste una vez aplicada la metodología de procesamiento de datos (Figura 3-8 y Figura 3-9).

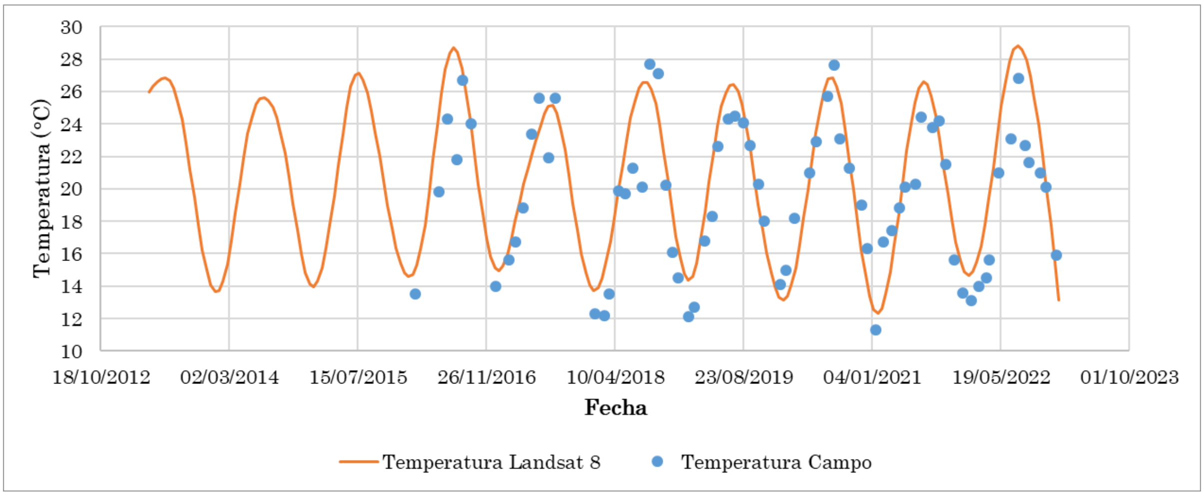

Figura 3-8: Serie de valores de temperatura superficial de Landsat 8 y los datos de campo disponibles en el punto de muestreo CAPTAÇÃO - CCHA (S) en el embalse PEDROGÃOARDILA

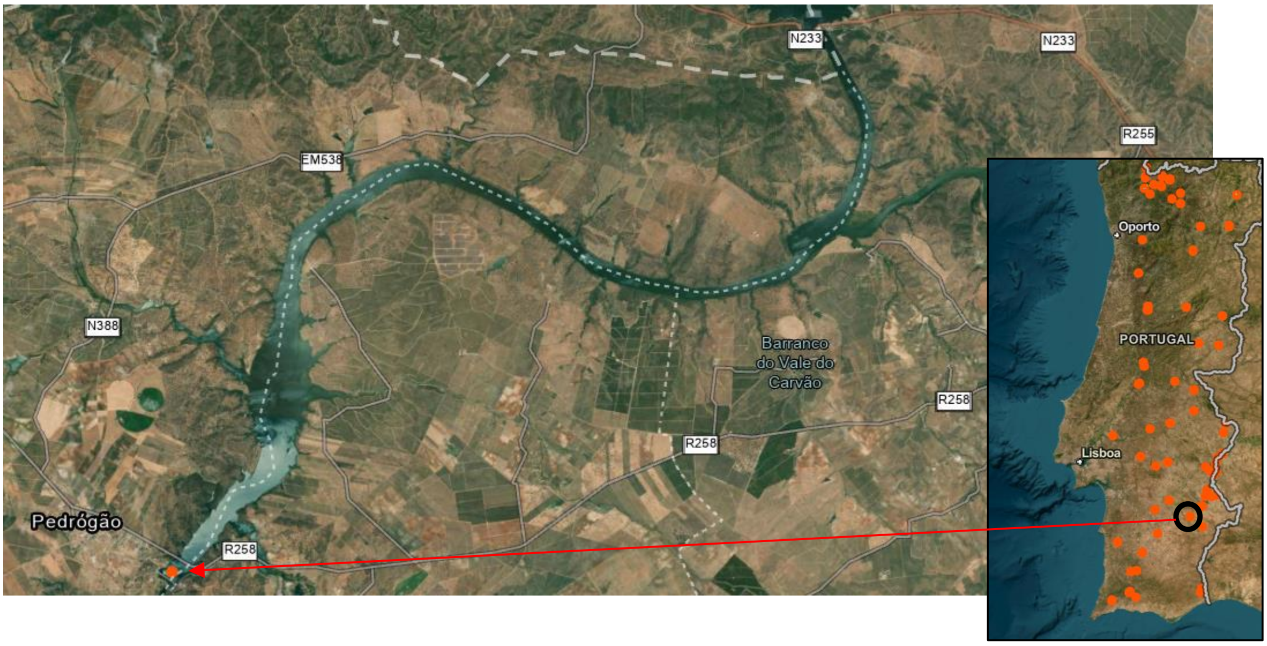

Figura 3-9: Localización del punto de muestreo CAPTAÇÃO - CCHA (S) en el embalse PEDROGÃOARDILA

Se compararon los valores de campo y de las imágenes con una coincidencia de más o menos 1 día. Se obtuvo un coeficiente de correlación de 0.83 (Figura 3-10).

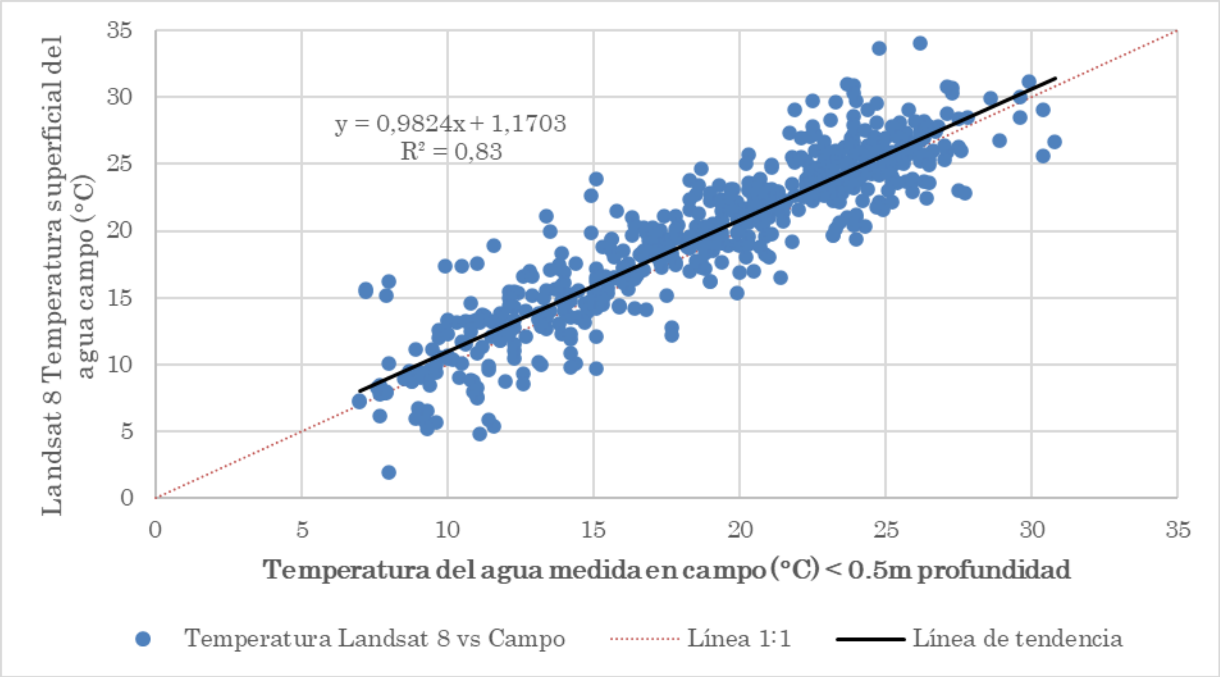

Figura 3-10: Regresión de valores de temperatura superficial del agua de los datos de campo y las imágenes Landsat 8 procesadas.

Por otro lado, se compararon los valores para cada estación de muestreo y se obtuvo el coeficiente de correlación de Pearson y su correspondiente p-valor (Tabla 3.3). Sólo se seleccionaron puntos de datos con tres o más coincidencias para calcular el coeficiente de correlación de Pearson.

Tabla 3.3: Resultado de la validación para cada punto de muestreo.

Punto de muestreo	**Número de datos**	**Coeficiente correlación Pearson**	**p-valor**
ALB. AGUIEIRA_est 1 perfil - CCHE	12	0,91	0,0000
ALB. AGUIEIRA_est 2 perfil - CCHE	12	0,92	0,0000
ALB. ALTO LINDOSO_est 2 perfil - CCHE	23	0,84	0,0000
ALB. ALTO RABAGÃO_est 1 perfil - CCHE	21	0,73	0,0002
ALB. ALTO RABAGÃO_est 2 perfil - CCHE	22	0,79	0,0000
ALB. BAIXO SABOR_est 1 perfil - CCHE	10	0,69	0,0278
ALB. BAIXO SABOR_est 2 perfil - CCHE	10	0,83	0,0029
ALB. CAIA (P)	5	0,92	0,0266
ALB. CANIÇADA_est 2 perfil - CCHE	19	0,84	0,0000
ALB. CASTELO BODE_est 1 perfil - CCHE	22	0,79	0,0000
ALB. CASTELO BODE_est 2 perfil - CCHE	22	0,81	0,0000
ALB. ENXOÉ INT (P)	6	0,76	0,0794
ALB. FOZ TUA_est 2 perfil - CCHE	5	0,98	0,0042
ALB. MONTE ROCHA (P)	8	0,89	0,0032
ALB. PARADELA_est 1 perfil - CCHE	20	0,81	0,0000

Punto de muestreo	Número de datos	Coeficiente correlación Pearson	p-valor
ALB. PARADELA_est 2 perfil - CCHE	20	0,80	0,0000
ALB. PRACANA_est 1 perfil - CCHE	7	0,98	0,0002
ALB. ROXO - CCHA (S)	5	0,81	0,0974
ALB. ROXO INT (P)	7	0,86	0,0130
ALB. SALAMONDE_est 2 perfil - CCHE	19	0,96	0,0000
ALB. SANTA CLARA 3 (P)	17	0,93	0,0000
ALB. TORRÃO_est 2 perfil - CCHE	22	0,94	0,0000
ALB. VENDA NOVA_est 1 perfil - CCHE	19	0,90	0,0000
ALB. VENDA NOVA_est 2 perfil - CCHE	19	0,97	0,0000
ALB. VILARINHO DAS FURNAS_est 1 perfil - CCHE	20	0,88	0,0000
ALB. VILARINHO DAS FURNAS_est 2 perfil - CCHE	20	0,76	0,0001
ALB. VILAR-TABUAÇO_est 1 perfil - CCHE	9	0,88	0,0017
ALB. VILAR-TABUAÇO_est 2 perfil - CCHE	21	0,89	0,0000
ALCARRACHE - CCHA (S)	5	0,39	0,5141
ALQUEVA - MOURÃO - CCHA (S)	7	0,74	0,0563
ALVITO - CCHA (S)	5	0,61	0,2743
SENHORA AJUDA - CCHA	9	0,92	0,0005

Finalmente, se obtuvieron 448 coincidencias en 32 puntos in situ en 23 masas de agua continentales. Para todas las coincidencias, el coeficiente de correlación de Pearson osciló entre 0,6 y 0,98 con todos los valores de p inferiores a 0,1, excepto en dos puntos de muestreo: Uno de ellos presentó valores del coeficiente de Pearson de 0,39 con p-valor mayor a 0,1 y otro un coeficiente de 0,61 y un p-valor mayor a 0.1. Esto quiere decir que en el 94% de los casos los valores de p fueron inferiores a 0,05, lo que indica una correlación suficientemente significativa. Esto apoya el uso de datos de teledetección en los análisis realizados.

3.4.5. Análisis de los cambios a largo plazo en la calidad de las aguas continentales en Portugal

Una vez validadas las series de temperatura superficial del agua de Landsat 8, se llevó a cabo el análisis de los cambios a largo plazo mediante análisis de tendencias, para lo cual para cada píxel en cada masa de agua se ajustó un modelo lineal y se obtuvo la pendiente y su correspondiente p-valor (Tabla 3.4).

Tabla 3.4: Resultado del análisis de tendencias para cada masa de agua. En rojo resaltados los valores mayores al 50%.

Masa de agua	Tendencia Significativa (p – valor <0.1) y positiva	Tendencia No significativa (p – valor >0.1)	Tendencia Significativa (p – valor <0.1) y negativa
69000139	45,6%	45,9%	8,5%
69000140	10,2%	73,1%	16,7%
69000144	5,1%	41,9%	53,0%
69000151	0,0%	63,6%	36,4%
69000152	0,2%	94,7%	5,1%
69000153	2,5%	75,8%	21,7%
69000155	30,3%	55,1%	14,7%
69000158	1,3%	59,8%	38,8%
69000159	16,4%	59,8%	23,8%
69000171	1,7%	69,6%	28,7%
69000172	0,0%	73,6%	26,4%
69000174	0,0%	81,6%	18,4%
69000175	21,0%	78,8%	0,2%
69000176	0,0%	75,8%	24,2%
69000182	0,0%	79,3%	20,7%
69000183	4,0%	93,8%	2,2%
69000186	20,3%	66,1%	13,6%
69000187	31,2%	68,2%	0,5%
69000190	0,0%	46,3%	53,7%
69000191	9,2%	87,8%	3,0%
69000195	1,9%	63,4%	34,7%
69000201	14,4%	73,1%	12,5%
69000203	41,8%	56,5%	1,6%
69000205	23,7%	75,0%	1,2%
69000207	0,0%	94,9%	5,1%
69000209	0,0%	69,3%	30,7%
69000210	0,0%	37,3%	62,7%
69000212	4,5%	93,8%	1,7%
69000213	0,0%	85,5%	14,5%
69000215	1,7%	46,4%	52,0%
69000216	52,5%	47,1%	0,4%
69000217	21,3%	74,7%	4,0%
69000218	81,0%	19,0%	0,0%
69000221	21,8%	74,0%	4,2%
69000222	0,0%	43,8%	56,2%
69000223	21,7%	78,3%	0,0%
69000224	0,1%	97,9%	2,0%
69000225	0,0%	99,9%	0,1%
69000226	0,0%	82,4%	17,6%
69000227	0,6%	89,4%	10,0%
69000229	0,0%	55,6%	44,4%
69000231	0,0%	98,1%	1,9%

Masa de agua	**Tendencia Significativa (p – valor <0.1) y positiva**	**Tendencia No significativa (p – valor >0.1)**	**Tendencia Significativa (p – valor <0.1) y negativa**
69000232	45,1%	54,8%	0,1%
69000233	0,1%	92,0%	7,9%
69000235	70,1%	29,8%	0,1%
69000237	0,0%	71,9%	28,1%
69000238	0,2%	87,7%	12,2%
69000241	0,3%	91,2%	8,4%
69000242	0,0%	10,6%	89,4%
69000243	0,0%	98,5%	1,5%
69000245	0,0%	73,8%	26,2%
69000246	0,0%	91,3%	8,7%
69000248	11,1%	85,1%	3,8%
69000249	15,8%	76,1%	8,1%
69000250	0,1%	19,4%	80,5%
69000251	0,0%	89,7%	10,3%
69000253	1,2%	83,7%	15,1%
69000255	0,0%	88,8%	11,2%
Grand Total	10,9%	67,2%	22,0%

En la Tabla 3.4 se observa que solo el 6% de las masas de agua presenta más de la mitad de sus píxeles con tendencia significativa positiva, en el 13% de las masas de agua la mayoría de sus píxeles (más de la mitad) tienen tendencia significativa negativa y en el 78% de los casos no tienen tendencia significativa. Esto significa que en las masas de agua de Portugal durante 2013 a 2023 no se observa una tendencia significativa en la mayoría de las masas de agua. Esto puede deberse al corto período de estudio, por lo que sería necesario ampliar la serie temporal.

En conclusión, los datos de temperatura superficial del agua medidos en las imágenes satelitales de Landsat 8 han sido validados con los datos medidos en campo. Por lo tanto, las series obtenidas pueden ser utilizadas para estudiar cambios a largo plazo de este parámetro de calidad, pero es necesario ampliar las series con otros satélites Landsat desde 1984 hasta la actualidad para identificar tendencias. Además, c los datos disponibles de los demás parámetros de la calidad del agua, es posible desarrollar modelos que correlacionen mediciones de campo con datos de series temporales de imágenes de teledetección utilizando Machine Learning. Por lo tanto, se planean investigaciones futuras para explorar más a fondo este aspecto, con el objetivo de mejorar los modelos predictivos y apoyar mejores estrategias de gestión de los recursos hídricos.

4. Discusión general y conclusiones

Esta tesis tiene como objetivo general estudiar la calidad de agua en masas de agua continentales a partir de datos de teledetección en la península Ibérica teniendo en cuenta su tamaño y su variabilidad estacional y a largo plazo. Este objetivo se ha alcanzado mediante tres objetivos específicos que han sido desarrollados en los artículos publicados y en el capítulo 3.4 Análisis de calidad del agua en Portugal.

Acerca del objetivo específico 1: identificar y evaluar sensores remotos y productos derivados que permitan estudiar la calidad de las masas de agua en la península Ibérica:

(1) En el artículo 1 se llevó a cabo la evaluación del uso del producto de reflectancia superficial de Landsat atmosféricamente corregido con LEDAPS en estudios de calidad de agua. Los resultados de la comparación entre los valores de reflectancia superficial de las bandas visibles y NIR del producto de Landsat y los datos de campo de reflectancia muestran una sobreestimación de los valores de reflectancia, que coincide con los resultados obtenidos por (Claverie et al., 2015; Maiersperger et al., 2013). A pesar de la sobreestimación detectada en las bandas visible y NIR, el enfoque de corrección atmosférica LEDAPS se ha aplicado al archivo histórico Landsat 5 disponible desde 1984 porque es un método riguroso que implica el uso de modelos de transferencia radiativa, los cuales son complicados de implementar y requieren datos de entrada que no siempre están disponibles. En esta investigación, se disponía de suficientes mediciones de DS in situ para obtener un modelo que relaciona DS y la reflectancia superficial de Landsat, pero no estaban disponibles los datos auxiliares necesarios para desarrollar una corrección atmosférica rigurosa. Por lo tanto, se decidió utilizar las imágenes corregidas y desarrollar un nuevo modelo para DS, similar a la metodología seguida por (Masek et al., 2006a). (2) Por otro lado, el objetivo específico 1 se abordó también en el artículo 1, donde se analizó el uso de las imágenes Landsat en la obtención de la transparencia medida a través del disco de Secchi. Los resultados mostraron que la validación de la ecuación propuesta para relacionar los valores de reflectancia de las imágenes Landsat atmosféricamente corregidas y los valores de transparencia medida en campo presenta resultados aceptables con un R^2 igual a 0,68, lo que respalda la hipótesis de que las mediciones in situ de DS están altamente correlacionadas con los valores de reflectancia de las bandas. Estos resultados concuerdan con otros autores, con R^2 variando de 0,4 a 0,94 (Chao

Rodríguez et al., 2014; Giardino et al., 2001; Hicks et al., 2013b; Olmanson et al., 2008; Soria et al., 2017; F. Wang et al., 2006). Aunque algunas de estas precisiones son superiores a las obtenidas en nuestro estudio, cabe señalar que, en varios de los estudios anteriores, con alta precisión de los modelos, éstos se desarrollaron para evaluar la variabilidad espacial del DS dentro de los lagos, pero no tuvieron en cuenta la variabilidad temporal. (3) Además, en el artículo 3 y en la estancia de investigación en Portugal (capítulo 3.4) se estudió el desempeño general del producto de temperatura superficial de Landsat con datos de campo en España y Portugal. Para el caso de España, se obtuvo un coeficiente de correlación de Pearson mayor a 0,6 y significativo ($p<0,1$) en todos los casos en los que coinciden las medidas de temperatura in situ con las imágenes Landsat 5 en una ventana de tres días. Para el caso de Portugal, se compararon los valores de campo y de las imágenes Landsat 8 con una coincidencia de más o menos 1 día y se obtuvo un coeficiente de correlación de 0,83, además se compararon los valores para cada estación de muestreo, obteniendo para todas las coincidencias el coeficiente de correlación de Pearson entre 0,6 y 0,98 con todos los valores de p inferiores a 0,1, excepto en dos puntos de muestreo. Esto determina que existe una correlación entre las series temporales de temperatura superficial de Landsat y la temperatura superficial in situ, y por lo tanto estas series temporales podrían ser suficientes para determinar tendencias estacionales históricas y evaluar la variabilidad interanual de las masas de agua. Esto es similar a los resultados de estudios anteriores en los que los autores concluyeron que, debido al alto rendimiento, las series temporales de los satélites Landsat pueden complementar el muestreo in situ tradicional proporcionando datos para la mayoría de las masas de agua durante un período prolongado (Baughman & Conaway, 2021; Duan et al., 2020; Schaeffer, Iiames, et al., 2018).

Por lo tanto, las imágenes Landsat demostraron ser una poderosa herramienta para estudiar la calidad del agua de las masas de agua continentales de la Península Ibérica, ya que la resolución espacial moderada y la amplia cobertura temporal de Landsat lo hacen particularmente adecuado para estudiar sus numerosos cuerpos de agua de diferentes tamaños. Especialmente, el producto de Landsat Colección 2 nivel 2 que incluye productos de temperatura superficial y reflectancia de superficie a nivel global, proporciona información relevante en el monitoreo de la calidad del agua, ya que permite derivar series de tiempo precisas de parámetros de calidad del agua como la transparencia del disco de Secchi y la temperatura superficial del agua. Esto es posible, dado que son productos atmosféricamente corregidos con métodos rigurosos, listos para ser utilizados y ampliamente empleados.

Acerca del objetivo específico 2: analizar la variación a nivel espacio – temporal de la calidad de agua a partir de determinados parámetros:

(1) En los artículos 1 y 2, a partir de las series de transparencia del agua medida con el disco de Secchi se estudió la variación espacio temporal de la calidad de masas de agua en las lagunas de gravera del Parque Regional del Sureste (PRSE) en Madrid, donde se pudo observar que su declaración como zona protegida en 1994 ha sido efectiva y ha incidido positivamente en la evolución de su calidad a lo largo de los años, aunque las masas de agua no han alcanzado el estado oligotrófico. Sin embargo, se observó un período de estancamiento entre 1989 y 2009, coincidiendo con la aparición de numerosos cuerpos de agua en la zona de explotación. Una vez que el área de los cuerpos de agua se estabilizó después de 2009, la calidad del agua aumentó significativamente en el área de estudio. A nivel estacional, se distinguen dos periodos de la transparencia: un pico en otoño e invierno (septiembre-febrero) cuando los valores de DS son superiores a la media y un periodo en verano (mayo-agosto) en el que los valores de DS son inferiores a la media. Estos resultados concuerdan con (Castagna et al., 2015; Naumenko, 2008; Rodrigo et al., 2015; Ziauddin et al., 2013), quienes concluyeron que en los meses más calurosos la transparencia del agua disminuye. Esta tendencia refleja principalmente el nivel de desarrollo de las comunidades biológicas y de la biomasa, dado que la radiación fotosintéticamente activa alcanza su máximo durante los meses más cálidos; y (2) en el artículo 3, a partir del análisis de tendencias se obtuvo que en la España peninsular la temperatura superficial de las masas de agua continentales ha aumentado durante 1994 hasta 2011. Esto es consistente con las tendencias en la temperatura de las masas de agua continentales en otros países del mundo (Aranda et al., 2021; Dokulil, 2014; Schneider et al., 2009; R. Wang et al., 2021). Los resultados presentados en este trabajo muestran que esta tendencia de calentamiento de los lagos y embalses en España representa una media de +0,037 °C al año en masas de agua con tendencia significativa, lo que supone un total de +0,592 °C durante todo el periodo de estudio. Estos resultados son consistentes con los obtenidos por (O'Reilly et al., 2015) para todo el mundo (+0,034 °C por año) y por (Woolway et al., 2020) para Europa (+0,035 °C por año). Sin embargo, son mucho más altos que los de (Virdis et al., 2020) para Cerdeña (+0,01 °C por año), y considerablemente inferiores a las estimadas por (Schneider & Hook, 2010) para Europa del Este (+0,06 °C por año). Las diferencias

pueden explicarse por la alta variabilidad espacial que pueden presentar las tendencias de temperatura superficial del agua, así como por variaciones en los períodos de estudio.

En general, a partir de las series espacio temporales de transparencia del agua y temperatura superficial derivadas de las imágenes Landsat ha sido posible estudiar las variaciones estacionales y a largo plazo de la calidad del agua. En la península ibérica, la transparencia del agua tiene sus máximos en otoño e invierno y sus mínimos en verano y la declaración como zona protegida en 1994 del PRSE ha ha tenido un impacto positivo en la evolución de su calidad a lo largo de los años. La temperatura superficial de las masas de agua en la España peninsular ha aumentado durante 1994 hasta 2011 con una media de +0,037 ºC al año.

Acerca del objetivo 3: estudiar la influencia de factores geográficos sobre determinados parámetros de calidad de agua.

Este objetivo se abordó en los artículos 2 y 3, donde se observa que en los meses más cálidos el disco de Secchi disminuye, lo que puede deberse al aumento de temperatura, dado que la transparencia se ve afectada por dos factores principales: las algas y las partículas en suspensión (Pal & Chakraborty, 2014). Esto, coincide con otras investigaciones como las del lago Ladoga (Naumenko, 2008), humedales de llanuras aluviales de la India (Naumenko, 2008), y la reserva del Parque Natural de la Albufera de Valencia (Rodrigo et al., 2015). La radiación global y la temperatura aumentan de diciembre a junio, con valores máximos en julio y valores mínimos en diciembre (Departamento de Infraestructuras y Sistemas Servicio de Redes Especiales y Vigilancia Atmosférica Centro Radiométrico Nacional, 2017), lo que es completamente inverso al de los valores de DS, donde los valores son más bajos en julio-agosto y más altos en diciembre-enero. Por su parte, la distribución de las tendencias de temperatura superficial del agua en España es altamente irregular debido a su complicada orografía y la diversidad de regiones climáticas. Si bien esta tendencia no puede atribuirse directamente a la altitud o al clima únicamente, es probable que esté influenciada por una combinación de factores climáticos y de otro tipo. Estos incluyen características locales (O'Reilly et al., 2015), altitud y posición geográfica (Stefanidis et al., 2022) y radiación solar (Woolway et al., 2020). Generalmente, los patrones espaciales de tendencia de temperatura superficial del agua y las tendencias de la temperatura del aire coinciden (Schneider & Hook, 2010; R. Wang et al., 2021; Woolway et al., 2020). Nuestros resultados muestran esta relación, particularmente en las depresiones de los ríos Ebro y Guadalquivir. Sin embargo, hay zonas donde los cuerpos de agua parecen calentarse más que el aire circundante (Austin & Colman, 2007; O'Reilly et al., 2015; Schneider & Hook, 2010). Sin embargo, se necesita más investigación para comprender completamente los procesos de calentamiento en las masas de agua de la Península Ibérica, ya que, si bien parecen estar influenciados por factores globales como la tendencia creciente de la temperatura del aire asociada al cambio climático (del Río et al., 2011; Ríos-Cornejo et al., 2015), existen otras influencias más locales como la geomorfología, la elevación y el clima que necesitan ser analizadas.

A partir del análisis del comportamiento de las isotermas, se observa que al final del período de 1994 a 2011, un número cada vez mayor de masas de agua había alcanzado temperaturas de 25°C, lo que se interpreta debido a una mayor longitud de esta isoterma en el 2011 respecto al año 1994. Sin embargo, no alcanzan esta temperatura las masas de agua situadas en la zona norte de la península. A medida que las temperaturas disminuyen en otoño, también hay una creciente prevalencia de masas de agua con temperaturas relativamente cálidas (20°C) situadas más al norte que al comienzo del período. Durante el invierno, hubo una disminución notable en la cantidad de masas de agua que se enfriaron con temperaturas que cayeron hasta 10°C o menos. Además, estas masas de agua fría también estaban situadas considerablemente más al norte en 2011 que en 1994. Estos resultados concuerdan con varios autores que estudiaron las variaciones interanuales de la temperatura superficial del agua y encontraron que las tendencias y los cambios de patrones más visibles ocurrieron durante las estaciones más frías (Aguilar-Lome et al., 2021; L. Huang et al., 2023; Niedrist et al., 2018; Öğlü et al., 2020; Virdis et al., 2020; Woolway et al., 2019).

Así se ha podido comprobar la influencia de factores geográficos en la calidad de agua. El comportamiento estacional de la transparencia puede explicarse por la relación entre el disco de Secchi y la temperatura, dado que la transparencia se ve afectada por dos factores principales: las algas y las partículas en suspensión, además, la transparencia del agua tiene un comportamiento inverso a la radiación global y la temperatura. Por otro lado, las tendencias de temperatura superficial del agua en España son altamente irregulares debido a su complicada orografía y la diversidad de regiones climáticas.

Puede decirse que se ha alcanzado el objetivo general de esta tesis, que es estudiar la calidad de agua en masas de agua continentales a partir de datos de teledetección en la península Ibérica teniendo en cuenta su tamaño y su variabilidad estacional y a largo plazo, por lo que se confirma que la teledetección es una herramienta valiosa para monitorear la calidad del agua de las masas de agua continentales en la Península Ibérica, y ha permitido abordar tareas de análisis ambiental no realizadas hasta ahora en este contexto geográfico. Por un lado, se ha llevado a cabo la validación de productos de teledetección con datos de campo de parámetros de calidad de agua, lo que ha permitido utilizar estos productos validados para analizar el comportamiento estacional y a largo plazo de la calidad de las masas de agua continentales, así como el estudio de factores externos que pueden afectar su variabilidad.

4.1. Conclusiones y líneas de investigación futuras

Las imágenes Landsat demostraron ser una poderosa herramienta para estudiar la calidad del agua de las masas de agua continentales de la Península Ibérica, ya que la resolución espacial moderada y la amplia cobertura temporal de Landsat lo hacen particularmente adecuado para estudiar sus numerosos cuerpos de agua de diferentes tamaños. Especialmente, el producto de Landsat Colección 2 nivel 2 que incluye productos de temperatura superficial y reflectancia de superficie a nivel global proporciona información relevante en el monitoreo de la calidad del agua, ya que permite derivar series de tiempo precisas de parámetros de calidad del agua como la transparencia del disco de Secchi y la temperatura superficial del agua. Esto es posible, dado que son productos atmosféricamente corregidos con métodos rigurosos, listos para ser utilizados y ampliamente empleados.

A partir de las series espacio temporales de transparencia del agua y temperatura superficial derivadas de las imágenes Landsat ha sido posible estudiar las variaciones estacionales y a largo plazo de la calidad del agua en la península Ibérica. En este contexto geográfico se ha podido constatar por primera vez que la transparencia del agua tiene sus máximos en otoño e invierno y sus mínimos en verano y herramientas legales de protección ambiental tales como la declaración como zona protegida PRSE tienen impacto positivo sobre la calidad de las aguas continentales. La temperatura superficial de las masas de agua en la España peninsular ha aumentado durante 1994 hasta 2011 con una media de +0,037 ºC al año.

Se ha comprobado que existe un comportamiento estacional de la transparencia del agua que puede explicarse por la relación entre el disco de Secchi y la temperatura, dado que la transparencia se ve afectada por dos factores principales: las algas y las partículas en suspensión, además, la transparencia del agua tiene un comportamiento inverso a la radiación global y la temperatura. Por otro lado, las tendencias de temperatura superficial del agua en España son altamente irregulares debido a su complicada orografía y la diversidad de regiones climáticas.

Es necesario estudiar las tendencias de la transparencia y la temperatura superficial del agua hasta la actualidad, para lo cual se deben actualizar las series con imágenes provenientes de sensores como Landsat 7, 8 y 9.

Además, se necesita más investigación para comprender completamente los procesos de calentamiento en las masas de agua de la Península Ibérica, ya que, si bien parecen estar influenciados por factores globales como la tendencia creciente de la temperatura del aire asociada al cambio climático, existen otras influencias más locales como la geomorfología, la elevación y el clima que necesitan ser analizadas.

4.2. Conclusions and future research lines

Landsat images has demonstrated its effectiveness as a powerful tool for studying the water quality of the Iberian Peninsula inland water bodies. The moderate spatial resolution and extensive temporal coverage offered by Landsat make it exceptionally well-suited for examining the diverse continental water bodies across the region. In particular, the Landsat Collection 2 Level 2 products, which include global surface temperature and surface reflectance data, provide valuable resources for water quality monitoring. These products, which are atmospherically corrected using rigorous methodologies, enable the accurate derivation of time series data for critical water quality parameters such as transparency and surface water temperature.

By utilizing the spatio-temporal series of water transparency and surface temperature derived from Landsat images, this study has been able to explore both seasonal and long-term variations in water quality across the Iberian Peninsula. Notably, this research has confirmed for the first time that water transparency reaches its highest levels in autumn and winter, while it declines in summer. Additionally, it has been shown that legal environmental protection measures, such as the designation of the Parque regional del Sureste (PRSE) as a protected area, have had a positive impact on the quality of continental waters. Furthermore, the study revealed a consistent increase in water surface temperatures across peninsular Spain from 1994 to 2011, with an average annual rise of +0.037 ºC.

The analysis has demonstrated that seasonal variations in water transparency are influenced by the interaction between Secchi disk measurements and environmental factors such as temperature and global radiation. Specifically, water transparency inversely correlates with global radiation and temperature, reflecting the effects of algae and suspended particles. Conversely, trends in water surface temperature exhibit considerable variability due to Spain complex orography and diverse climatic regions.

To build upon these findings, it is crucial to continue updating the time series with data from newer Landsat missions, including Landsat 7, 8, and 9.

Further research is also needed to gain a deeper understanding of the warming processes affecting the water bodies of the Iberian Peninsula. While current trends are associated with global factors such as climate change and increasing air temperatures, local influences such as geomorphology, elevation, and specific climatic conditions must also be analysed to fully understand their impacts on water temperature trends.

Bibliografía

Abdelal, Q., Assaf, M. N., Al-Rawabdeh, A., Arabasi, S., & Rawashdeh, N. A. (2022). Assessment of Sentinel-2 and Landsat-8 OLI for Small-Scale Inland Water Quality Modeling and Monitoring Based on Handheld Hyperspectral Ground Truthing. *Journal of Sensors*, *2022*. https://doi.org/10.1155/2022/4643924

Adler-Golden, S. M., Matthew, M. W., Bernstein, L. S., Levine, R. Y., Berk, A., Richtsmeier, S. C., Acharya, P. K., Anderson, G. P., Felde, J. W., Gardner, J. A., Hoke, M. L., Jeong, L. S., Pukall, B., Ratkowski, A. J., & Burke, H. K. (1999). Atmospheric correction for shortwave spectral imagery based on MODTRAN4. *Imaging Spectrometry V*, *3753*, 61–69. https://doi.org/10.1117/12.366315

Adrian, R., O'Reilly, C. M., Zagarese, H., Baines, S. B., Hessen, D. O., Keller, W., Livingstone, D. M., Sommaruga, R., Straile, D., Van Donk, E., Weyhenmeyer, G. A., & Winder, M. (2009). Lakes as sentinels of climate change. *Limnology and Oceanography*, *54*(6), 2283–2297. https://doi.org/10.4319/LO.2009.54.6_PART_2.2283

Adusei, Y. Y., Quaye-Ballard, J., Adjaottor, A. A., & Mensah, A. A. (2021). Spatial prediction and mapping of water quality of Owabi reservoir from satellite imageries and machine learning models. *The Egyptian Journal of Remote Sensing and Space Science*, *24*(3), 825–833. https://doi.org/10.1016/J.EJRS.2021.06.006

Aguilar-Lome, J., Soca-Flores, R., & Gómez, D. (2021). Evaluation of the Lake Titicaca's surface water temperature using LST MODIS time series (2000–2020). *Journal of South American Earth Sciences*, *112*, 103609. https://doi.org/10.1016/J.JSAMES.2021.103609

Alcântara, E., Bernardo, N., Watanabe, F., Rodrigues, T., Rotta, L., Carmo, A., Shimabukuro, M., Gonçalves, S., & Imai, N. (2016). Estimating the CDOM absorption coefficient in tropical inland waters using OLI/Landsat-8 images. *Remote Sensing Letters*, *7*(7), 661–670. https://doi.org/10.1080/2150704X.2016.1177242

Alcântara, E., Curtarelli, M., & Stech, J. (2016). Estimating total suspended matter using the particle backscattering coefficient: results from the

Itumbiara hydroelectric reservoir (Goiás State, Brazil). *Remote Sensing Letters*, *7*(4), 397–406. https://doi.org/10.1080/2150704X.2015.1137646

Alvarez-Cobelas, M., Riolobos, P., Himi, Y., Sánchez- Carrillo, S., García-Avilés, J., & Hidalgo, J. (2000). Estudio físico-químico de los ambientes estancados del Parque Regional del Sureste de la Comunidad de Madrid. *Centro de Investigaciones Ambientales de La Comunidad de Madrid "Fernando González Bernáldez."*

Amado-Alvarez, J., Pérez-Cutillas, P., Alatorre-Cejudo, L. C., Olguín-López, J. L., Ramírez-Valle, O., Segovia-Ortega, E. F., & Alarcón-Cabañero, J. J. (2019). Análisis multiespectral para la estimación de la turbidez como indicador de la calidad del agua en embalses del estado de Chihuahua, México. *Revista Geográfica de América Central*, *1*(62), 49–77. https://doi.org/10.15359/RGAC.62-1.2

Aranda, A. C., Rivera-Ruiz, D., Rodríguez-López, L., Pedreros, P., Arumí-Ribera, J. L., Morales-Salinas, L., Fuentes-Jaque, G., & Urrutia, R. (2021). Evidence of Climate Change Based on Lake Surface Temperature Trends in South Central Chile. *Remote Sensing 2021, Vol. 13, Page 4535*, *13*(22), 4535. https://doi.org/10.3390/RS13224535

Arias-Rodriguez, L. F., Duan, Z., Díaz-Torres, J. de J., Basilio Hazas, M., Huang, J., Kumar, B. U., Tuo, Y., & Disse, M. (2021). Integration of Remote Sensing and Mexican Water Quality Monitoring System Using an Extreme Learning Machine. *Sensors 2021, Vol. 21, Page 4118*, *21*(12), 4118. https://doi.org/10.3390/S21124118

Arias-Rodriguez, L. F., Tüzün, U. F., Duan, Z., Huang, J., Tuo, Y., & Disse, M. (2023). Global Water Quality of Inland Waters with Harmonized Landsat-8 and Sentinel-2 Using Cloud-Computed Machine Learning. *Remote Sensing*, *15*(5), 1390. https://doi.org/10.3390/RS15051390/S1

Austin, J. A., & Colman, S. M. (2007). Lake Superior summer water temperatures are increasing more rapidly than regional temperatures: A positive ice-albedo feedback. *Geophysical Research Letters*, *34*(6). https://doi.org/10.1029/2006GL029021

Bangira, T., Matongera, T. N., Mabhaudhi, T., & Mutanga, O. (2024). Remote sensing-based water quality monitoring in African reservoirs, potential and limitations of sensors and algorithms: A systematic review. *Physics and*

Chemistry of the Earth, Parts A/B/C, *134*, 103536. https://doi.org/10.1016/J.PCE.2023.103536

Barreneche, J. M., Guigou, B., Gallego, F., Barbieri, A., Smith, B., Fernández, M., Fernández, V., & Pahlevan, N. (2023). Monitoring Uruguay's freshwaters from space: An assessment of different satellite image processing schemes for chlorophyll-a estimation. *Remote Sensing Applications: Society and Environment*, *29*, 100891. https://doi.org/10.1016/J.RSASE.2022.100891

Baughman, C. A., & Conaway, J. S. (2021). Comparison of Historical Water Temperature Measurements with Landsat Analysis Ready Data Provisional Surface Temperature Estimates for the Yukon River in Alaska. *Remote Sensing 2021, Vol. 13, Page 2394*, *13*(12), 2394. https://doi.org/10.3390/RS13122394

Bernardo, N., Carmo, A., Rotta, L., & Alcântara, E. (2020). Single tuned algorithm to estimate the SPM concentration in a cascade reservoir system using OLI/L8 images. *Advances in Space Research*, *66*(11), 2583–2596. https://doi.org/10.1016/J.ASR.2020.08.035

Bernardo, N., do Carmo, A., Park, E., & Alc'ntara, E. (2019). Retrieval of Suspended Particulate Matter in Inland Waters with Widely Differing Optical Properties Using a Semi-Analytical Scheme. *Remote Sensing 2019, Vol. 11, Page 2283*, *11*(19), 2283. https://doi.org/10.3390/RS11192283

Blanchet, C. C., Arzel, C., Davranche, A., Kahilainen, K. K., Secondi, J., Taipale, S., Lindberg, H., Loehr, J., Manninen-Johansen, S., Sundell, J., Maanan, M., & Nummi, P. (2022). Ecology and extent of freshwater browning - What we know and what should be studied next in the context of global change. *Science of The Total Environment*, *812*, 152420. https://doi.org/10.1016/J.SCITOTENV.2021.152420

Bonansea, M., Rodriguez, M. C., Pinotti, L., & Ferrero, S. (2015). Using multi-temporal Landsat imagery and linear mixed models for assessing water quality parameters in Río Tercero reservoir (Argentina). *Remote Sensing of Environment*, *158*, 28–41. https://doi.org/10.1016/J.RSE.2014.10.032

Caballero, I., Roca, M., Santos-Echeandía, J., Bernárdez, P., & Navarro, G. (2022). *Use of the Sentinel-2 and Landsat-8 Satellites for Water Quality Monitoring: An Early Warning Tool in the Mar Menor Coastal Lagoon*. https://doi.org/10.3390/rs14122744

Cao, N., Zhang, F., Liu, C., Chan, N. W., Tan, M. L., Shi, J., & Lin, X. (2023). Spatio-temporal analysis of colored dissolved organic matter over Ebinur Lake in Xinjiang, China. *Ecological Informatics*, *78*, 102339. https://doi.org/10.1016/J.ECOINF.2023.102339

Cao, Z., Duan, H., Song, Q., Shen, M., Ma, R., & Liu, D. (2018). Evaluation of the sensitivity of China's next-generation ocean satellite sensor MWI onboard the Tiangong-2 space lab over inland waters. *International Journal of Applied Earth Observation and Geoinformation*, *71*, 109–120. https://doi.org/10.1016/J.JAG.2018.05.012

Cao, Z., Ma, R., Liu, M., Duan, H., Xiao, Q., Xue, K., & Shen, M. (2022). Harmonized Chlorophyll-a Retrievals in Inland Lakes From Landsat-8/9 and Sentinel 2A/B Virtual Constellation Through Machine Learning. *IEEE Transactions on Geoscience and Remote Sensing*, *60*. https://doi.org/10.1109/TGRS.2022.3207345

Castagna, S. E. D., De Luca, D. A., & Lasagna, M. (2015). Eutrophication of Piedmont Quarry Lakes (North-Western Italy): Hydrogeological Factors, Evaluation of Trophic Levels and Management Strategies. *Journal of Environmental Assessment Policy and Management*, *17*(4). https://doi.org/10.1142/S1464333215500362

Chao Rodríguez, Y., El Anjoumi, A., Domínguez Gómez, J. A., Rodríguez Pérez, D., & Rico, E. (2013). Using Landsat image time series to study a small water body in Northern Spain. *Environ. Monit. Assess.* https://doi.org/10.1007/s10661-014-3634-8

Chao Rodríguez, Y., El Anjoumi, A., Domínguez Gómez, J. A., Rodríguez Pérez, D., & Rico, E. (2014). Using Landsat image time series to study a small water body in Northern Spain. *Environmental Monitoring and Assessment*, *186*(6). https://doi.org/10.1007/s10661-014-3634-8

Chegoonian, A. M., Pahlevan, N., Zolfaghari, K., Leavitt, P. R., Davies, J. M., Baulch, H. M., & Duguay, C. R. (2023). Comparative Analysis of Empirical and Machine Learning Models for Chla Extraction Using Sentinel-2 and Landsat OLI Data: Opportunities, Limitations, and Challenges. *Canadian Journal of Remote Sensing*, *49*(1), 2215333. https://doi.org/10.1080/07038992.2023.2215333

Chen, J., Zhu, W. N., Tian, Y. Q., & Yu, Q. (2017). Estimation of Colored Dissolved Organic Matter from Landsat-8 Imagery for Complex Inland Water: Case Study of Lake Huron. *IEEE Transactions on Geoscience and Remote Sensing*, *55*(4), 2201–2212. https://doi.org/10.1109/TGRS.2016.2638828

Chen, M., Xiao, F., Wang, Z., Feng, Q., Ban, X., Zhou, Y., & Hu, Z. (2022). An Improved QAA-Based Method for Monitoring Water Clarity of Honghu Lake Using Landsat TM, ETM+ and OLI Data. *Remote Sensing 2022, Vol. 14, Page 3798*, *14*(15), 3798. https://doi.org/10.3390/RS14153798

Chen, Q., Zhang, Y., Ekroos, A., & Hallikainen, M. (2004). The role of remote sensing technology in the EU water framework directive (WFD). *Environmental Science & Policy*, *7*(4), 267–276. https://doi.org/10.1016/J.ENVSCI.2004.05.002

Chen, Z., Zhang, S. R., Coster, A. J., & Fang, G. (2015). EOF analysis and modeling of GPS TEC climatology over North America. *Journal of Geophysical Research: Space Physics*, *120*(4), 3118–3129. https://doi.org/10.1002/2014JA020837

Chu, H. J., Kong, S. J., & Chang, C. H. (2018). Spatio-temporal water quality mapping from satellite images using geographically and temporally weighted regression. *International Journal of Applied Earth Observation and Geoinformation*, *65*, 1–11. https://doi.org/10.1016/J.JAG.2017.10.001

Claverie, M., Vermote, E. F., Franch, B., & Masek, J. G. (2015). Evaluation of the Landsat-5 TM and Landsat-7 ETM + surface reflectance products. *Remote Sensing of Environment*, *169*, 390–403. https://doi.org/10.1016/J.RSE.2015.08.030

Coelho, C., Heim, B., Foerster, S., Brosinsky, A., & de Araújo, J. C. (2017). In Situ and Satellite Observation of CDOM and Chlorophyll-a Dynamics in Small Water Surface Reservoirs in the Brazilian Semiarid Region. *Water 2017, Vol. 9, Page 913*, *9*(12), 913. https://doi.org/10.3390/W9120913

Concha, J. A., & Schott, J. R. (2016). Retrieval of color producing agents in Case 2 waters using Landsat 8. *Remote Sensing of Environment*, *185*, 95–107. https://doi.org/10.1016/J.RSE.2016.03.018

Copeland, C. (2016). *Clean Water Act: A Summary of the Law*. www.crs.gov

Cui, Y., Yan, Z., Wang, J., Hao, S., & Liu, Y. (2022). Deep learning–based remote sensing estimation of water transparency in shallow lakes by combining

Landsat 8 and Sentinel 2 images. *Environmental Science and Pollution Research*, *29*(3), 4401–4413. https://doi.org/10.1007/S11356-021-16004-9/FIGURES/7

Dallosch, M. A., & Creed, I. F. (2021). Optimization of landsat Chl-a retrieval algorithms in freshwater lakes through classification of optical water types. *Remote Sensing*, *13*(22), 4607. https://doi.org/10.3390/RS13224607/S1

Dave, A., Chaplot, N., Chander, S., Gujarati, A., Singh, R. P., Patel, H. M., & Patel, U. D. (2019). Assessment of Water Quality Parameters for Some Inland Water Bodies of Western India Using Landsat 8 Data. *World Environmental and Water Resources Congress 2019: Groundwater, Sustainability, Hydro-Climate/Climate Change, and Environmental Engineering - Selected Papers from the World Environmental and Water Resources Congress 2019*, 98–107. https://doi.org/10.1061/9780784482346.010

Dekker, & Hestir. (2012). Evaluating the feasibility of systematic inland water quality monitoring with satellite remote sensing. *Publications.Csiro.Au*. https://publications.csiro.au/rpr/download?pid=csiro:EP117441&dsid=DS10

del Río, S., Herrero, L., Pinto-Gomes, C., & Penas, A. (2011). Spatial analysis of mean temperature trends in Spain over the period 1961–2006. *Global and Planetary Change*, *78*(1–2), 65–75. https://doi.org/10.1016/J.GLOPLACHA.2011.05.012

Departamento de Infraestructuras y Sistemas Servicio de Redes Especiales y Vigilancia Atmosférica Centro Radiométrico Nacional. (2017). Resumen mensual de la radiación solar diciembre 2017. In *Agencia Estatal de Meteorología*.

Deutsch, E. S., Cardille, J. A., Koll-Egyed, T., & Fortin, M. J. (2021). Landsat 8 Lake Water Clarity Empirical Algorithms: Large-Scale Calibration and Validation Using Government and Citizen Science Data from across Canada. *Remote Sensing 2021, Vol. 13, Page 1257*, *13*(7), 1257. https://doi.org/10.3390/RS13071257

Deutsch, E. S., Fortin, M. J., & Cardille, J. A. (2022). Assessing the current water clarity status of ~100,000 lakes across southern Canada: A remote sensing approach. *Science of The Total Environment*, *826*, 153971. https://doi.org/10.1016/J.SCITOTENV.2022.153971

Dokulil, M. T. (2014). Impact of climate warming on European inland waters. *Inland Waters*, *4*(1), 27–40. https://doi.org/10.5268/IW-4.1.705

Domínguez Gómez, J. A., Chuvieco Salinero, E., & Sastre Merlín, A. (2009). Monitoring transparency in inland water bodies using multispectral images. *International Journal of Remote Sensing*, *30*(6), 1567–1586. https://doi.org/10.1080/01431160802513811

Domínguez Gómez, J. A., & Peña, R. (1999). Trophic state assessment in two gravel pits (El Campillo & El Porcal) using airborne imagery. *Limnetica*, *16*.

Domínguez Gómez, J. A., tes.), E. C. S. (dir., tes), A. S. M. (codir., (pres.), S. C. F., (secr.), F. M. S., (voc.), N. C. D., (voc.), M. J. L. G., & (voc.), S. M. P. (2002). *Estudio de la calidad del agua de las lagunas de gravera mediante teledetección*. https://portalcientifico.uah.es/documentos/6142af4527af2147d14444c9

Domínguez, J. A., Peña, R., & Sastre, A. (1997). Detección de cambios en los humedales del río Jarama entre 1988 y 1992 y evaluación de estado trófico de las lagunas del Campillo, el Porcal y las Madres en 1992 mediante imágenes Landsat TM. *Teledetección Aplicada a La Gestión de Recursos Naturales y Medio Litoral Marino*, 339–351.

Doña, C., Sánchez, J. M., Caselles, V., Domínguez, J. A., & Camacho, A. (2014). Empirical relationships for monitoring water quality of lakes and reservoirs through multispectral images. *IEEE Journal of Selected Topics in Applied Earth Observations and Remote Sensing*, *7*(5), 1632–1641. https://doi.org/10.1109/JSTARS.2014.2301295

Dörnhöfer, K., & Oppelt, N. (2016). Remote sensing for lake research and monitoring – Recent advances. *Ecological Indicators*, *64*, 105–122. https://doi.org/10.1016/J.ECOLIND.2015.12.009

Duan, S. B., Li, Z. L., Zhao, W., Wu, P., Huang, C., Han, X. J., Gao, M., Leng, P., & Shang, G. (2020). Validation of Landsat land surface temperature product in the conterminous United States using in situ measurements from SURFRAD, ARM, and NDBC sites. *Https://Doi.Org/10.1080/17538947.2020.1862319*, *14*(5), 640–660. https://doi.org/10.1080/17538947.2020.1862319

Dunn, R. J. K., Talavera, L., Antonio Domínguez-Gómez, J., Navarro, N., & Rodríguez-Santalla, I. (2024). Analysing Spatiotemporal Variability of

Chlorophyll-a Concentration and Water Surface Temperature in Coastal Lagoons of the Ebro Delta (NW Mediterranean Sea, Spain). *Journal of Marine Science and Engineering 2024, Vol. 12, Page 941*, *12*(6), 941. https://doi.org/10.3390/JMSE12060941

Du, Y., Song, K., Liu, G., Wen, Z., Fang, C., Shang, Y., Zhao, F., Wang, Q., Du, J., & Zhang, B. (2020). Quantifying total suspended matter (TSM) in waters using Landsat images during 1984–2018 across the Songnen Plain, Northeast China. *Journal of Environmental Management*, *262*, 110334. https://doi.org/10.1016/J.JENVMAN.2020.110334

EC. (2000). Directive 2000/60/EC of the European Parliament and of the Council of 23 October 2000 establishing a framework for Community action in the field of water policy. *Official Journal of the European Parliament*, *L327*. https://doi.org/10.1039/ap9842100196

El-Alem, A., & Chokmani, K. (2022). A Machine Learning-Based Regional Hybrid Model for Remote Retrieving Turbidity from Landsat Imagery. *IEEE Geoscience and Remote Sensing Letters*, *19*. https://doi.org/10.1109/LGRS.2021.3115986

Erena, M., Domínguez, J. A., Aguado-Giménez, F., Soria, J., & García-Galiano, S. (2019). Monitoring Coastal Lagoon Water Quality through Remote Sensing: The Mar Menor as a Case Study. *Water 2019, Vol. 11, Page 1468*, *11*(7), 1468. https://doi.org/10.3390/W11071468

Fukushima, T., Ozaki, N., Kaminishi, H., Harasawa, H., & Matsushige, K. (2000). Forecasting the changes in lake water quality in response to climate changes, using past relationships between meteorological conditions and water quality. *HYDROLOGICAL PROCESSES*, *14*, 593–604. https://doi.org/10.1002/(SICI)1099-1085(20000228)14:3

Ghirardi, N., Pinardi, M., Nizzoli, D., Viaroli, P., & Bresciani, M. (2023). The Long-Term Detection of Suspended Particulate Matter Concentration and Water Colour in Gravel and Sand Pit Lakes through Landsat and Sentinel-2 Imagery. *Remote Sensing*, *15*(23), 5564. https://doi.org/10.3390/RS15235564/S1

Giardino, C., Bresciani, M., Stroppiana, D., Oggioni, A., & Morabito, G. (2014). Optical remote sensing of lakes: an overview on Lake Maggiore. *Journal of Limnology*, *73*(s1), 201–214. https://doi.org/10.4081/JLIMNOL.2014.817

Giardino, C., Pepe, M., Brivio, P. A., Ghezzi, P., & Zilioli, E. (2001). Detecting chlorophyll, Secchi disk depth and surface temperature in a sub-alpine lake using Landsat imagery. *Science of the Total Environment*, *268*(1–3). https://doi.org/10.1016/S0048-9697(00)00692-6

Gilabert, M. A., Conese, C., & Maselli, F. (1994). An atmospheric correction method for the automatic retrieval of surface reflectances from tm images. *International Journal of Remote Sensing*, *15*(10), 2065–2086. https://doi.org/10.1080/01431169408954228

Godah, W., Szelachowska, M., & Krynski, J. (2018). Application of the PCA/EOF method for the analysis and modelling of temporal variations of geoid heights over Poland. *Acta Geodaetica et Geophysica*, *53*(1), 93–105. https://doi.org/10.1007/S40328-017-0206-8/TABLES/3

Guo, H., Tian, S., Jeanne Huang, J., Zhu, X., Wang, B., & Zhang, Z. (2022). Performance of deep learning in mapping water quality of Lake Simcoe with long-term Landsat archive. *ISPRS Journal of Photogrammetry and Remote Sensing*, *183*, 451–469. https://doi.org/10.1016/J.ISPRSJPRS.2021.11.023

Guo, H., Zhu, X., Jeanne Huang, J., Zhang, Z., Tian, S., & Chen, Y. (2023). An enhanced deep learning approach to assessing inland lake water quality and its response to climate and anthropogenic factors. *Journal of Hydrology*, *620*, 129466. https://doi.org/10.1016/J.JHYDROL.2023.129466

Hafeez, S., Wong, M. S., Abbas, S., & Asim, M. (2022). Evaluating Landsat-8 and Sentinel-2 Data Consistency for High Spatiotemporal Inland and Coastal Water Quality Monitoring. *Remote Sensing*, *14*(13), 3155. https://doi.org/10.3390/RS14133155/S1

Ha, N. T. T., Koike, K., Nhuan, M. T., Canh, B. D., Thao, N. T. P., & Parsons, M. (2017). Landsat 8/OLI Two bands ratio algorithm for chlorophyll-a concentration mapping in hypertrophic waters: An application to west lake in Hanoi (Vietnam). *IEEE Journal of Selected Topics in Applied Earth Observations and Remote Sensing*, *10*(11), 4919–4929. https://doi.org/10.1109/JSTARS.2017.2739184

Hestir, E. L., Brando, V. E., Bresciani, M., Giardino, C., Matta, E., Villa, P., & Dekker, A. G. (2015). Measuring freshwater aquatic ecosystems: The need for a hyperspectral global mapping satellite mission. *Remote Sensing of Environment*, *167*. https://doi.org/10.1016/j.rse.2015.05.023

He, Y., Gong, Z., Zheng, Y., & Zhang, Y. (2021). Inland Reservoir Water Quality Inversion and Eutrophication Evaluation Using BP Neural Network and Remote Sensing Imagery: A Case Study of Dashahe Reservoir. *Water 2021, Vol. 13, Page 2844*, *13*(20), 2844. https://doi.org/10.3390/W13202844

Hicks, B. J., Stichbury, G. A., Brabyn, L. K., Allan, M. G., & Ashraf, S. (2013a). Hindcasting water clarity from Landsat satellite images of unmonitored shallow lakes in the Waikato region, New Zealand. *Environmental Monitoring and Assessment*, *185*(9), 7245–7261. https://doi.org/10.1007/S10661-013-3098-2/TABLES/8

Hicks, B. J., Stichbury, G. A., Brabyn, L. K., Allan, M. G., & Ashraf, S. (2013b). Hindcasting water clarity from Landsat satellite images of unmonitored shallow lakes in the Waikato region, New Zealand. *Environmental Monitoring and Assessment*, *185*(9). https://doi.org/10.1007/s10661-013-3098-2

HovmÖller, E. (1949). The Trough-and-Ridge diagram. *Tellus*, *1*(2), 62–66. https://doi.org/10.3402/TELLUSA.V1I2.8498

Huang, L., Wang, X., Yan, Y., Jin, L., Yang, K., Chen, A., Zheng, R., Ottlé, C., Wang, C., Cui, Y., & Piao, S. (2023). Attribution of Lake Surface Water Temperature Change in Large Lakes Across China Over Past Four Decades. *Journal of Geophysical Research: Atmospheres*, *128*(21), e2022JD038465. https://doi.org/10.1029/2022JD038465

Huang, Y., Liu, H., Hinkel, K., Beck, R., Yu, B., & Wu, J. (2015). Analysis of water temperature variability of Arctic lakes using Landsat-8 data. *International Geoscience and Remote Sensing Symposium (IGARSS)*, *2015-November*, 2501–2503. https://doi.org/10.1109/IGARSS.2015.7326318

Huang, Y., Liu, H., Hinkel, K., Yu, B., Beck, R., & Wu, J. (2017). Analysis of Thermal Structure of Arctic Lakes at Local and Regional Scales Using in Situ and Multidate Landsat-8 Data. *Water Resources Research*, *53*(11), 9642–9658. https://doi.org/10.1002/2017WR021335

Imen, S., Chang, N. Bin, & Yang, Y. J. (2015). Developing the remote sensing-based early warning system for monitoring TSS concentrations in Lake Mead. *Journal of Environmental Management*, *160*, 73–89. https://doi.org/10.1016/J.JENVMAN.2015.06.003

IOCCG. (2010). *Atmospheric Correction for Remotely-Sensed Ocean-Colour Products. 10*. http://www.ioccg.org

Jakovljevic, G., Álvarez-Taboada, F., & Govedarica, M. (2023). Long-Term Monitoring of Inland Water Quality Parameters Using Landsat Time-Series and Back-Propagated ANN: Assessment and Usability in a Real-Case Scenario. *Remote Sensing 2024, Vol. 16, Page 68*, *16*(1), 68. https://doi.org/10.3390/RS16010068

Jimenez-Munoz, J. C., Cristobal, J., Sobrino, J. A., Sòria, G., Ninyerola, M., & Pons, X. (2009). Revision of the single-channel algorithm for land surface temperature retrieval from landsat thermal-infrared data. *IEEE Transactions on Geoscience and Remote Sensing*, *47*(1), 339–349. https://doi.org/10.1109/TGRS.2008.2007125

Kloiber, S. M., Brezonik, P. L., Olmanson, L. G., & Bauer, M. E. (2002). A procedure for regional lake water clarity assessment using Landsat multispectral data. *Remote Sensing of Environment*, *82*(1), 38–47. https://doi.org/10.1016/S0034-4257(02)00022-6

Koll-Egyed, T., Cardille, J. A., & Deutsch, E. (2021). Multiple images improve lake CDOM estimation: Building better landsat 8 empirical algorithms across southern canada. *Remote Sensing*, *13*(18), 3615. https://doi.org/10.3390/RS13183615/S1

Kong, X., Li, Y., Wang, L., & Liu, H. (2024). Lake Surface Temperature Retrieval Study Based on Landsat 8 Satellite Imagery—A Case Study of Poyang Lake. *Atmosphere 2024, Vol. 15, Page 428*, *15*(4), 428. https://doi.org/10.3390/ATMOS15040428

Kramer, G., Filho, W. P., de Carvalho, L. A. S., Trindade, P. M. P., da Rosa, C. N., & Dezordi, R. (2023). Performance and validation of water surface temperature estimates from Landsat 8 of the Itaipu Reservoir, State of Paraná, Brazil. *Environmental Monitoring and Assessment*, *195*(1), 1–17. https://doi.org/10.1007/S10661-022-10677-6/FIGURES/6

Kutser, T. (2012). The possibility of using the Landsat image archive for monitoring long time trends in coloured dissolved organic matter concentration in lake waters. *Remote Sensing of Environment*, *123*, 334–338. https://doi.org/10.1016/J.RSE.2012.04.004

Kutser, T., Paavel, B., Verpoorter, C., Ligi, M., Soomets, T., Toming, K., Casal, G., Zhang, Y., Giardino, C., Li, L., Mishra, D. R., & Thenkabail, P. S. (2016). Remote Sensing of Black Lakes and Using 810 nm Reflectance Peak for

Retrieving Water Quality Parameters of Optically Complex Waters. *Remote Sensing 2016, Vol. 8, Page 497*, *8*(6), 497. https://doi.org/10.3390/RS8060497

Lamaro, A. A., Mariñelarena, A., Torrusio, S. E., & Sala, S. E. (2013). Water surface temperature estimation from Landsat 7 ETM+ thermal infrared data using the generalized single-channel method: Case study of Embalse del Río Tercero (Córdoba, Argentina). *Advances in Space Research*, *51*(3), 492–500. https://doi.org/10.1016/J.ASR.2012.09.032

Ledesma, M. M., Bonansea, M., Ledesma, C. R., Rodríguez, C., Carreño, J., & Pinotti, L. (2019). Estimation of chlorophyll-a concentration using Landsat 8 in the Cassaffousth reservoir. *Water Supply*, *19*(7), 2021–2027. https://doi.org/10.2166/WS.2019.080

Lehmann, M. K., Nguyen, U., Muraoka, K., & Allan, M. G. (2019). Regional trends in remotely sensed water clarity over 18 years in the Rotorua Lakes, New Zealand. *New Zealand Journal of Marine and Freshwater Research*, *53*(4), 513–535. https://doi.org/10.1080/00288330.2019.1609051

Li, J., Yu, Q., Tian, Y. Q., Becker, B. L., Siqueira, P., & Torbick, N. (2018). Spatio-temporal variations of CDOM in shallow inland waters from a semi-analytical inversion of Landsat-8. *Remote Sensing of Environment*, *218*, 189–200. https://doi.org/10.1016/J.RSE.2018.09.014

Liu, Y., Islam, A., & Gao, J. (2003). Quantification of shallow water quality parameters by means of remote sensing. *Progress in Physical Geography*, *27*(1), 24–43. https://doi.org/10.1191/0309133303PP357RA

Livingstone, D. M., Lotter, A. F., & Walkert, I. R. (1999). The Decrease in Summer Surface Water Temperature with Altitude in Swiss Alpine Lakes: A Comparison with Air Temperature Lapse Rates. *Arctic, Antarctic, and Alpine Research*, *31*(4), 341–352. http://about.jstor.org/terms

Li, W. ;, Yang, Q. ;, Ma, Y. ;, Yang, Y. ;, Song, K. ;, Zhang, J. ;, Wen, Z. ;, Lake, Q., Li, W., Yang, Q., Ma, Y., Yang, Y., Song, K., Zhang, J., Wen, Z., & Liu, G. (2022). Remote Sensing Estimation of Long-Term Total Suspended Matter Concentration from Landsat across Lake Qinghai. *Water 2022, Vol. 14, Page 2498*, *14*(16), 2498. https://doi.org/10.3390/W14162498

Lobo, F. L., Costa, M. P. F., & Novo, E. M. L. M. (2015). Time-series analysis of Landsat-MSS/TM/OLI images over Amazonian waters impacted by gold mining activities. *Remote Sensing of Environment*, *157*, 170–184. https://doi.org/10.1016/J.RSE.2014.04.030

Lu, S., Bian, Y., Chen, F., Lin, J., Lyu, H., Li, Y., Liu, H., Zhao, Y., Zheng, Y., & Lyu, L. (2023). An operational approach for large-scale mapping of water clarity levels in inland lakes using landsat images based on optical classification. *Environmental Research*, *237*, 116898. https://doi.org/10.1016/J.ENVRES.2023.116898

Lymburner, L., Botha, E., Hestir, E., Anstee, J., Sagar, S., Dekker, A., & Malthus, T. (2016). Landsat 8: Providing continuity and increased precision for measuring multi-decadal time series of total suspended matter. *Remote Sensing of Environment*, *185*, 108–118. https://doi.org/10.1016/J.RSE.2016.04.011

Maciel, D. A., Pahlevan, N., Barbosa, C. C. F., Martins, V. S., Smith, B., O'Shea, R. E., Balasubramanian, S. V., Saranathan, A. M., & Novo, E. M. L. M. (2023). Towards global long-term water transparency products from the Landsat archive. *Remote Sensing of Environment*, *299*, 113889. https://doi.org/10.1016/J.RSE.2023.113889

Magee, M. R., & Wu, C. H. (2017). Response of water temperatures and stratification to changing climate in three lakes with different morphometry. *Hydrology and Earth System Sciences*, *21*(12), 6253–6274. https://doi.org/10.5194/HESS-21-6253-2017

Mahmoudi, P., Mohammadi, · M, & Daneshmand, · H. (2019). Investigating the trend of average changes of annual temperatures in Iran. *International Journal of Environmental Science and Technology*, *16*(3), 1079–1092. https://doi.org/10.1007/s13762-018-1664-4

Maiersperger, T. K., Scaramuzza, P. L., Leigh, L., Shrestha, S., Gallo, K. P., Jenkerson, C. B., & Dwyer, J. L. (2013). Characterizing LEDAPS surface reflectance products by comparisons with AERONET, field spectrometer, and MODIS data. *Remote Sensing of Environment*, *136*, 1–13. https://doi.org/10.1016/J.RSE.2013.04.007

Malahlela, O. E. (2019). Spatio-temporal assessment of inland surface water quality using remote sensing data in the wake of changing climate. *IOP Conference Series: Earth and Environmental Science*, *227*(6), 062012. https://doi.org/10.1088/1755-1315/227/6/062012

Malakar, N. K., Hulley, G. C., Hook, S. J., Laraby, K., Cook, M., & Schott, J. R. (2018). An Operational Land Surface Temperature Product for Landsat Thermal Data: Methodology and Validation. *IEEE Transactions on Geoscience and Remote Sensing*, *56*(10), 5717–5735. https://doi.org/10.1109/TGRS.2018.2824828

Malthus, T. J., Hestir, E. L., Dekker, A. G., & Brando, V. E. (2012). The case for a global inland water quality product. *International Geoscience and Remote Sensing Symposium (IGARSS)*, 5234–5237. https://doi.org/10.1109/IGARSS.2012.6352429

Mancino, G., Nolè, A., Urbano, V., Amato, M., & Ferrara, A. (2009). Assessing water quality by remote sensing in small lakes: the case study of Monticchio lakes in southern Italy. *IForest - Biogeosciences and Forestry*, *2*(4), 154. https://doi.org/10.3832/IFOR0507-002

Markogianni, V., Dimitriou, E., & Karaouzas, I. (2014). Water quality monitoring and assessment of an urban Mediterranean lake facilitated by remote sensing applications. *Environmental Monitoring and Assessment*, *186*(8), 5009–5026. https://doi.org/10.1007/S10661-014-3755-0/FIGURES/6

Markogianni, V., Kalivas, D., Petropoulos, G. P., & Dimitriou, E. (2020). Estimating Chlorophyll-a of Inland Water Bodies in Greece Based on Landsat Data. *Remote Sensing 2020, Vol. 12, Page 2087*, *12*(13), 2087. https://doi.org/10.3390/RS12132087

Markogianni, V., Kalivas, D., Petropoulos, G. P., & Dimitriou, E. (2022). Modelling of Greek Lakes Water Quality Using Earth Observation in the Framework of the Water Framework Directive (WFD). *Remote Sensing 2022, Vol. 14, Page 739*, *14*(3), 739. https://doi.org/10.3390/RS14030739

Markogianni, V., Kalvas, D., Petropoulos, G. P., & Dimitriou, E. (2018). An Appraisal of the Potential of Landsat 8 in Estimating Chlorophyll-a, Ammonium Concentrations and Other Water Quality Indicators. *Remote Sensing 2018, Vol. 10, Page 1018*, *10*(7), 1018. https://doi.org/10.3390/RS10071018

Martins, S., Chokmani, K., Alcântara, E., Ogashawara, I., & El-Alem, A. (2018). Mapping the coloured dissolved organic matter absorption coefficient in a eutrophic reservoir using remotely sensed images. *Inland Waters*, *8*(4), 488–504. https://doi.org/10.1080/20442041.2018.1482153

Martins, V. S., Kaleita, A., Barbosa, C. C. F., Fassoni-Andrade, A. C., De, F., Lobo, L., & Novo, E. M. L. M. (2018). *Remote sensing of large reservoir in the drought years: Implications on surface water change and turbidity variability of Sobradinho reservoir (Northeast Brazil).* https://doi.org/10.1016/j.rsase.2018.11.006

Masek, J. G., Vermote, E. F., Saleous, N. E., Wolfe, R., Hall, F. G., Huemmrich, K. F., Gao, F., Kutler, J., & Lim, T. K. (2006a). A landsat surface reflectance dataset for North America, 1990-2000. *IEEE Geoscience and Remote Sensing Letters*, *3*(1), 68–72. https://doi.org/10.1109/LGRS.2005.857030

Masek, J. G., Vermote, E. F., Saleous, N. E., Wolfe, R., Hall, F. G., Huemmrich, K. F., Gao, F., Kutler, J., & Lim, T. K. (2006b). A landsat surface reflectance dataset for North America, 1990-2000. *IEEE Geoscience and Remote Sensing Letters*, *3*(1), 68–72. https://doi.org/10.1109/LGRS.2005.857030

Masocha, M., Dube, T., Nhiwatiwa, T., & Choruma, D. (2018). Testing utility of Landsat 8 for remote assessment of water quality in two subtropical African reservoirs with contrasting trophic states. *Geocarto International*, *33*(7), 667–680. https://doi.org/10.1080/10106049.2017.1289561

Matthews, M. W. (2011). A current review of empirical procedures of remote sensing in inland and near-coastal transitional waters. *International Journal of Remote Sensing*, *32*(21), 6855–6899. https://doi.org/10.1080/01431161.2010.512947

McFeeters, S. K. (1996). The use of the Normalized Difference Water Index (NDWI) in the delineation of open water features. *International Journal of Remote Sensing*, *17*(7), 1425–1432. https://doi.org/10.1080/01431169608948714

Meng, H., Zhang, J., & Zheng, Z. (2022). Retrieving Inland Reservoir Water Quality Parameters Using Landsat 8-9 OLI and Sentinel-2 MSI Sensors with Empirical Multivariate Regression. *International Journal of Environmental Research and Public Health 2022, Vol. 19, Page 7725*, *19*(13), 7725. https://doi.org/10.3390/IJERPH19137725

Mohsen, A., Elshemy, M., & Zeidan, B. (2021). Water quality monitoring of Lake Burullus (Egypt) using Landsat satellite imageries. *Environmental Science and Pollution Research*, *28*(13), 15687–15700. https://doi.org/10.1007/S11356-020-11765-1/FIGURES/5

Mooij, W. M., De Senerpont Domis, L. N., & Hülsmann, S. (2008). The impact of climate warming on water temperature, timing of hatching and young-of-the-year growth of fish in shallow lakes in the Netherlands. *Journal of Sea Research*, *60*(1–2), 32–43. https://doi.org/10.1016/J.SEARES.2008.03.002

Moran, M. S., Jackson, R. D., Slater, P. N., & Teillet, P. M. (1992). Evaluation of simplified procedures for retrieval of land surface reflectance factors from satellite sensor output. *Remote Sensing of Environment*, *41*(2–3), 169–184. https://doi.org/10.1016/0034-4257(92)90076-V

Moritz, S., & Bartz-Beielstein, T. (2016). imputeTS: Time Series Missing Value Imputation in R. *R Package Version 1.7*.

Morrice, J. A., Danz, N. P., Regal, R. R., Kelly, J. R., Niemi, G. J., Reavie, E. D., Hollenhorst, T., Axler, R. P., Trebitz, A. S., Cotter, A. M., & Peterson, G. S. (2008). Human influences on water quality in Great Lakes coastal wetlands. *Environmental Management*, *41*(3), 347–357. https://doi.org/10.1007/S00267-007-9055-5/TABLES/5

Moses, W. J., Gitelson, A. A., Perk, R. L., Gurlin, D., Rundquist, D. C., Leavitt, B. C., Barrow, T. M., & Brakhage, P. (2012). Estimation of chlorophyll-a concentration in turbid productive waters using airborne hyperspectral data. *Water Research*, *46*(4), 993–1004. https://doi.org/10.1016/J.WATRES.2011.11.068

Moss, B. (2012). Cogs in the endless machine: Lakes, climate change and nutrient cycles: A review. *Science of The Total Environment*, *434*, 130–142. https://doi.org/10.1016/J.SCITOTENV.2011.07.069

Mouw, C. B., Greb, S., Aurin, D., DiGiacomo, P. M., Lee, Z., Twardowski, M., Binding, C., Hu, C., Ma, R., Moore, T., Moses, W., & Craig, S. E. (2015). Aquatic color radiometry remote sensing of coastal and inland waters: Challenges and recommendations for future satellite missions. *Remote Sensing of Environment*, *160*, 15–30. https://doi.org/10.1016/J.RSE.2015.02.001

Mushtaq, F., Nee Lala, M. G., & Mantoo, A. G. (2022). Trophic State Assessment of a Freshwater Himalayan Lake Using Landsat 8 OLI Satellite Imagery: A Case Study of Wular Lake, Jammu and Kashmir (India). *Earth and Space Science*, *9*(3), e2021EA001653. https://doi.org/10.1029/2021EA001653

Naciones Unidas. (2018). *La Agenda 2030 y los Objetivos de Desarrollo Sostenible: una oportunidad para América Latina y el Caribe*. www.issuu.com/publicacionescepal/stacks

Nascimento Silva, H. A., Laneve, G., Rosato, A., & Panella, M. (2017). Retrieving chlorophyll-a levels, transparency and tss concentration from multispectral satellite data by using artificial neural networks. *Progress in Electromagnetics Research Symposium*, *2017-November*, 2876–2883. https://doi.org/10.1109/PIERS-FALL.2017.8293624

Naumenko, M. A. (2008). Seasonality and trends in the Secchi disk transparency of Lake Ladoga. *Hydrobiologia*, *599*(1). https://doi.org/10.1007/s10750-007-9198-7

Nazeer, M., Nichol, J. E., & Yung, Y. K. (2014). Evaluation of atmospheric correction models and Landsat surface reflectance product in an urban coastal environment. *International Journal of Remote Sensing*, *35*(16), 6271–6291. https://doi.org/10.1080/01431161.2014.951742

Niedrist, G. H., Psenner, R., & Sommaruga, R. (2018). Climate warming increases vertical and seasonal water temperature differences and inter-annual variability in a mountain lake. *Climatic Change*, *151*(3–4), 473–490. https://doi.org/10.1007/S10584-018-2328-6/FIGURES/5

Odermatt, D., Gitelson, A., Brando, V. E., & Schaepman, M. (2012). Review of constituent retrieval in optically deep and complex waters from satellite imagery. *Remote Sensing of Environment*, *118*, 116–126. https://doi.org/10.1016/J.RSE.2011.11.013

Öğlü, B., Möls, T., Kaart, T., Cremona, F., & Kangur, K. (2020). Parameterization of surface water temperature and long-term trends in Europe's fourth largest lake shows recent and rapid warming in winter. *Limnologica*, *82*, 125777. https://doi.org/10.1016/J.LIMNO.2020.125777

Oliphant, T., Tsoeleng, L. T., Mhangara, P., & Malahlela, O. E. (2018). Mapping chlorophyll-a concentrations in a cyanobacteria- and algae-impacted Vaal Dam using Landsat 8 OLI data. *South African Journal of Science*, *114*(9/10). https://doi.org/10.17159/SAJS.2018/4841

Olmanson, L. G., Bauer, M. E., & Brezonik, P. L. (2008). A 20-year Landsat water clarity census of Minnesota's 10,000 lakes. *Remote Sensing of Environment*, *112*(11), 4086–4097. https://doi.org/10.1016/J.RSE.2007.12.013

Olmanson, L. G., Page, B. P., Finlay, J. C., Brezonik, P. L., Bauer, M. E., Griffin, C. G., & Hozalski, R. M. (2020). Regional measurements and spatial/temporal analysis of CDOM in 10,000+ optically variable Minnesota lakes using Landsat 8 imagery. *Science of The Total Environment*, *724*, 138141. https://doi.org/10.1016/J.SCITOTENV.2020.138141

O'Reilly, C. M., Sharma, S., Gray, D. K., Hampton, S. E., Read, J. S., Rowley, R. J., Schneider, P., Lenters, J. D., McIntyre, P. B., Kraemer, B. M., Weyhenmeyer, G. A., Straile, D., Dong, B., Adrian, R., Allan, M. G., Anneville, O., Arvola, L., Austin, J., Bailey, J. L., … Zhang, G. (2015). Rapid and highly variable warming of lake surface waters around the globe. *Geophysical Research Letters*, *42*(24), 10,773-10,781. https://doi.org/10.1002/2015GL066235

Pahlevan, N., Mangin, A., Balasubramanian, S. V., Smith, B., Alikas, K., Arai, K., Barbosa, C., Bélanger, S., Binding, C., Bresciani, M., Giardino, C., Gurlin, D., Fan, Y., Harmel, T., Hunter, P., Ishikaza, J., Kratzer, S., Lehmann, M. K., Ligi, M., … Warren, M. (2021). ACIX-Aqua: A global assessment of atmospheric correction methods for Landsat-8 and Sentinel-2 over lakes, rivers, and coastal waters. *Remote Sensing of Environment*, *258*, 112366. https://doi.org/10.1016/J.RSE.2021.112366

Pahlevan, N., Smith, B., Alikas, K., Anstee, J., Barbosa, C., Binding, C., Bresciani, M., Cremella, B., Giardino, C., Gurlin, D., Fernandez, V., Jamet, C., Kangro, K., Lehmann, M. K., Loisel, H., Matsushita, B., Hà, N., Olmanson, L., Potvin, G., … Ruiz-Verdù, A. (2022). Simultaneous retrieval of selected optical water quality indicators from Landsat-8, Sentinel-2, and Sentinel-3. *Remote Sensing of Environment*, *270*, 112860. https://doi.org/10.1016/J.RSE.2021.112860

Pal, S., & Chakraborty, K. (2014). *Importance of some physical and chemical characteristics of water bodies in relation to the incidence of zooplanktons: A review*. https://www.researchgate.net/publication/305601143

Papoutsa, C., Akylas, E., & Hadjimitsis, D. (2014). Trophic state index derivation through the remote sensing of case-2 water bodies in the Mediterranean region. *Central European Journal of Geosciences*, *6*(1), 67–78. https://doi.org/10.2478/S13533-012-0161-4/MACHINEREADABLECITATION/RIS

Peng, Z., Yang, K., Shang, C., Duan, H., Tang, L., Zhang, Y., Cao, Y., & Luo, Y. (2022). Attribution analysis of lake surface water temperature changing —

taking China's six main lakes as example. *Ecological Indicators*, *145*, 109651. https://doi.org/10.1016/J.ECOLIND.2022.109651

Peterson, K. T., Sagan, V., & Sloan, J. J. (2020). Deep learning-based water quality estimation and anomaly detection using Landsat-8/Sentinel-2 virtual constellation and cloud computing. *GIScience & Remote Sensing*, *57*(4), 510–525. https://doi.org/10.1080/15481603.2020.1738061

Ponkina, E., Illiger, P., Krotova, O., & Bondarovich, A. (2021). Do ARMA Models Provide Better Gap Filling in Time Series of Soil Temperature and Soil Moisture? The Case of Arable Land in the Kulunda Steppe, Russia. *Land 2021, Vol. 10, Page 579*, *10*(6), 579. https://doi.org/10.3390/LAND10060579

Prats, J., Reynaud, N., Rebière, D., Peroux, T., Tormos, T., & Danis, P. A. (2018). LakeSST: Lake Skin Surface Temperature in French inland water bodies for 1999-2016 from Landsat archives. *Earth System Science Data*, *10*(2), 727–743. https://doi.org/10.5194/ESSD-10-727-2018

Pratt, B., & Chang, H. (2012). Effects of land cover, topography, and built structure on seasonal water quality at multiple spatial scales. *Journal of Hazardous Materials*, *209–210*, 48–58. https://doi.org/10.1016/J.JHAZMAT.2011.12.068

Ptak, M., Sojka, M., Choiński, A., & Nowak, B. (2018). Effect of Environmental Conditions and Morphometric Parameters on Surface Water Temperature in Polish Lakes. *Water 2018, Vol. 10, Page 580*, *10*(5), 580. https://doi.org/10.3390/W10050580

Ramsar. (1971). *Convención Relativa a los Humedales de Importancia Internacional Especialmente como Hábitat de Aves Acuáticas*.

Rani, M., Rehman, S., Sajjad, H., Alare, R. S., Chaudhary, B. S., Patairiya, S., Rawat, J. S., Chetri, T., Patel, S., & Kumar, P. (2019). NIR-red algorithms-based model for chlorophyll-a retrieval in highly turbid Inland Densu River Basin in South-East Ghana, West Africa. *IET Image Processing*, *13*(8), 1328–1332. https://doi.org/10.1049/IET-IPR.2018.6145

Raymond Hunt, E., Daughtry, C. S. T., Eitel, J. U. H., & Long, D. S. (2011). Remote sensing leaf chlorophyll content using a visible band index. *Agronomy Journal*, *103*(4), 1090–1099. https://doi.org/10.2134/AGRONJ2010.0395

Ren, J., Zheng, Z., Li, Y., Lv, G., Wang, Q., Lyu, H., Huang, C., Liu, G., Du, C., Mu, M., Lei, S., & Bi, S. (2018). Remote observation of water clarity patterns in Three Gorges Reservoir and Dongting Lake of China and their probable linkage to the Three Gorges Dam based on Landsat 8 imagery. *Science of The Total Environment*, *625*, 1554–1566. https://doi.org/10.1016/J.SCITOTENV.2018.01.036

Ríos-Cornejo, D., Penas, Á., Álvarez-Esteban, R., & del Río, S. (2015). Links between teleconnection patterns and mean temperature in Spain. *Theoretical and Applied Climatology*, *122*(1–2), 1–18. https://doi.org/10.1007/S00704-014-1256-2/TABLES/2

Robert, E., Kergoat, L., Soumaguel, N., Merlet, S., Martinez, J. M., Diawara, M., & Grippa, M. (2017). Analysis of Suspended Particulate Matter and Its Drivers in Sahelian Ponds and Lakes by Remote Sensing (Landsat and MODIS): Gourma Region, Mali. *Remote Sensing 2017, Vol. 9, Page 1272*, *9*(12), 1272. https://doi.org/10.3390/RS9121272

Rodrigo, M. A., Rojo, C., Segura, M., Alonso-Guillén, J. L., Martín, M., & Vera, P. (2015). The role of charophytes in a Mediterranean pond created for restoration purposes. *Aquatic Botany*, *120*(PA), 101–111. https://doi.org/10.1016/J.AQUABOT.2014.05.004

Rodrigues, T., Alcântara, E., Watanabe, F., & Imai, N. (2017). Retrieval of Secchi disk depth from a reservoir using a semi-analytical scheme. *Remote Sensing of Environment*, *198*, 213–228. https://doi.org/10.1016/J.RSE.2017.06.018

Rubin, H. J., Lutz, D. A., Steele, B. G., Cottingham, K. L., Weathers, K. C., Ducey, M. J., Palace, M., Johnson, K. M., & Chipman, J. W. (2021). Remote Sensing of Lake Water Clarity: Performance and Transferability of Both Historical Algorithms and Machine Learning. *Remote Sensing 2021, Vol. 13, Page 1434*, *13*(8), 1434. https://doi.org/10.3390/RS13081434

Rueda, F., Schladow, G., Rueda, F., & Schladow, G. (2009). Mixing and stratification in lakes of varying horizontal length scales: Scaling arguments and energy partitioning. *Limnology and Oceanography*, *54*(6), 2003–2017. https://doi.org/10.4319/LO.2009.54.6.2003

Schaeffer, B. A., Iiames, J., Dwyer, J., Urquhart, E., Salls, W., Rover, J., & Seegers, B. (2018). An initial validation of Landsat 5 and 7 derived surface water temperature for U.S. lakes, reservoirs, and estuaries. *Https://Doi.Org/10.1080/01431161.2018.1471545*, *39*(22), 7789–7805. https://doi.org/10.1080/01431161.2018.1471545

Schaeffer, B. A., Seegers, B. N., Loftin, K. A., Werdell, P. J., & Stumpf, R. P. (2018). Performance metrics for the assessment of satellite data products: an ocean color case study. *Optics Express, Vol. 26, Issue 6, Pp. 7404-7422*, *26*(6), 7404–7422. https://doi.org/10.1364/OE.26.007404

Schneider, P., & Hook, S. J. (2010). Space observations of inland water bodies show rapid surface warming since 1985. *Geophysical Research Letters*, *37*(22). https://doi.org/10.1029/2010GL045059

Schneider, P., Hook, S. J., Radocinski, R. G., Corlett, G. K., Hulley, G. C., Schladow, S. G., & Steissberg, T. E. (2009). Satellite observations indicate rapid warming trend for lakes in California and Nevada. *Geophysical Research Letters*, *36*(22). https://doi.org/10.1029/2009GL040846

Setiawan, F., Matsushita, B., Hamzah, R., Jiang, D., & Fukushima, T. (2019). Long-Term Change of the Secchi Disk Depth in Lake Maninjau, Indonesia Shown by Landsat TM and ETM+ Data. *Remote Sensing 2019, Vol. 11, Page 2875*, *11*(23), 2875. https://doi.org/10.3390/RS11232875

Shahzad, M. I., Meraj, M., Nazeer, M., Zia, I., Inam, A., Mehmood, K., & Zafar, H. (2018). Empirical estimation of suspended solids concentration in the Indus Delta Region using Landsat-7 ETM+ imagery. *Journal of Environmental Management*, *209*, 254–261. https://doi.org/10.1016/J.JENVMAN.2017.12.070

Sima, S., Ahmadalipour, A., & Tajrishy, M. (2013). Mapping surface temperature in a hyper-saline lake and investigating the effect of temperature distribution on the lake evaporation. *Remote Sensing of Environment*, *136*, 374–385. https://doi.org/10.1016/J.RSE.2013.05.014

Simon, R. N., Tormos, T., & Danis, P. A. (2014a). Retrieving water surface temperature from archive LANDSAT thermal infrared data: Application of the mono-channel atmospheric correction algorithm over two freshwater reservoirs. *International Journal of Applied Earth Observation and Geoinformation*, *30*(1), 247–250. https://doi.org/10.1016/J.JAG.2014.01.005

Simon, R. N., Tormos, T., & Danis, P.-A. (2014b). Retrieving water surface temperature from archive LANDSAT thermal infrared data: Application of the mono-channel atmospheric correction algorithm over two freshwater reservoirs. *International Journal of Applied Earth Observation and Geoinformation*, *30*, 247–250. https://doi.org/10.1016/j.jag.2014.01.005

Somasundaram, D., Zhang, F., Ediriweera, S., Wang, S., Yin, Z., Li, J., & Zhang, B. (2021). Patterns, Trends and Drivers of Water Transparency in Sri Lanka Using Landsat 8 Observations and Google Earth Engine. *Remote Sensing 2021, Vol. 13, Page 2193*, *13*(11), 2193. https://doi.org/10.3390/RS13112193

Song, K., Liu, G., Wang, Q., Wen, Z., Lyu, L., Du, Y., Sha, L., & Fang, C. (2020). Quantification of lake clarity in China using Landsat OLI imagery data. *Remote Sensing of Environment*, *243*, 111800. https://doi.org/10.1016/J.RSE.2020.111800

Song, K., Wang, Q., Liu, G., Jacinthe, P. A., Li, S., Tao, H., Du, Y., Wen, Z., Wang, X., Guo, W., Wang, Z., Shi, K., Du, J., Shang, Y., Lyu, L., Hou, J., Zhang, B., Cheng, S., Lyu, Y., & Fei, L. (2022). A unified model for high resolution mapping of global lake (>1 ha) clarity using Landsat imagery data. *Science of The Total Environment*, *810*, 151188. https://doi.org/10.1016/J.SCITOTENV.2021.151188

Soria, X., Vicente, E., Durán, C., … J. S.-X. C. de, & 2017, undefined. (2017). Uso de imágenes Landsat-8 para la estimación de la profundidad del disco de Secchi en aguas continentales. *Researchgate.Net*, 293–296. https://www.researchgate.net/profile/Juan-Soria-3/publication/324862532_Uso_de_imagenes_Landsat-8_para_la_estimacion_de_la_profundidad_del_disco_de_Secchi_en_aguas_continentales/links/5ae846b7a6fdcc03cd8e0ef2/Uso-de-imagenes-Landsat-8-para-la-estimacion-de-la-profundidad-del-disco-de-Secchi-en-aguas-continentales.pdf

Stefanidis, K., Varlas, G., Papaioannou, G., Papadopoulos, A., & Dimitriou, E. (2022). Trends of lake temperature, mixing depth and ice cover thickness of European lakes during the last four decades. *Science of The Total Environment*, *830*, 154709. https://doi.org/10.1016/J.SCITOTENV.2022.154709

Stendera, S., Adrian, • R, Bonada, • N, Cañ Edo-Argü, • M, Hugueny, • B, Januschke, • K, Pletterbauer, • F, Hering, • D, Stendera, S., Januschke, Á. K., Hering, Á. D., Adrian, R., Bonada, N., Cañedo-Argüelles, Á. M., & Pletterbauer, F. (2012). Drivers and stressors of freshwater biodiversity patterns across different ecosystems and scales: a review. *Hydrobiologia 2012 696:1*, *696*(1), 1–28. https://doi.org/10.1007/S10750-012-1183-0

Sun, Q., Luo, W., Dong, X., Lei, S., Mu, M., & Zeng, S. (2024). Landsat observations of total suspended solids concentrations in the Pearl River Estuary, China, over the past 36 years. *Environmental Research*, *249*, 118461. https://doi.org/10.1016/J.ENVRES.2024.118461

Surisetty, V. V. A. K., Sahay, A., Ramakrishnan, R., Samal, R. N., & Rajawat, A. S. (2018). Improved turbidity estimates in complex inland waters using combined NIR–SWIR atmospheric correction approach for Landsat 8 OLI data. *International Journal of Remote Sensing*, *39*(21), 7463–7482. https://doi.org/10.1080/01431161.2018.1471538

Sverdrup, H., Munk, W., & Persson, A. (2017). The Story of the Hovmöller Diagram: An (Almost) Eyewitness Account. *Bulletin of the American Meteorological Society*, *98*(5), 949–957. https://doi.org/10.1175/BAMS-D-15-00234.1

Tanner, K. B., Cardall, A. C., & Williams, G. P. (2022). A Spatial Long-Term Trend Analysis of Estimated Chlorophyll-a Concentrations in Utah Lake Using Earth Observation Data. *Remote Sensing*, *14*(15), 3664. https://doi.org/10.3390/RS14153664/S1

Tao, H., Song, K., Liu, G., Wang, Q., Wen, Z., Hou, J., Shang, Y., & Li, S. (2022). Analysis of Spatio-Temporal Dynamics of Chinese Inland Water Clarity at Multiple Spatial Scales between 1984 and 2018. *Remote Sensing*, *14*(20), 5091. https://doi.org/10.3390/RS14205091/S1

Tavares, M. H., Cunha, A. H. F., Motta-Marques, D., Ruhoff, A. L., Cavalcanti, J. R., Fragoso, C. R., Bravo, J. M., Munar, A. M., Fan, F. M., & Rodrigues, L. H. R. (2019). Comparison of Methods to Estimate Lake-Surface-Water Temperature Using Landsat 7 ETM+ and MODIS Imagery: Case Study of a Large Shallow Subtropical Lake in Southern Brazil. *Water 2019, Vol. 11, Page 168*, *11*(1), 168. https://doi.org/10.3390/W11010168

Tebbs, E. J., Remedios, J. J., & Harper, D. M. (2013). Remote sensing of chlorophyll-a as a measure of cyanobacterial biomass in Lake Bogoria, a hypertrophic, saline–alkaline, flamingo lake, using Landsat ETM +. *Remote Sensing of Environment*, *135*, 92–106. https://doi.org/10.1016/J.RSE.2013.03.024

Tian, D., Zhao, X., Gao, L., Liang, Z., Yang, Z., Zhang, P., Wu, Q., Ren, K., Li, R., Yang, C., Li, S., Wang, M., He, Z., Zhang, Z., & Chen, J. (2024). Estimation of water quality variables based on machine learning model and cluster analysis-based empirical model using multi-source remote sensing data in inland reservoirs, South China. *Environmental Pollution*, *342*, 123104. https://doi.org/10.1016/J.ENVPOL.2023.123104

Topp, S. N., Pavelsky, T. M., Jensen, D., Simard, M., & Ross, M. R. V. (2020). Research Trends in the Use of Remote Sensing for Inland Water Quality Science: Moving Towards Multidisciplinary Applications. *Water 2020, Vol. 12, Page 169*, *12*(1), 169. https://doi.org/10.3390/W12010169

US EPA. (2012). *What is GLWQA? | US EPA*. https://www.epa.gov/glwqa/what-glwqa

van Buuren, S., & Groothuis-Oudshoorn, K. (2011). mice: Multivariate Imputation by Chained Equations in R. *Journal of Statistical Software*, *45*(3), 1–67. https://doi.org/10.18637/JSS.V045.I03

Vanhellemont, Q., & Ruddick, K. (2018). Atmospheric correction of metre-scale optical satellite data for inland and coastal water applications. *Remote Sensing of Environment*, *216*, 586–597. https://doi.org/10.1016/J.RSE.2018.07.015

Vermote, E. F., Tanré, D., Deuzé, J. L., Herman, M., & Morcrette, J. J. (1997). Second simulation of the satellite signal in the solar spectrum, 6s: an overview. *IEEE Transactions on Geoscience and Remote Sensing*, *35*(3), 675–686. https://doi.org/10.1109/36.581987

Villota-González, F. H., Sulbarán-Rangel, B., Zurita-Martínez, F., Gurubel-Tun, K. J., & Zúñiga-Grajeda, V. (2023). Assessment of Machine Learning Models for Remote Sensing of Water Quality in Lakes Cajititlán and Zapotlán, Jalisco—Mexico. *Remote Sensing*, *15*(23), 5505. https://doi.org/10.3390/RS15235505/S1

Vinh, P. Q., Has, N. T. T., Binh, N. T., Thang, N. N., Oanh, L. T., & Thao, N. T. P. (2019). Developing algorithm for estimating chlorophyll-a concentration in the Thac Ba Reservoir surface water using Landsat 8 Imagery. *Vietnam Journal of Earth Sciences*, *41*(1), 10–20. https://doi.org/10.15625/0866-7187/41/1/13542

Virdis, S. G. P., Soodcharoen, N., Lugliè, A., & Padedda, B. M. (2020). Estimation of satellite-derived lake water surface temperatures in the western Mediterranean: Integrating multi-source, multi-resolution imagery and a long-term field dataset using a time series approach. *Science of The Total*

Environment, *707*, 135567. https://doi.org/10.1016/J.SCITOTENV.2019.135567

Wang, C., Li, W., Chen, S., Li, D., Wang, D., & Liu, J. (2018). The spatial and temporal variation of total suspended solid concentration in Pearl River Estuary during 1987–2015 based on remote sensing. *Science of The Total Environment*, *618*, 1125–1138. https://doi.org/10.1016/J.SCITOTENV.2017.09.196

Wang, D., Ma, R., Xue, K., & Loiselle, S. A. (2019). The Assessment of Landsat-8 OLI Atmospheric Correction Algorithms for Inland Waters. *Remote Sensing 2019, Vol. 11, Page 169*, *11*(2), 169. https://doi.org/10.3390/RS11020169

Wang, F., Han, L., Kung, H. T., & van Arsdale, R. B. (2006). Applications of Landsat-5 TM imagery in assessing and mapping water quality in Reelfoot Lake, Tennessee. *International Journal of Remote Sensing*, *27*(23), 5269–5283. https://doi.org/10.1080/01431160500191704

Wang, J., & Chen, X. (2024). A new approach to quantify chlorophyll-a over inland water targets based on multi-source remote sensing data. *Science of The Total Environment*, *906*, 167631. https://doi.org/10.1016/J.SCITOTENV.2023.167631

Wang, L., Xu, M., Liu, Y., Liu, H., Beck, R., Reif, M., Emery, E., Young, J., & Wu, Q. (2020). Mapping Freshwater Chlorophyll-a Concentrations at a Regional Scale Integrating Multi-Sensor Satellite Observations with Google Earth Engine. *Remote Sensing 2020, Vol. 12, Page 3278*, *12*(20), 3278. https://doi.org/10.3390/RS12203278

Wang, Q., Song, K., Wen, Z., Shang, Y., Li, S., Fang, C., Du, J., Zhao, F., & Liu, G. (2021). Long-term remote sensing of total suspended matter using Landsat series sensors in Hulun Lake, China. *International Journal of Remote Sensing*, *42*(4), 1379–1397. https://doi.org/10.1080/01431161.2020.1829154

Wang, Q., Song, K., Xiao, X., Jacinthe, P. A., Wen, Z., Zhao, F., Tao, H., Li, S., Shang, Y., Wang, Y., & Liu, G. (2022). Mapping water clarity in North American lakes and reservoirs using Landsat images on the GEE platform with the RGRB model. *ISPRS Journal of Photogrammetry and Remote Sensing*, *194*, 39–57. https://doi.org/10.1016/J.ISPRSJPRS.2022.09.014

Wang, R., Yan, X., Niu, Z., & Chen, W. (2021). Long-Term Changes in Inland Water Surface Temperature across China Based on Remote Sensing Data. *Journal of Hydrometeorology*, *22*(2), 523–532. https://doi.org/10.1175/JHM-D-20-0104.1

Watanabe, F. S. Y., Alcântara, E., Rodrigues, T. W. P., Imai, N. N., Barbosa, C. C. F., & Rotta, L. H. da S. (2015). Estimation of Chlorophyll-a Concentration and the Trophic State of the Barra Bonita Hydroelectric Reservoir Using OLI/Landsat-8 Images. *International Journal of Environmental Research and Public Health 2015, Vol. 12, Pages 10391-10417*, *12*(9), 10391–10417. https://doi.org/10.3390/IJERPH120910391

Weeks, S., Werdell, P. J., Schaffelke, B., Canto, M., Lee, Z., Wilding, J. G., & Feldman, G. C. (2012). Satellite-Derived Photic Depth on the Great Barrier Reef: Spatio-Temporal Patterns of Water Clarity. *Remote Sensing 2012, Vol. 4, Pages 3781-3795*, *4*(12), 3781–3795. https://doi.org/10.3390/RS4123781

Wermuth, L., Faria de Sousa, L. F. M., Sander de Carvalho, L. A., Nascimento, N., & Silva, T. (2022). *USING LANDSAT 8 IMAGES FOR MONITORING SURFACE WATER TEMPERATURE IN AN URBAN TROPICAL RESERVOIR*. 5351–5358. https://doi.org/10.3850/IAHR-39WC2521711920221047

Whittaker, E. T. (1922). On a New Method of Graduation. *Proceedings of the Edinburgh Mathematical Society*. https://doi.org/10.1017/S0013091500077853

Williamson, C. E., Saros, J. E., Vincent, W. F., & Smol, J. P. (2009). Lakes and reservoirs as sentinels, integrators, and regulators of climate change. *Limnology and Oceanography*, *54*(6part2), 2273–2282. https://doi.org/10.4319/LO.2009.54.6_PART_2.2273

Woolway, R. I., Jones, I. D., Maberly, S. C., French, J. R., Livingstone, D. M., Monteith, D. T., Simpson, G. L., Thackeray, S. J., Andersen, M. R., Battarbee, R. W., Degasperi, C. L., Evans, C. D., Eyto, E. De, Feuchtmayr, H., Hamilton, D. P., Kernan, M., Krokowski, J., Rimmer, A., Rose, K. C., … Weyhenmeyer, G. A. (2016). Diel surface temperature range scales with lake size. *PLoS One*, *11*(3), e0152466 (14 pp.). https://doi.org/10.1371/JOURNAL.PONE.0152466

Woolway, R. I., Kraemer, B. M., Lenters, J. D., Merchant, C. J., O'Reilly, C. M., & Sharma, S. (2020). Global lake responses to climate change. *Nature Reviews Earth & Environment 2020 1:8*, *1*(8), 388–403. https://doi.org/10.1038/s43017-020-0067-5

Woolway, R. I., Weyhenmeyer, G. A., Schmid, M., Dokulil, M. T., de Eyto, E., Maberly, S. C., May, L., & Merchant, C. J. (2019). Substantial increase in minimum lake surface temperatures under climate change. *Climatic Change*, *155*(1), 81–94. https://doi.org/10.1007/S10584-019-02465-Y

Yang, F., He, B., Zhou, Y., Li, W., Zhang, X., & Feng, Q. (2023). Trophic status observations for Honghu Lake in China from 2000 to 2021 using Landsat Satellites. *Ecological Indicators*, *146*, 109898. https://doi.org/10.1016/J.ECOLIND.2023.109898

Yang, H., Du, Y., Zhao, H., & Chen, F. (2022). Water Quality Chl-a Inversion Based on Spatio-Temporal Fusion and Convolutional Neural Network. *Remote Sensing 2022, Vol. 14, Page 1267*, *14*(5), 1267. https://doi.org/10.3390/RS14051267

Yang, X., Jiang, Y., Deng, X., Zheng, Y., & Yue, Z. (2020). Temporal and Spatial Variations of Chlorophyll a Concentration and Eutrophication Assessment (1987–2018) of Donghu Lake in Wuhan Using Landsat Images. *Water 2020, Vol. 12, Page 2192*, *12*(8), 2192. https://doi.org/10.3390/W12082192

Yang, Y., Zhang, X., Gao, W., Zhang, Y., & Hou, X. (2023). Improving lake chlorophyll-a interpreting accuracy by combining spectral and texture features of remote sensing. *Environmental Science and Pollution Research*, *30*(35), 83628–83642. https://doi.org/10.1007/S11356-023-28344-9/FIGURES/9

Yang, Z., Gong, C., Lu, Z., Wu, E., Huai, H., Hu, Y., Li, L., & Dong, L. (2023). Combined Retrievals of Turbidity from Sentinel-2A/B and Landsat-8/9 in the Taihu Lake through Machine Learning. *Remote Sensing 2023, Vol. 15, Page 4333*, *15*(17), 4333. https://doi.org/10.3390/RS15174333

Yépez, S., Velásquez, G., Torres, D., Saavedra-Passache, R., Pincheira, M., Cid, H., Rodríguez-López, L., Contreras, A., Frappart, F., Cristóbal, J., Pons, X., Flores, N., & Bourrel, L. (2024). Spatiotemporal Variations in Biophysical Water Quality Parameters: An Integrated In Situ and Remote Sensing Analysis of an Urban Lake in Chile. *Remote Sensing 2024, Vol. 16, Page 427*, *16*(2), 427. https://doi.org/10.3390/RS16020427

Yin, Z., Yin, Z., Yin, Z., Li, J., Li, J., Li, J., Liu, Y., Zhang, F., Zhang, F., Wang, S., Wang, S., Xie, Y., Xie, Y., Gao, M., & Gao, M. (2022). Decline of suspended particulate matter concentrations in Lake Taihu from 1984 to 2020:

observations from Landsat TM and OLI. *Optics Express, Vol. 30, Issue 13, Pp. 22572-22589*, *30*(13), 22572–22589. https://doi.org/10.1364/OE.454814

You, Q., Fang, N., Liu, L., Yang, W., Zhang, L., & Wang, Y. (2019). Effects of land use, topography, climate and socio-economic factors on geographical variation pattern of inland surface water quality in China. *PLOS ONE*, *14*(6), e0217840. https://doi.org/10.1371/JOURNAL.PONE.0217840

Zandaryaa, S. (2018). *The UNESCO-IHP IIWQ World Water Quality Portal-Whitepaper-International Initiative on Water Quality (IIWQ)*.

Zanter, K. (2021). *LSDS-1618 Landsat 4-7 Collection 2 (C2) Level 2 Science Product (L2SP) Guide*.

Zeng, W., Xu, K., Cheng, S., Zhao, L., & Yang, K. (2023). Regional Remote Sensing of Lake Water Transparency Based on Google Earth Engine: Performance of Empirical Algorithm and Machine Learning. *Applied Sciences (Switzerland)*, *13*(6), 4007. https://doi.org/10.3390/APP13064007/S1

Zhang, F., Li, J., Yan, B., Yu, J., Wang, C., Wang, S., Shen, Q., Wu, Y., & Zhang, B. (2021). Tracking historical chlorophyll-a change in the guanting reservoir, Northern China, based on landsat series inter-sensor normalization. *International Journal of Remote Sensing*, *42*(10), 3918–3937. https://doi.org/10.1080/01431161.2021.1875149

Zhang, H., Xue, B., Wang, G., Zhang, X., & Zhang, Q. (2022). Deep Learning-Based Water Quality Retrieval in an Impounded Lake Using Landsat 8 Imagery: An Application in Dongping Lake. *Remote Sensing 2022, Vol. 14, Page 4505*, *14*(18), 4505. https://doi.org/10.3390/RS14184505

Zhang, Y., Zhang, Y., Shi, K., Zha, Y., Zhou, Y., & Liu, M. (2016). A Landsat 8 OLI-Based, Semianalytical Model for Estimating the Total Suspended Matter Concentration in the Slightly Turbid Xin'anjiang Reservoir (China). *IEEE Journal of Selected Topics in Applied Earth Observations and Remote Sensing*, *9*(1), 398–413. https://doi.org/10.1109/JSTARS.2015.2509469

Zhang, Y., Zhang, Y., Shi, K., Zhou, Y., & Li, N. (2021). Remote sensing estimation of water clarity for various lakes in China. *Water Research*, *192*, 116844. https://doi.org/10.1016/J.WATRES.2021.116844

Zhao, C., Zhang, Y., Guo, W., & Baqa, M. F. (2022). Dynamics and Drivers of Water Clarity Derived from Landsat and In-Situ Measurement Data in Hulun Lake from 2010 to 2020. *Water 2022, Vol. 14, Page 1189*, *14*(8), 1189. https://doi.org/10.3390/W14081189

Zhao, X., Xu, H., Ding, Z., Wang, D., Deng, Z., Wang, Y., Lu, Z., Wang, G., Wu, T., & Li, W. (2021). Comparing deep learning with several typical methods in prediction of assessing chlorophyll-a by remote sensing: a case study in Taihu Lake, China. *Water Supply*, *21*(7), 3710–3724. https://doi.org/10.2166/WS.2021.137

Zhu, W., Huang, L., Sun, N., Chen, J., & Pang, S. (2020). Landsat 8-observed water quality and its coupled environmental factors for urban scenery lakes: A case study of West Lake. *Water Environment Research*, *92*(2), 255–265. https://doi.org/10.1002/WER.1240

Ziauddin, G., Chakraborty, S. K., Jaiswar, A. K., & Bhaumik, U. (2013). PRODUCTIVITY STUDY IN RELATION TO TEMPERATURE AND TRANSPARENCY IN THE EUPHOTIC ZONE OF SELECTED TROPICAL FRESHWATER FLOODPLAIN WETLANDS OF WEST BENGAL. In *N Save Nature to Survive* (Vol. 7, Issue 4). https://www.researchgate.net/publication/280832042

Anexos

Anexo 1. Resumen de 117 artículos científicos que utilizan Landsat para analizar los parámetros de calidad de agua.

Anexo 1: Resumen de 117 artículos científicos que utilizan Landsat para analizar los parámetros de calidad de agua.

Autores	Área de estudio	Período de estudio	Parámetro de calidad de a	Satélite	Método	Bandas	Modelo obtenido	Errores	Clasificación
(Caballero et al., 2022)	Mar menor lagoon (Spain)	2021	Turbidity	Landsat 8	Empirical Models	Band 4	$T = \frac{A_T \rho_w}{1 - \rho_w/C} + B_T$	2.04 FNU	Técnicos con alguna aplicación ambiental.
(Bonansea et al., 2015)	Río Tercero reservoir (Argentina)	2003-2010	Temperature	Landsat 5	Empirical Models	Thermal	$T = \text{K2}/\ln(\text{K1}/\text{L}_\lambda + 1)$	Not reported	Técnicos con alguna aplicación ambiental.
(Bonansea et al., 2015)	Río Tercero reservoir (Argentina)	2003-2010	Chl-a	Landsat 5	Empirical Models	Band 2 and 3	$\ln(\text{Chl-a})_{\text{Low AR}} = 0.94 + 20.61 * \rho2 + 23.60 * \rho3 + 0.15 * \text{WST}$ $\ln(\text{Chl-a})_{\text{High AR}} = (0.94 + 0.24) + 20.61 * \rho2 + 23.60 * \rho3 + 0.15 * \text{WST}$	RMSE= 7,25%	Técnicos con alguna aplicación ambiental.
(Bonansea et al., 2015)	Río Tercero reservoir (Argentina)	2003-2010	Transparency	Landsat 5	Empirical Models	Band 4 and 1	$\ln(\text{SDT})_{\text{Low AR}} = 1.42 - 68.72 * \rho_4 + 0.98 * (\rho_4/\rho_4)$ $\ln(\text{SDT})_{\text{High AR}} = (1.74 - 0.17) - 68.72 * \rho_4 + 0.98 * (\rho_4/\rho_1)$	RMSE= 30,87%	Técnicos con alguna aplicación ambiental.
(Chao Rodríguez et al., 2013)	Lake Arreo (Spain)	2000-2012	Temperature	Landsat 5	Empirical Models	Thermal	$T = \frac{k_2}{\log\left(\frac{k_1}{R[\text{TM6}]} + 1\right)}$	RMSE: 4.18 °C	Técnicos con alguna aplicación ambiental.
(Chao Rodríguez et al., 2013)	Lake Arreo (Spain)	2000-2012	Chl-a	Landsat 5	Empirical Models	Band 1 and 2	$[\text{Chla}] = 0.0979\, e^{2.5926 \frac{R[\text{TM2}]}{R[\text{TM1}]}}$		Técnicos con alguna aplicación ambiental.
(Chao Rodríguez et al., 2013)	Lake Arreo (Spain)	2000-2012	Transparency	Landsat 5	Empirical Models	Band 1 and 2	$\text{SD} = -10.281 \frac{R\text{TM2} - R\text{TM1}}{R\text{TM2} + R\text{TM1}} + 4.5753$	RMSE: 0.48 m	Técnicos con alguna aplicación ambiental.
(Hicks et al., 2013)	34 lakes (New Zealand)	2000-2009	TSS	Landsat 5	Semi-empirical models	Band 4	TSS = −52.817 + 1,449.4 × B4	R2: 0.939	Puramente técnicos
(Hicks et al., 2013)	34 lakes (New Zealand)	2000-2009	Turbidity	Landsat 5	Semi-empirical models	Band 4	TURB = −63.717 + 1,587.8 × B4	R2: 0.924	Puramente técnicos
(Hicks et al., 2013)	34 lakes (New Zealand)	2000-2009	Transparency	Landsat 5	Semi-empirical models	Band 1 and 3	Ln(SDT) = −2.0298 + 2.7517 × Ln(B1:B3) −0.6022 × Ln(B1)	R2: 0.670	Puramente técnicos
(Kutser, 2012)	Lake Malären (Sweden)	1984–2011	CDOM	Landsat 5	Semi-empirical models	Ratio band 2 and 3	$y = 4.294x^{2.105}$	R2: 0.62	Puramente técnicos
(Lobo et al., 2015)	Tapajós River Basin (Brazil)	1973-2013	SPM	Landsat 5	Semi-empirical models	Red band	y = 2.64 * (x-2.27)^0.45	R2: 0.94	Ambientales sobre análisis de tendencias temporales o espaciales
(Mancino et al., 2009)	Monticchio lakes (Italy)	2001	Chl-a	Landsat 5	Empirical Models	Band 1, 2 and 3	$Chl - a = a + b\frac{TM3}{TM2} + c\frac{TM1}{TM2} + dTM2 + e\frac{TM2}{TM1}$	R2: 0.82	Puramente técnicos
(Mancino et al., 2009)	Monticchio lakes (Italy)	2001	Transparency	Landsat 5	Empirical Models	Band 1, 2 and 3	$SD = a + b\frac{TM3}{TM2} + c\frac{TM1}{TM2} + dTM1 + e\frac{TM2}{TM1}$	R2: 0,72	Puramente técnicos
(Simon et al., 2014)	Lake Bariousses, Lake Bimont (France)	2006-2013	Temperature	Landsat 5	Semi-Analytical Models	Band 6	(Jimenez-Munoz et al., 2009)	R2>0.9, RMSE: 1–2°C	Técnicos con alguna aplicación ambiental.
(Imen et al., 2015)	Lake Mead (United States)	2005-2009	TSS	Landsat 5	Machine Learning Models		Not reported. Nonlinear autoregressive neural network with external input (N	R2: 0.98, RMSE: of 0.5	Ambientales sobre análisis de tendencias temporales o espaciales
(Lymburner et al., 2016)	19 lakes (Australia)	1988-2013	TSS	Landsat 5	Semi-Analytical Models	$\text{TSM index} = (\text{green} + \text{red})/2$	TM & ETM+ $y = 3983x^{1.6246}$ OLI $y = 3957x^{1.6436}$	R2 = 0.97	Técnicos con alguna aplicación ambiental.
(Concha & Schott, 2016)	Long Pond and Cranberry Pond (United States)	3 dates (2013, 2014, 2015)	Chl-a	Landsat 8	Semi-empirical models	440 nm	least square error minimization algorithm	R2: 0,84	Técnicos con alguna aplicación ambiental.
(Concha & Schott, 2016)	Long Pond and Cranberry Pond (United States)	3 dates (2013, 2014, 2015)	TSS	Landsat 8	Semi-empirical models	440 nm	least square error minimization algorithm	R2: 0,88	Técnicos con alguna aplicación ambiental.
(Concha & Schott, 2016)	Long Pond and Cranberry Pond (United States)	3 dates (2013, 2014, 2015)	CDOM	Landsat 8	Semi-empirical models	440 nm	least square error minimization algorithm	R2: 0,98	Técnicos con alguna aplicación ambiental.
(Shahzad et al., 2018)	Indus Delta Region (Pakistan)	November 6, 2001; March 2	TSS	Landsat 7	Empirical Models	Band 1, 2 , 3, 4 y 5	$\text{NDSSI} = \frac{\text{B1}-\text{B4}}{\text{B1}+\text{B4}}$ $\text{SSC}_{\text{FRM}} = \text{a} + \text{b B1} + \text{c B2} + \text{d B3} + \text{e B5} + \text{f NDSSI}$	RMSE: 67.24 mg/L, MAE: 54.75 mg/L,; R2: 0,88	Puramente técnicos
(Malahlela, 2019)	5 Dams (South Africa)	2014 - 2018	TSS	Landsat 8	Semi-empirical models		$\text{NSMI} = \frac{(\rho_{\text{red}}) + (\rho_{\text{green}}) - (\rho_{\text{blue}})}{(\rho_{\text{red}}) + (\rho_{\text{green}}) + (\rho_{\text{blue}})}$ $\text{WSRI} = 1 - \frac{(\rho_{\text{SWIR}} - \rho_{\text{blue}})}{\rho_{\text{red}}}$ $\text{EGRI} = \frac{\rho_{\text{green}}}{(\rho_{\text{coastal}} + \rho_{\text{blue}})}$ 2.34 + (2.0 * NDVI) + (4.91 * NSMI) – (4.05 * EGRI) + (0.14 * WSRI)	R2 >0.7	Puramente técnicos
(Wang et al., 2018)	Pearl River Estuary (China)	1987–2015	TSS	Landsat 5-9	Semi-empirical models	Near infrared and red band	$Log(TSS) = \frac{-b \pm \sqrt{b^2 - 4a\left(c - \frac{Log(R_1)}{Log(R_2)}\right)}}{2a}, \left(b^2 - 4a\left(c - \frac{Log(R_1)}{Log(R_2)}\right) \geq 0\right)$	RMSE: 11.06 mg/L	Ambientales sobre análisis de tendencias temporales o espaciales
(Chen et al., 2017)	Lake Huron (Canada-United States)	2013	CDOM	Landsat 5	Semi-empirical models	Band 3 and 4	$C_{CDOM}(400) = 40.75e^{-2.463(R(563)/R(655))}$	R2=0.949 , RMSE =0.504 m−1	Puramente técnicos
(J. Wang & Chen, 2024)	Erhai Lake (China)	2013 - 2021	Chl-a	Landsat 8	Machine Learning Models	16 Spectral Index, Visible a	4R_rhos_10SI	R2 > 0.82, MAE < 1.3 mg m−3, RMSE < 1.7 mg m−3, and MAPE < 16 %.	Técnicos con alguna aplicación ambiental.
(He et al., 2021)	Dashahe Reservoir (China)	2013-2018 (2 images/year)	Chl-a	Landsat 8	Machine Learning Models	Bands 1 to 7	0.001B1 + 0.0926B2 + 0.009B3 − 0.111B4 + 0.081B5 − 0.075B6 + 0.039B7 + 6.	R2: 0,88, RMSE: 4.81	Ambientales sobre análisis de tendencias temporales o espaciales
(He et al., 2021)	Dashahe Reservoir (China)	2013-2018 (2 images/year)	Transparency	Landsat 8	Machine Learning Models	Bands 1 to 7	0.0050 × B2 + 0.0009 × B3 − 0.0058 × B4 + 0.0006 × B5 − 0.0111 × B6 + 0.0125	R2: 0.87, RMSE: 0.41	Ambientales sobre análisis de tendencias temporales o espaciales
(He et al., 2021)	Dashahe Reservoir (China)	2013-2018 (2 images/year)	Phosphorous	Landsat 8	Machine Learning Models	Bands 1 to 7	−0.00003 × B2 + 0.00003 × B3 + 0.00005 × B4 − 0.00004 × B5 + 0.0005 × B6 −	R2: 0.96, RMSE: 0.01	Ambientales sobre análisis de tendencias temporales o espaciales
(Dave et al., 2019)	Narmada River and Reserviors (Bargi, Ukai, and Ujjani) (India)	2017-2018	Chl-a	Landsat 8	Semi-empirical models	Bands 1, 2 and 3	Chlorophyll-a = -11.734×Rrs(B1/B3)+11.064 Chlorophyll-a=65.55×Rrs(B2/B3)- 31.419	R2:0.62, RMSE: 27.85%; R2=0.72, RMSE=23.69%	Puramente técnicos
(Dave et al., 2019)	Narmada River and Reserviors (Bargi, Ukai, and Ujjani) (India)	2017-2018	Turbidity	Landsat 8	Semi-empirical models	Bands 3, 4 and 5	0.38 − 0.0034*Rrs(B3) + 0.00621*Rrs(B4) − 0.0016*Rrs(B5)	R2: 0.62, RMSE: 34.70%	Puramente técnicos
(Bangira et al., 2024)	Olushandja Dam (Namibia)	2014- 2015	Turbidity	Landsat 8	Semi-empirical models	Bands 2, 3, 4 and 5	=15.31856 − 956.806(λ2) − 747.376 (λ3) + 1,742.455 (λ4) + 165.173(λ5)	R2 = 0.767	Ambientales sobre análisis de tendencias temporales o espaciales
(Bangira et al., 2024)	Olushandja Dam (Namibia)	2014- 2015	TSS	Landsat 8	Semi-empirical models	Bands 2, 3, 4 and 5	=27.08987 + 10.80036(λ2) − 507.708(λ3) + 95.37331(λ4) + 27.8424(λ5)	R2 = 0.284	Ambientales sobre análisis de tendencias temporales o espaciales
(Bangira et al., 2024)	Olushandja Dam (Namibia)	2014- 2015	Phosphorous	Landsat 8	Semi-empirical models	Bands 2, 3, 4 and 5	=− 0.00309 − 8.78139(λ2) − 4.99958(λ3) + 15.31713(λ4) − 0.3916(λ5)	R2 = 0.907	Ambientales sobre análisis de tendencias temporales o espaciales
(Masocha et al., 2018)	two reservoirs (Zimbabwe)	June 2013	Transparency	Landsat 8	Semi-empirical models	Bands 2 and 4	Chivero −7.4 + 3.6 * Band 2/4 Mazvikadei −9.4 + 5.3 * Band 2/4	R2 > 0.70	Ambientales sobre análisis de tendencias temporales o espaciales
(Masocha et al., 2018)	two reservoirs (Zimbabwe)	June 2013	Turbidity	Landsat 8	Semi-empirical models	Bands 2 and 4	Chivero −590.0 + 1445.9 * Band 4/2 Mazvikadei −51.1 + 137.5 * Band 4/2 (	R2 ≥ 0.6	Ambientales sobre análisis de tendencias temporales o espaciales
(Masocha et al., 2018)	two reservoirs (Zimbabwe)	June 2013	Chl-a	Landsat 8	Semi-empirical models	Bands 4 and 5	Chivero 65.7–4932.7 * Band 4 (Mazvikadei −26.5 + 67.4 * Band 5/4	R2 > 0.84, R2 = 0.69	Ambientales sobre análisis de tendencias temporales o espaciales
(Mohsen et al., 2021)	Lake Burullus (Egypt)	2010-2013	Chl-a	Landsat 7	Semi-empirical models	Band 1 and 3	Chl - a (µg/l) = - 4955.494 + 1464.215(B1/B3) + 4239.486(B3/B1) - 2592.982 (PC4)	R2 = 0.86; RMSE= 34.60	Técnicos con alguna aplicación ambiental.
(Mohsen et al., 2021)	Lake Burullus (Egypt)	2010-2013	TSS	Landsat 7	Semi-empirical models	Band 1 and 5	ln(TSS) (mg/l) = 8.102 + 61.766(B3 - B1) - 0.04(B1/B5)	R2 = 0.67, RMSE= 0.35	Técnicos con alguna aplicación ambiental.
(Mohsen et al., 2021)	Lake Burullus (Egypt)	2010-2013	Temperature	Landsat 7	Semi-empirical models	Band 6	$T = \frac{K_2}{\ln\left(\frac{K_1}{L_\lambda} + 1\right)}$	Not reported	Técnicos con alguna aplicación ambiental.
(Guo et al., 2023)	Lake Simcoe (Canada)	2013-2019	Chl-a	Landsat 8	Machine Learning Models	Bands 1-5, OC2, OC3, BGR,	Not reported	MAE ≤20.17%	Ambientales sobre análisis de tendencias temporales o espaciales
(Guo et al., 2023)	Lake Simcoe (Canada)	2013-2019	Phosphorous	Landsat 8	Machine Learning Models	Bands 1-5, OC2, OC3, BGR,	Not reported	MAE ≤20.17%	Ambientales sobre análisis de tendencias temporales o espaciales
(Guo et al., 2023)	Lake Simcoe (Canada)	2013-2019	Transparency	Landsat 8	Machine Learning Models	Bands 1-5, OC2, OC3, BGR,	Not reported	MAE ≤20.17%	Ambientales sobre análisis de tendencias temporales o espaciales
(Bernardo et al., 2019)	six reservoirs (Brazil)	2014 y 2016	TSS	Landsat 8	Semi-Analytical Models	561 nm and 665 nm.	Not reported. robust bio-optical model	r = 0.65, nRMSE = 18.70%	Puramente técnicos
(Du et al., 2020)	Songnen Plain (China)	1984 to 2018	TSS	Landsat 5, 7 and 8	Semi-empirical models	Red/Blue bands	b3 $y = 0.318e^{6.7756x}$	R2: 0.758	Ambientales sobre análisis de tendencias temporales o espaciales
(Yang, Du, et al., 2022)	Baiyangdian lake (China)	July 2019 - September 2019	Chl-a	Landsat 8	Machine Learning Models	Not reported	Not reported	R2 = 0.879	Técnicos con alguna aplicación ambiental.
(Arias-Rodriguez et al., 2021)	Five lakes (Mexico)	2012-2018	Chl-a	Landsat 8	Machine Learning Models	Not reported	Not reported	R2 = 0.18	Puramente técnicos
(Arias-Rodriguez et al., 2021)	Five lakes (Mexico)	2012-2018	Turbidity	Landsat 8	Machine Learning Models	Not reported	Not reported	R2 = 0.48	Puramente técnicos
(Arias-Rodriguez et al., 2021)	Five lakes (Mexico)	2012-2018	TSS	Landsat 8	Machine Learning Models	Not reported	Not reported	R2 = 0.42	Puramente técnicos
(Arias-Rodriguez et al., 2021)	Five lakes (Mexico)	2012-2018	Transparency	Landsat 8	Machine Learning Models	Not reported	Not reported	R2 = 0.33	Puramente técnicos
(Arias-Rodriguez et al., 2023)	Global (United States, France, Italy, Germany, Greece, Norway, Polan	2021-2022	Chl-a	Landsat 8	Machine Learning Models	FERT: Original bands + red	Random Forest + FERT	R2 0.81, RMSE: 23.92	Técnicos con alguna aplicación ambiental.
(Arias-Rodriguez et al., 2023)	Global (United States, France, Italy, Germany, Greece, Norway, Polan	2021-2022	Turbidity	Landsat 8	Machine Learning Models	FERT: Original bands + red	SVM + FERT	R2: 0.97, RMSE: 9.21	Técnicos con alguna aplicación ambiental.
(Arias-Rodriguez et al., 2023)	Global (United States, France, Italy, Germany, Greece, Norway, Polan	2021-2022	TSS	Landsat 8	Machine Learning Models	FERT: Original bands + red	SVM + FERT	R2: 0.89, RMSE: 16.02	Técnicos con alguna aplicación ambiental.
(Arias-Rodriguez et al., 2023)	Global (United States, France, Italy, Germany, Greece, Norway, Polan	2021-2022	Transparency	Landsat 8	Machine Learning Models	FERT: Original bands + red	Random Forest + FERT	R2: 0.88, RMSE: 1.18	Técnicos con alguna aplicación ambiental.
(Arias-Rodriguez et al., 2023)	Global (United States, France, Italy, Germany, Greece, Norway, Polan	2021-2022	Phosphorous	Landsat 8	Machine Learning Models	FERT: Original bands + red	Random Forest + FERT	R2: 0.84, RMSE: 0.15	Técnicos con alguna aplicación ambiental.
(Zhang et al., 2022)	Dongping Lake (China)	2013-2018	Chl-a	Landsat 8	Machine Learning Models	all bands and different ratio	convolutional long short-term memory (ConvLSTM) model	R2: 0.80	Técnicos con alguna aplicación ambiental.
(Zhang et al., 2022)	Dongping Lake (China)	2013-2018	Phosphorous	Landsat 8	Machine Learning Models	all bands and different ratio	convolutional long short-term memory (ConvLSTM) model	R2: 0.83	Técnicos con alguna aplicación ambiental.
(Markogianni et al., 2018)	Trichonis Lake (Greece)	October 2013 and August 20	Chl-a	Landsat 8	Semi-empirical models	Band 1, 2 and 3	Chl-a = −38.621 + 92.050 × [(B2/(B1 + B2 + B3)] + 2239.647 × [(B1 + B2)/2]	R2 = 0.92	Puramente técnicos
(Q. Wang et al., 2021)	Hulun Lake (China)	1986 - 2017	TSS	Landsat 7 and 8	Semi-empirical models	Band 4 (Landsat7), Band 5 (Landsat8)	$\text{TSM(Landsat OLI)} = 1060.38 \times \text{R}_{\text{rs,NIR}} - 21.08$ $\text{TSM(Landsat ETM+)} = 4582.6 \times \text{R}_{\text{rs,NIR}} - 17.18$	Landsat7: R2 = 0.89; Landsat8: R2 = 0.80	Ambientales sobre análisis de tendencias temporales o espaciales
(Zhu et al., 2020)	West Lake (China)	2013 - 2017	TSS	Landsat 8	Semi-empirical models	Band 3 and 4	$a_p(440) = 0.167 \times e^{6.22x}$	R2 = 0.82 and RMSE = 2.05 m−1	Técnicos con alguna aplicación ambiental.
(Abdelal et al., 2022)	King Talal Dam (Jordan)	2018 - 2019	Chl-a	Landsat 8	Semi-empirical models	Band 4 and 5	$y = 19332e^{-5.379x}$	R2: 0,71, RMSE: 39,88 mg/m3	Técnicos con alguna aplicación ambiental.
(Abdelal et al., 2022)	King Talal Dam (Jordan)	2018 - 2019	Turbidity	Landsat 8	Semi-empirical models	Band 1 and 3	y = 3.0221e 2.0488x	R2: 0,64; RMSE: 0,90 NTU	Puramente técnicos
(Lehmann et al., 2019)	23 lakes in Rotorua Lakes Region (New Zealand)	1999 - 2018	Transparency	Landsat 7 and Landsat 8	Empirical Models	Band blue, red, green	Secchi depth = 5.411–1,045 R_b + 47,870 R_b^2 − 678,400 R_b^3 + (9.674 R_b − 4.056 R_r) / R_g	r2 = 0.49, RMSE = 2.2 m	Ambientales sobre análisis de tendencias temporales o espaciales
(Tian et al., 2024)	Qianwu reservoir, Longjing reservoir and Nanshan reservoir (China)	2021-2022	Chl-a	Landsat 7	Semi-empirical models	Band 1, 2 and 3	(B2+B3)/(B1+B1)	R2: 0,47	Ambientales sobre análisis de tendencias temporales o espaciales
(Tian et al., 2024)	Qianwu reservoir, Longjing reservoir and Nanshan reservoir (China)	2021-2022	TSS	Landsat 7	Semi-empirical models	Band 3, 4 and 5	(B3+B5)/(B4+B4)	R2: 0.62	Ambientales sobre análisis de tendencias temporales o espaciales
(Tian et al., 2024)	Qianwu reservoir, Longjing reservoir and Nanshan reservoir (China)	2021-2022	Turbidity	Landsat 7	Semi-empirical models	Band 2, 3 and 4	B4/(B3–B2)	R2: 0,44	Ambientales sobre análisis de tendencias temporales o espaciales
(Y. Yang et al., 2023)	Lake Dianchi (China)	1998 - 2020	Chl-a	Landsat 5 and 8	Machine Learning Models	BLUE, GREEN, RED, NIR	not reported	MAE = 15.22 µg·L−1, bias = 9.69%, MAPE = 47.09%	Puramente técnicos
(Zeng et al., 2023)	4 Yunnan Plateau lakes (China)	January 2013–August 2022	Transparency	Landsat 8	Empirical Models	Not reported	Not reported	RMSE: 0.7715m, MAE: 0.5559m, R2: 0.8641	Puramente técnicos
(Zeng et al., 2023)	4 Yunnan Plateau lakes (China)	January 2013–August 2022	Transparency	Landsat 8	Machine Learning Models	Not reported	Not reported	RMSE: 0.2358m, MAE: 0.0659m, R2: 0.9873	Puramente técnicos
(Dallosch & Creed, 2021)	Lakes (United States and Sweden)	1984–2016	Chl-a	Landsat 5, 7 and 8	Machine Learning Models	Not reported	B/R	R2: 0.91,	Técnicos con alguna aplicación ambiental.
(Robert et al., 2017)	Agoufou Lake (Mali)	2000-2017	TSS	Landsat 7 and 8	Semi-empirical models	NIR and red bands	Not reported	R2:0,84	Técnicos con alguna aplicación ambiental.
(El-Alem & Chokmani, 2022)	Lakes in Quebec (Canada)	2014-2017	Turbidity	Landsat 7 and 8	Machine Learning Models	Red, Blue and SWIR1	Not reported	R2=0.99	Puramente técnicos
(Erena et al., 2019)	Mar menor lagoon (Spain)	2015-2017	Turbidity	Landsat 8	Semi-empirical models	Band 3 and 4	Turbidity (NTU) = 1.7746·exp{9.1066[(Ref$_{\text{GREEN}}$ − Ref$_{\text{RED}}$)/Ref$_{\text{GREEN}}$ + Ref$_{\text{RED}}$)]}	R2 = 0.775	Ambientales sobre análisis de tendencias temporales o espaciales
(Erena et al., 2019)	Mar menor lagoon (Spain)	2015-2017	Chl-a	Landsat 8	Semi-empirical models	Band 2 and 3	[Cla] (mg/m^3) = 0.6386·exp{4.7513[(Ref$_{\text{GREEN}}$ − Ref$_{\text{BLUE}}$)/Ref$_{\text{GREEN}}$ + Ref$_{\text{BLUE}}$)]}	R2 = 0.8867	Ambientales sobre análisis de tendencias temporales o espaciales
(Oliphant et al., 2018)	the Vaal Dam (South Africa)	2014–2016	Chl-a	Landsat 8	Semi-empirical models	Bands 3, 4 and 5	$\text{chl-}a = \frac{\exp^{(22.7800-(0.0025 \times \beta_4)+(0.0001 \times \beta_5))}}{(1+\exp^{(22.7800-(0.0025 \times \beta_4)+(0.0001 \times \beta_5))})}$ $\text{chl-}a = \frac{\exp^{(6.9989+(0.0027 \times \beta_3))}}{(1+\exp^{(6.9989+(0.0027 \times \beta_3))})}$ $\text{chl-}a = \frac{\exp^{(1.090+(36.308 \times \beta_3))}}{(1+\exp^{(1.090+(36.308 \times \beta_3))})}$	k (2014): 0.74, k (2015): 0.30, k(2016): 0.43	Técnicos con alguna aplicación ambiental.
(Deutsch et al., 2022)	lakes across southern (Canada)	2017–2020	Transparency	Landsat 8	Empirical Models	Bands 2 and 4	$\text{SD} = \exp^{(0.37+2.15*\ln(\text{Blue/ Red}))}$	R2 = 0.65	Técnicos con alguna aplicación ambiental.
(Deutsch et al., 2021)	lakes across southern (Canada)	2013–2019	Transparency	Landsat 8	Semi-empirical models	Bands 2 and 4	$\text{SD} = \exp^{(0.37+2.15*\ln(\text{Blue/ Red}))}$	RMSE: 1.75, Bias: 0.261, R2: 0.645	Puramente técnicos

(Y. Zhang et al., 2016)	Xin'anjiang Reservoir (China)	December 2013 - April 2015	TSS	Landsat 8	Semi-Analytical Models	Band 4	$\mathrm{TSM} \propto a \times (R_{rs}^{-1}(\lambda_1) - R_{rs}^{-1}(\lambda_2)) \times R_{rs}(\lambda_3) + b.$ $\mathrm{TSM} = 38.08 \times [0.42 \times ((R_{rs}(450-515)+R_{rs}(525-600))^{-1} - (R_{rs}(525-600)+R_{rs}(630-680))^{-1}) \times R_{rs}(630-680) + 0.24] - 3.39.$	R 2 = 0.85, NRMSE = 23%	Técnicos con alguna aplicación ambiental.
(Y. Zhang et al., 2021)	various lakes (China)	2016 - 2018	Transparency	Landsat 5, 7 and 8	Semi-empirical models	Band red	$\mathrm{SDD} = 0.0046 R_{rs}(\mathrm{red})^{-1.26}$	R2: 0.73, MRE: 34.2%, NRMSE: 55.4%	Puramente técnicos
(Markogianni et al., 2020)	50 lake water bodies (Greece)	2013–2016 and 2018	Chl-a	Landsat 7 and 8	Semi-empirical models	Blue, red, swir bands	$\log Chla = 3.599 - 0.63 \times \left(\frac{blue}{red}\right) - 2.183 \times \left(\frac{\ln red}{\ln swir2}\right).$	natural (R = 0.78; RMSE = 1.3 μg/L) and artificial lakes (R = 0.76; RMSE = 1.29 μg/L)	Técnicos con alguna aplicación ambiental.
(Villota-González et al., 2023)	Cajititlán and Zapotlán lakes (Mexico)	2013-2023	Chl-a	Landsat 8	Machine Learning Models	L8-b3 (green), L8-b4 (red)	Not reported	r2 = 0.71, RMSE = 6.16 mg/m3, MAE = 4.97 mg/m3	Puramente técnicos
(Villota-González et al., 2023)	Cajititlán and Zapotlán lakes (Mexico)	2013-2023	TSS	Landsat 8	Machine Learning Models	L8-b3 (green), L8-b4 (red)	Not reported	r2 = 0.72, RMSE = 2.71 mg/L, MAE = 2.12 mg/L	Puramente técnicos
(Villota-González et al., 2023)	Cajititlán and Zapotlán lakes (Mexico)	2013-2023	Turbidity	Landsat 8	Machine Learning Models	L8-b3 (green), L8-b4 (red)	Not reported	r2 = 0.75, RMSE = 2.05 NTU, MAE = 1.10 NTU	Puramente técnicos
(Coelho et al., 2017)	Marengo, Paus Branco and São Nicolau reservoirs (Brazil)	2014-2015	Chl-a	Landsat 8	Semi-empirical models	Band 2 and 5	$\mathrm{Chl} = 14.70 \times I2^{2.94}$	NSE = 0.66, RMR = 0.57, PBIAS = 0.24	Técnicos con alguna aplicación ambiental.
(Coelho et al., 2017)	Marengo, Paus Branco and São Nicolau reservoirs (Brazil)	2014-2015	CDOM	Landsat 8	Semi-empirical models	band 3	$\mathrm{CDOM} = 0.59 \times I5^{-0.53}$	NSE = 0.89, RMR = 0.56 and PBIAS = 0.09	Técnicos con alguna aplicación ambiental.
(Meng et al., 2022)	Shanmei Reservoir (China)	2020 - 2022	Turbidity	Landsat 8-9	Semi-empirical models	Bands 2, 3 and 4	$y = -2.78 \times x + 2.30$ (B2 − B4)/B3	R2: 0,80	Ambientales sobre análisis de tendencias temporales o espaciales
(Meng et al., 2022)	Shanmei Reservoir (China)	2020 - 2022	Chl-a	Landsat 8-9	Semi-empirical models	Bands 2, 3 and 4	$y = -14.61 \times x + 10.98$ B2/(B3 + B4)	R2: 0,70	Ambientales sobre análisis de tendencias temporales o espaciales
(Yin et al., 2022)	Lake Taihu (China)	1984 - 2020	TSS	Landsat 5 and 8	Semi-empirical models	Bands red, green and NIR	TM:$1.66 * e^{2.91*X}$ OLI: $2.02 * e^{2.99*X}$ $(R_{rs}(red) + R_{rs}(NIR)) / R_{rs}(green)$	R2 TM:0.83, R2 OLI:0.81	Técnicos con alguna aplicación ambiental.
(Guo et al., 2022)	Lake Simcoe (Canada)	1984 - 2020	Chl-a	Landsat 5, 7 and 8	Machine Learning Models	Not reported	Not reported	MAE = 32.57%, Bias = 10.61%	Ambientales sobre análisis de tendencias temporales o espaciales
(Guo et al., 2022)	Lake Simcoe (Canada)	1984 - 2020	Phosphorous	Landsat 5, 7 and 8	Machine Learning Models	Not reported	Not reported	MAE = 42.58%, Bias = −2.82%	Ambientales sobre análisis de tendencias temporales o espaciales
(Cui et al., 2022)	Chaohu Lake, Shengjin Lake, and Jiaogang Lake (China)	2013–2019	Transparency	Landsat 8	Machine Learning Models	Not reported	Not reported	R2 = 0.89, RMSE = 11.48 cm, and RPD =3.0	Puramente técnicos
(Chegoonian et al., 2023)	Buffalo Pound Lake (Canada)	2014–2020	Chl-a	Landsat 8	Machine Learning Models	Not reported	Not reported	MAPE: 40.23, RMSE: 27.43	Puramente técnicos
(Bernardo et al., 2020)	Tietê River Cascade System (Brazil)	2014 and 2016	TSS	Landsat 8	Semi-empirical models	Bands 2 and 3	TSS= 10.34 × [561 nm/482 nm]-12.32; B3/B2	RMSE = 6.5 mg/L, nRMSE = 32.97% and MAPE = 47.05%	Puramente técnicos
(Cao et al., 2022)	Yunnan–Guizhou Plateau (China)	2013 to 2022	CDOM	Landsat 8 and 9	Machine Learning Models	Band 3	Not reported. Mixing density network	R2 = 0.73, MdSA = 59.4%	Técnicos con alguna aplicación ambiental.
(Alcântara et al., 2016)	Barra Bonita hydroelectric reservoir (Brazil)	May and October 2014	CDOM	Landsat 8	Semi-empirical models	Bands 2 and 4	$a_{\mathrm{CDOM}}(440) = 2.70 \times \left(\frac{R_{rs}(650)}{R_{rs}(480)}\right)^2 - 6.14 \times \frac{R_{rs}(650)}{R_{rs}(480)} + 4.19$	R2 = 0.70, RMSE: 10.65%	Puramente técnicos
(M. Chen et al., 2022)	Honghu Lake (China)	1987–2020	Transparency	Landsat 5, 7 and 8	Semi-Analytical Models	656nm	adaptation of QAA_v6	R = 0.66, RMSE = 0.34	Técnicos con alguna aplicación ambiental.
(Zhao et al., 2022)	Hulun Lake (China)	2010 to 2020	Transparency	Landsat 5, 7 and 8	Semi-empirical models	Red, Blue and NIR	[red/(blue-near-infrared) $y = e^{(-31.752+69.103x-39.08x^2)}$	RMSE = 0.055 m, MAE = 0.003 m	Técnicos con alguna aplicación ambiental.
(Markogianni et al., 2014)	Koumoundourou Lake (Greece)	2003 - 2011	Chl-a	Landsat 5	Semi-empirical models	Band 2 and 4	B2/B4 $y = 3.0527x^2 - 22.821x + 45.438$	R2: 0.85	Técnicos con alguna aplicación ambiental.
(Li et al., 2018)	Lake Huron (Canada-United States)	2013 and 2015	CDOM	Landsat8	Semi-Analytical Models	Band 3	Shallow Water Bio-optical Properties (SBOP) algorithm	RMSE = 0.17, R2 = 0.87	Ambientales sobre análisis de tendencias temporales o espaciales
(Kutser et al., 2016)	Nohipalu Mustjärv, Meelva, and Mustjärv lakes (Estonia)	July 2013	Chl-a	Landsat8	Semi-empirical models	Band 5	Not reported	R2: 0.70	Técnicos con alguna aplicación ambiental.
(L. Wang et al., 2020)	12 lakes (United States)	2013 - 2017	Chl-a	Landsat 7 and 8	Machine Learning Models	Not reported	Not reported	RMSE: 4.424, MAPE: 34.17%	Puramente técnicos
(Watanabe et al., 2015)	Barra Bonita reservoir (Brazil)	2013-2014	Chl-a	Landsat8	Semi-empirical models	Bands 3 and 5	−149.72 + 2557.24(NIR/Green) + −2565.99(NIR/Green)²	NRMSE: 82.39%; MAPE: 36.02%; bias: -126.47; MNB: 35.13%; R2:0.1929	Técnicos con alguna aplicación ambiental.
(Peterson et al., 2020)	Several waterbodies in Midwestern (United States)	2013–2018	Chl-a	Landsat8	Machine Learning Models	all bands and different rati	Not reported	R2:0.88	Técnicos con alguna aplicación ambiental.
(Peterson et al., 2020)	Several waterbodies in Midwestern (United States)	2013–2018	Turbidity	Landsat8	Machine Learning Models	all bands and different rati	Not reported	R2:0.84	Técnicos con alguna aplicación ambiental.
(Ledesma et al., 2019)	Cassaffousth reservoir (Argentina)	2016 -2017	Chl-a	Landsat8	Semi-empirical models	Bands 2, 4, 6, 7 and 8	$\log Chl\text{-}a = 1.04 + 1.64 * \frac{b_{\mathrm{blue}}}{b_{\mathrm{red}}} - 0.53 * \frac{b_{\mathrm{SWIR-1}}}{b_{\mathrm{pan}}} - 7.26 * b_{\mathrm{pan}} - 0.23 * \frac{b_{\mathrm{SWIR-2}}}{b_{\mathrm{SWIR-1}}}$	R2: 0.87	Técnicos con alguna aplicación ambiental.
(Amado-Alvarez et al., 2019)	Vírgenes dam, the Colina lake, and La Boquilla dam (Mexico)	22 de marzo de 2011	Turbidity	Landsat 5	Semi-empirical models	Bands 2 and 3	TM2/TM3	R2: -0.80	Técnicos con alguna aplicación ambiental.
(Hafeez et al., 2022)	Eight lakes (China)	2013-2019	TSS	Landsat8	Semi-empirical models	Not reported	Not reported	Not reported	Puramente técnicos
(F. Zhang et al., 2021)	Guanting Reservoir (China)	1985 -2019	Chl-a	Landsat 5, 7 and 8	Semi-empirical models	NIR and Blue	(RNIR – RB)/(RNIR + RB)	MRE: 25.7%, RMSE: 5.65 mg m–3	Técnicos con alguna aplicación ambiental.
(Koll-Egyed et al., 2021)	128 Southern lakes (Canada)	2017 - 2019	CDOM	Landsat 8	Semi-empirical models	Band 2, 3 and 4	ln(CDOM(a440)) = a − b(ln(B3/B4)) − c(ln(B2)	R2: 0.66; RMSE: 0.59	Puramente técnicos
(Lu et al., 2023)	107 lakes and reservoirs in Yangtze Plain (China)	1984 - 2020	Transparency	Landsat 5, 7 and 8	Semi-empirical models	Bands 1, 3 and 4	Rrs(443)/Rrs(655) - Rrs(443)/Rrs(560)	R2 = 0.87, MAPE = 28.04%, RMSE = 0.76 m	Técnicos con alguna aplicación ambiental.
(Song et al., 2020)	2759 lakes (China)	2013–2018	Transparency	Landsat 8	Semi-empirical models	bands 2 and 4	Not reported	R2 = 0.75	Técnicos con alguna aplicación ambiental.
(Z. Yang et al., 2023)	Taihu Lake	2018 - 2022	Turbidity	Landsat 8 and 9	Machine Learning Models	NIR bands	Not reported	R2 = 0.93, MAPE = 16.20%	Técnicos con alguna aplicación ambiental.
(Nascimento Silva et al., 2017)	Reservoir of Tocantins river (Brazil)	2007 - 2014	Chl-a	Landsat 7	Machine Learning Models	Not reported	Not reported	Not reported	Puramente técnicos
(Nascimento Silva et al., 2017)	Reservoir of Tocantins river (Brazil)	2007 - 2014	Transparency	Landsat 7	Machine Learning Models	Not reported	Not reported	Not reported	Puramente técnicos
(Nascimento Silva et al., 2017)	Reservoir of Tocantins river (Brazil)	2007 - 2014	TSS	Landsat 7	Machine Learning Models	Not reported	Not reported	Not reported	Puramente técnicos
(Rodrigues et al., 2017)	Nav reservoir (Brazil)	2014 -2016	Transparency	Landsat 8	Semi-Analytical Models	Not reported	QAAv5	RMSD 0.32 - 0.90 m, MAPE 8.65 - 19.75%	Puramente técnicos
(W. ; Li et al., 2022)	Lake Qinghai (China)	1986 to 2020	TSS	Landsat 5, 7 and 8	Empirical Models	Red Band	TSM = 381.97 Rrs(Red) − 0.4805	R2: 0.81, MRE: 17.91%, and RMSE: 0.61 mg/L	Técnicos con alguna aplicación ambiental.
(Ha et al., 2017)	10 hypertrophic lakes in Hanoi (Vietnam)	2015 - 2016	Chl-a	Landsat 8	Empirical Models	Band 2 and 3	GrB2: R(562)/R(483) $\mathrm{Chl}_a(\mu g/L) = 28.1 \cdot e^{0.72 \cdot \mathrm{GrB}_2}$	r2=0.82	Técnicos con alguna aplicación ambiental.
(Papoutsa et al., 2014)	Asprokremmos Reservoir (Cyprus)	May 2010–October 2010	Turbidity	Landsat 7	Empirical Models	Band 3	Band 3	R2 = 0.85	Técnicos con alguna aplicación ambiental.
(Jakovljevic et al., 2023)	main water bodies (Serbia)	1984-2021	TSS	Landsat 5, 7 and 8	Machine Learning Models	Not reported	Not reported	RMSE: 1.89	Puramente técnicos
(Jakovljevic et al., 2023)	main water bodies (Serbia)	1984-2021	Chl-a	Landsat 5, 7 and 8	Machine Learning Models	Not reported	Not reported	RMSE: 0.34	Puramente técnicos
(Jakovljevic et al., 2023)	main water bodies (Serbia)	1984-2021	Phosphorous	Landsat 5, 7 and 8	Machine Learning Models	Not reported	Not reported	RMSE: 0.04	Puramente técnicos
(X. Zhao et al., 2021)	Taihu Lake (China)	2017	Chl-a	Landsat 8	Machine Learning Models	Band 3 and 4	NDV: B4/B3 $Y = 14.85988184091882 * x^{(-4.582236735711132)}$	MSE: 1.436	Puramente técnicos
(Alcântara, Curtarelli, et al., 20	Itumbiara hydroelectric reservoir (Brazil)	2014	TSS	Landsat 8	Semi-Analytical Models	Band 3	$\mathrm{TSM} = 0.907 + 5.479 \times bbp(561) + \xi$	R2 = 0.82, RMSE = 41.39%	Puramente técnicos
(Ren et al., 2018)	Three Gorges and Dongting Lake (China)	2013 - 2017	Transparency	Landsat 8	Semi-empirical models	red and green	$Z_{SD} = 1.7351^* \exp\left(-2.141^* \frac{R_{rs}(B4)}{R_{rs}(B3)}\right)$	MAPE: 21.68%, RMSE: 0.076 m	Puramente ambientales
(Adusei et al., 2021)	Owabi reservoir (Ghana)	Dec 2019	Turbidity	Landsat 8	Machine Learning Models	Green, blue and red	Not reported	R2: 0.99, RMSE: 0.29	Puramente técnicos
(Adusei et al., 2021)	Owabi reservoir (Ghana)	Dec 2019	TSS	Landsat 8	Machine Learning Models	Green, blue , red and SWIR	Not reported	R2: 0.99, RMSE: 0.45	Puramente técnicos
(Maciel et al., 2023)	300+ water bodies (global)	1985-2022	Transparency	Landsat 5, 7 and 8	Machine Learning Models	all bands and 2 semi-analyt	Not reported	ε ~ 39% and β ~ 8%	Puramente técnicos
(Lamaro et al., 2013)	Río Tercero (Argentina)	2000-2006	Temperature	Landsat 7	Semi-Analytical Models	Thermal	single-channel generalized method (SCGM)	R2: 0.9584, RMS = 1.0426	Puramente técnicos
(Ghirardi et al., 2023)	Gravel and sand Pit lakes in Po River basin (Italy)	1990 to 2021	TSS	Landsat 5, 7 and 8	Empirical Models	Red	Not reported	R2: 0.85, MAE: 1.12, RMSE: 1.59	Técnicos con alguna aplicación ambiental.
(Papoutsa, Akylas, et al., 2014)	four different Case-2 waters (Cyprus and Greece)	2010	Transparency	Landsat 5	Semi-empirical models	Band2/Band3	$y = 102e^{-0.24x}$	R2=0.89	Puramente técnicos
(Barreneche et al., 2023)	Continental water bodies (Uruguay)	2004–2020	Chl-a	Transparency	Semi-empirical models	Not reported	Mixture Density Networks (MDNs)	MSA: 80.41%, e: 64.42%	Puramente técnicos
(Rubin et al., 2021)	Several lakes (United States)	1984–2017	Transparency	Landsat 5, 7 and 8	Machine Learning Models	NIR, Green, Blue, red	Random Forest	MAE: 0.47 m–0.86 m, RMSE: 0.66m–1.13 m	Puramente técnicos
(Vinh et al., 2019)	Thac Ba Reservoir (Vietnam)	2018	Chl-a	Landsat 5, 7 and 8	Empirical Models	green and red band	B3 / B4 **y=3.24*x+7.68**	R2 = 0.82; RMSE ~ 5%	Técnicos con alguna aplicación ambiental.
(Martins et al., 2018)	Funil hydroeletric reservoir (Brazil)	1995 to 2010	CDOM	Landsat 5	Semi-empirical models	B4/B1	B4/B1	R2 = 0.91, p < 0.0001, RMSE = 7%	Técnicos con alguna aplicación ambiental.
(Sun et al., 2024)	Pearl River Estuary (China)	1987-2022	TSS	Landsat 5, 7 and 8	Semi-Analytical Models	Not reported	quasi-analytical algorithm (QAA) algorithm	MAPE = 24.44%, RMSE = 12.86 mg/L, and R2 = 0.7	Técnicos con alguna aplicación ambiental.
(V. S. Martins et al., 2018)	Sobradinho reservoir (Brazil)	2013–2017	Turbidity	Landsat 8	Empirical Models	Red	$Y_i = 0.026 * X_i^{(0.451)}$	R2: 0.822	Ambientales sobre análisis de tendencias temporales o espaciales
(Olmanson et al., 2020)	10.000+ Minnesota lakes (United States)	2015 and 2016	CDOM	Landsat 8	Semi-empirical models	3, 4 and 5	$\ln(a_{440}) = a(R_{rs}(B4)/R_{rs}(B3)) + b(R_{rs}(B5)/R_{rs}(B3)) + c$	R2 = 0.83, RMSE = 0.52	Ambientales sobre análisis de tendencias temporales o espaciales
(Surisetty et al., 2018)	Chilika Lagoon (India)	2014	Turbidity	Landsat 8	Empirical Models	bands 3 and 4	Band 4/band 3 $T = 23.09\left(\frac{r - 0.233}{1.28 - r}\right)$	R2 = 0.87	Técnicos con alguna aplicación ambiental.
(Q. Wang et al., 2022)	Several lakes (United States, canada and Mexico)	1990–2019	Transparency	Landsat 5, 7 and 8	Semi-empirical models	blue/green plus blue/red	$\mathrm{LN(SDD)_{OLI}} = -0.76 * \mathrm{R/B} + 5.11 * \mathrm{B/G} - 1.37$ $\mathrm{LN(SDD)_{ETM+}} = -2.36\mathrm{R/B} + 3.65\mathrm{B/G} + 1.48$ $\mathrm{LN(SDD)_{TM}} = -2.81 * \mathrm{R/B} + 2.73 * \mathrm{B/G} + 2.96$	R2 = 0.78, MAPE = 30.85 %	Técnicos con alguna aplicación ambiental.
(N. Cao et al., 2023)	Ebinur Lake (China)	2014 - 2021	CDOM	Landsat 8	Semi-Analytical Models	443 nm, 483 nm, 561 nm, 6	Quasi-Analytical Algorithm Dissolved Organic Matter (QAA-CDOM) model	R2: 0.69, RMSE: 0.12 m−1	Técnicos con alguna aplicación ambiental.
(Tao et al., 2022)	10.814 lakes (China)	1984 - 2018	Transparency	Landsat 5, 7 and 8	Empirical Models	Red and blue	red/blue	R2 = 0.79, RMSE = 100.30 cm	Puramente ambientales
(X. Yang et al., 2020)	Donghu Lake (China)	1987–2018	Chl-a	Landsat 5, 7 and 8	Semi-empirical models	green and red band	[(Green − Red)/(Green + Re $y = 2712.522x^3 + 1817.634x^2 - 1100.945x + 149.714$	R2: 0.831, RE: 6.509%, RMSE: 19.846μg/L	Técnicos con alguna aplicación ambiental.
(Somasundaram et al., 2021)	550 reservoirs (Sri Lanka)	2013 to 2020	Transparency	Landsat 8	Semi-Analytical Models	443,483,555, and 670	quasi-analytical algorithm: QAA_v6	RMSE: 32.60cm, MAD: 28.44cm, R2: 0.67	Ambientales sobre análisis de tendencias temporales o espaciales
(Markogianni et al., 2022)	50 lakes (Greece)	2013–2016 and 2018	Chl-a	Landsat 7 and 8	Semi-empirical models	Blue, red, swir2	$\log\mathrm{Chl}a = 3.599 - 0.63 * \left(\frac{\mathrm{blue}}{\mathrm{red}}\right) - 2.183 * \left(\frac{\mathrm{lnred}}{\mathrm{lnswir2}}\right)$	Not reported	Técnicos con alguna aplicación ambiental.
(Markogianni et al., 2022)	50 lakes (Greece)	2013–2016 and 2018	Transparency	Landsat 7 and 8	Semi-empirical models	Blue, red, green and swir2	$\mathrm{SQRT(Secchi)_{general}} = 1.215 - 2.479 * \left(\mathrm{blue} + \mathrm{red} + \frac{\mathrm{red}}{\mathrm{blue}}\right) + 3.394 * \left(\frac{\mathrm{lngreen}}{\mathrm{lnswir2}}\right)$	Secchigeneral: R = 0.78; RMSE = 0.24 m), natural (Secchinatural; R = 0.95; RMSE = 0.14 m) and artificial (Secchiartificial; R = 0.62; RMSE = 0.1 m	Técnicos con alguna aplicación ambiental.
(Markogianni et al., 2022)	50 lakes (Greece)	2013–2016 and 2018	Phosphorous	Landsat 7 and 8	Semi-empirical models	red and swir1	$\mathrm{LogTPgeneral} = -1.425 + 0.452 * \log\mathrm{Chl}a - 0.573 * \left(\frac{\mathrm{lnred}}{\mathrm{lnswir1}}\right)$	TPgeneral (R = 0.71; RMSE = 1.41 mg/L) and TPnatural model (R = 0.93; RMSE = 1.43 mg/L)	Técnicos con alguna aplicación ambiental.
(Pahlevan et al., 2022)	Global	Not reported	Chl-a	Landsat 8	Machine Learning Models	Not reported	Not reported	e: 59.1, RMSLD: 0.86	Puramente técnicos
(Pahlevan et al., 2022)	Global	Not reported	TSS	Landsat 8	Machine Learning Models	Not reported	Not reported	e: 0.74, RMSLD: 40.6	Puramente técnicos
(Pahlevan et al., 2022)	Global	Not reported	CDOM	Landsat 8	Machine Learning Models	Not reported	Not reported	e: 37.9, RMSLD: 0.53	Puramente técnicos
(Mushtaq et al., 2022)	Wular Lake (India)	October 2018	Chl-a	Landsat 8	Semi-empirical models	NIR, Blue and Green	$[\rho w(865) - \rho w(482)/\rho w(561)]$ $y = 126.27x + 62.24$	R2 = 0.89, SEE: 0.77 μg/L, MAPE: 5.83%	Técnicos con alguna aplicación ambiental.
(Mushtaq et al., 2022)	Wular Lake (India)	October 2018	Transparency	Landsat 8	Semi-empirical models	NIR	$[\rho w^{-1}(865)]$ $y = 0.01e^{0.57x}$	R2 = 0.84, SEE: 0.11 μg/L, MAPE: 13.93%	Técnicos con alguna aplicación ambiental.
(Tebbs et al., 2013)	Lake Bogoria (Kenya)	2003-2005	Chl-a	Landsat 7	Empirical Models	NIR	$\mathrm{Chl} - a = (53 \pm 52) + (8259 \pm 1013) R_{835} \pm 55\ \mu g\ l^{-1}.$	R2 = 0.847; Standard error, SE = 55 μg l− 1	Técnicos con alguna aplicación ambiental.
(Wermuth et al., 2022)	Pampulha reservoir (Brazil)	2013-2020	Temperature	Landsat 8	Semi-Analytical Models	Thermal	the Split-Window (SW) algorithm	RMSE = 1.48 C, R2 = 0.63	Técnicos con alguna aplicación ambiental.
(Song et al., 2022)	Global	1984–2020	Transparency	Landsat 5, 7 and 8	Semi-empirical models	Red and blue	$\mathrm{Ln(SDD)} = -2.93 \times \mathrm{R/B} + 2.83 \times \mathrm{B/G} + 2.81$	R2 = 0.76, MAPE = 38.8%	Ambientales sobre análisis de tendencias temporales o espaciales
(F. Yang et al., 2023)	Honghu Lake (China)	2000-2021	Transparency	Landsat 5, 7 and 8	Semi-empirical models	Not reported	Not reported	R2 = 0.723, RMSE = 4.971	Técnicos con alguna aplicación ambiental.
(Setiawan et al., 2019)	Lake Maninjau (Indonesia)	1987–2018	Transparency	Landsat 7	Semi-empirical models	1, 2 and 3	–1.18 + 3.45(TM1/TM2) – 2.67(TM3/TM2)	R2: 0.60, RMSE: 1.01 m	Técnicos con alguna aplicación ambiental.
(Yépez et al., 2024)	Laguna Grande de San Pedro de la Paz (Chile)	2014–2022	Chl-a	Landsat 8	Semi-empirical models	3 and 5	green chlorophyll index (GCI): (B5/B3) − 1 $Chla = 1.97 \times e^{(-1.46 \times GCI)}$	R2: 0.88	Técnicos con alguna aplicación ambiental.
(Yépez et al., 2024)	Laguna Grande de San Pedro de la Paz (Chile)	2014–2022	Turbidity	Landsat 8	Semi-empirical models	4 and 5	red + NIR spectral index: B4 + B5 $Turbidity = 0.51 \times e^{(130.75 \times (Red+NIR))}$	R2: 0.79	Técnicos con alguna aplicación ambiental.
(Tanner et al., 2022)	Utah Lake (United States)	1984 to 2021	Chl-a	Landsat 5, 7 and 8	Semi-empirical models	SWIR1 and Blue	$\mathrm{chl\text{-}a} = e^{\left(-1.53 + 2.55\frac{b5}{b1} - 1.15 \times \ln(b1)\right)}$	Not reported	Ambientales sobre análisis de tendencias temporales o espaciales
(Huang et al., 2015)	Alaska lakes (United States)	July to August 2013	Temperature	Landsat 8	Empirical Models	Thermal	single window algorithm	Not reported	Técnicos con alguna aplicación ambiental.
(Tavares et al., 2019)	Lake Mangueira (Brazil)	Not reported	Temperature	Landsat 7	Empirical Models	Thermal	single window algorithm	Not reported	Puramente técnicos
(Prats et al., 2018)	442 inland water bodies (France)	1999–2016	Temperature	Landsat 5 and 7	Semi-Analytical Models	Thermal	Adaptation COARE 3.0 algorithm	Not reported	Puramente técnicos
(Kong et al., 2024)	Poyang Lake (China)	2020 -2021	Temperature	Landsat 8	Semi-Analytical Models	Thermal	Split-Window Algorithm	Not reported	Técnicos con alguna aplicación ambiental.
(Kramer et al., 2023)	Itaipu Reservoir (Brazil)	2015-2017	Temperature	Landsat 8	Semi-Analytical Models	Thermal	Planck Equation algorithm	Not reported	Puramente técnicos
(Huang et al., 2017)	Arctic Lakes (United States)	2013	Temperature	Landsat 8	Semi-Analytical Models	Thermal	single thermal band	Not reported	Puramente técnicos